Title

Investigating the Factors Influencing Charge Transport in Chemically-Doped Semiconducting Polymer Thin Films and Their Impact on Thermoelectric Properties

Author

Duong, Quynh Muc

Publication Date

2024

Peer reviewed|Thesis/dissertation

UNIVERSITY OF CALIFORNIA

Los Angeles

Investigating the Factors Influencing Charge Transport in Chemically-Doped Semiconducting Polymer Thin Films and Their Impact on Thermoelectric Properties

A dissertation submitted in partial satisfaction of the

requirements for the degree Doctor of Philosophy

in Chemistry

by

Quynh Muc Duong

2024

ABSTRACT OF THE DISSERTATION

Investigating the Factors Influencing Charge
Transport in Chemically-Doped Semiconducting Polymer Thin Films
and Their Impact on Thermoelectric Properties

by

Quynh Muc Duong
Doctor of Philosophy in Chemistry
University of California, Los Angeles, 2024
Professor Benjamin J. Schwartz, Chair

Semiconducting polymers are an intriguing class of materials that have been attracting increasing attention over the years. As their name suggests, semiconducting polymers are used in similar fields as their inorganic counterparts, but they offer several advantages that make them particularly desirable. These polymers are solution-processable, flexible, and have intrinsically low thermal conductivity, all of which are important for applications such as wearable thermoelectric devices. The low thermal conductivity, in particular, contributes to the thermoelectric efficiency of these devices, making them a natural choice for such applications.

However, like all materials in their developing stages, semiconducting polymers are not without drawbacks. In their pristine form, the use of semiconducting polymers in thermoelectric devices is limited by low electrical conductivity due to low intrinsic charge carrier density and mobility. To address these issues, we employ various dopants and doping methods to introduce

carriers into semiconducting polymer thin films. Additionally, we developed a setup to rub-align semiconducting polymer thin films to study the effects of changing the molecular morphology on charge transport characteristics and doping. We characterize doped polymer films using techniques such as four-point probe conductivity, temperature-dependent conductivity, Seebeck coefficient measurements, Hall effect measurements, wide-angle X-ray scattering, and steady-state spectroscopy.

The first part of this dissertation (Chapter 2) explores the effects of the ambient environment, particularly humidity, on semiconducting polymer films doped with a novel doping method recently reported in the literature called "anion-exchange." The anion exchange doping method greatly enhances doping efficiency and also allows control of over the choice of counterion that accompanies the doped charge carrier. The counterion comes from an electrolyte solution, however, the electrolytes used are often made from hygroscopic salts. We show that these counterions can draw water into polymer films doped via anion exchange, which greatly reduces conductivity by acting as traps for carriers.

The second part of the dissertation (Chapters 3 and 4) investigates the effect of rub-aligned polymer thin films on doping and charge transport. Charge transport in semiconducting polymer films is often limited by their semicrystalline nature, where poor mobility can be caused by structural defects like bends or kinks that create energetic barriers. One way to reduce such defects is through a novel "high-temperature rub-aligning" method to straighten and molecularly align the polymer chains. Our study showed that conductivity greatly improves with this method, however, we also found that literature reports of this improvement were exaggerated because the method to measure anisotropic conductivity is highly dependent on electrode geometry, and previous work did not take this into account. Additionally, rub-aligned films provide insights into the effect of

different polymorphs on the doping process. We found that rub-aligning creates two polymorphs that happen to have face-on and edge-on structures. We found that face-on polymorph, whose structure is more similar to the final doped structure, has a lower barrier to doping than the edge-on polymorph, which requires a greater structural rearrangement to dope.

For the final part of this dissertation (Chapter 5), we used a holistic approach to understanding the effect of different dopants, doping methods, and structure on charge transport in doped semiconducting polymer thin films. By taking advantage of temperature-dependent measurements and models based on the Boltzmann transport formalism, we demonstrated that the factor dominating charge transport in doped semiconducting polymer thin films is highly dependent on the type of dopants and the doping method. Our finding demonstrates that the relationship between the Seebeck coefficient and conductivity of doped P3HT films can be improved either by reducing Coulomb interactions or by adding additional charge transport pathways through doping the of amorphous regions. The latter is shown by an increase in the correlation length between domains.

This dissertation of Quynh Muc Duong is approved.

Xiangfeng Duan

Alexander M. Spokoyny

Qibing Pei

Benjamin J. Schwartz, Committee Chair

University of California, Los Angeles

2024

TABLE OF CONTENTS

List of Figures and Schemes

Acknowledgements

First and foremost, I would like to express my deepest gratitude to my parents for their selfless sacrifices and unwavering devotion. As immigrants starting from almost nothing, our journey was definitely not easy. Their perseverance through all the hardships taught me the value of hard work and the importance of giving my best in everything I do. Their belief in my potential has always been greater than my own, constantly driving me to achieve my dreams.

I am also deeply grateful to my partner, Evie, who has stood by me throughout my graduate school journey. Through all the ups and downs, your support has been a constant source of strength. Your patience and understanding during countless stressful times have meant more to me than words can express. Your encouragement and love have been my anchor, providing the comfort and motivation I needed to keep going.

I am also deeply grateful to my advisor, Prof. Ben Schwartz, for taking me as your student and taking a chance with me. Without you, I may not have continued in graduate school. Your mentorship style, which encouraged me to explore science independently and nurtured my creativity, has been immensely valuable. Additionally, I deeply appreciate your openness and kindness; you always made me feel comfortable voicing my opinions. Thanks to you, I have not only learned a great deal about science but have also gained confidence in myself and my abilities.

Although the general goal of most graduate school programs would be to train students to become independent researcher. However, collaboration is equally as important and I was fortunate enough to have an opportunity to be able to collaborate with Prof. Sarah Tolbert and her groups. It was a very close collaboration and as such she is very much a second advisor to me. I am also very grateful for her advice both research and navigating graduate school. I will always be grateful for her help during my toughest moment in graduate school.

Lastly, but certainly not least, I want to extend my gratitude to my friends, collaborators, and fellow alumni. Starting afresh is always challenging, so I am grateful to have had many people to turn to throughout my time in graduate school. Ken has been more than a labmate; he's been a reliable friend with whom I can discuss anything, whether science-related or not. Similarly, I have worked most closely with Charlene and Diego throughout my graduate studies. They are both friends and wonderful people to work with. I especially want to thank Diego for his patience during the long and intricate experiments we conducted together; these projects would not have been possible without his assistance.

I also want to express my appreciation to Eric, our post-doc, for his valuable scientific insights and friendship. Additionally, I am grateful to our alumni, Matthew and Dane, whose guidance was instrumental when I first joined the lab. Special thanks go to Alex for her kindness and willingness to assist in the lab. Whenever I need guidance on lab materials or the appropriate solvents for my polymers, she is the first person I ask. I also want to give a big thanks to the rest of our lab team, especially those on the experimentalist side (Zerina, Reid, Kara, and Stephanie), for working alongside me and all the help they've provided.

Chapter 2 is a version of Q. M. Duong*, D. Garcia Vidales*, and B. J. Schwartz, "The Effects of Humidity on the Electrical Properties and Carrier Mobility of Semiconducting Polymers Anion-Exchange Doped with Hygroscopic Salts," Both Q. M. Duong and D. Garcia Vidales contributed equally to the data collection. B. J. Schwartz is the PI and/or project director. The manuscript was published in Applied Physics Letters. Duong, Q. M.; Garcia Vidales, D.; Schwartz, B. J. The Effects of Humidity on the Electrical Properties and Carrier Mobility of Semiconducting Polymers Anion-Exchange Doped with Hygroscopic Salts. Appl. Phys. Lett. 2023, 123 (20), 202101. https://doi.org/10.1063/5.0169905.

Chapter 3 is a version of Y. Wu*, Q. M. Duong*, A. F. Simafranca, C. Z. Salamat, B. J. Schwartz and S. H. Tolbert, " Crystal Structure Control of the Energetics of Chemical Doping in Rub-Aligned P3HT Films," All authors wrote the manuscript, with Y. Wu and Q. M. Duong contributing equally. Y. Wu collected and analyzed the x-ray diffraction, Q. M. Duong built the setup and fabricated rub-aligned semiconducting polymer films and collected polarized UV-Vis-NIR spectroscopy data, A. F. Simafranca provided additional analysis of the x-ray diffraction, C. Z. Salamat collected the diffraction data, B. J. Schwartz and S. H. Tolbert were the PIs and/or project directors. The manuscript was published in ACS Materials Letters. Wu, Y.; Duong, Q. M.; Simafranca, A. F.; Salamat, C. Z.; Schwartz, B. J.; Tolbert, S. H. Crystal Structure Control of the Energetics of Chemical Doping in Rub-Aligned P3HT Films. ACS Mater. Lett. 2024, 6 (2), 489–497. https://doi.org/10.1021/acsmaterialslett.3c01543.

Chapter 4 is a version of Q. M. Duong*, D. Garcia Vidales*, C. Z. Salamat, S. H. Tolbert and B. J. Schwartz, "Measuring the Anisotropic Sheet Resistance of Rub-Aligned Doped Semiconducting Polymer Films: the Role of Electrode Geometry". Q. M. Duong led this project and wrote the majority of the manuscript. Both Q. M. Duong and D. Garcia Vidales contributed equally to the data collection. Q. M. Duong built the setup and fabricated rub-aligned semiconducting polymer films and collected electrical and optical data, D. Garcia Vidales collected electrical and optical data, C. Z. Salamat collected the diffraction data, S. H. Tolbert, and B. J. Schwartz were the PIs and/or project directors. The manuscript was published in Physical Review Applied. Duong, Q. M.; Garcia Vidales, D.; Salamat, C. Z.; Tolbert, S. H.; Schwartz, B. J. Measuring the Anisotropic Conductivity of Rub-Aligned Doped Semiconducting Polymer Films: The Role of Electrode Geometry. Phys. Rev. Appl. 2024, 21 (2), 024006. https://doi.org/10.1103/PhysRevApplied.21.024006.

Chapter 5 is a version of Q. M. Duong*, D. Garcia Vidales*, C. Z. Salamat, X. Liu, A. Ready, H. A. Khunaizi, Z. Mehmedović, A. M. Spokoyny, S. H. Tolbert and B. J. Schwartz, "Control of the Seebeck Coefficient Conductivity relationship in Doped Semiconducting Polymer Thin Films through counterion coulomb binding and mesoscale correlation length". Both Q. M. Duong and D. Garcia Vidales contributed equally to the data collection. Q. M. Duong built the setup to measure Seebeck coefficient and temperature-dependent conductivity and collected electrical and optical data. D. Garcia Vidales collected electrical and optical data, C. Z. Salamat collected and analyzed x-ray diffraction data, X. Liu collected and analyzed x-ray diffraction data, A. Ready synthesized the dodecaborane clusters, H. A. Khunaizi synthesized the dodecaborane clusters, Z. Mehmedović made some of the sample for anion-exchange used for x-ray difraction, A. M. Spokoyny, S. R., Tolbert, and B. J. Schwartz were the PIs and/or project directors. The manuscript will be submitted for publication shortly after filing this dissertation.

VITA

2015 B.S. in Chemistry, Summa Cum Laude, California State Polytechnic University, Pomona

2019 Medical Device Engineer II (R&D – Electrochemistry), Dexcom Inc.

2021 M.S. in Chemistry, UCLA

2024 George Gregory Dissertation Award, UCLA

Publications

Q. M. Duong, D. Garcia Vidales, C. Z. Salamat, A. Ready, A. M. Spokoyny, S. H. Tolbert and B. J. Schwartz, "Deconvoluting the Effect of Coulomb Traps, Energetic Disorder, and Trap Filling on Thermoelectric Properties of Poly(3-hexylthiophene) Films," (In preparation)

Q. M. Duong, D. Garcia Vidales, C. Z. Salamat, S. H. Tolbert and B. J. Schwartz, "Measuring the Anisotropic Sheet Resistance of Rub-Aligned Doped Semiconducting Polymer Films: the Role of Electrode Geometry," Phys. Rev. Appl. 21, 024006, 1-10 (2024); DOI: 10.1103/PhysRevApplied.21.024006.

Y. Wu, **Q. M. Duong**, A. F. Simafranca, C. Z. Salamat, B. J. Schwartz and S. H. Tolbert, "Tuning the Crystal Structure of P3HT by Rub-Aligning Controls the Propensity for Chemical Doping," ACS Mater. Lett. 4, 489-97 (2024); DOI: 10.1021/acsmaterialslett.3c01543.

Q. M. Duong, D. Garcia Vidales and B. J. Schwartz, "The Effects of Humidity on the Electrical Properties and Carrier Mobility of Semiconducting Polymers Anion-Exchange Doped with Hygroscopic Salts," Appl. Phys. Lett. 123, 202101, 1-6 (2023); DOI: 10.1063/5.0169905.

M. F. Jimoh, M. F. El-Kady, G. S. Carson, M. B. Anderson, **Q. Duong**, and R. B. Kaner, Template-Free Route to PEDOT Nanofibers for 3D Electrodes with Ultrahigh Capacitance and Excellent Cycling Stability, Energy Storage Mater. 61, 102850 (2023). DOI: 10.1016/j.ensm.2023.102850

K. J. Winchell, P. Y. Yee, Y. L. Li, A. F. Simafranca, J. Chang, C. Beren, X. Liu, D. Garcia Vidales, R. J. Thompson, C. Z. Salamat, **Q. M. Duong**, R. S. Jordan, B. J. Schwartz, W. M. Gelbart, Y. Rubin and S. H. Tolbert, "Designing Cationic Conjugated Polymers for Amphiphilic Assembly into Micelles with Straight Chains," Macromol. 56, 3160-70 (2023); DOI: 10.1021/acs.macromol.2c02057.

CHAPTER 1

Introduction

Due to their wide band gap and semicrystalline nature, semiconducting polymers exhibit both low intrinsic carrier density and poor carrier mobility at room temperature. According to the familiar equation for electrical conductivity (σ),

$$\sigma = qn\mu, \tag{1}$$

where q is the elementary charge, n is the carrier density, and μ is the carrier mobility, these two terms determine the material's conductivity. To increase carrier density, a common approach is to chemically dope the semiconducting polymer. For *p*-type polymers, this involves using an oxidizing agent with a favorable electron affinity compared to the polymer's ionization energy.[1] The polymer can then undergo integer charge transfer with the dopant to create a radical cation (and dopant counterion). The resulting charge carrier is a positive hole, which coupled with the accompanying distortion of the backbone, is also called a polaron.

The formation of a polaron is also accompanied by a change in the electronic band structure.[2] In semiconducting polymers, doping leads to changes in the polymer backbone, shifting from a predominantly aromatic to a quinoid structure.[2,3] Unlike conventional inorganic semiconductors, where an intrinsic atom is replaced with an impurity atom in the lattice to introduce mid-gap states that become conductive, in contrast, the mid-gap states in semiconducting polymers arise from the change in the polymer's electronic structure due to the backbone transformation.

Figure 1.1 depicts a schematic of the changes in the electronic band structure of a semiconducting polymer after doping and the formation of polarons. The appearance of two

midgap states following doping results in two new optical transitions, labelled P1 and P2, which are detectable using UV-Vis-NIR spectroscopy. These transitions, which are characteristic of the formation of polarons, are frequently used as indicators to confirm doping. Although other transitions, labeled as P3 and P3', are theoretically possible, they are often weak or not observed at all due to symmetry restrictions.[4]

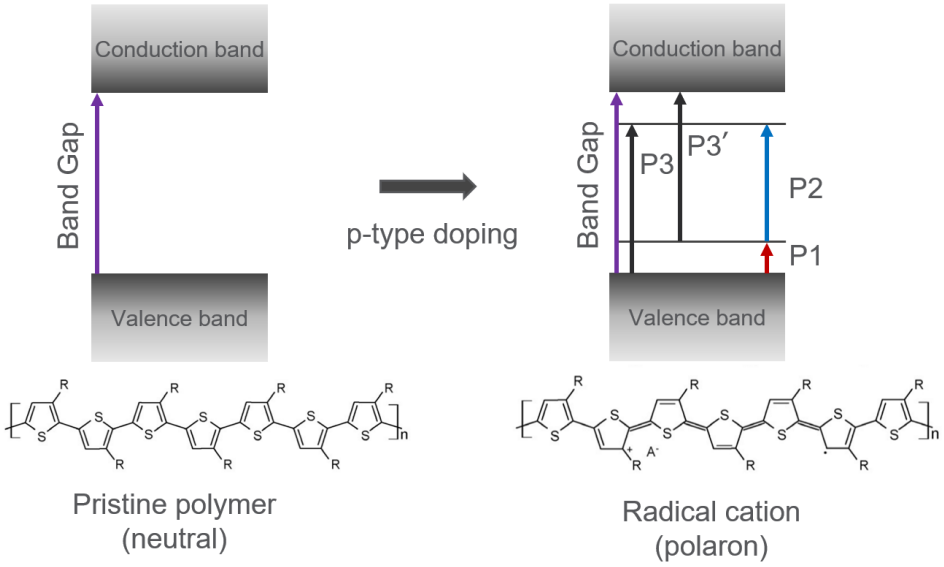

Figure 1. 1 Changes in the electronic band structure of a generic thiophene-based semiconducting polymer undergoing *p*-type doping to form a radical cation (polaron). The formation of polarons leads to new mid gap states, resulting in optical transitions (called P1 and P2) that can be observed using UV-Vis spectroscopy. The P3 and P3' transitions in most cases are not observed due to selection rules based on symmetry.

Although enhancing carrier density does improve electrical conductivity, it represents only half of the contribution to conductivity, equation (1); the other half is determined by carrier mobility. Unlike carrier density, which can be relatively straightforwardly increased by using

strong enough dopants to oxidize the semiconducting polymer, enhancing the carrier mobility is more complex. Carrier mobility largely depends on the polymer film's morphology, but other factors such as the electronic structure, carrier-counterion interactions, and carrier density also influence carrier mobility.

Semiconducting thin films are commonly fabricated using the spin-coating method. Films processed using this method often have a "semi-crystalline" morphology, consisting of a combination of crystalline regions and regions with varying degrees of structural disorder as shown in **Figure 1.2**.

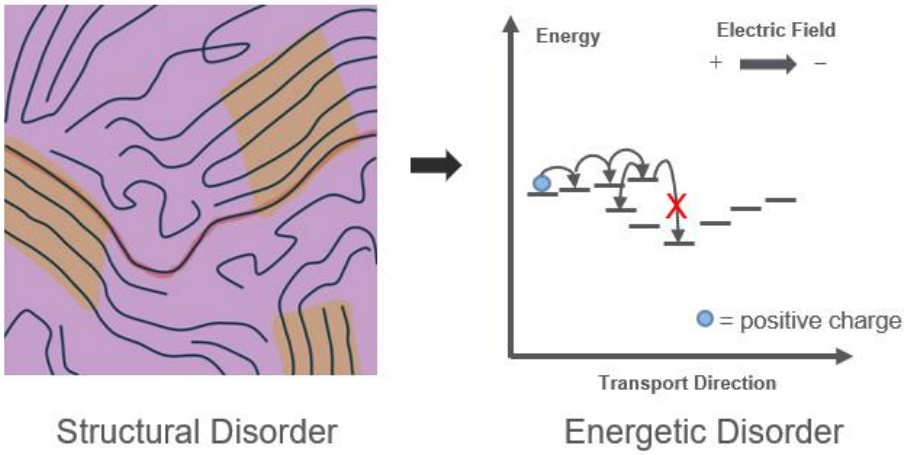

Figure 1. 2. An illustration of the semicrystalline morphology in semiconducting polymer thin films: yellow-highlighted indicates crystalline regions while purple denotes amorphous regions. Polymer chains may exhibit structural defects, such as bends or kinks, indicated by the red-highlighted polymer chain. These defects cause energetic disorder, leading to charge localization due to the introduction of energy barriers.

Charge transport in the crystalline regions is considered to be band-like, where charge carriers can move from one site to another with little to no trapping, resulting in high carrier

mobility. However, as the charge carriers move out of the crystalline region, they can encounter structural defects, such as bends or kinks in the polymer chain. These structural defects not only change the energy of the involved sites but also introduce an energetic barrier that the charge carriers need to overcome in order to move forward. Provided there is enough thermal energy, the charge carriers can surmount the barrier. However, if there isn't enough thermal energy, the charge carriers can become localized or trapped, leading to a drop in carrier mobility. The charge transport mechanism in this case is described as hopping, and the mobility increases with increasing temperature, which contrasts with band-like mobility that decreases with increasing temperature.

In addition to structural defects, the electrostatic interaction between the charge carrier and the counterion in the polymer matrix is another factor that can affect carrier mobility.[5,6] In conventional chemical doping, after the formation of a radical cation or polaron, the dopant, which gains an extra electron, remains in the polymer matrix and serves as the counterion. Since the polaron and counterion have opposite charges, they are attracted to each other. The strength of this interaction, following Coulomb's law, has an inverse relationship with the distance between the two charges. For counterions that are closely adjacent to the polymer backbone, this interaction is much stronger and thus can result in highly trapped charge carriers.

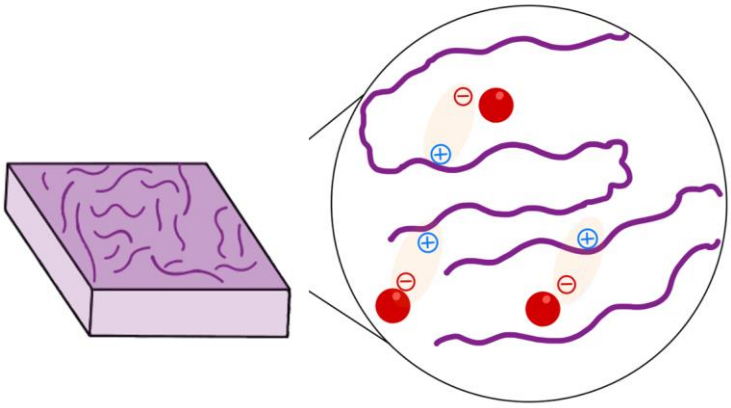

Figure 1. 3. Illustration of interaction between the positive polaron on the polymer chain and the dopant counterion in doped semiconducting polymer thin films. As this interaction is purely electrostatic, the strength of the interaction depends inversely on the distance between the counterion and the polaron that is residing on the polymer backbone.

Although often forgotten, the carrier density itself also plays a role in carrier mobility. As polymer doping increases, so does its dielectric constant. At high doping levels, the dielectric constant helps reduce Coulomb interactions through charge screening.[7] A recent literature report has proposed a model based on the Boltzmann transport formalism that provides a more direct relation between carrier density and charge transport.[8] The model follows a Marcus theory-based approach, describing each hopping site as a potential well. Increasing the carrier density causes nearby sites or potential wells to overlap, thus lowering the barrier to hopping.

All these factors typically interact simultaneously, making them difficult to deconvolute. This dissertation aims to understand and disentangle the various elements affecting charge transport in doped semiconducting polymer films, offering strategies to address these challenges and insights into improving charge transport. Since the focus is on factors beyond the polymer

itself, we used poly(3-hexylthiophene-2,5-diyl) (P3HT) as our main semiconducting polymer. P3HT is extensively studied and serves as an excellent workhorse polymer for exploring new dopant systems and other effects. In addition to the polymer, we used 2,3,5,6-tetrafluoro-7,7,8,8-tetracyanoquinodimethane (F_4TCNQ), also widely studied, as our main dopants. This combination of P3HT and F_4TCNQ will serves as a reference system in our studies.

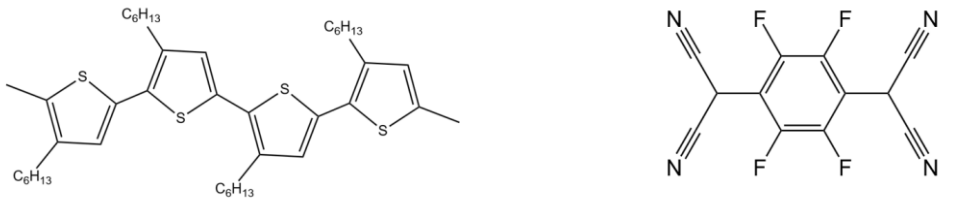

Figure 1. 4. The chemical structures of the semiconducting polymer P3HT (a) and the dopant F_4TCNQ (b) are shown. The combination of P3HT doped using F_4TCNQ is widely studied and frequently used as a reference system for comparison.

In Chapter 2 of this dissertation, we investigate the effect of the ambient environment, specifically humidity, on the electrical conductivity of semiconducting polymer films doped using a novel method called "anion-exchange.".[9] This method has been reported to greatly enhance doping efficiency in semiconducting polymer films. The anion-exchange doping method involves two main steps. The first step is similar to the conventional sequential processing doping method,[10,11] where the polymer film is doped using an initiator dopant such as F_4TCNQ. However, in this case, doping occurs in the presence of a concentrated electrolyte or salt. The high dielectric constant of the electrolyte solution, which swells the polymer film, lowers the barrier to ionization, promoting charge transfer reactions. In the second step, the dopant's anion is exchanged with one of the salt's anions, making it the new counterion for the doped polymer.

Although films doped using this method are reported to be both highly doped and electrically stable over time, there is one caveat: the salts used in the electrolyte solution typically contain highly hygroscopic anions. Despite this, there had been no reports on the impact of humidity on semiconducting polymer films doped using the anion-exchange method. In this work, we investigated the impact of humidity by utilizing three different anions with varying degrees of hygroscopicity. Our results show a strong correlation between the percent drop in electrical conductivity and the hygroscopicity of the anions used. Further investigation using Hall effect measurements indicates that the changes in electrical conductivity are primarily due to changes in carrier mobility rather than carrier density, suggesting that humidity is not dedoping the films. Using UV-Vis-NIR spectroscopy, we demonstrated that the humidity or water absorbed into the film acts as trap sites, leading to more localized polarons than in films without absorbed water. Although the drop in mobility upon humidity exposure is generally undesirable, these doped semiconducting films can serve as resistance-based humidity sensors, as the water absorption effect is reversible.

Chapters 3 and 4 shift focus to the impact of changing the morphology of semiconducting polymer thin films to enhance charge transport. As previously discussed, structural defects such as bends or kinks can lead to the localization of charge carriers and reduce carrier mobility. One novel method to minimize these structural defects is to molecularly align the semiconducting polymer films by mechanical rubbing. This novel method, first reported by Brinkmann's group, has been shown to significantly enhance the electrical conductivity of doped semiconducting polymer thin films.[12-17]

Rub-aligning is a post-film processing method. After the film is fabricated, it is heated to near its glass transition temperature and subjected to a shearing force applied by a rotating microfiber wheel with a controlled downward force. This shearing process pulls the polymer chains in the rubbing direction, helping to straighten and align the film. The result is a film with enhanced crystalline morphology and a preferred orientation of polymer chains.

Chapter 3 first explores the changes in morphology of rub-aligned films. We used polarized UV-Vis-NIR spectroscopy and Grazing-Incidence Wide-Angle X-ray Scattering (GIWAXS) to study these changes and their impact on the doping process. Polarized UV-Vis-NIR spectroscopy takes advantage of the fact that the transition dipole of P3HT is mainly along its polymer backbone. Successful alignment is indicated by significant absorption when light is polarized in the rubbing direction and minimal absorption when light is polarized perpendicularly. Our setup was able to achieved a relatively high dichroic ratio of up to ~14, indicating significant alignment. Additionally, we observed an increased in polymer conjugation length based on changes in the P3HT neutral absorption.

GIWAXS results showed enhanced crystallinity and anisotropic diffraction patterns. We also observed the formation of a new polymorph with a face-on orientation, in addition to the commonly observed edge-on orientation that is also seen in non-aligned films. The face-on polymorph is not only less dense but also structurally closer to the final doped state, making it easier to dope compared to the edge-on P3HT polymorphs in aligned films.

With the morphology explored, Chapter 4 focuses on the electrical properties of doped rub-aligned P3HT films. After rub-aligning, these doped films are expected to exhibit enhanced carrier mobility and conductivity due to the reduction in structural defects. However, this enhancement

should primarily be observed in the parallel direction, as the formation of face-on polymorphs hinders conduction in the perpendicular direction because of the insulating side chains, negatively impacting carrier mobility. Interestingly, some literature reports on rub-aligned P3HT do not observe this behavior.

By measuring the anisotropic electrical conductivity, we demonstrated that parallel conductivity is indeed enhanced while perpendicular conductivity decreases, agreeing with our GIWAXS analysis. We also identified that the discrepancies in the literature are likely due to use of incorrect methods for measuring anisotropic conductivity, as well as potential underestimation of the average film thickness. Additionally, we showed that the anisotropic conductivity can be accurately measured using a simple rectangular geometry with four electrodes at the corners, rather than the standard Hall bar geometry, which is more challenging to fabricate.

In addition to electrical conductivity measurements, we also performed Hall effect measurements to determine the carrier density and thus calculate the carrier mobility via equation (1). Our results indicate that the Hall effect is highly sensitive to the direction of the current. Depending on whether the current is sourced in the parallel or perpendicular direction, the dominant charge transport mechanism differs. In the parallel direction, charge transport is dominated by band-like mechanism, while in the perpendicular direction, it is dominated by hopping mechanism. This mixture of charge transport mechanisms leads to direction-dependent Hall effect measurements, where the ratio of band-like to hopping carriers can either underestimate or overestimate carrier density and, consequently, the carrier mobility.

Chapter 5 takes an ambitious step forward by aiming to deconvolute the various factors affecting charge transport and relate them not only to the electrical conductivity but also to the

Seebeck coefficient for thermoelectric applications. In thermoelectrics, efficiency is described by the thermoelectric figure of merit, *ZT*:

$$ZT = \frac{\sigma S^2}{\kappa} T \tag{2}$$

There are three factors that contribute to *ZT*: the electrical conductivity, the Seebeck coefficient (*S*), which is the voltage induced by temperature difference, and the thermal conductivity (κ). The temperature (*T*) is introduced to make the quantity unitless. Our study focuses on the connections between the Seebeck coefficient and electrical conductivity. To improve efficiency, both high electrical conductivity and a high Seebeck coefficient are desired. However, these two factors are typically anticorrelated.

To understand why conductivity and the Seebeck coefficient are related, we can take advantage of the Boltzmann transport formalism.[16] Using this formalism, the electrical conductivity can be described as the total contribution of electrical conductivity at each energy level (σ_E) within the Fermi window ($\frac{\partial f_0}{\partial E}$).

$$\sigma = \int \sigma_E \left(-\frac{\partial f_0}{\partial E}\right) dE \tag{3}$$

This single state conductivity, also known as the transport function, is related to the mobility of the charge carriers. The Seebeck coefficient, which is related to the energy carried by the charge carriers weighted by their contribution to the total conductivity, is given by the Fritzsche generalized equation:[16]

$$S = -\frac{k_B}{q} \int \left(\frac{E - E_F}{k_B T}\right) \left(\frac{\sigma_E}{\sigma}\right) \left(-\frac{\partial f_0}{\partial E}\right) dE \tag{4}$$

In this equation, k_B is the Boltzmann constant, E is the energy of the charge, and E_F is the Fermi energy. Although not explicit in the expression, the anticorrelation between the Seebeck coefficient and electrical conductivity arises because increasing the carrier density to enhance the conductivity shifts the Fermi level closer to the average energy of the carrier, affecting the (E - E_F) term in equation (4). The equation also implies that if conductivity is increased by improving charge transport rather than through carrier density, it is possible to enhance conductivity without negatively affecting the Seebeck coefficient.

To study whether we can improve the Seebeck-coefficient versus conductivity relationship by enhancing charge transport, we selected different dopants and doping methods to dope P3HT, each providing varying charge transport characteristics. We then measured their temperature-dependent electrical conductivity and Seebeck coefficient. The chosen dopants and methods are F_4TCNQ, dodecaborane (DDB)-based dopants, and anion-exchange.

F_4TCNQ-doped films serve as a reference point and are expected to exhibit the poorest charge transport among the methods compared. F_4TCNQ lacks sufficient oxidizing power to fully dope all regions in the films. Additionally, the F_4TCNQ anion acts as a Coulomb trap as it often sits close to the polymer backbone.[19] In contrast, the anion-exchange method enhances doping efficiency due to the presence of the electrolyte solution, which lowers the barrier to dope the amorphous regions. DDB-based dopants were selected for their strong oxidizing power and large size, which significantly reduces Coulomb interactions and consequently the hopping barrier.[5,6] Each dopant and doping method possess unique characteristics that affect charge transport differently, thereby influencing the Seebeck-coefficient versus conductivity relationship.

To investigate the charge transport properties of these dopants and doping methods, we employed two techniques: the Hall effect, to obtain macroscopic carrier mobility, and temperature-dependent conductivity measurements, to determine the barrier height for hopping transport. Results from Hall effect measurements showed that both anion-exchange and DDB-based dopants exhibited similar carrier mobility at the same carrier density, while F_4TCNQ-doped films had much lower carrier mobility. This trend also corresponded with their Seebeck-coefficient versus conductivity relationships, with anion-exchange and DDB-based dopants showing more favorable relationships compared to F_4TCNQ.

However, temperature-dependent conductivity measurements revealed that DDB-based dopants had a lower hopping barrier compared to F_4TCNQ, while the anion-exchange method showed a slightly higher hopping barrier. These findings highlight the complexity of the factors affecting charge transport properties. By using UV-Vis-NIR spectroscopy, GIWAXS, and fitting to a semi-empirical model based on Boltzmann transport formalism, we conclude that the factors contributing to enhanced charge transport in DDB-based dopants differ from those in the anion-exchange method. DDB-based dopants improve charge transport by reducing Coulomb trapping, while the anion-exchange method enhances it by creating additional pathways through doping the amorphous regions. Grazing incidence small-angle X-ray scattering (GISAXS) measurements reveal that these additional pathways manifest as larger lengthscale correlations between domains.

1.1 References

[1] Kiefer, D.; Kroon, R.; Hofmann, A. I.; Sun, H.; Liu, X.; Giovannitti, A.; Stegerer, D.; Cano, A.; Hynynen, J.; Yu, L.; Zhang, Y.; Nai, D.; Harrelson, T. F.; Sommer, M.; Moulé, A. J.; Kemerink, M.; Marder, S. R.; McCulloch, I.; Fahlman, M.; Fabiano, S.; Müller, C. Double Doping of Conjugated Polymers with Monomer Molecular Dopants. *Nat. Mater.* **2019**, *18* (2), 149–155. https://doi.org/10.1038/s41563-018-0263-6.

[2] Voss, M. G.; Scholes, D. T.; Challa, J. R.; Schwartz, B. J. Ultrafast Transient Absorption Spectroscopy of Doped P3HT Films: Distinguishing Free and Trapped Polarons. *Faraday Discuss.* **2019**, *216*, 339–362. https://doi.org/10.1039/C8FD00210J.

[3] Xu, B.; Gopalan, S.-A.; Gopalan, A.-I.; Muthuchamy, N.; Lee, K.-P.; Lee, J.-S.; Jiang, Y.; Lee, S.-W.; Kim, S.-W.; Kim, J.-S.; Jeong, H.-M.; Kwon, J.-B.; Bae, J.-H.; Kang, S.-W. Functional Solid Additive Modified PEDOT:PSS as an Anode Buffer Layer for Enhanced Photovoltaic Performance and Stability in Polymer Solar Cells. *Sci. Rep.* **2017**, *7* (1), 45079. https://doi.org/10.1038/srep45079.

[4] Wang, C.; Duong, D. T.; Vandewal, K.; Rivnay, J.; Salleo, A. Optical Measurement of Doping Efficiency in Poly(3-Hexylthiophene) Solutions and Thin Films. *Phys. Rev. B* **2015**, *91* (8), 085205. https://doi.org/10.1103/PhysRevB.91.085205.

[5] Aubry, T. J.; Winchell, K. J.; Salamat, C. Z.; Basile, V. M.; Lindemuth, J. R.; Stauber, J. M.; Axtell, J. C.; Kubena, R. M.; Phan, M. D.; Bird, M. J.; Spokoyny, A. M.; Tolbert, S. H.; Schwartz, B. J. Tunable Dopants with Intrinsic Counterion Separation Reveal the Effects of Electron Affinity on Dopant Intercalation and Free Carrier Production in Sequentially Doped Conjugated Polymer Films. *Adv. Funct. Mater.* **2020**, *30* (28), 2001800. https://doi.org/10.1002/adfm.202001800.

[6] Aubry, T. J.; Axtell, J. C.; Basile, V. M.; Winchell, K. J.; Lindemuth, J. R.; Porter, T. M.; Liu, J.-Y.; Alexandrova, A. N.; Kubiak, C. P.; Tolbert, S. H.; Spokoyny, A. M.; Schwartz, B. J. Dodecaborane-Based Dopants Designed to Shield Anion Electrostatics Lead to Increased Carrier Mobility in a Doped Conjugated Polymer. *Adv. Mater.* **2019**, *31* (11), 1805647. https://doi.org/10.1002/adma.201805647.

[7] Warren, R.; Blom, P. W. M.; Koch, N. Molecular *p* -Doping Induced Dielectric Constant Increase of Polythiophene Films Determined by Impedance Spectroscopy. *Appl. Phys. Lett.* **2023**, *122* (15), 152108. https://doi.org/10.1063/5.0146194.

[8] Gregory, S. A.; Hanus, R.; Atassi, A.; Rinehart, J. M.; Wooding, J. P.; Menon, A. K.; Losego, M. D.; Snyder, G. J.; Yee, S. K. Quantifying Charge Carrier Localization in Chemically Doped Semiconducting Polymers. *Nat. Mater.* **2021**, *20* (10), 1414–1421. https://doi.org/10.1038/s41563-021-01008-0.

[9] Yamashita, Y.; Tsurumi, J.; Ohno, M.; Fujimoto, R.; Kumagai, S.; Kurosawa, T.; Okamoto, T.; Takeya, J.; Watanabe, S. Efficient Molecular Doping of Polymeric Semiconductors Driven by Anion Exchange. *Nature* **2019**, *572* (7771), 634–638. https://doi.org/10.1038/s41586-019-1504-9.

[10] Ayzner, A. L.; Tassone, C. J.; Tolbert, S. H.; Schwartz, B. J. Reappraising the Need for Bulk Heterojunctions in Polymer−Fullerene Photovoltaics: The Role of Carrier Transport in All-Solution-Processed P3HT/PCBM Bilayer Solar Cells. *J. Phys. Chem. C* **2009**, *113* (46), 20050–20060. https://doi.org/10.1021/jp9050897.

[11] Hawks, S. A.; Aguirre, J. C.; Schelhas, L. T.; Thompson, R. J.; Huber, R. C.; Ferreira, A. S.; Zhang, G.; Herzing, A. A.; Tolbert, S. H.; Schwartz, B. J. Comparing Matched Polymer:Fullerene Solar Cells Made by Solution-Sequential Processing and Traditional Blend

Casting: Nanoscale Structure and Device Performance. *J. Phys. Chem. C* **2014**, *118* (31), 17413–17425. https://doi.org/10.1021/jp504560r.

[12] Biniek, L.; Pouget, S.; Djurado, D.; Gonthier, E.; Tremel, K.; Kayunkid, N.; Zaborova, E.; Crespo-Monteiro, N.; Boyron, O.; Leclerc, N.; Ludwigs, S.; Brinkmann, M. High-Temperature Rubbing: A Versatile Method to Align π-Conjugated Polymers without Alignment Substrate. *Macromolecules* **2014**, *47* (12), 3871–3879. https://doi.org/10.1021/ma500762x.

[13] Hamidi-Sakr, A.; Biniek, L.; Bantignies, J.-L.; Maurin, D.; Herrmann, L.; Leclerc, N.; Lévêque, P.; Vijayakumar, V.; Zimmermann, N.; Brinkmann, M. A Versatile Method to Fabricate Highly In-Plane Aligned Conducting Polymer Films with Anisotropic Charge Transport and Thermoelectric Properties: The Key Role of Alkyl Side Chain Layers on the Doping Mechanism. *Adv. Funct. Mater.* **2017**, *27* (25), 1700173. https://doi.org/10.1002/adfm.201700173.

[14] Hamidi-Sakr, A.; Biniek, L.; Fall, S.; Brinkmann, M. Precise Control of Lamellar Thickness in Highly Oriented Regioregular Poly(3-Hexylthiophene) Thin Films Prepared by High-Temperature Rubbing: Correlations with Optical Properties and Charge Transport. *Adv. Funct. Mater.* **2016**, *26* (3), 408–420. https://doi.org/10.1002/adfm.201504096.

[15] Untilova, V.; Hynynen, J.; Hofmann, A. I.; Scheunemann, D.; Zhang, Y.; Barlow, S.; Kemerink, M.; Marder, S. R.; Biniek, L.; Müller, C.; Brinkmann, M. High Thermoelectric Power Factor of Poly(3-Hexylthiophene) through In-Plane Alignment and Doping with a Molybdenum Dithiolene Complex. *Macromolecules* **2020**, *53* (15), 6314–6321. https://doi.org/10.1021/acs.macromol.0c01223.

[16] Untilova, V.; Biskup, T.; Biniek, L.; Vijayakumar, V.; Brinkmann, M. Control of Chain Alignment and Crystallization Helps Enhance Charge Conductivities and Thermoelectric Power

Factors in Sequentially Doped P3HT:F4TCNQ Films. *Macromolecules* **2020**, *53* (7), 2441–2453. https://doi.org/10.1021/acs.macromol.9b02389.

[17] Vijayakumar, V.; Zhong, Y.; Untilova, V.; Bahri, M.; Herrmann, L.; Biniek, L.; Leclerc, N.; Brinkmann, M. Bringing Conducting Polymers to High Order: Toward Conductivities beyond 105 S Cm−1 and Thermoelectric Power Factors of 2 mW M−1 K−2. *Adv. Energy Mater.* **2019**, *9* (24), 1900266. https://doi.org/10.1002/aenm.201900266.

[18] Fritzsche, H. A General Expression for the Thermoelectric Power. *Solid State Commun.* **1971**, *9* (21), 1813–1815. https://doi.org/10.1016/0038-1098(71)90096-2.

[19] Stanfield, D. A.; Mehmedović, Z.; Schwartz, B. J. Vibrational Stark Effect Mapping of Polaron Delocalization in Chemically Doped Conjugated Polymers. *Chem. Mater.* **2021**, *33* (21), 8489–8500. https://doi.org/10.1021/acs.chemmater.1c02934.

CHAPTER 2

The Effects of Humidity on the Electrical Properties and Carrier Mobility of Semiconducting Polymers Anion-Exchange Doped with Hygroscopic Salts

Chapter 2 describes our work on understanding the effect of humidity on electrical properties on semiconducting polymers thin films containing hygroscopic salts. This work used a combination of UV-Vis-NIR spectroscopy and Hall effect measurement to show that the water absorbed by the hygroscopic anions act as traps and can negatively impact the carrier mobility.

This chapter was reprinted with permission from Duong, Q. M..; Garcia-Vidales D.; Schwartz, B. J.; and AIP Publishing. "The Effects of Humidity on the Electrical Properties and Carrier Mobility of Semiconducting Polymers Anion-Exchange Doped with Hygroscopic Salts," Appl. Phys. Lett. 123, 202101, 1-6 (2023); DOI: 10.1063/5.0169905.

A reprint of the supporting information is given in Appendix A.

2.1 Introduction

Thanks to their ease of processing, structural tunability, low intrinsic thermal conductivity, and biocompatibility, interest in using semiconducting polymers for applications such as biosensors or thermoelectric generators has grown steadily.[1-3] Due to their intrinsically low carrier density, conjugated polymers need to be electrically doped to meet the performance standards demanded by many applications. The most common way to do this is through chemical doping, a process that introduces a small molecule that can undergo a charge transfer reaction with the semiconducting polymer; since most conjugated polymers are p-type materials, oxidizing agents are chosen to create mobile hole charge carriers.[4-6] The extent of chemical doping depends mainly on the polymer's ionization energy and the dopant's electron affinity,[7] as well as the concentration of the dopant that is used.[8]

Recently, Yamashita and coworkers have introduced a novel method referred to as anion-exchange doping,[9] which provides several advantages over conventional chemical doping. The method involves exposing a conjugated polymer film to a solution containing both a chemical dopant and a high concentration of electrolyte. The dopant oxidizes the polymer, and the dopant counterion is then exchanged out by mass action for the electrolyte anion from solution. This method not only provides control over the choice of counterion in doped semiconducting polymer films, but it also can achieve doping levels much higher than those reached via conventional doping: for example, Yamashita and co-workers were able to obtain nearly one carrier per monomer unit for the polymer poly(2,5-bis(3-tetradecylthiophen-2-yl)thieno[3,2-b]thiophene) (PBTTT) and the dopant 2,3,5,6-tetrafluoro-7,7,8,8-tetracyanoquinodimethane (F_4TCNQ) in the presence of different electrolytes.[9] The ability to choose the counterion inside the doped film can

make doped films more stable under ambient conditions,[9] and also can help tune the effect of coulomb interaction between the free carriers on the polymer backbone and its compensating charge, which is important for controlling carrier mobility.[9,10]

Because of all its advantages, multiple groups are now employing anion exchange doping when using semiconducting polymers in different applications. In the course of our exploration of anion exchange doping, however, we have discovered one potentially serious drawback: the typical electrolyte salts used in anion exchange doping, such as bis(trifluoromethane)sulfonimide lithium (LiTFSI), are generally highly hygroscopic, which means that the electrical behavior of anion-exchange-doped polymer films can be highly sensitive to the ambient humidity. In this work, we show that exposure of anion-exchange-doped polymer films to even moderate humidity can decrease the carrier mobility by over a factor of 3. This means that workers who study the properties of such films need to make sure they do so in a humidity-controlled environment.

There are of course previous studies on the influence of moisture on trap formation in semiconducting polymers.[11,12-17] Zuo and coworkers reported that the dielectric effect of water in nanovoids of semiconducting polymer thin films can create carrier traps that can be ~0.3-0.5 eV deep.[14] These traps can be mitigated by solvent annealing to reduce the number of nanovoids[14] or by filling the nanovoids with dopants that displace the water.[11,13,18] Another approach to mitigate the effects of water inhabiting nanovoids is to use conjugated polymers with denser side chain placement, such as regioregular poly(3-hexylthiophene-2,5-diyl) (P3HT),[17] which is a workhorse material in the field.

The aforementioned moisture studies were done on pristine or very lightly-doped semiconducting polymer films used in either organic field-effect transistors or solar cells, and none

of these studies examined the film's electrical conductivity or the effects of different doping methods. Here, we investigate the effect of humidity on the electrical conductivity, carrier density, and carrier mobility of both conventionally-doped and anion-exchange-doped P3HT films. In particular, we study the effects of moisture on P3HT films doped via the anion-exchange method using LiTFSI, and find a dramatic drop in electrical conductivity with increasing ambient humidity. We then use Hall effect measurements to show that the drop in conductivity with increasing humidity is primarily due to changes in carrier mobility and not due to dedoping. We also show that the effect of humidity on charge transport is quasi-reversible, and that the electrical conductivity changes almost linearly with humidity. We demonstrate the salt's hygroscopicity is key in the drop of electrical conductivity by comparing the properties of anion-exchange-doped P3HT films with LiTFSI to those exchanged with a less hygroscopic salt, lithium hexafluorophosphate ($LiPF_6$).[19-22] It is important to note that this distinction in hygroscopic behavior between LiTFSI and $LiPF_6$ generally holds true under typical ambient relative humidity conditions.[19-22] Under condition that is close to vacuum-dry, the distinction in hygroscopicity may not be as clear as the hygroscopic trends for ionic liquid is dependent on surrounding water content.[23,24] Nevertheless, our work specifically focuses on ambient relative humidity conditions, where LiTFSI shows more hygroscopic behavior than $LiPF_6$. Overall, in addition to the care needed to control the humidity when studying these materials, anion-exchange doped conjugated polymer films could possibly serve a role as resistance-based humidity sensors.

2.2 Results and Discussions

2.2.1. Fabrication and Doping Process for Semiconducting Polymer Thin Films

The goal of this study is to investigate the impact of humidity on conjugated polymer films doped both conventionally and with anion-exchange doping. To conduct this comparison, we start with 112-nm thick P3HT films spin-cast from a 2% w/v solution in o-dichlorobenzene. For the conventional doping method, we sequentially dope the P3HT films using different concentrations of F_4TCNQ dissolved in n-butyl acetate (n-BA). For the anion-exchange doping process, we follow the same procedure as for the conventional doping method, but with the addition of a high concentration of LiTFSI (30 mg/mL) or $LiPF_6$ (5 mg/mL) dissolved in the same solution as the F_4TCNQ. All of the processing steps were carried out in the inert atmosphere of a glove box with effectively 0% relative humidity (RH). Details of the materials we use and the casting and doping conditions are given in the Supporting Information (SI).

2.2.2. Methods for Measuring Electrical Conductivity and Hall Effect

To investigate the effect humidity plays on the electrical properties of doped conjugated polymer films, we chose dopant concentrations that resulted in similar electrical conductivity values with the two different doping methods (and thus with counterions with different degrees of hygroscopicity). The concentrations we focus on for anion-exchanged (AE) and conventional (Conv) doping were 0.1 mg/mL F_4TCNQ + 30 mg/mL LiTFSI, 0.1 mg/mL F_4TCNQ + 5 mg/mL $LiPF_6$, and 0.5 mg/mL F_4TCNQ respectively; results with additional doping concentrations are given in the Supporting Information (SI). After preparing doped P3HT films with these different processing conditions, we measured their electrical conductivities in three different environments with different RH levels. First, the conductivity was measured in the inert atmosphere of an Ar-

filled glovebox (Ar Glovebox) with effectively 0% humidity. The samples were then transferred out of the Ar glovebox and exposed to ambient air for roughly 5 minutes before the conductivity was re-measured (Ambient Air). The air-exposed samples were then purged with Ar for 5 minutes prior to measuring the conductivity for a third time (Ar Purged). We chose a 5-minute purge because the electrical conductivity of the samples no longer changed past that time.

2.2.3. Results from Electrical Conductivity and Hall Effect Measurements

Table 2.1 shows the electrical conductivities, measured via the van der Pauw 4-point-probe method with electrodes placed at the corners of our 1.5 x 1.5 cm samples, of 97% regioregular P3HT films doped using the conventional and anion-exchange methods in environments with different RHs. The conventionally-doped samples have the same electrical conductivity in all three different environments within error. The anion-exchange-doped samples with both salts, however, show a significant drop in conductivity when taken from the inert, 0% RH environment of the Ar Glovebox and introduced to the ambient environment (~36% and ~40% RH for LiTFSI and $LiPF_6$, respectively). The drop in conductivity is quite significant, with the LiTFSI anion-exchanged sample showing a conductivity loss nearly a factor of four. The samples anion-exchanged using $LiPF_6$ also exhibit a considerable reduction in conductivity, but the decrease is only about a factor of 2. This difference in the humidity-induced conductivity drop between $LiPF_6$ and LiTFSI makes sense in light of the fact that $LiPF_6$ is less hygroscopic.[18-20] We also saw very similar results for P3HT samples created using different dopant concentrations and P3HT regioregularities, as

demonstrated in **Fig. S1** and elsewhere in the SI, indicating that the humidity effect is not system specific.

Since the drop in conductivity is seen only with the anion-exchange doping method and not with conventional doping, it seems clear that the humidity effect involves the hygroscopic anions that were exchanged into the doped films. The hygroscopic nature of LiTFSI and its effect on electronic transport is well-documented in the mixed organic/inorganic perovskite solar cell community, where LiTFSI is often employed as an additive to enhance the p-doping of 2,2′7,7′-tetrakis-(N,N-di-p-methoxyphenyl-amine)-9,9′-spirobifluorene(spiro-MeOTAD).[20,25-28] However, in the case of perovskite materials, the consequence of using LiTFSI is more severe than just the introduction of carrier traps, as adsorbed water can dissolve the material.[29]

To verify that it is water in the ambient environment that causes the large drop in conductivity for the anion-exchange-doped P3HT films, we attempted to restore the conductivity by flowing either dry air or argon gas into our ambient conductivity measurement setup; **Table 2.1** shows that doing so yielded partial recovery of the conductivity. However, we were able to fully recover the original conductivity measured in the Ar glovebox by subjecting the films to a vacuum/purging process. This process involved 4 cycles where the films were placed under rough-pump vacuum for 5 minutes, followed by an Ar-gas refill (the green X in Figure S2 in the SI shows the fully-recovered conductivity value for the 0.1 mg/mL LiTFSI-anion-exchanged sample after undergoing this process). All of this is consistent with the idea that an initially "dry" anion-exchange-doped sample readily absorbs water due to hygroscopic counterions upon exposure to moist air. Surface-level adsorbed water can easily be removed simply by purging with dry gas, resulting in partial restoration of the electrical conductivity. However, exposing the samples to the

vacuum/purging process enables the complete removal of water from deeper within the films, leading to full recovery of the electrical conductivity.

It may not be surprising that for conventionally-doped P3HT films, the non-hygroscopic F_4TCNQ dopants are not affected by humidity, but we were still intrigued to observe no moisture-related trap effects induced by water adsorption into nanovoids in these films.[17] We believe that this could be due to a combination of our use of 97% regioregular P3HT, which has densely-packed side-chains, combined with the space-filling properties of the non-hygroscopic F_4TCNQ dopants,[11,17] which together mitigate water-related traps and their influence on electrical conductivity. Another possibility of this insensitivity of this behavior to humidity could be due to left over neutral F_4TCNQ. Previous studies have indicated that neutral additives featuring with strong electron-withdrawing nitrile groups can effectively bind with water molecules, thereby hindering the formation of water-induced traps on the polymer backbone.[30] However, our UV-Vis-NIR spectrum (Figure S3) confirmed that our films do not contain neutral F_4TCNQ. In this experiment, we intentionally chose a relatively low dopant concentration to prevent the left-over of unreacted neutral F_4TCNQ, a phenomenon that typically occurs at significantly higher dopant concentrations. As a result, we do not believe that this behavior of conventionally doped films is due the neutral F_4TCNQ interaction with water. Instead, we believe that the mechanism is more likely due to void-filling/repelling.

	Environment	**Conductivity (S/cm)**	**Hall Mobility ($cm^2V^{-1}s^{-1}$)**	**Hall Carrier Density ($x\ 10^{20}\ cm^{-3}$)**
0.5 mg/mL Conventional	Ambient	3.03 ± 0.20	0.029 ± 0.006	6.4 ± 0.94
	Ar Purged	2.98 ± 0.20	0.029 ± 0.005	6.3 ± 0.84
	Ar Glovebox	3.18 ± 0.16	N/A	N/A
	Ambient	0.75 ± 0.15	0.014 ± 0.0004	3.3 ± 0.74

0.1 mg/mL AE (LiTFSI)	Ar Purged	1.65 ± 0.14	0.042 ± 0.005	2.5 ± 0.51
	Ar Glovebox	2.88 ± 0.55	N/A	N/A
0.1 mg/mL AE ($LiPF_6$)	Ambient	3.66 ± 0.28	0.037 ± 0.003	6.1 ± 0.63
	Ar Purged	3.89 ± 0.24	0.040 ± 0.004	6.1 ± 0.65
	Ar Glovebox	6.74 ± 0.59	N/A	N/A

Table 2. 1. Electrical conductivities of anion-exchange- (AE) and conventionally- (Conv) doped P3HT films measured under different environmental conditions. The dopant concentrations for AE were 0.1 mg/mL F_4TCNQ + 30 mg/mL LiTFSI and 0.1 mg/mL F_4TCNQ + 5mg/mL $LiPF_6$, while the conventionally-doped samples used 0.5 mg/mL F_4TCNQ. Exposure to humidity dramatically lowers the conductivity of anion-exchanged-doped samples, whereas conventionally-doped samples show no conductivity change within error. Hall mobility and carrier densities were all obtained on the same set of samples. Unfortunately, due to logistical constraints, we are unable to perform Hall measurements inside the Ar glove box.

To understand the molecular-level causes of the conductivity decrease of anion-exchange-doped P3HT samples upon exposure to humidity, we also conducted Hall effect measurements on the same set of samples. **Table 2.1** shows the Hall carrier mobilities and densities obtained both in ambient air and after argon purging; unfortunately, logistical constraints prevented us from placing our Hall effect set-up in the Ar dry-box where the samples were fabricated. The results indicate that the mobile carrier density remains unaffected within error by ambient humidity for both the anion-exchange- and conventionally-doped samples; in other words, humidity does not cause de-doping. Given the high stability of the TFSI and PF_6 anions, they are expected to not react chemically or undergo any redox reactions in the presence of moisture.[9,31-34] Instead, the drop

in electrical conductivity observed in the anion-exchanged samples upon exposure to humid environments primarily stems from a decline in carrier mobility. This agrees with previous studies suggesting that water can act as shallow traps in semiconducting polymer films.[11-17]

2.2.4. Results from IR Spectroscopy

To further investigate the idea that the primary effect of humidity on anion-exchange-doped films is to reduce the carrier mobility, we utilized IR spectroscopy to investigate the trapping of carriers that results from humidity exposure. It is well-established in the literature that the degree of carrier delocalization and thus carrier mobility is reflected in the position of the so-called "P1" polaron absorption band in the IR: less trapped or more delocalized polarons show a red-shifted P1 band, while trapped polarons that are more localized and have lower mobilities are associated with more blueshifted P1 bands.[10,30,35] Thus, we took the 0.1 mg/mL AE (LiTFSI) and 0.5 mg/mL Conv samples that had been exposed to ambient conditions and monitored their near-IR absorption as a function of time as the sample was purged with dry N_2 gas.

Figure 2.1.a shows the results of this experiment, plotting the evolution of the blue side of the P1 absorption as the N_2 purging time increases for the humidity-exposed anion-exchange-doped P3HT sample; we chose to focus on the blue side because it better reflects the presence of more highly trapped polarons in the films,[10,28-37] and because the red side of the P1 band overlaps with the water O-H stretch near 2700 nm (see inset), making it hard to disentangle competing effects. The data show that with longer N_2 purging times, the intensity of the blue side of the P1 absorption diminishes, indicating a drop in the number of trapped polarons in the film. Moreover, despite the complication arising from the water O-H stretch, there is an observable isobestic point near 2900 nm (see inset) where the redder side of the P1 band increases with purging time. This

shows that purging with dry gas causes the conversion of trapped polarons into more mobile polarons via the removal of moisture.

In contrast, for the conventionally-doped P3HT sample, shown in **Figure 2.1.b**, there are no changes in the intensity of the P1 band with purging time, indicating that changing the humidity does not alter the trapping of polarons in conventionally doped P3HT films; both results are consistent with the way the carrier mobility changes in response to humidity, as shown in **Table 2.1.** We note that because of the way we performed the baseline (either under ambient conditions for the anion-exchange-doped sample or after N_2 purging for the conventionally-doped sample), the water absorption feature near 2700 nm appears to go in opposite directions in the two panels of **Figure 2.1**.

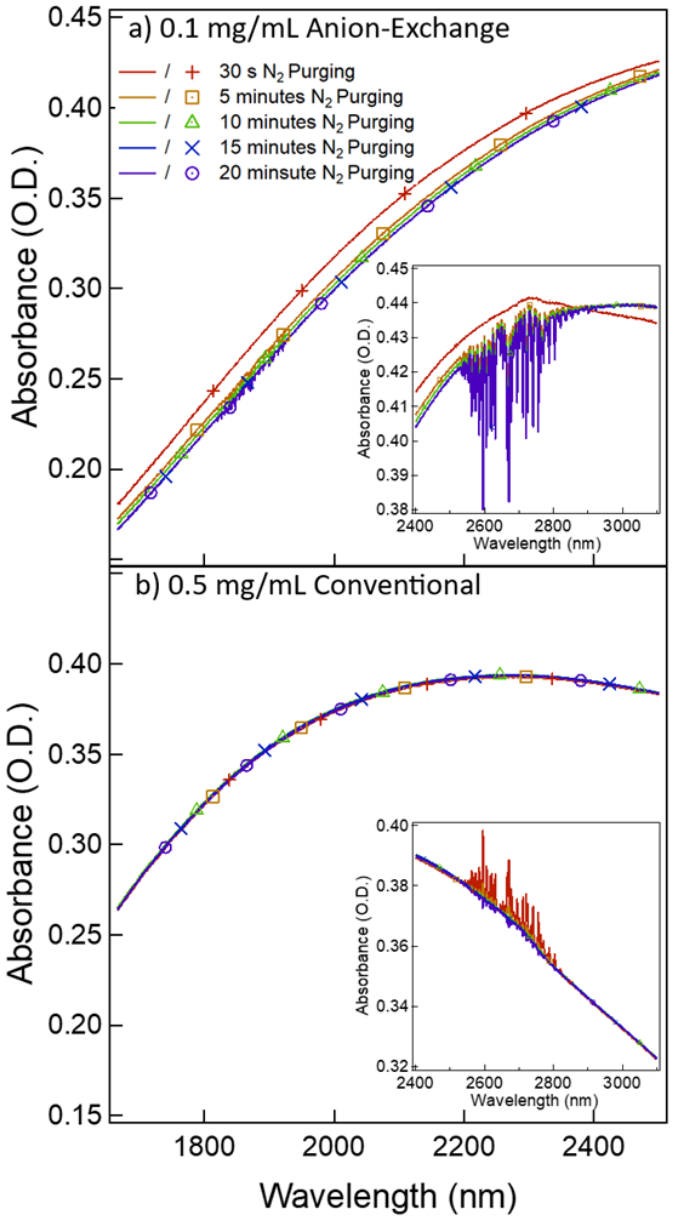

Figure 2. 1. Figure 1. UV Vis of 0.1 mg/mL F_4TCNQ + 30 mg/mL LiTFSI (AE) and 0.5 mg/mL F_4TCNQ (Conv) samples. The blue side of the P1 polaron absorption, which is associated with trapped carriers, for (a) an anion-exchange-doped P3HT film and (b) a conventionally-doped P3HT film that had been exposed to ambient conditions as a function of time after purging with

dry N2. Purging clearly decreases the blue P1 absorption for the anion-exchange-doped sample while having no effect on the conventionally-doped sample, consistent with the idea that humidity lowers the mobility of carriers in the anion-exchange-doped films (cf. **Fig. 2.1.b**). The inset in **Figure 2.1.a** and **2.1.b** show the same spectra extended deeper into the IR region, including the absorption of the water O-H stretch near 2700 nm (this absorption appears to go in opposite directions in the two panels because of the way the spectra were base-lined; see text).

2.2.5. Controlled Relative Humidity versus Electrical Conductivity Measurements

Finally, to verify that the decrease in conductivity in anion-exchange-doped P3HT samples is specifically caused by humidity rather than other ambient gases such as O2, we performed a set of measurements in ambient conditions under controlled RH. This was accomplished by placing 0.1 mg/mL anion-exchange-doped samples using both LiTFSI and $LiPF_6$ inside an air-filled desiccator containing drierite to control the humidity, and then measuring the electrical conductivity as a function of RH. The results are presented in **Figure 2.2**, which shows a remarkably linear relationship between the change in electrical conductivity (relative to that measured at 15% RH, the lowest we could achieve with this set-up) and relative humidity for the air-exposed anion-exchange-doped films. We note that for RH lower than ~20%, the linear relationship between conductivity and RH appears to lessen relative to what is observed at higher RH. This is because, as with the purging experiments described above, drierite is not capable of removing water from deep within the film. However, even with some trapped water, the nearly linear relationship between RH and conductivity depicted in **Figure 2.2** suggests that anion-exchange-doped films employing hygroscopic salts can possibly serve as viable materials for resistance-based humidity-sensing applications. It is worth mentioning that the trend observe in

Figure 2.2 is very similar to that of organic field-effect transistor (OFET)-type humidity sensor.[38,39] While OFET-type humidity sensor typically utilize pristine polymer rather than doped ones, the underlying sensing mechanism is basically the same. In both cases, water acts as trap leading to a decrease in charge carrier mobility. Despite their similar mechanisms, our resistance-based humidity sensing approach offers a significant advantage in terms of simplicity of production, as it doesn't require the fabrication of a field-effect transistor.

The data in **Fig. 2.2** also show that the slope of the relative change in conductivity vs. RH for LiTFSI-exchanged samples (green squares) is considerably higher than that of $LiPF_6$-exchanged samples (blue triangles), consistent with the idea that $TFSI^-$ is a more hygroscopic anion than PF_6^-.[18-20] The conventionally-doped samples (red circles) show no response to changes in humidity within error, as discussed above, consistent with the idea that hydrophobic F_4TCNQ prevents water from interacting with the charge carriers in doped P3HT.[20,26] These observations further confirm our hypothesis exposure to water vapor is what is responsible for the observed decline in conductivity.

As previously noted, our research distinguishes itself from prior studies found in the literature. The distinction lies in the water-trap phenomenon observed in our work, which is primarily driven by the anions present in the doped films rather than water infiltrating the void spaces within the pristine polymer. Given the doping of our films, it is highly improbable that water fills the nanovoids, as these voids are likely occupied by the counterions. This is evidence by films doped with the non-hygroscopic F_4TCNQ being insensitive to moisture, but known hygroscopic anions such as TFSI- and PF_6^- show drop in conductivity with when introduced to ambient humidity.

While it is widely acknowledged that both TFSI and PF_6 are hygroscopic under ambient humidity conditions, their hygroscopic nature is not solely determined by the strength of their interaction with water. It also depends on how water molecules bind around the ions, a factor defined as water sorption capacity per ion pair. Several studies have demonstrated that, under ambient temperature and humidity conditions, TFSI- possesses a higher capacity to absorb water than PF_6^- anion.[19-22] This observation implies a higher number of water molecules surrounding the TFSI- ¬anion. Furthermore, the extent of water absorption seems to exhibit a connection with both the relative basicity of the anions and the ratio of hydrophobic fluorine atoms to the total number of atoms within the anions.[19,21,22] This suggests that P3HT films with TFSI- not only exhibits a stronger affinity for water but can also accommodate more water, thus leading to a more significant drop in conductivity when compared to P3HT films containing PF_6^-.

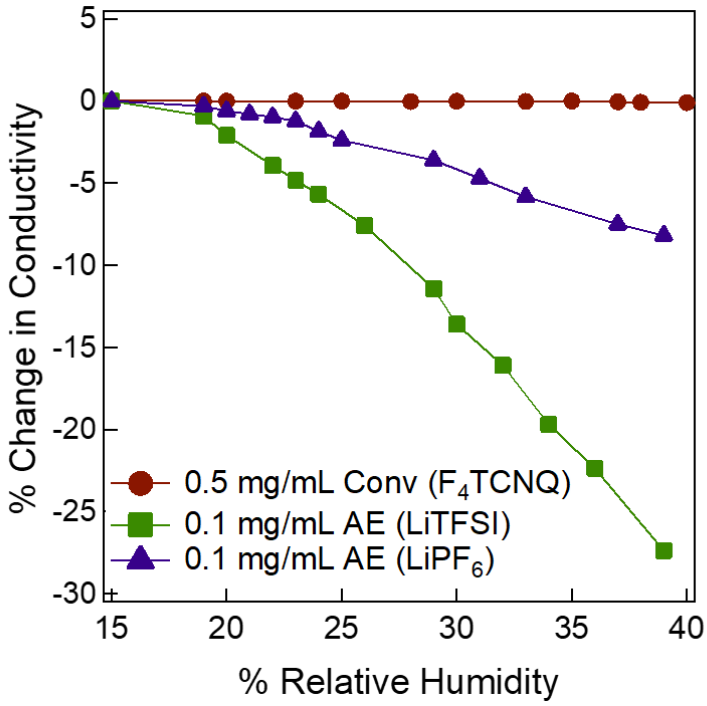

Figure 2. 2. Electrical conductivity of conventionally- (0.5 mg/mL F_4TCNQ, red circles) and anion-exchange-doped (0.1 mg/mL F_4TCNQ with 30 mg/mL LiTFSI, green squares, and 0.1 mg/mL F_4TCNQ with 5 mg/mL $LiPF_6$, purple triangles) P3HT films as a function of percent relative humidity in air. The ordinate plots the relative change in conductivity compared to that measured at 15% RH, the lowest we could obtain with this set-up. The conductivity change is highly linear down to ~20% RH, suggesting that the doped polymer films anion-exchanged with LiTFSI could possibly be used as resistance-based humidity sensors.

2.3. Conclusion

In summary, our study has demonstrated a high sensitivity of the electrical properties of conjugated polymer films anion-exchange-doped with hygroscopic salts, such as LiTFSI, to humidity. Given that one of the advantages of anion-exchange doping is that it creates more air-stable samples, our results show that it is crucial to consider the impact of the environment, and

particularly RH, to make accurate measurements and interpretations. We verified that it is the hygroscopic nature of anions like $TFSI^-$ that is responsible for the change in electrical behavior with RH by showing that less hygroscopic anions like PF_6^- show a smaller conductivity change with RH, and that non-hygroscopic dopants like F_4TCNQ show no changes with RH at all. Through Hall effect measurements and IR spectroscopy, we established that the decrease in electrical conductivity caused by humidity is a result of water-induced trapping affecting the transport of charge carriers; exposure to moisture does not appear to affect the doped carrier density. The effects of humidity on the conductivity of anion-exchange films are reversible, as long as sufficient efforts are made to remove deeply-trapped water from within the doped films by using a combination of vacuum and humidity-free gas purging. Finally, it appears that the decrease in electrical conductivity shows a roughly linear relationship with relative humidity, suggesting that anion-exchange-doped conjugated polymers hold potential for humidity-sensing applications.

2.4. References

1. Swager, T. M. 50th Anniversary Perspective: Conducting/Semiconducting Conjugated Polymers. A Personal Perspective on the Past and the Future. Macromolecules 2017, 50 (13), 4867–4886. https://doi.org/10.1021/acs.macromol.7b00582.

2. Mei, J. What's next for Semiconducting Polymers. J. Polym. Sci. 2022, 60 (3), 287–289. https://doi.org/10.1002/pol.20220014.

3. Dimov, I. B.; Moser, M.; Malliaras, G. G.; McCulloch, I. Semiconducting Polymers for Neural Applications. Chem. Rev. 2022, 122 (4), 4356–4396. https://doi.org/10.1021/acs.chemrev.1c00685.

4. Lüssem, B.; Keum, C.-M.; Kasemann, D.; Naab, B.; Bao, Z.; Leo, K. Doped Organic Transistors. Chem. Rev. 2016, 116 (22), 13714–13751. https://doi.org/10.1021/acs.chemrev.6b00329.

5. Sun, H.; Guo, X.; Facchetti, A. High-Performance n-Type Polymer Semiconductors: Applications, Recent Development, and Challenges. Chem 2020, 6 (6), 1310–1326. https://doi.org/10.1016/j.chempr.2020.05.012..Lopez, J.; Mackanic, D. G.; Cui, Y.; Bao, Z., Designing polymers for advanced battery chemistries. Nature Reviews Materials **2019**, 4, (5), 312-330.

6. Scaccabarozzi, A. D.; Basu, A.; Aniés, F.; Liu, J.; Zapata-Arteaga, O.; Warren, R.; Firdaus, Y.; Nugraha, M. I.; Lin, Y.; Campoy-Quiles, M.; Koch, N.; Müller, C.; Tsetseris, L.; Heeney, M.; Anthopoulos, T. D. Doping Approaches for Organic Semiconductors. Chem. Rev. 2022, 122 (4), 4420–4492. https://doi.org/10.1021/acs.chemrev.1c00581.

7. Jacobs, I. E.; Moulé, A. J. Controlling Molecular Doping in Organic Semiconductors. Adv. Mater. 2017, 29 (42), 1703063. https://doi.org/10.1002/adma.201703063.

8. Fontana, M. T.; Stanfield, D. A.; Scholes, D. T.; Winchell, K. J.; Tolbert, S. H.; Schwartz, B. J. Evaporation vs Solution Sequential Doping of Conjugated Polymers: F 4 TCNQ Doping of Micrometer-Thick P3HT Films for Thermoelectrics. J. Phys. Chem. C 2019, 123 (37), 22711–22724. https://doi.org/10.1021/acs.jpcc.9b05069.

9. Yamashita, Y.; Tsurumi, J.; Ohno, M.; Fujimoto, R.; Kumagai, S.; Kurosawa, T.; Okamoto, T.; Takeya, J.; Watanabe, S. Efficient Molecular Doping of Polymeric Semiconductors Driven by Anion Exchange. Nature 2019, 572 (7771), 634–638. https://doi.org/10.1038/s41586-019-1504-9.

10. Aubry, T. J.; Winchell, K. J.; Salamat, C. Z.; Basile, V. M.; Lindemuth, J. R.; Stauber, J. M.; Axtell, J. C.; Kubena, R. M.; Phan, M. D.; Bird, M. J.; Spokoyny, A. M.; Tolbert, S. H.; Schwartz, B. J. Tunable Dopants with Intrinsic Counterion Separation Reveal the Effects of Electron Affinity on Dopant Intercalation and Free Carrier Production in Sequentially Doped Conjugated Polymer Films. Adv. Funct. Mater. 2020, 30 (28), 2001800. https://doi.org/10.1002/adfm.202001800.

11. Haneef, H. F.; Zeidell, A. M.; Jurchescu, O. D. Charge Carrier Traps in Organic Semiconductors: A Review on the Underlying Physics and Impact on Electronic Devices. J. Mater. Chem. C 2020, 8 (3), 759–787. https://doi.org/10.1039/C9TC05695E.

12. Nikolka, M.; Nasrallah, I.; Rose, B.; Ravva, M. K.; Broch, K.; Sadhanala, A.; Harkin, D.; Charmet, J.; Hurhangee, M.; Brown, A.; Illig, S.; Too, P.; Jongman, J.; McCulloch, I.; Bredas, J.-L.; Sirringhaus, H. High Operational and Environmental Stability of High-Mobility Conjugated Polymer Field-Effect Transistors through the Use of Molecular Additives. Nat. Mater. 2017, 16 (3), 356–362. https://doi.org/10.1038/nmat4785.

13. Zuo, G.; Linares, M.; Upreti, T.; Kemerink, M. General Rule for the Energy of Water-Induced Traps in Organic Semiconductors. Nat. Mater. 2019, 18 (6), 588–593. https://doi.org/10.1038/s41563-019-0347-y.

14. Zuo, G.; Li, Z.; Andersson, O.; Abdalla, H.; Wang, E.; Kemerink, M. Molecular Doping and Trap Filling in Organic Semiconductor Host–Guest Systems. J. Phys. Chem. C 2017, 121 (14), 7767–7775. https://doi.org/10.1021/acs.jpcc.7b01758.

15. Kotadiya, N. B.; Mondal, A.; Blom, P. W. M.; Andrienko, D.; Wetzelaer, G.-J. A. H. A Window to Trap-Free Charge Transport in Organic Semiconducting Thin Films. Nat. Mater. 2019, 18 (11), 1182–1186. https://doi.org/10.1038/s41563-019-0473-6.

16. Iqbal, H. F.; Waldrip, M.; Chen, H.; McCulloch, I.; Jurchescu, O. D. Elucidating the Role of Water-Related Traps in the Operation of Polymer Field-Effect Transistors. Adv. Electron. Mater. 2021, 7 (9), 2100393. https://doi.org/10.1002/aelm.202100393.

17. Yaron, D. J.; Kowalewski, T. Beware the Nanovoids. Nat. Mater. 2019, 18 (11), 1154–1155. https://doi.org/10.1038/s41563-019-0502-5.

18. Hein, M. P.; Zakhidov, A. A.; Lüssem, B.; Jankowski, J.; Tietze, M. L.; Riede, M. K.; Leo, K. Molecular Doping for Control of Gate Bias Stress in Organic Thin Film Transistors. Appl. Phys. Lett. 2014, 104 (1), 013507. https://doi.org/10.1063/1.4861168.

19. Wu, T.; Zhuang, R.; Zhao, R.; Zhao, R.; Zhu, L.; Liu, G.; Wang, R.; Zhao, K.; Hua, Y. Understanding the Effects of Fluorine Substitution in Lithium Salt on Photovoltaic Properties and Stability of Perovskite Solar Cells. ACS Energy Lett. 2021, 6 (6), 2218–2228. https://doi.org/10.1021/acsenergylett.1c00685.

20. Cao, Y.; Chen, Y.; Sun, X.; Zhang, Z.; Mu, T. Water Sorption in Ionic Liquids: Kinetics, Mechanisms and Hydrophilicity. Phys. Chem. Chem. Phys. 2012, 14 (35), 12252–12262. https://doi.org/10.1039/C2CP41798G.

21. Goh, S.; Jang, G.; Ma, S.; Park, J.; Ban, H.; Lee, C. U.; Lee, J.; Moon, J. Understanding the Influence of Anion Exchange on the Hole Transport Layer for Efficient and Humidity-Stable Perovskite Solar Cells. ACS Sustain. Chem. Eng. 2021, 9 (49), 16730–16740. https://doi.org/10.1021/acssuschemeng.1c05848.

22. Cammarata, L.; G. Kazarian, S.; A. Salter, P.; Welton, T. Molecular States of Water in Room Temperature Ionic Liquids. Phys. Chem. Chem. Phys. 2001, 3 (23), 5192–5200. https://doi.org/10.1039/B106900D.

23. McDaniel, J. G.; Verma, A. On the Miscibility and Immiscibility of Ionic Liquids and Water. J. Phys. Chem. B 2019, 123 (25), 5343–5356. https://doi.org/10.1021/acs.jpcb.9b02187.

24. O'Mahony, A. M.; Silvester, D. S.; Aldous, L.; Hardacre, C.; Compton, R. G. Effect of Water on the Electrochemical Window and Potential Limits of Room-Temperature Ionic Liquids. J. Chem. Eng. Data 2008, 53 (12), 2884–2891. https://doi.org/10.1021/je800678e.

25. Cappel, U. B.; Daeneke, T.; Bach, U. Oxygen-Induced Doping of Spiro-MeOTAD in Solid-State Dye-Sensitized Solar Cells and Its Impact on Device Performance. Nano Lett. 2012, 12 (9), 4925–4931. https://doi.org/10.1021/nl302509q.

26. Lu, J.; Scully, A. D.; Sun, J.; Tan, B.; Chesman, A. S. R.; Ruiz Raga, S.; Jiang, L.; Lin, X.; Pai, N.; Huang, W.; Cheng, Y.-B.; Bach, U.; Simonov, A. N. Multiple Roles of Cobalt Pyrazol-Pyridine Complexes in High-Performing Perovskite Solar Cells. J. Phys. Chem. Lett. 2019, 10 (16), 4675–4682. https://doi.org/10.1021/acs.jpclett.9b01783.

27. Huang, L.; Hu, Z.; Xu, J.; Zhang, K.; Zhang, J.; Zhang, J.; Zhu, Y. Efficient and Stable Planar Perovskite Solar Cells with a Non-Hygroscopic Small Molecule Oxidant Doped Hole Transport Layer. Electrochimica Acta 2016, 196, 328–336. https://doi.org/10.1016/j.electacta.2016.03.002.

28. Kwon, H.; Won Lim, J.; Han, J.; Na Quan, L.; Kim, D.; Shin, E.-S.; Kim, E.; Kim, D.-W.; Noh, Y.-Y.; Chung, I.; Ha Kim, D. Towards Efficient and Stable Perovskite Solar Cells Employing Non-Hygroscopic F4-TCNQ Doped TFB as the Hole-Transporting Material. Nanoscale 2019, 11 (41), 19586–19594. https://doi.org/10.1039/C9NR05719F.

29. Fu, Q.; Tang, X.; Huang, B.; Hu, T.; Tan, L.; Chen, L.; Chen, Y. Recent Progress on the Long-Term Stability of Perovskite Solar Cells. Adv. Sci. 2018, 5 (5), 1700387. https://doi.org/10.1002/advs.201700387.

30. Nikolka, M.; Schweicher, G.; Armitage, J.; Nasrallah, I.; Jellett, C.; Guo, Z.; Hurhangee, M.; Sadhanala, A.; McCulloch, I.; Nielsen, C. B.; Sirringhaus, H. Performance Improvements in Conjugated Polymer Devices by Removal of Water-Induced Traps. Adv. Mater. 2018, 30 (36), 1801874. https://doi.org/10.1002/adma.201801874.

31. Lux, S. F.; Terborg, L.; Hachmöller, O.; Placke, T.; Meyer, H.-W.; Passerini, S.; Winter, M.; Nowak, S. LiTFSI Stability in Water and Its Possible Use in Aqueous Lithium-Ion Batteries: PH Dependency, Electrochemical Window and Temperature Stability. J. Electrochem. Soc. 2013, 160 (10), A1694. https://doi.org/10.1149/2.039310jes.

32. Kalhoff, J.; Eshetu, G. G.; Bresser, D.; Passerini, S. Safer Electrolytes for Lithium-Ion Batteries: State of the Art and Perspectives. ChemSusChem 2015, 8 (13), 2154–2175. https://doi.org/10.1002/cssc.201500284.

33. Liu, M.; Vatamanu, J.; Chen, X.; Xing, L.; Xu, K.; Li, W. Hydrolysis of LiPF6-Containing Electrolyte at High Voltage. ACS Energy Lett. 2021, 6 (6), 2096–2102. https://doi.org/10.1021/acsenergylett.1c00707

34. Suo, L.; Borodin, O.; Gao, T.; Olguin, M.; Ho, J.; Fan, X.; Luo, C.; Wang, C.; Xu, K. "Water-in-Salt" Electrolyte Enables High-Voltage Aqueous Lithium-Ion Chemistries. Science 2015, 350 (6263), 938–943. https://doi.org/10.1126/science.aab1595.

35. Scholes, D. T.; Yee, P. Y.; Lindemuth, J. R.; Kang, H.; Onorato, J.; Ghosh, R.; Luscombe, C. K.; Spano, F. C.; Tolbert, S. H.; Schwartz, B. J. The Effects of Crystallinity on Charge Transport and the Structure of Sequentially Processed F 4 TCNQ-Doped Conjugated Polymer Films. Adv. Funct. Mater. 2017, 27 (44), 1702654. https://doi.org/10.1002/adfm.201702654.

36. Aubry, T. J.; Axtell, J. C.; Basile, V. M.; Winchell, K. J.; Lindemuth, J. R.; Porter, T. M.; Liu, J.-Y.; Alexandrova, A. N.; Kubiak, C. P.; Tolbert, S. H.; Spokoyny, A. M.; Schwartz, B. J. Dodecaborane-Based Dopants Designed to Shield Anion Electrostatics Lead to Increased Carrier Mobility in a Doped Conjugated Polymer. Adv. Mater. 2019, 31 (11), 1805647. https://doi.org/10.1002/adma.201805647.

37. Voss, M. G.; Scholes, D. T.; Challa, J. R.; Schwartz, B. J. Ultrafast Transient Absorption Spectroscopy of Doped P3HT Films: Distinguishing Free and Trapped Polarons. Faraday Discuss. 2019, 216, 339–362. https://doi.org/10.1039/C8FD00210J.

38. Wu, S.; Wang, G.; Xue, Z.; Ge, F.; Zhang, G.; Lu, H.; Qiu, L. Organic Field-Effect Transistors with Macroporous Semiconductor Films as High-Performance Humidity Sensors. ACS Appl. Mater. Interfaces 2017, 9 (17), 14974–14982. https://doi.org/10.1021/acsami.7b01865.

39. Zhu, Y.; Zhang, Y.; Yu, J.; Zhou, C.; Yang, C.; Wang, L.; Wang, L.; Ma, L.; Wang, L. J. Highly-Sensitive Organic Field Effect Transistor Sensors for Dual Detection of Humidity and NO2. Sens. Actuators B Chem. 2023, 374, 132815. https://doi.org/10.1016/j.snb.2022.132815.

40. Tang, C. G.; Syafiqah, M. N.; Koh, Q.-M.; Ang, M. C.-Y.; Choo, K.-K.; Sun, M.-M.; Callsen, M.; Feng, Y.-P.; Chua, L.-L.; Png, R.-Q.; Ho, P. K. H. Water Binding and Hygroscopicity in π-Conjugated Polyelectrolytes. Nat. Commun. 2023, 14 (1), 3978. https://doi.org/10.1038/s41467-023-39215-9.

CHAPTER 3

Crystal Structure Control of the Energetics of Chemical Doping in Rub-Aligned P3HT Films

Chapter 3 describes our work on the chemical doping of face-on and edge-on polymorphs in rub-aligned P3HT films. This chapter covers a comprehensive analysis using polarized UV-Vis-NIR spectroscopy and GIWAXS on doped rub-aligned P3HT films to thoroughly understand the relationship between structure and doping.

This chapter was reprinted with permission from Wu, Y.; Duong, Q. M.; Simafranca, A. F.; Salamat, C. Z.; Schwartz, B. J.; Tolbert, S. H. " Crystal Structure Control of the Energetics of Chemical Doping in Rub-Aligned P3HT Films," ACS Mater. Lett. 4, 489-97 (2024); DOI: 10.1021/acsmaterialslett.3c01543.

A reprint of the supporting information is given in Appendix B.

3.1 Introduction

Semiconducting polymers are predicted to find wide use in future electronic devices because of their low cost, versatility, scalability, and solution processability.[1–8] Undoped semiconducting polymers are inherently poor electrical conductors due to their wide band gaps and low density of intrinsic charge carriers.[9] As a result, doping is required to generate carriers and make semiconducting polymers more conductive.[10] Similar to impurity doping in inorganic semiconductors, doping in semiconducting polymers occurs via charge transfer between the polymer and dopant molecules that are introduced into the polymer film.[11] Electrons can be either injected into the polymer conduction band (n-type) or withdrawn from the polymer valence band (p-type) to determine the majority carrier type.[12,13] Most studies focus on p-type semiconducting polymers due to their higher stability in air compared to n-type materials.[14]

In addition to selecting a dopant with a redox level that matches or exceeds the valence band energy of a semiconducting polymer, it is also critical to understand the structural changes of the polymer that take place during dopant introduction. Semiconducting polymer films are usually semicrystalline, containing both crystalline and amorphous regions.[15] Our previous work has shown that the polymer's degree of crystallinity can significantly affect charge carrier mobility by controlling where the dopants reside in the polymer film's structure.[16] Compared with amorphous regions, crystalline regions are generally easier to dope, and the resulting carriers have higher mobilities.[16,17] This means that the doped polymer film conductivity is governed by the structure and extent of the crystalline regions.[18]

It has been well established that when semiconducting polymers are doped, dopant molecules almost always intercalate into the lamellar side-chain regions of the polymer

crystallites.[16,19–22] Due to limited space in the lamellar region, the crystallite structure often undergoes a phase transition to accommodate the dopant molecules, resulting in a new packing geometry with a wider lamellar region, less tilting of the side chains with respect to the π-stacks, and an overall less dense packing of polymer chains.[16,20,23] Many doped conjugated polymer systems, including doped polymers that have undergone anion exchange, exhibit such a structural rearrangement.[19,20,24–26] Our previous work showed that even very large (~2 nm diameter) dodecaborane-based dopants intercalate into the lamellar side-chain region of polymer crystallites, in this case leading to a near doubling of the crystallite lamellar spacing.[17,27] Intercalation of dopants into the side chain region does not happen if there is a steric hindrance in this region or if the processing conditions allow planar dopants such as 2,3,5,6-tetrafluoro-7,7,8,8-tetracyanoquino-dimethane (F4TCNQ) to π-stack with the polymer backbone, changing the nature of the doping.[28–30]

Among doped semiconducting polymers, the F4TCNQ-doped poly(3-hexylthiophene-2,5-diyl) (P3HT) system is one of the most studied. P3HT crystallites have a monoclinic unit cell with side chains that are tipped away from the aromatic ring plane to better fill space.31 When cast as a thin film, P3HT has been shown to form both edge-on (i.e., alkyl side chains contacting the substrate) and face-on (i.e., backbone rings contacting the substrate) crystallites depending on processing conditions and substrate interfacial energy.[32–39] Although as-deposited semiconducting polymer films are typically isotropic with regard to the in-plane rotational angle (φ), there are a number of methods for aligning crystallites within the film, which range from strain-based or float-casting methods to the use of textured substrates.[38,40–44] Work from Brinkmann and co-workers produced aligned P3HT films by rub-alignment, resulting in highly crystalline and aligned

polymers. These researchers used electron diffraction (ED) to show that the rub-aligned films have both face-on- and edge-on-oriented P3HT polymorphs.[20,24,30–33] In subsequent studies, they also used aligned films to better understand how the P3HT crystal structure changed upon doping. They found that when F4TCNQ intercalates into the polymer lamellar side chain region, the side-chain angle relative to the thiophene ring (i.e., the side chain "tilt" angle) is reduced, resulting in an altered unit cell structure characterized by an increased lamellar spacing and a decreased π-stack spacing.[20] We note, however, that the use of ED in their work, which can only probe in-plane periodicity, means that the observed structural changes were based on examining the lamellar distance in the face-on-oriented doped P3HT polymorph and the π-stacking distance in the edge-on-oriented polymorph, so structural differences between the edge-on and face-on oriented populations could not be discerned.

In this work, we build on these previous studies of structural changes during doping by using grazing-incidence wide-angle x-ray scattering (GIWAXS)[45] to fully characterize the structures of both the edge-on and face-on polymorphs in rub-aligned P3HT films. GIWAXS reveals that although the two polymorphs have similar crystal structures, the chain packing is, in fact, somewhat different. The face-on polymorph has a structure that is less dense than that observed in standard, unaligned P3HT films, and is thus slightly more similar to the doped structure. Conversely, the rub-aligned edge-on domains appear to be compacted by the alignment process so that they have a denser structure that is even more different from the doped geometry than unaligned P3HT. We then show that the structural changes associated with doping are not a gradual evolution, but instead occur as an abrupt first-order phase transition. By starting with a very low dopant concentration and increasing the degree of doping in small steps, we can capture

a region where both the undoped and F4TCNQ-doped P3HT polymorphs coexist. We find that the less-dense P3HT polymorph dopes first, followed by the denser polymorph at higher doping concentrations. We argue that this results from the fact that the denser polymorph must change its crystal structure more to make space for the F4TCNQ- counterion, making the doping-induced phase transition harder. This finding demonstrates that even minor variations in the initial polymer crystallite structure strongly influences the ease of doping and suggests a new strategy to design polymers that are easier to dope.

3.2. Results and Discussions

3.2.1. Fabrication and Doping of Rub-aligned P3HT Films

To carry out our studies, we utilized the high-temperature rub-alignment method introduced by Brinkmann and coworkers to obtain highly aligned P3HT films.[46] First, P3HT (Rieke metals inc., Mn = 50-70 kg/mol, regioregularity 91-94%) was spin-coated onto glass substrates from 1,2-dichlorobenzene (ODCB) to produce films of uniform thickness. The P3HT films were then rub-aligned using a microfiber wheel while being heated in an inert atmosphere (see the Supporting Information (SI), for more details). The degree of film alignment was characterized using polarized absorption spectroscopy, in which polarized incident light was oriented either parallel (||) or perpendicular (⊥) to the direction of rub alignment.

3.2.2. Polarized UV-Vis-NIR Spectroscopy

Figure 3.1.a shows the polarized visible-NIR absorption spectra of unaligned (yellow curve) and rub-aligned (red curve for || and blue curve for ⊥) P3HT films. The polarized absorbance spectra of the aligned film show significant anisotropy, with a dichroic ratio I||/I⊥ = ~14 at 610 nm, comparable to previous rub-aligned P3HT work.[47,48] The absorption spectra of the

rub-aligned film in both polarizations are quite different from the unaligned film, showing that rub-alignment significantly alters the structure of the film. The absorption spectrum of unaligned P3HT shows a progression of vibronic peaks at 2.03 eV (0-0 transition, A0-0) and 2.23 eV (0-1 transition, A0-1), with an A0-0/A0 1 peak ratio of 0.53. The aligned P3HT film shows a parallel-polarized absorption spectrum with a larger A0-0/A0-1 peak ratio (0.63). This results from improved intrachain coupling caused by backbone straightening during rub-aligning.[49–51] In the perpendicular-polarized absorption spectrum, rub-aligned P3HT has a blue-shifted absorbance peak with no vibronic features, corresponding to the absorbance of short or amorphous polymer chains that were not successfully oriented by the rub-aligning process.[20]

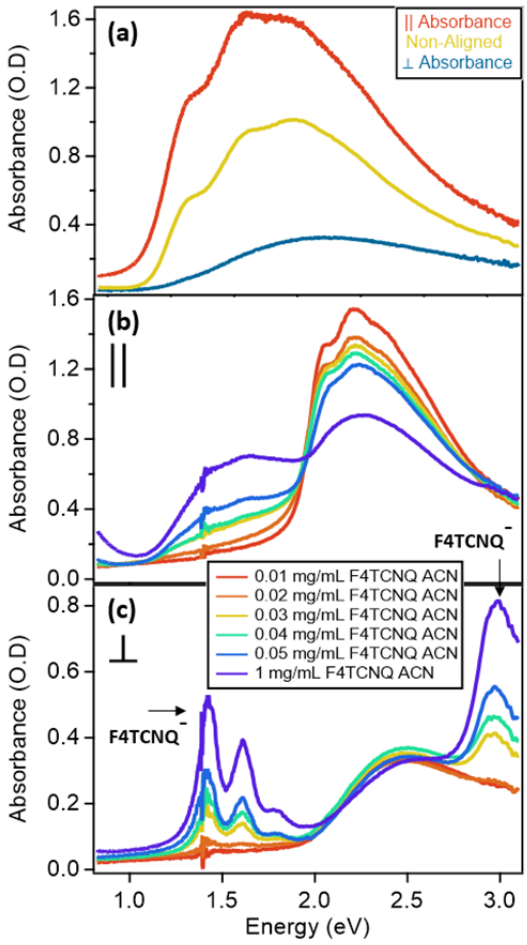

Figure 3. 1. Polarized Visible-NIR absorbance of (a) an unaligned P3HT film (yellow curve) and a rub-aligned P3HT film with light polarized parallel (||, red curve) and perpendicular (⊥, blue curve) to the rub direction. The absorption anisotropy of the rub-aligned P3HT film is ~14 near the absorption maximum, indicating a high degree of chain alignment. Visible-NIR absorption of aligned P3HT sequentially doped with F4TCNQ at different concentrations using light polarized (b) parallel and (c) perpendicular to the rub-alignment direction. The P2 band observed near 1.5 eV and the decrease of the ~2.2 eV neutral P3HT absorption seen in the parallel polarization are both indicative of doping and thus, polaron formation. As seen previously, the polaron absorption

is only visible with parallel polarization, while the $F4CTNQ^{-}$ absorption only appears with perpendicular polarization, indicating that the long axis of the $F4TCNQ^{-}$ molecule is oriented perpendicular to the P3HT backbone, consistent with the conclusions in Refs. 21 and 45.

3.2.3. Grazing Incidence Wide Angle X-ray Scattering (GIWAXS)

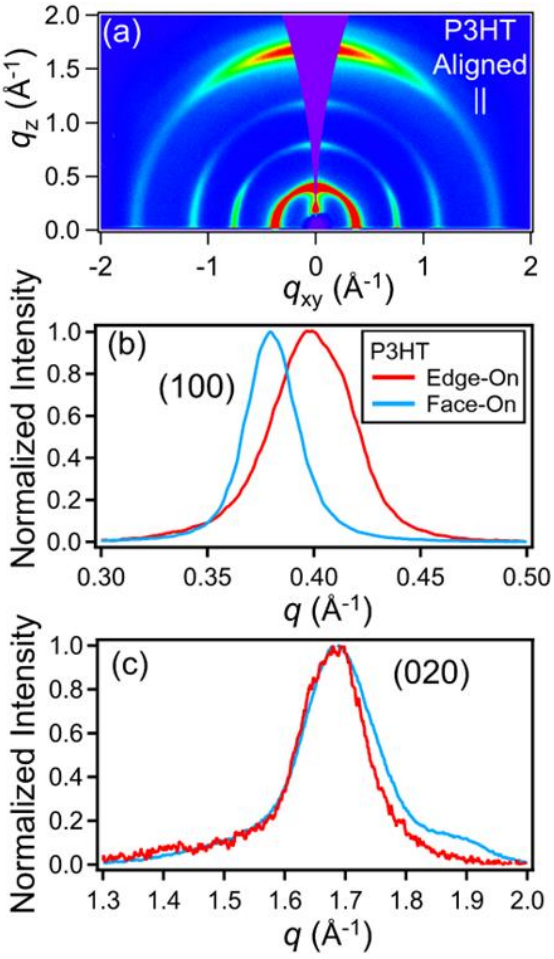

Figure 3. 2. (a) 2-D GIWAXS pattern for rub-aligned P3HT with the beam oriented along the rub direction, showing that unlike non-aligned films that have only edge-on-oriented crystallites, the rub-aligned film has both face-on- and edge-on-oriented crystallites. Integrated (b) (100) lamellar and (c) (020) π-stacking peaks of rub-aligned P3HT can be obtained by selective integration of the

data in (a) for both the edge-on- (red curves) and face-on-oriented (blue curves) crystallites. The data make clear that the face-on-oriented P3HT crystallites have a larger lamellar side-chain spacing and a slightly smaller π-stacking distance compared to the edge-on-oriented crystallites.

Although polarized absorption spectroscopy can determine the degree of polymer film alignment, direct structural measurements such as GIWAXS are necessary to provide details on the structure and orientation of the polymer crystallites within the film.[45,52] The crystallites in unaligned P3HT films usually adopt an edge-on orientation with the out-of-plane diffraction peaks corresponding to the lamellar direction and the in-plane diffraction peak corresponding to the π-stacking distance (see **Figure S4a**).[22] We note that the P3HT monomer repeat distance and the π-stacking distance have comparable length scales, so these two peaks can sometimes be difficult to distinguish.[20] **Figure 3.2.a** shows the 2-D GIWAXS diffraction pattern for a rub-aligned P3HT film in which the incident X-ray beam is parallel to the rub-alignment direction. Unlike data collected on unaligned films, both lamellar and π-stacking diffraction peaks are seen in both the in-plane and out-of-plane directions, indicating the coexistence of edge-on-oriented and face-on-oriented P3HT polymorphs.[20,48] Radial integration of the diffraction peaks in the in-plane and out-of-plane directions, however, reveals differences between the crystal structures of the face-on- and edge-on-oriented polymorphs. The face-on P3HT polymorph has a larger lamellar distance (dlamellar = 16.64 Å) compared to the edge-on polymorph (dlamellar = 16.03 Å), as seen in **Figures 3.2.b, c**. In comparison to unaligned P3HT (dlamellar = 16.36 Å), we find that the layer spacing of the face-on polymorph is expanded in a less dense structure, while the layer spacing in the edge-on polymorph is compressed, corresponding to a denser structure (see SI Table S1).

Here, we take advantage of the fact that we can directly observe both the lamellar and π-stacking peaks of the two differently oriented polymorphs together to show that these subtle differences in structure between the edge-on and face-on P3HT polymorphs affect the energetics of doping. To examine changes in the crystal structure during doping, we treated rub-aligned P3HT films with very low concentrations of F4TCNQ and slowly increased the dopant concentrations to capture the doping phase transitions of both the edge-on and face-on P3HT polymorphs.

All films were doped by sequential processing (SqP), in which a pre-cast rub-aligned P3HT films is exposed to the F4TCNQ using a solvent that swells but does not dissolve the polymer, and is then spun off after a brief soaking period. We have shown previously that the SqP doping method largely preserves the initial film morphology in terms of crystallite orientation and film crystallinity.[53] In agreement with this idea, the polarized absorption spectra of rub-aligned P3HT films doped with different concentrations of F4TCNQ are shown in **Figure 3.1.b, c**; retention of the anisotropic features in each polarization direction confirms that the film alignment is retained through the SqP doping process.[20] As is well documented, doping P3HT bleaches the bandgap transition (~2.25 eV) and generates new intra-band electronic states, creating the transition labeled "P2" near 1.6 eV that is seen in the parallel-polarized absorption spectrum shown in **Figure 3.1.b.**[54] In contrast, the absorption of the $F4TCNQ^{-}$ anion is seen predominantly in the perpendicularly polarized absorption spectrum (**Figure 3.1.c**).[20,22] This difference between parallel- and perpendicular-polarized spectra indicates that the F4TCNQ dopant counterions sit in the crystallites with their long axis oriented perpendicular to the P3HT backbone.[20,55,56] Taken together, the data in **Figure 3.1** indicate that at these low doping concentrations, the F4TCNQ dopant is predominantly found within the crystalline regions of the film. This agrees with previous

work that also found that crystalline regions of P3HT dope more easily than amorphous regions.[16,57]

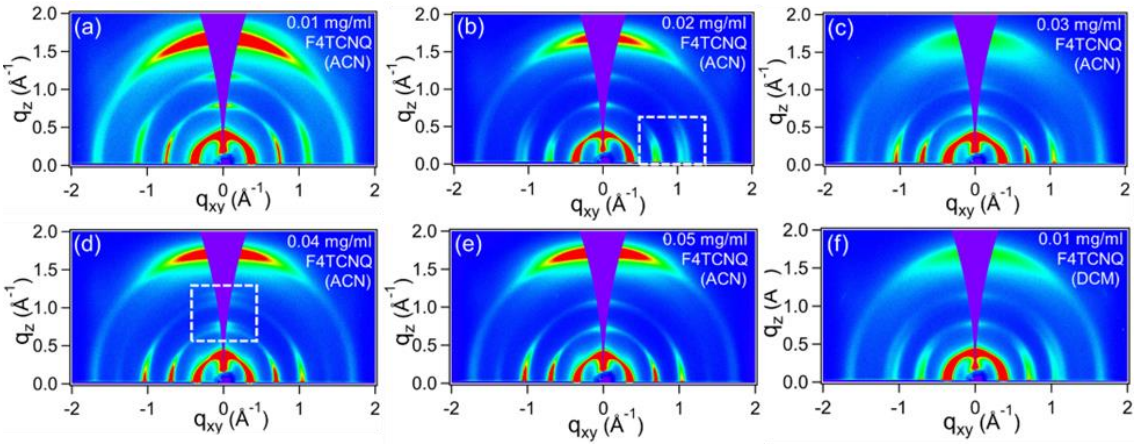

Figure 3. 3. (a)-(e) 2-D GIWAXS patterns of rub-aligned P3HT films sequentially doped with different concentrations of F4TCNQ in CH3CN (acetonitrile, ACN), taken with the beam oriented parallel to the rub direction. Face-on-oriented P3HT crystallites dope first, at 0.02 mg/mL F4TCNQ, followed by the denser edge-on-oriented P3HT crystallites, which dopes at 0.04 mg/mL F4TCNQ. (f) 2-D GIWAXS pattern of rub-aligned P3HT doped with 0.01 mg/mL F4TCNQ in dichloromethane (DCM). DCM swells the polymer more than ACN, allowing for faster doping kinetics. In agreement with this idea, the less dense face-on polymorph is already about half doped at this low F4TCNQ, but the denser edge-on polymorph remains undoped, indicating that the different doping levels are not a kinetic effect. See **Figure S6** for the full DCM data set; all the trends are the same, but values are shifted to lower F4TCNQ concentrations.

We can gain structural insight into the nature of the doping process in these aligned films using GIWAXS. **Figures 3.3.a-e** show GIWAXS diffraction patterns of the doped samples whose spectroscopy is characterized in **Figures 3.1.b, c**. As seen with the undoped aligned P3HT films,

the doped samples exhibit lamellar and π-stacking diffraction peaks in both the in-plane and out-of-plane directions, indicating that the co-existence of face-on- and edge-on-oriented crystallites is retained after sequential doping. When P3HT is initially doped by F4TCNQ, the undoped P3HT lamellar (h00) peaks shifts to a new position at lower q, a process that is the hallmark of a doping-induced phase transition.[16] Structurally, this change corresponds to reduction of the "tilt" of the side chains with respect to the π-stacks, which produces additional space for F4TCNQ- to insert into the polymer crystallites.[20,21] Similar peak shifts are also observed in unaligned P3HT, as shown in **SI Figures S4, S5**.[58] Importantly, the data presented in **Figures S4, S5, 6, and 7** indicates that this structural change is not a gradual process, but is instead a sharp first-order phase transition that occurs at very low doping levels. The lattice rearranges and expands to make space for the dopant counterion, in a structural change that is shown pictorially in **Figure 3.4.f**. After the phase transition, only small additional structural changes generally occur as the doping level is increased over a large range. This sharp structural change allows us to define the on-set of doping in each of the polymer population. When both the doped and undoped phases are present in equal amounts, we define the system as being at the mid-point of the doping-induced phase transition. Interestingly, we find that that the face-on and edge-on polymorphs do not undergo this phase transitions at the same doping concentration.

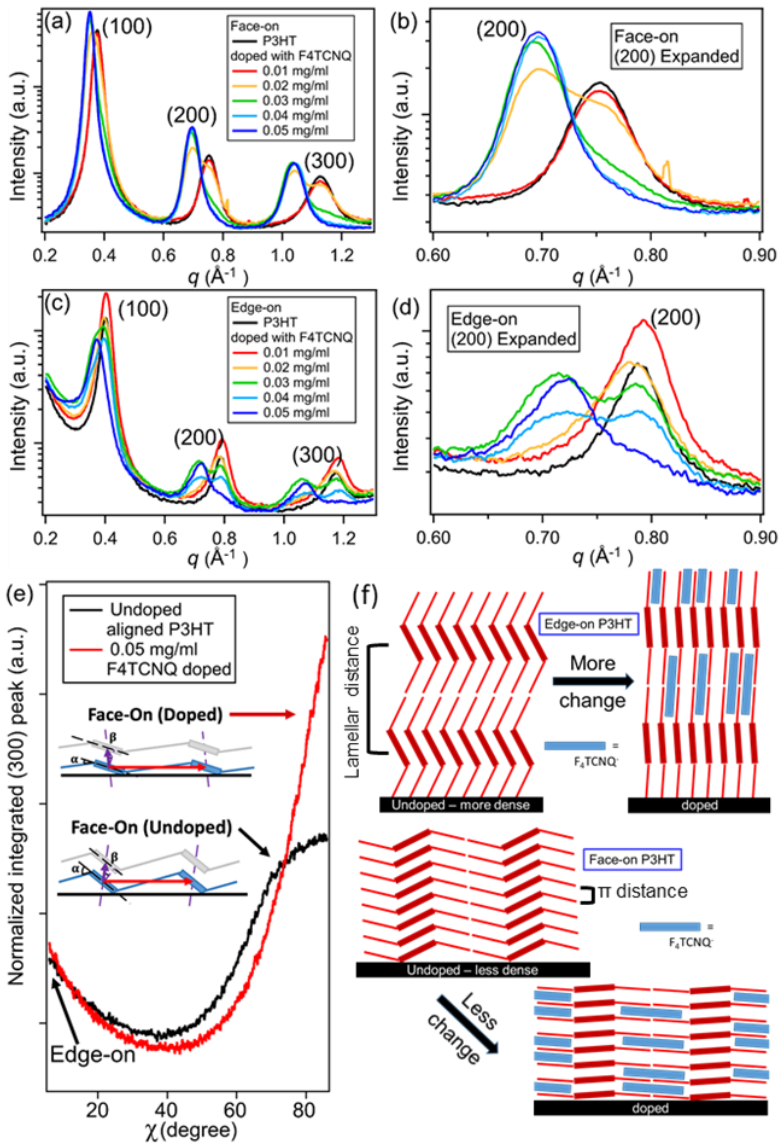

Figure 3. 4. 1-D integrated GIWAXS patterns showing (a, c) the lamellar scattering of rub-aligned, sequentially doped P3HT films. Panel a) shows the less-dense face-on-oriented polymorph observed in the in-plane direction, and c) shows the denser edge-on-oriented polymorph observed in the out-of-plane direction. Panels (b,d) show zoomed-in traces for the (200) peak for both polymorphs. The double peaks indicate coexistence of undoped and doped phases. The face-on-oriented P3HT polymorph dopes first at 0.02 mg/mL F4TCNQ, followed by the edge-on-

polymorph at 0.04 mg/ml. (e) 1-D radially integrated GIWAXS patterns of the lamellar (300) peak of undoped (black curve) and 0.05 mg/mL F4TCNQ-doped (red curve) rub-aligned P3HT plotted against the altitudinal angle χ. Compared with undoped P3HT, the doped face-on-oriented crystallites has a narrower χ-distribution. Structural modeling indicates that the decrease in lamellar angle during doping (inset structures, angles indicated on the χ-axis by dashed lines) is insufficient to produce the observed decrease in the χ-distribution. The change is thus attributed to improved alignment of the doped face-on crystallites with respect to the substrate. See the SI for modeling details. (f) Cartoons of the structural changes that occur in the face-on and edge-on domains upon doping.

We start by examining the doping of the less-dense face-on P3HT polymorph by looking at the progression of the in-plane lamellar peaks as a function of F4TCNQ concentration. **Figure 3.3b** shows that the less-dense face-on polymorph possesses two lamellar (h00) peaks at a doping level of 0.02 mg/ml (inside white box), corresponding to the midpoint of the phase transition. To more accurately observe this transition, radial integrations of the lamellar peaks in **Figure 3.3.a-e** are shown as 1-D patterns in **Figure 3.4.a** (face-on) and **Figure 3.4.c** (edge-on). The (200) peaks in **Figures 3.4a, c** are enlarged in **Figures 3.4.b**, d to better see the doping-induced lamellar peak splitting. **Figure 3.4.b** (orange curve) clearly shows that the less-dense face-on-oriented P3HT polymorph has a split lamellar peak when the F4TCNQ dopant concentration is 0.02 mg/ml. At 0.03 mg/ml F4TCNQ concentration (**Figure 3.4.b**, green curve), the phase transition is almost complete, with only a small residual undoped lamellar peak observed at ~0.76 Å-1. The light blue and dark blue curves in **Figure 3.4.b** indicate that the less-dense face-on aligned P3HT polymorph is fully doped at 0.04 mg/ml and higher F4TCNQ concentrations.

Next, we inspect the doping process of the denser edge-on P3HT polymorph by observing the progression of the out-of-plane (h00) peaks. Crucially, the edge-on polymorph does not show doubled (h00) peaks at a doping level of 0.02 mg/mL F4TCNQ, a concentration for which (h00) peak splitting is observed for the face-on polymorph **(Figure 3.3.b**). This indicates that the edge-on and face-on polymorphs become doped at different dopant concentrations because the two polymorphs have a different ease of doping. Instead, the edge-on aligned P3HT polymorph starts its phase transition process at a higher dopant concentration of 0.03 mg/mL F4TCNQ (**Figure 3.3.c**), and has approximately equal peak heights at 0.04 mg/mL F4TCNQ **(Figure 3.3.d**, inside the white box). The green and light blue curves in **Figure 3.4.d** confirm that the doping-induced phase transition for the edge-on polymorph occurs around 0.035 mg/mL F4TCNQ. This phase transition is then complete at 0.05 mg/ml F4TCNQ (dark blue curve). Overall, the data clearly shows that in rub-aligned P3HT films contain two different populations, and that the less-dense, face-on polymorph dopes first and then, only at higher dopant concentrations, does the denser, edge-on polymorph dope.

The observed dependence of the doping order on the initial crystallite orientation leads to the question of whether the difference in doping onset for the face-on- and edge-on-oriented polymorphs in aligned P3HT films is due to different doping energetics or different doping kinetics. For example, if the face-on-oriented crystallites were primarily located at the upper part of the film because of the rubbing process, it could be kinetically easier to deliver F4TCNQ to those top domains during solution doping, compared to crystallites located closer to the substrate. This is a really issue because the data shown in **Figures 3.3** and **3.4** were taken on rub-aligned P3HT films that were sequentially doped using acetonitrile (ACN), which does not swell the films

significantly, leading to slow F4TCNQ diffusion kinetics. Thus, to make sure that F4TCNQ diffusion was not controlling the observed order of the doping phase transition, we repeated the experiment using dichloromethane (DCM) as the doping solvent. DCM is an excellent swelling solvent for P3HT,[59] allowing large molecules like fullerenes[17] or dodecaborane derivatives[27] to penetrate through thick polymer films all the way to the substrate. **Figure 3.3.f** (along with additional data in **SI Figures S6 and S7**) shows that the use of DCM lowers the concentration needed to start the doping phase transition to 0.01 mg/mL F4TCNQ for the less-dense face-on polymorph, consistent with better swelling and easier dopant infiltration. However, the data shows that even with DCM as the solvent, the standard face-on-oriented P3HT polymorph still dopes first, and the denser edge-on polymorph does not dope until 0.03 mg/mL F4TCNQ (**Figure S6**), producing the exact same trend as that seen with ACN. This finding indicates that any kinetic limitations of solvent swelling are not enough to explain the observed orientation-dependent doping order, leading to the conclusion that the propensity of the face-on polymorph to dope first must be a thermodynamic effect that results from the added energy penalty of rearranging the denser edge-on polymorph.

To better understand the preferential doping of the face-on crystallites, we examined GIWAXS data on doped samples doped at a broader range of concentrations. Lattice spacings for the lamellar and π-stacking distances for both the doped and undoped versions of face-on-oriented, edge-on-oriented, and un-aligned P3HT polymorphs are given in Table S1. As discussed above, the un-doped edge-on-oriented polymorph has a smaller lamellar distance than the standard face-on polymorph in the undoped state, and this difference persists after the initial doping induced phase transitions (**Figure 3.4**). After treatment with 0.05 mg/mL F4TCNQ, the lamellar spacing

in the less-dense face-on polymorph expand to 18.01 Å, while the denser edge-on polymer remains at only 17.62 Å. After full doping at higher concentrations, however, the structure change in the edge-on polymorph 'catches-up' and both polymorphs approach the unaligned structure. The lamellar spacing of the unaligned P3HT sit at 18.18 Å, while the aligned face-on and edge-on lamellar distances are only slightly smaller at 18.10 Å and 17.95 Å, respectively (**Figure S8**). This indicates that more total structural change is required to make space for F4TCNQ- anions in the denser edge-on P3HT lattice, and only part of that change can be driven upon initial doping. Together, these results suggest that thermodynamic energy difference in the doping process for the face-on and edge-on polymorphs are the primary reason that different F4TCNQ concentrations are needed to induce doping.[60]

The well-aligned, highly crystalline structure of these films also allows us to explore the role of substrate interactions in controlling the energetics of doping. **Figure 3.4.e** shows 1-D radially integrated patterns for the χ-angular distribution (the χ-angle is defined relative to the qz-axis, i.e., the azimuthal angle relative to the normal of the plane of the film) for the (300) lamellar peak for the undoped and fully doped (0.05 mg/ml F4TCNQ) rub-aligned P3HT. The in-plane (300) peak of the face-on-oriented polymorph has a narrower χ-angle distribution (~15° half-width at half-maximum, HWHM) when doped than when undoped (~30°). In contrast, the edge-on-oriented polymorph has similar HWHM values when doped (~14°) and undoped (~17°). As discussed above, the broad distribution in the undoped face-on case results from of the tilt of the π-stacks with respect to the unit cell, which makes it difficult for the stacks to sit flat on the Si substrate (see **Figure 3.4.a**, inset); it is this same tip that makes most P3HT films adopt an edge-on orientation. The reduction in χ-angle upon doping results in part from a change in this tilt of

the π-stacks relative to the substrate (estimated to be ~12° undoped and ~5° doped for face-on crystallites), but this alone is insufficient to produce the observed spread of angles. We hypothesize that the remaining change results from alignment of the now reasonably flat π-stacks with the flat Si substrate. This substrate alignment may add an additional energetic term that favors doping of the face-on domains, and it should also improve vertical conduction through the film. We present the detailed model for the way the crystallite orientation of the polymorphs changes upon doping in the SI in **Figures S9-S13**.

3.3. Conclusion

In summary, we have shown that rub-aligned P3HT contains two different crystalline polymorphs: the face-on domains are less-dense than unaligned P3HT, and have a crystal structure that is slightly more similar to doped P3HT. In contrast, the edge-on domains are compacted by the rub-alignment process and show a denser structure with a compressed lamellar spacing that is even more different from doped P3HT that unaligned samples. The two polymorphs show well-separated diffraction peaks in GIWAXS measurements, which allowed us to investigate how differences in a crystallite's initial structure change its propensity to be doped. During doping, we found that the less-dense face-on-oriented polymorph undergoes a first-order, doping-induced phase transition more easily (at lower doping concentrations) than the denser edge-on polymorph. The face-on-oriented crystallites were also observed to better align with the substrate after doping, indicating that substrate interactions may also be energetically important. The difference in propensity to dope is attributed to differences in the starting structures, which requires more or less structural change to reach the final doped configuration. Canonically, only the redox energy of the dopant and the polymer are invoked in discussing how easily a polymer can be doped, but this

finding suggests that the extent of structure change upon doping can also be a significant energetic term. It also suggests that designing new polymers with crystallite structures that closely resemble their doped structures is a potential strategy for inducing the formation of more stable doped phases that can be produced at lower dopant concentrations.

Although this study examined only one polymer/dopant pair, the conclusions have implications for any polymer system where the energetics of doping controls performance. For example, the electrochemical doping that occurs in organic electrochemical transistors (OECTs) induces a nearly identical phase transition through ion injection to the one described here.[61,62] Designing polymers to facilitate this structural change could positively influence the energetics of OECTs. Having an initial structure that more closely resembles the final doped state can theoretically enhance the power efficiency of OECTs by lowering the threshold voltage (Vt) between the on and off states, impacting power consumption and noise margins.[63,64] Vt is most directly linked to the electrochemical potential,[65–67] which in turn maps on to chemical potential and the dopant concentration in our chemical doping experiments. Minimizing the reorganization energy associated with chemical doping is thus a viable route to reduce Vt in OECTs.

3.4. References

1. Forrest, S. R. The Path to Ubiquitous and Low-Cost Organic Electronic Appliances on Plastic. *Nature* **2004**, *428* (6986), 911–918. DOI: 10.1038/nature02498.

2. Tiwari, S.; Singh, A. K.; Joshi, L.; Chakrabarti, P.; Takashima, W.; Kaneto, K.; Prakash, R. Poly-3-Hexylthiophene Based Organic Field-Effect Transistor: Detection of Low Concentration of Ammonia. *Sens. Actuators B Chem.* **2012**, *171–172*, 962–968. DOI: 10.1016/j.snb.2012.06.010.

3. Hou, L.; Zhang, X.; Cotella, G. F.; Carnicella, G.; Herder, M.; Schmidt, B. M.; Pätzel, M.; Hecht, S.; Cacialli, F.; Samorì, P. Optically Switchable Organic Light-Emitting Transistors. *Nat. Nanotechnol.* **2019**, *14* (4), 347–353. DOI: 10.1038/s41565-019-0370-9.

4. Chung, D.-Y.; Huang, J.; Bradley, D. D. C.; Campbell, A. J. High Performance, Flexible Polymer Light-Emitting Diodes (PLEDs) with Gravure Contact Printed Hole Injection and Light Emitting Layers. *Org. Electron.* **2010**, *11* (6), 1088–1095. DOI: 10.1016/j.orgel.2010.03.010.

5. Rezvani, M.; Farajollahi, F.; Nikfarjam, A.; Bakhtiarpour, P.; Saydanzad, E. Effect of Solvents, Their Mixture and Thermal Annealing on the Performance of Solution Processed Polymer Light-Emitting Diodes. *Materials* **2013**, *6* (5), 1994–2006. DOI: 10.3390/ma6051994.

6. Zhang, S.; Ye, L.; Hou, J. Breaking the 10% Efficiency Barrier in Organic Photovoltaics: Morphology and Device Optimization of Well-Known PBDTTT Polymers. *Adv. Energy Mater.* **2016**, *6* (11), 1502529. DOI: 10.1002/aenm.201502529.

7. Nelson, J. Polymer:Fullerene Bulk Heterojunction Solar Cells. *Mater. Today* **2011**, *14* (10), 462–470. DOI: 10.1016/S1369-7021(11)70210-3.

8. Qiu, L.; Zheng, X.; Zhang, J.; Yang, Y.; Cao, W.; Dong, Y.; Xia, D.; Zhou, X.; Fan, R. Insights into the Mechanism of Solid-State Metal Organic Complexes as Controllable and Stable p-Type Dopants in Efficient Planar Perovskite Solar Cells. *ACS. Appl. Mater. Interfaces* **2020**, *12* (1), 546–555. DOI: 10.1021/acsami.9b16341.

9. Tremel, K.; Ludwigs, S. Morphology of P3HT in Thin Films in Relation to Optical and Electrical Properties. **2014**, pp 39–82. In: Ludwigs, S. (eds) P3HT Revisited – From Molecular Scale to Solar Cell Devices. Advances in Polymer Science, vol 265. Springer, Berlin, Heidelberg. DOI: 10.1007/12_2014_288.

10. Heeger, A. J. Semiconducting Polymers: The Third Generation. *Chem. Soc. Rev.* **2010**, *39* (7), 2354. DOI: 10.1039/b914956m.

11. Oba, F.; Tatsumi, K.; Adachi, H.; Tanaka, I. N - and p-Type Dopants for Cubic Silicon Nitride. *Appl. Phys. Lett.* **2001**, *78* (11), 1577–1579. DOI: 10.1063/1.1354667.

12. Yang, C.; Jin, W.; Wang, J.; Ding, Y.; Nong, S.; Shi, K.; Lu, Y.; Dai, Y.; Zhuang, F.; Lei, T.; Di, C.; Zhu, D.; Wang, J.; Pei, J. Enhancing the N-Type Conductivity and Thermoelectric Performance of Donor–Acceptor Copolymers through Donor Engineering. *Adv. Mater.* **2018**, *30* (43). DOI: 10.1002/adma.201802850.

13. Yoon, S. E.; Kang, Y.; Jeon, G. G.; Jeon, D.; Lee, S. Y.; Ko, S.; Kim, T.; Seo, H.; Kim, B.; Kim, J. H. Conjugated Polymers: Exploring Wholly Doped Conjugated Polymer Films Based on Hybrid Doping: Strategic Approach for Optimizing Electrical Conductivity and Related Thermoelectric Properties (Adv. Funct. Mater. 42/2020). *Adv. Funct. Mater.* **2020**, *30* (42). DOI: 10.1002/adfm.202070276.

14. Griggs, S.; Marks, A.; Bristow, H.; McCulloch, I. n-Type Organic Semiconducting Polymers: Stability Limitations, Design Considerations and Applications. *J. Mater. Chem. C.* **2021** 9, 8099–8128. DOI: 10.1039/D1TC02048J

15. Noriega, R.; Rivnay, J.; Vandewal, K.; Koch, F. P. V.; Stingelin, N.; Smith, P.; Toney, M. F.; Salleo, A. A General Relationship between Disorder, Aggregation and Charge Transport in Conjugated Polymers. *Nat. Mater.* **2013**, *12* (11), 1038–1044. DOI: 10.1038/nmat3722.

16. Scholes, D. T.; Yee, P. Y.; Lindemuth, J. R.; Kang, H.; Onorato, J.; Ghosh, R.; Luscombe, C. K.; Spano, F. C.; Tolbert, S. H.; Schwartz, B. J. The Effects of Crystallinity on Charge Transport and the Structure of Sequentially Processed F_4TCNQ-Doped Conjugated Polymer Films. *Adv. Funct. Mater.* **2017**, *27* (44), 1702654. DOI: 10.1002/adfm.201702654.

17. Aubry, T. J.; Axtell, J. C.; Basile, V. M.; Winchell, K. J.; Lindemuth, J. R.; Porter, T. M.; Liu, J.; Alexandrova, A. N.; Kubiak, C. P.; Tolbert, S. H.; Spokoyny, A. M.; Schwartz, B. J. Dodecaborane-Based Dopants Designed to Shield Anion Electrostatics Lead to Increased Carrier Mobility in a Doped Conjugated Polymer. *Adv. Mater.* **2019**, *31* (11). DOI: 10.1002/adma.201805647.

18. Alberga, D.; Perrier, A.; Ciofini, I.; Mangiatordi, G. F.; Lattanzi, G.; Adamo, C. Morphological and Charge Transport Properties of Amorphous and Crystalline P3HT and PBTTT: Insights from Theory. *Phys. Chem. Chem. Phys.* **2015**, *17* (28), 18742–18750. DOI: 10.1039/C5CP02769A.

19. Yamashita, Y.; Tsurumi, J.; Ohno, M.; Fujimoto, R.; Kumagai, S.; Kurosawa, T.; Okamoto, T.; Takeya, J.; Watanabe, S. Efficient Molecular Doping of Polymeric Semiconductors Driven by Anion Exchange. *Nature* **2019**, *572* (7771), 634–638. DOI: 10.1038/s41586-019-1504-9.

20. Hamidi-Sakr, A.; Biniek, L.; Bantignies, J.-L.; Maurin, D.; Herrmann, L.; Leclerc, N.; Lévêque, P.; Vijayakumar, V.; Zimmermann, N.; Brinkmann, M. A Versatile Method to Fabricate Highly In-Plane Aligned Conducting Polymer Films with Anisotropic Charge Transport and Thermoelectric Properties: The Key Role of Alkyl Side Chain Layers on the Doping Mechanism. *Adv. Funct. Mater.* **2017**, *27* (25), 1700173. DOI: 10.1002/adfm.201700173.

21. Untilova, V.; Zeng, H.; Durand, P.; Herrmann, L.; Leclerc, N.; Brinkmann, M. Intercalation and Ordering of F6TCNNQ and F4TCNQ Dopants in Regioregular Poly(3-Hexylthiophene) Crystals: Impact on Anisotropic Thermoelectric Properties of Oriented Thin Films. *Macromolecules* **2021**, *54* (13), 6073–6084. DOI: 10.1021/acs.macromol.1c00554.

22. Untilova, V.; Biskup, T.; Biniek, L.; Vijayakumar, V.; Brinkmann, M. Control of Chain Alignment and Crystallization Helps Enhance Charge Conductivities and Thermoelectric Power Factors in Sequentially Doped P3HT:F $_4$ TCNQ Films. *Macromolecules* **2020**, *53* (7), 2441–2453. DOI: 10.1021/acs.macromol.9b02389.

23. Kohno, S.; Yamashita, Y.; Kasuya, N.; Mikie, T.; Osaka, I.; Takimiya, K.; Takeya, J.; Watanabe, S. Controlled Steric Selectivity in Molecular Doping towards Closest-Packed Supramolecular Conductors. *Commun. Mater.* **2020**, *1* (1), 79. DOI: 10.1038/s43246-020-00081-3.

24. Vijayakumar, V.; Zaborova, E.; Biniek, L.; Zeng, H.; Herrmann, L.; Carvalho, A.; Boyron, O.; Leclerc, N.; Brinkmann, M. Effect of Alkyl Side Chain Length on Doping Kinetics, Thermopower, and Charge Transport Properties in Highly Oriented F $_4$ TCNQ-Doped PBTTT Films. *ACS Appl. Mater. Interfaces.* **2019**, *11* (5), 4942–4953. DOI: 10.1021/acsami.8b17594.

25. Karpov, Y.; Kiriy, N.; Formanek, P.; Hoffmann, C.; Beryozkina, T.; Hambsch, M.; Al-Hussein, M.; Mannsfeld, S. C. B.; Büchner, B.; Debnath, B.; Bretschneider, M.; Krupskaya, Y.; Lissel, F.; Kiriy, A. Sequentially Processed P3HT/CN6-CP $^{\bullet-}$ NBu $^{4+}$ Films: Interfacial or Bulk Doping? *Adv. Electron. Mater.* **2020**, *6* (5). DOI: 10.1002/aelm.201901346.

26. Kiefer, D.; Kroon, R.; Hofmann, A. I.; Sun, H.; Liu, X.; Giovannitti, A.; Stegerer, D.; Cano, A.; Hynynen, J.; Yu, L.; Zhang, Y.; Nai, D.; Harrelson, T. F.; Sommer, M.; Moulé, A. J.; Kemerink, M.; Marder, S. R.; McCulloch, I.; Fahlman, M.; Fabiano, S.; Müller, C. Double Doping of Conjugated Polymers with Monomer Molecular Dopants. *Nat. Mater.* **2019**, *18* (2), 149–155. DOI: 10.1038/s41563-018-0263-6.

27. Aubry, T. J.; Winchell, K. J.; Salamat, C. Z.; Basile, V. M.; Lindemuth, J. R.; Stauber, J. M.; Axtell, J. C.; Kubena, R. M.; Phan, M. D.; Bird, M. J.; Spokoyny, A. M.; Tolbert, S. H.; Schwartz, B. J. Tunable Dopants with Intrinsic Counterion Separation Reveal the Effects of Electron Affinity on Dopant Intercalation and Free Carrier Production in Sequentially Doped Conjugated Polymer Films. *Adv. Funct. Mater.* **2020**, *30* (28). DOI: 10.1002/adfm.202001800.

28. Thomas, E. M.; Davidson, E. C.; Katsumata, R.; Segalman, R. A.; Chabinyc, M. L. Branched Side Chains Govern Counterion Position and Doping Mechanism in Conjugated Polythiophenes. *ACS Macro. Lett.* **2018**, *7* (12), 1492–1497. DOI: 10.1021/acsmacrolett.8b00778.

29. Jacobs, I. E.; Cendra, C.; Harrelson, T. F.; Bedolla Valdez, Z. I.; Faller, R.; Salleo, A.; Moulé, A. J. Polymorphism Controls the Degree of Charge Transfer in a Molecularly Doped Semiconducting Polymer. *Mater. Horiz.* **2018**, *5* (4), 655–660. DOI: 10.1039/C8MH00223A.

30. Stanfield, D. A.; Wu, Y.; Tolbert, S. H.; Schwartz, B. J. Controlling the Formation of Charge Transfer Complexes in Chemically Doped Semiconducting Polymers. *Chem. Mater.* **2021**, *33* (7), 2343–2356. DOI: 10.1021/acs.chemmater.0c04471.

31. Kayunkid, N.; Uttiya, S.; Brinkmann, M. Structural Model of Regioregular Poly(3-Hexylthiophene) Obtained by Electron Diffraction Analysis. *Macromolecules* **2010**, *43* (11), 4961–4967. DOI: 10.1021/ma100551m.

32. Aubry, T. J.; Ferreira, A. S.; Yee, P. Y.; Aguirre, J. C.; Hawks, S. A.; Fontana, M. T.; Schwartz, B. J.; Tolbert, S. H. Processing Methods for Obtaining a Face-On Crystalline Domain Orientation in Conjugated Polymer-Based Photovoltaics. *J. Phys. Chem. C* **2018**, *122* (27), 15078–15089. DOI: 10.1021/acs.jpcc.8b02859.

33. Guo, X.; Marks, T. J. Plastic Solar Cells with Engineered Interfaces. **2013**, 86220K. In: Proc. SPIE 8622, Organic Photonic Materials and Devices XV, Tabor, C. E., Kajzar, F., Kaino, T., Koike, Y., Eds. DOI: 10.1117/12.2013491.

34. Watanabe, S.; Tanaka, H.; Ito, H.; Kuroda, S.; Mori, T.; Marumoto, K.; Shimoi, Y. Direct Determination of Interfacial Molecular Orientations in Field-Effect Devices of P3HT/PCBM Composites by Electron Spin Resonance. *Org. Electron.* **2011**, *12* (4), 716–723. DOI: 10.1016/j.orgel.2011.01.024.

35. Skrypnychuk, V.; Boulanger, N.; Yu, V.; Hilke, M.; Mannsfeld, S. C. B.; Toney, M. F.; Barbero, D. R. Enhanced Vertical Charge Transport in a Semiconducting P3HT Thin Film on Single Layer Graphene. *Adv. Funct. Mater.* **2015**, *25* (5), 664–670. DOI: 10.1002/adfm.201403418.

36. Meredig, B.; Salleo, A.; Gee, R. Ordering of Poly(3-Hexylthiophene) Nanocrystallites on the Basis of Substrate Surface Energy. *ACS Nano* **2009**, *3* (10), 2881–2886. DOI: 10.1021/nn800707z.

37. Agbolaghi, S.; Abbaspoor, S.; Massoumi, B.; Sarvari, R.; Sattari, S.; Aghapour, S.; Charoughchi, S. Conversion of Face-On Orientation to Edge-On/Flat-On in Induced-Crystallization of Poly(3-hexylthiophene) via Functionalization/Grafting of Reduced Graphene Oxide with Thiophene Adducts. *Macromol. Chem. Phys.* **2018**, *219* (4). DOI: 10.1002/macp.201700484.

38. Piliego, C.; Holcombe, T. W.; Douglas, J. D.; Woo, C. H.; Beaujuge, P. M.; Fréchet, J. M. J. Synthetic Control of Structural Order in *N* -Alkylthieno[3,4- *c*]Pyrrole-4,6-Dione-Based Polymers for Efficient Solar Cells. *J. Am. Chem. Soc.* **2010**, *132* (22), 7595–7597. DOI: 10.1021/ja103275u.

39. Chen, M. S.; Niskala, J. R.; Unruh, D. A.; Chu, C. K.; Lee, O. P.; Fréchet, J. M. J. Control of Polymer-Packing Orientation in Thin Films through Synthetic Tailoring of Backbone Coplanarity. *Chem. Mater.* **2013**, *25* (20), 4088–4096. DOI: 10.1021/cm402489a.

40. Imanishi, M.; Kajiya, D.; Koganezawa, T.; Saitow, K. Uniaxial Orientation of P3HT Film Prepared by Soft Friction Transfer Method. *Sci. Rep.* **2017**, *7* (1), 5141. DOI: 10.1038/s41598-017-05396-9.

41. Li, J.; Xue, M.; Xue, N.; Li, H.; Zhang, L.; Ren, Z.; Yan, S.; Sun, X. Highly Anisotropic P3HT Film Fabricated via Epitaxy on an Oriented Polyethylene Film and Solvent Vapor Treatment. *Langmuir* **2019**, *35* (24), 7841–7847. DOI: 10.1021/acs.langmuir.9b00402.

42. Suzuki, S.; Sugimura, R.; Kozaki, M.; Keyaki, K.; Nozaki, K.; Ikeda, N.; Akiyama, K.; Okada, K. Highly Efficient Photoproduction of Charge-Separated States in Donor−Acceptor-Linked Bis(Acetylide) Platinum Complexes. *J. Am. Chem. Soc.* **2009**, *131* (30), 10374–10375. DOI: 10.1021/ja904241r.

43. Nagamatsu, S.; Takashima, W.; Kaneto, K.; Yoshida, Y.; Tanigaki, N.; Yase, K.; Omote, K. Backbone Arrangement in "Friction-Transferred" Regioregular Poly(3-Alkylthiophene)s. *Macromolecules* **2003**, *36* (14), 5252–5257. DOI: 10.1021/ma025887t.

44. Pandey, M.; Nagamatsu, S.; Pandey, S. S.; Hayase, S.; Takashima, W. Enhancement of Carrier Mobility along with Anisotropic Transport in Non-Regiocontrolled Poly (3-Hexylthiophene) Films Processed by Floating Film Transfer Method. *Org. Electron.* **2016**, *38*, 115–120. DOI: 10.1016/j.orgel.2016.08.003.

45. Rivnay, J.; Mannsfeld, S. C. B.; Miller, C. E.; Salleo, A.; Toney, M. F. Quantitative Determination of Organic Semiconductor Microstructure from the Molecular to Device Scale. *Chem. Rev.* **2012**, *112* (10), 5488–5519. DOI: 10.1021/cr3001109.

46. Biniek, L.; Pouget, S.; Djurado, D.; Gonthier, E.; Tremel, K.; Kayunkid, N.; Zaborova, E.; Crespo-Monteiro, N.; Boyron, O.; Leclerc, N.; Ludwigs, S.; Brinkmann, M. High-Temperature Rubbing: A Versatile Method to Align π-Conjugated Polymers without Alignment Substrate. *Macromolecules* **2014**, *47* (12), 3871–3879. DOI: 10.1021/ma500762x.

47. Hartmann, L.; Tremel, K.; Uttiya, S.; Crossland, E.; Ludwigs, S.; Kayunkid, N.; Vergnat, C.; Brinkmann, M. 2D Versus 3D Crystalline Order in Thin Films of Regioregular Poly(3-Hexylthiophene) Oriented by Mechanical Rubbing and Epitaxy. *Adv. Funct. Mater.* **2011**, *21* (21), 4047–4057. DOI: 10.1002/adfm.201101139.

48. Hamidi-Sakr, A.; Biniek, L.; Fall, S.; Brinkmann, M. Precise Control of Lamellar Thickness in Highly Oriented Regioregular Poly(3-Hexylthiophene) Thin Films Prepared by High-Temperature Rubbing: Correlations with Optical Properties and Charge Transport. *Adv. Funct. Mater.* **2016**, *26* (3), 408–420. DOI: 10.1002/adfm.201504096.

49. Ghosh, R.; Pochas, C. M.; Spano, F. C. Polaron Delocalization in Conjugated Polymer Films. *J. Phys. Chem. C* **2016**, *120* (21), 11394–11406. DOI: 10.1021/acs.jpcc.6b02917.

50. Ghosh, R.; Luscombe, C. K.; Hambsch, M.; Mannsfeld, S. C. B.; Salleo, A.; Spano, F. C. Anisotropic Polaron Delocalization in Conjugated Homopolymers and Donor–Acceptor Copolymers. *Chem. Mater.* **2019**, *31* (17), 7033–7045. DOI: 10.1021/acs.chemmater.9b01704.

51. Clark, J.; Chang, J.-F.; Spano, F. C.; Friend, R. H.; Silva, C. Determining Exciton Bandwidth and Film Microstructure in Polythiophene Films Using Linear Absorption Spectroscopy. *Appl. Phys. Lett.* **2009**, *94* (16). DOI: 10.1063/1.3110904.

52. Hexemer, A.; Müller-Buschbaum, P. Advanced Grazing-Incidence Techniques for Modern Soft-Matter Materials Analysis. *IUCrJ* **2015**, *2* (1), 106–125. DOI: 10.1107/S2052252514024178.

53. Scholes, D. T.; Hawks, S. A.; Yee, P. Y.; Wu, H.; Lindemuth, J. R.; Tolbert, S. H.; Schwartz, B. J. Overcoming Film Quality Issues for Conjugated Polymers Doped with F_4TCNQ by Solution Sequential Processing: Hall Effect, Structural, and Optical Measurements. *J. Phys. Chem. Lett.* **2015**, *6* (23), 4786–4793. DOI: 10.1021/acs.jpclett.5b02332.

54. Bredas, J. L.; Street, G. B. Polarons, Bipolarons, and Solitons in Conducting Polymers. *Acc. Chem. Res.* **1985**, *18* (10), 309–315. DOI: 10.1021/ar00118a005.

55. Nagamatsu, S.; Pandey, S. S. Ordered Arrangement of F4TCNQ Anions in Three-Dimensionally Oriented P3HT Thin Films. *Sci. Rep.* **2020**, *10* (1), 20020. DOI: 10.1038/s41598-020-77022-0.

56. Stanfield, D. A.; Mehmedović, Z.; Schwartz, B. J. Vibrational Stark Effect Mapping of Polaron Delocalization in Chemically Doped Conjugated Polymers. *Chem. Mater.* **2021**, *33* (21), 8489–8500. DOI: 10.1021/acs.chemmater.1c02934.

57. Voss, M. G.; Scholes, D. T.; Challa, J. R.; Schwartz, B. J. Ultrafast Transient Absorption Spectroscopy of Doped P3HT Films: Distinguishing Free and Trapped Polarons. *Faraday Discuss* **2019**, *216*, 339–362. DOI: 10.1039/C8FD00210J.

58. Cook, J. B.; Lin, T. C.; Kim, H.-S.; Siordia, A.; Dunn, B. S.; Tolbert, S. H. Suppression of Electrochemically Driven Phase Transitions in Nanostructured MoS_2 Pseudocapacitors Probed Using *Operando* X-Ray Diffraction. *ACS Nano* **2019**, acsnano.8b06381. DOI: 10.1021/acsnano.8b06381.

59. Aguirre, J. C.; Hawks, S. A.; Ferreira, A. S.; Yee, P.; Subramaniyan, S.; Jenekhe, S. A.; Tolbert, S. H.; Schwartz, B. J. Sequential Processing for Organic Photovoltaics: Design Rules for Morphology Control by Tailored Semi-Orthogonal Solvent Blends. *Adv. Energy Mater.* **2015**, *5* (11), 1402020. DOI: 10.1002/aenm.201402020.

60. Wu, E. C.-K.; Salamat, C. Z.; Tolbert, S. H.; Schwartz, B. J. Molecular Dynamics Study of the Thermodynamics of Integer Charge Transfer vs Charge-Transfer Complex Formation in Doped Conjugated Polymers. *ACS Appl. Mater. Interfaces* **2022**, *14* (23), 26988–27001. DOI: 10.1021/acsami.2c06449.

61. Das, P.; Zayat, B.; Wei, Q.; Salamat, C. Z.; Magdău, I. B.; Elizalde-Segovia, R.; Rawlings, D.; Lee, D.; Pace, G.; Irshad, A.; Ye, L.; Schmitt, A.; Segalman, R. A.; Miller, T. F.; Tolbert, S. H.; Dunn, B. S.; Narayan, S. R.; Thompson, B. C. Dihexyl-Substituted Poly(3,4-Propylenedioxythiophene) as a Dual Ionic and Electronic Conductive Cathode Binder for Lithium-Ion Batteries. *Chem. Mater.* **2020**, *32* (21), 9176–9189. DOI: 10.1021/acs.chemmater.0c02601.

62. Bischak, C. G.; Flagg, L. Q.; Yan, K.; Rehman, T.; Davies, D. W.; Quezada, R. J.; Onorato, J. W.; Luscombe, C. K.; Diao, Y.; Li, C. Z.; Ginger, D. S. A Reversible Structural Phase Transition by Electrochemically-Driven Ion Injection into a Conjugated Polymer. *J. Am. Chem. Soc.* **2020**, *142* (16), 7434–7442. DOI: 10.1021/jacs.9b12769.

63. Doris, S. E.; Pierre, A.; Street, R. A. Dynamic and Tunable Threshold Voltage in Organic Electrochemical Transistors. *Adv. Mater.* **2018**, *30* (15). DOI: 10.1002/adma.201706757.

64. Tan, S. T. M.; Lee, G.; Denti, I.; LeCroy, G.; Rozylowicz, K.; Marks, A.; Griggs, S.; McCulloch, I.; Giovannitti, A.; Salleo, A. Tuning Organic Electrochemical Transistor Threshold Voltage Using Chemically Doped Polymer Gates. *Adv. Mater.* **2022**, *34* (33). DOI: 10.1002/adma.202202359.

65. Cendra, C.; Giovannitti, A.; Savva, A.; Venkatraman, V.; McCulloch, I.; Salleo, A.; Inal, S.; Rivnay, J. Role of the Anion on the Transport and Structure of Organic Mixed Conductors. *Adv. Funct. Mater.* **2019**, *29* (5). DOI: 10.1002/adfm.201807034.

66. Flagg, L. Q.; Bischak, C. G.; Onorato, J. W.; Rashid, R. B.; Luscombe, C. K.; Ginger, D. S. Polymer Crystallinity Controls Water Uptake in Glycol Side-Chain Polymer Organic Electrochemical Transistors. *J. Am. Chem. Soc.* **2019**, *141* (10), 4345–4354. DOI: 10.1021/jacs.8b12640.

67. Schmode, P.; Savva, A.; Kahl, R.; Ohayon, D.; Meichsner, F.; Dolynchuk, O.; Thurn-Albrecht, T.; Inal, S.; Thelakkat, M. The Key Role of Side Chain Linkage in Structure Formation and Mixed Conduction of Ethylene Glycol Substituted Polythiophenes. ACS Appl. Mater. Interfaces 2020, 12 (11), 13029–13039. DOI: 10.1021/acsami.9b21604.

CHAPTER 4

Measuring the anisotropic conductivity of rub-aligned doped semiconducting polymer films: The role of electrode geometry

Chapter 4 delves into our understanding of the anisotropic conductivity in rub-aligned P3HT films. It details the methods used to measure this anisotropic conductivity and identifies various issues with how some literature reports these measurements for rub-aligned films. Furthermore, this chapter explores the challenges associated with Hall effect measurements on rub-aligned polymer films.

This chapter was reprinted with permission from Duong, Q. M.; Garcia-Vidales D..; Salamat, C. Z.; Tolbert, S. H.; Schwartz, B. J. " Measuring the anisotropic conductivity of rub-aligned doped semiconducting polymer films: The role of electrode geometry" Phys. Rev. Appl. 21, 024006, 1-10 (2024); DOI: 10.1103/PhysRevApplied.21.024006.

A reprint of the supporting information is given in Appendix C.

4.1. Introduction

With their intrinsically low thermal conductivities, semiconducting conjugated polymers such as poly(3-hexylthiophene-2,5-diyl) (P3HT) are materials with promising potential for thermoelectric applications. [1]– [3] However, pristine semiconducting polymers also possess poor electrical conductivity, σ, which affects the thermoelectric efficiency zT:

$$zT = \frac{S^2\sigma}{\kappa}T, \quad (1)$$

where S is the Seebeck coefficient, σ is the electrical conductivity, κ is the thermal conductivity, and T is the temperature. The electrical conductivity of semiconducting polymer films is in turn determined by carrier density n and mobility μ: $\sigma = ne\mu$, where e is the fundamental charge.

The carrier density in semiconducting polymers can be increased by doping; most conjugated polymers are p-type materials and thus can be doped with strong oxidizing agents, such as 2,3,5,6-tetrafluoro-7,7,8,8-tetracyanoquinodimethane (F4TCNQ). The carrier mobility, however, is heavily dependent on a doped polymer film's morphology. In general, most conjugated polymers are semicrystalline, which means that outside of the relatively small crystallites, the chains in conjugated polymer films can bend, twist, and entangle, resulting in randomly-oriented ordered and amorphous regions. This bending and twisting can break the conjugation, leading to a broad distribution of conjugated sites with different energies. [4] Charge transport in the presence of such site disorder is generally poor and mainly dictated by thermally-activated hopping. [4]–[6]

One route to reduce energetic disorder and thus improve carrier mobility is to molecularly align the chains in doped conjugated polymer films. A versatile way to achieve this is via high-temperature rubbing, a method pioneered by Brinkmann and coworkers, which macroscopically

aligns the polymer chains along the rubbing direction. [7–14] The rubbing process significantly enhances the electrical conductivity compared to non-aligned films, with reports of the conductivity of F4TCNQ-doped P3HT films increasing from 9 to 160 S/cm after rub alignment.[7]

Although the electrical conductivity of rub-aligned doped conjugated polymer films is significantly enhanced compared to that of non-aligned films, the charge transport in such films is anisotropic. [7], [15]– [17] This is because carrier transport mainly occurs along the conjugated backbone and between chains that are π-stacked; transport is not facile through the electrically insulative side chains that confer solubility. [18] Thus, anisotropic electrical conductivity measurements are often reported in terms of conductivities parallel (∥) and perpendicular (⊥) to the rubbing direction, [7–14,19] and these values can differ by a factor of 3.5 to 8. [7,9] Here, our goal is to explore the merits of different methods for measuring anisotropic electrical conductivities in rub-aligned doped conjugated polymer films.

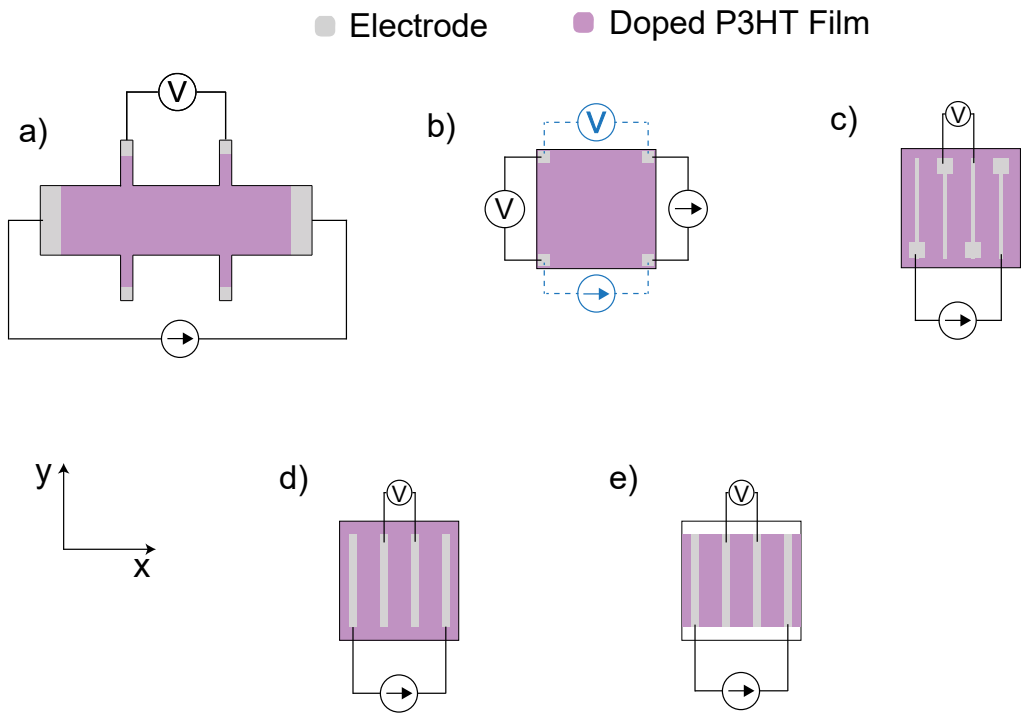

Figure 4. 1. Geometries of the three methods for anisotropic conductivity measurements on doped, rub-aligned conjugated polymers explored in this work: a) the standard six-contact Hall bar geometry; b) the rectangular geometry via the Montgomery method, where the source current and voltage measurements are rotated by 90° (blue and black diagrams) along the principal x and y axes; c) the four-line geometry similar to that used by Brinkmann and coworkers; [7,9–14] d) the rectangular four-line geometry; and e) the rectangular four-line confined geometry. Here, the purple shading represents the aligned, doped P3HT film, the gray shading shows the positions of the electrodes, the arrow indicates a current source, and V indicates a voltage measurement.

The standard way to obtain anisotropic conductivities and/or resistivities is using a four-point probe measurement with electrodes arranged in the Hall bar geometry, which is shown in **Figure 4.1a**. The source and sink electrodes are placed on opposite ends of a rectangular strip,

confining current flow to a single direction. However, fabricating a Hall bar electrode geometry is often not simple or convenient, and only one conductivity direction can be measured per sample. This is particularly problematic for rub-aligned conjugated polymer films, for which there is a great deal of sample-to-sample variation as well as variances between different locations on the same sample, so that it can be challenging to compare conductivities in different directions taken on different samples or even in different places on the same film.

Here, we show that the anisotropic conductivity of rub-aligned films can be measured accurately using a simpler rectangular geometry (**Figure 4.1b**) based on the revised Montgomery method, [20], [21] which also provides the advantage that the parallel and perpendicular conductivities of rub-aligned films can be measured on the same sample and location. We also explore the possibility of performing Hall effect measurements on rub-aligned films using this rectangular geometry and we show that four-line (**Figure 4.1c**) measurements used by Brinkmann and coworkers for anisotropically-conducting doped conjugated polymer samples significantly overestimate the conductivity.

4.2 Results and Discussions

4.2.1. Montgomery's Method for Measuring Anisotropic Conductivity

The Montgomery method [22] is a technique that combines the work of Wasscher, [23] Van der Pauw, [24] and Logan, Rice, and Wick [25] to deconvolute the different directional resistivities in anisotropic materials. Unlike the Hall bar geometry, the samples used in the Montgomery method are fabricated into a simple rectangular geometry, as shown in **Error! Reference source not found.b**, with electrodes placed at each corner. The method requires that the direction of the components of the resistivity (ρ_i) be along the sample's principal axes, $i = x$ or

y. Since the directions of the resistivity components are known in rub-aligned films through polarized UV-Vis spectroscopy, only two resistance measurements are needed to solve for the film's anisotropic conductivity.

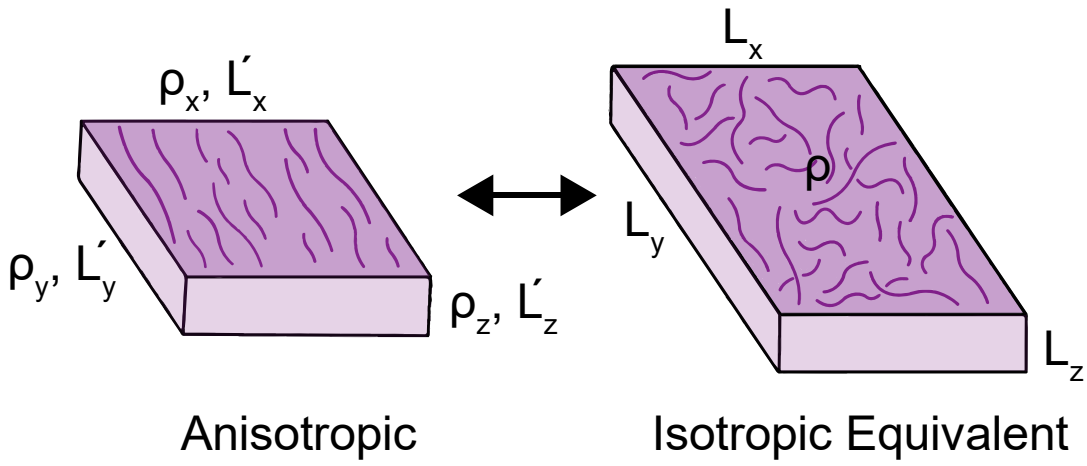

Figure 4. 2. Schematic of the Wassher transformation of anisotropically-conducting samples with conductivity ρ_i along the principal axes with lengths L_i' into an isotropically-conducting equivalent with lengths L_i. The key step of the Montgomery method is mapping the anisotropically-conducting sample onto that of an isotropic equivalent using the Wasscher transformation, which treats the anisotropic sample as isotropic but with dimensions proportional to its anisotropic resistivity. [23]

Figure 4. 2. Schematic of the Wassher transformation of anisotropically-conducting samples with conductivity ρ_i along the principal axes with lengths L_i' into an isotropically-conducting equivalent with lengths L_i. The key step of the Montgomery method is mapping the anisotropically-conducting sample onto that of an isotropic equivalent using the Wasscher transformation, which treats the anisotropic sample as isotropic but with dimensions proportional to its anisotropic resistivity. [23] . illustrates the relationship between the anisotropic sample and

its isotropic equivalent. Both L_i' and L_i have units of length, with the prime referring to the anisotropic samples and the non-primed variables referring to the isotropic equivalent. Through the Wasscher transformation, the anisotropic problem is now an isotropic one with a single resistivity ρ:

$$\rho = H_x E R_x = H_y E R_y, \tag{2}$$

where the isotropic resistivity is based on the resistances (R_i) measured in the in-plane principal directions with two correction factors, H_i and E. The correction factors H_i account for the finite lateral dimensions, while E accounts for the finite thickness of the isotropic sample. [20,21] Logan, Rice, and Wick solved the above relation using the method of images and obtained a series for the correction factors. [25]

A revision of the Montgomery method by dos Santos and coworkers [20] simplified the series by showing that only the first term was needed to obtain a good approximation. For this revised version, the H_i's are simplified to:

$$H_x \approx \left(\frac{\pi}{8}\right) \sinh\left(\frac{\pi L_y}{L_x}\right) \quad \text{and} \quad H_y \approx \left(\frac{\pi}{8}\right) \sinh\left(\frac{\pi L_x}{L_y}\right). \tag{3}$$

The H_i correction factors in Eq. 3 only depend on the ratio between the isotropic in-plane dimensions L_x and L_y. The value of this ratio is proportional to the resistance ratio measured in the two principal directions. Using the definition $\sinh(x) = \frac{e^x - e^{-x}}{2}$ and Eqs. 2 and 3, dos Santos and coworkers obtained the following approximation that can be used to calculate the H_i's:

$$\frac{L_y}{L_x} \cong \frac{1}{2}\left[\frac{1}{\pi}\ln\frac{R_y}{R_x} + \sqrt{\left(\frac{1}{\pi}\ln\frac{y}{R_x}\right)^2 + 4}\right]. \quad (4)$$

With the help of Equation 4, the correction factors H_i can be easily obtained through two resistance measurements along the principal axes, allowing the anisotropic resistivity components to be straightforwardly determined by reversing the Wasscher transformation, as summarized in Equations 5: [20,21]

$$\rho_x \approx \left(\frac{\pi}{8}\right) E' \left(\frac{L'_y}{L'_x}\right)\left(\frac{L_x}{L_y}\right) R_y \sinh\left[\frac{\pi L_x}{L_y}\right] = \frac{1}{\sigma_x} \quad (5)$$

and

$$\rho_y \approx \left(\frac{\pi}{8}\right) E' \left(\frac{L'_x}{L'_y}\right)\left(\frac{L_y}{L_x}\right) R_x \sinh\left[\frac{\pi L_x}{L_y}\right] = \frac{1}{\sigma_y}$$

For thin film samples, the effective anisotropic thickness E' can be replaced with the actual sample thickness L'_z. With the revised Montgomery method, the anisotropic conductivities can thus be obtained with two simple resistance measurements without having to fabricate multiple rub-aligned samples. Furthermore, Equations 5 also give us a generic relation between the anisotropic resistivity components and the anisotropic conductivity (σ_x and σ_y).

4.2.2 Fabrication of Doped of Rub-aligned P3HT Films and Polarized UV-Vis-NIR spectroscopy

To test how well this formalism works on doped, aligned films of semiconducting polymers, we employed the high-temperature rub-aligning method to create anisotropic P3HT films. [7–9] The polymer films were made by spin coating regioregular (97%) P3HT (Ossila) onto glass substrates. After allowing them to dry, the P3HT films were then rub-aligned at 140 ^{o}C using a homemade setup consisting of a microfiber polishing wheel that can sbe applied to the film with

a reproducible force in an inert atmosphere (see **Figure S14** and other details in the Supporting Materials (SM) [26]). Polarized UV-Vis spectroscopy (**Fig. S15** in the SI) showed that the dichroic ratio ($I_{\parallel}/I_{\perp}$) of the absorbance at 610 nm (2.03 eV) was ≥ 10, comparable to the highest dichroic ratios previously reported for rub-aligned P3HT. [7–14,19] We also see a small enhancement of the 0-0 vibrational peak relative to the 0-1, which is indicative of the stronger intrachain coupling that results from straightening the polymer chains. [7,30–32]

After successfully rub-aligning the P3HT films, we then chemically doped them using the sequential processing (SqP) method, which involves exposing the samples to a solution of the dopant in a solvent that swells but does not dissolve the underlying polymer film. [31,33–35] One set of aligned P3HT samples was doped with a solution of 3 mg/mL F_4TCNQ (Ossila) in *n*-butyl acetate (*n*-BA). The second set of samples was doped using the anion-exchange method [36] by exposing the films to a solution of 3 mg/mL F_4TCNQ in *n*-BA that was co-dissolved with 30 mg/mL of bis(trifluoromethane)sulfonimide lithium (LiTFSI) electrolyte. The anion exchange method allows for higher doping levels than conventional doping methods and also provides control over the counterion present in the rub-aligned doped polymer film. [19]

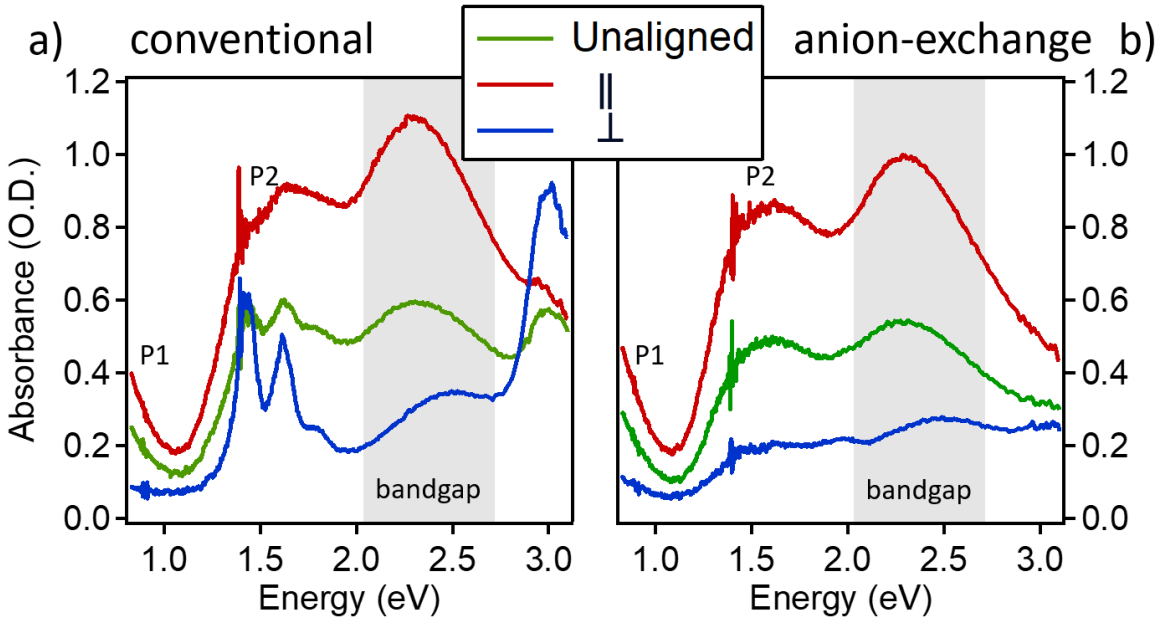

Figure 4. 3. Polarized UV-Vis absorption spectra (red curves, light polarized parallel (∥) to the rubbing direction; blue curves, light polarized perpendicular (⊥) to the rubbing direction) of rub-aligned doped P3HT films; the green curves show the corresponding spectrum of an unaligned doped P3HT film. Panel a) shows the results for conventional doping with F4TCNQ, while panel b) displays the results for doping via the anion-exchange method in the presence of LiTFSI. The noise near 1.4 eV is due to a lamp change in the instrument.

Figure 4. 3 shows polarized UV-Visible absorption spectra for the rub-aligned P3HT films doped with each of these two methods. For the conventional doping method, **Fig. 4. 3a** shows that with light polarized ∥ to the rubbing direction probes the neutral P3HT band-bap absorption near 2.2 eV as well as the so-called P2 (~1.6 eV) and P1 (< 1 eV) peaks associated with the presence of polarons (charge carriers). With light polarized in the ⊥ direction, we see that the neutral polymer absorption is significantly blue-shifted to ~2.4 eV, and we also see F_4TCNQ anion peaks

at ~1.4, 1.6, and 3.0 eV. The small presence of these anion peaks seen in the parallel direction indicates that not all of the doped polymer chains are fully aligned in the rubbing direction.

In contrast to the conventional doping method, the polarized absorption spectra of the anion-exchange-doped films are shown in **Fig. 4. 3b** no longer show the presence of the F_4TCNQ anion, indicating that the F_4TCNQ anions were successfully exchanged with TFSI anions. [19,36] We also observe the presence of the P1 and P2 polaron absorption features in the perpendicular direction, indicating that the extra doping power afforded by the anion-exchange method allows for doping some of the amorphous regions that remain in the aligned film. This idea is also supported by a decrease in the intensity of the blue-shifted P3HT bandgap peak in the perpendicular direction: with anion exchange, there are fewer undoped and more doped conjugated segments that are not aligned along the rubbing direction. [19] Thus, our use of conventional and anion exchange doping allows us to get better insights into how having carriers in different regions (aligned and crystalline in the conventionally doped films vs. crystalline and amorphous in the anion-exchange doped films) affect the anisotropic electrical conductivity.

4.2.3. Electrical Conductivity Measurements

	Rectangular Non-Aligned	**Hall Bar Non-Aligned**	**Rectangular Aligned (∥, ⊥)**	**Hall Bar Aligned (∥, ⊥)**
Conventional *Conductivity* (S/cm)	4.66 ± 0.30	4.25 ± 1.18	8.28 ± 0.12, 0.63 ± 0.09	9.89 ± 2.81, 0.91 ± 0.31
Anion-Exchange *Conductivity* (S/cm)	12.36 ± 0.19	11.07 ± 0.36	33.95 ± 0.09, 3.22 ± 0.36	47.43 ± 23.3, 3.41± 0.66

Table 4. 1. Conductivity of non-aligned and rub-aligned doped P3HT films measured using both the Hall bar (**Fig. 4. 1a**) and rectangular (**Fig. 4. 1b**) electrode geometries.

For our electrical measurements on the rub-aligned, doped P3HT films, we limited the source current to 10 μA to avoid injecting excess charges and to minimize sample heating, even though we found that for all of our samples in both the Hall bar and rectangular geometries, the current could be sourced up to 1 mA without any evidence of non-ohmic behavior. We also note the rub-aligned P3HT films are quite rough, [10,11] so that it is not straightforward to determine the thickness of these films. (The Brinkmann group suggests melting the films, which destroys their alignment, and then using UV-Vis spectroscopy to determine the average thickness post-melt). [7–13]

The primary and most commonly employed method for assessing the morphology and thickness of a thin film is either via profilometry or atomic force microscopy (AFM). **Figure S18** (see SM [26]) displays 3-D surface profiles of non-aligned and rub-aligned P3HT films, both doped and undoped, obtained using profilometry. We note that the rub-aligning process significantly increases the surface roughness of the films, as imperfections on the surface of the microfiber polishing wheel cut grooves and ridges into the relatively soft polymer underneath. This increased roughness makes it difficult to accurately measure the rub-aligned thickness by the traditional method of making a cut into the film to expose the substrate and performing a line scan to determine the film thickness as the height of the step adjacent to the cut.

Thus, for our rub-aligned samples, instead of relying on a few individual line scans that can show large variations, we elected to determine the average thickness over a large area of each sample, as documented in **Table S8** of the SM [26]. We find that despite the rough topology, the average thickness and surface roughness of our rub-aligned films are reproducible, giving us confidence when comparing sheet resistances or conductivities between samples or measurements with different electrode geometries.

One feature worth noting is that the average profilometry-determined thickness of our rub-aligned films appears greater than the non-aligned films from which they were prepared. This appears counterintuitive, as the rubbing process is expected to remove polymer material, so that the rub-aligned films would be expected to become thinner. However, the roughness features on the surface of the film are comparable to or smaller in size than the profilometer tip diameter, which is thus unable to properly measure the depth of the grooves rubbed into the films' surfaces. The conductivities we report in **Table 4.1** use the average thickness determined by the 3-D profilometry scans are thus likely underestimated since the thickness we use to calculate the conductivities is likely overestimated, as discussed in more detail in the SI. This slight systematic error, however, does not affect our comparison of the use of different electrode geometries to measure the anisotropic conductivity of our rub-aligned samples.

Error! Reference source not found. summarizes the electrical conductivity measurements for our conventionally- and anion-exchange-doped non-aligned and rub-aligned P3HT films. The reported values were averaged from at least 3 independent samples. The conductivity measured via the rectangular geometry are the same within error as those measured using the Hall bar geometry, verifying that the rectangular method can accurately measure the

anisotropic conductivity of aligned doped conjugated polymer films. The modest discrepancies between the conductivities obtained using the two methods are largely due to sample-to-sample variations, as it is quite challenging to make precisely identical rub-aligned films, and of necessity, the measurements with different electrode geometries have to be taken on different samples. Fortunately, the rectangular geometry allows both the parallel and perpendicular measurements to be taken simultaneously on the same sample, a significant advantage over the Hall bar geometry.

The parallel and perpendicular conductivities for the rub-aligned P3HT films doped with the conventional method are 8.28 $\pm$ 0.12 and 0.63 $\pm$ 0.09 S/cm (averaged values from the modified Montgomery method), respectively. As has been discussed previously, [7–9] the doped rub-aligned films show a higher parallel conductivity compared to doped non-aligned films (4.66 $\pm$ 0.30 S/cm), the result of improved charge transport in the rub-aligned direction. The conductivity of the rub-aligned doped films in the perpendicular direction, however, is significantly lower than that of the non-aligned film. In addition to the fact that carrier transport in the $\perp$ direction largely involves hopping between polymer chains, the decreased perpendicular conductivity may also result from the fact that rub-alignment induces a change in the texturing of the polymer.

Charge transport within doped semiconducting polymers is anisotropic on a molecular scale, since it is easier for carriers to move along the conjugated backbone of the polymer or between π-stacked chains than along the direction of the insulating side groups.[18,] [37–40] When spin-cast into thin films, P3HT crystallites tend to be edge-on oriented with respect to the substrate, so that the best molecular directions for electrical conductivity both lie in plane. However, rub-alignment of P3HT films results in the formation of both edge-on and face-on oriented crystallites, [7–14] as shown in **Figure S18** of the SM [26]. Thus, even though highly-oriented

polymer chains should have enhanced charge transport due to reduced energetic disorder, the fact that some crystallites now have their insulating side-chains lying in-plane may hinder the mobility of carriers on the molecular scale. This diminished conduction in the perpendicular direction has also been observed in a recent report involving rub-aligned doped conjugated polymer films utilizing the Hall bar geometry. [19] Numerous studies in the field of organic solar cells have also indicated that charge transport through the side chains is considerably less effective than traversing the π-stacks or following the polymer backbone. [41–44]

It is worth noting that our finding that the perpendicular conductivity of the rub-aligned doped P3HT film is lower than that of an isotropic film, which we believe makes sense, is in contrast to results presented by Untilova and coworkers. [7] These workers reported conductivity values for aligned doped conjugated polymers in the perpendicular direction that equaled or exceeded the conductivity of the corresponding non-aligned polymer samples. As we will discuss in more detail below, we believe that this result is an artifact of the fact that this group used a 4-line electrode geometry, shown in **Fig. 4. 1c**, [7] which is not appropriate for determining the conductivity of anisotropically-conducting samples.

For the rub-aligned P3HT films doped with the anion-exchange method, the parallel and perpendicular conductivities are much higher than those doped with the conventional methods, 33.95 $\pm$ 0.09 and 3.22 $\pm$ 0.36 S/cm, respectively. The higher conductivities make sense given that the anion-exchange method leads to higher doping levels, which is consistent with the more depleted neutral P3HT bandgap absorption seen in **Fig. 4. 3b**. It is worth noting that despite the fact that anion exchange dopes the amorphous regions as well as the crystalline regions of the P3HT film, the anisotropy in the observed conductivities is actually slightly higher than that of the

conventionally-doped films. This suggests that electrical conduction through the amorphous regions is not substantial, even when the films are highly doped. [45]

4.2.4. Hall Effect Measurements

		Rectangular Non-Aligned	**Hall Bar Non-Aligned**	**Rectangular Aligned (∥, ⊥)**	**Hall Bar Aligned (∥, ⊥)**
Conventional	$Hall\ Carrier\ Density\ (cm^{-}$	$3.7 \times 10^{20} \pm 1.3 \times 10^{19}$	$4.2 \times 10^{20} \pm 1.9\ 10^{20}$	$6.2 \times 10^{20} \pm 1.4 \times 10^{20}$	$3.3 \times 10^{20} \pm 8.7 \times 10^{19}$, $1.0 \times 10^{21} \pm 1.0 \times 10^{21}$
	Mobility $(cm^2/V \cdot s)$	0.08 ± 0.005	0.09 ± 0.06	0.08 ± 0.02, 0.007 ± 0.002	0.2 ± 0.09, 0.01 ± 0.008
Anion-Exchange	$Hall\ Carrier\ Density\ (cm^{-}$	$4.7 \times 10^{20} \pm 3.6\times 10^{19}$	$4.3 \times 10^{20} \pm 5.4 \times 10^{19}$	$9.0 \times 10^{20} \pm 5.8\times 10^{19}$	$5.5 \times 10^{19} \pm 4.5 \times 10^{19}$, $8.7 \times 10^{20} \pm 7.7 \times 10^{20}$
	Mobility $(cm^2/V \cdot s)$	0.17 ± 0.01	0.16 ± 0.03	0.24 ± 0.03, 0.022 ± 0.004	7.10 ± 3.11, 0.03 ± 0.02

Table 4. 2. DC field-and-current reversed Hall effect measurements for conventional and anion-exchange-doped non-aligned and rub-aligned P3HT films using both the Hall bar and rectangular electrode geometries.

In addition to conductivity measurements, we also performed Hall effect measurements on the rub-aligned doped P3HT films in an effort to obtain insights into anisotropic carrier mobility. Typically, the Hall bar geometry is used to determine anisotropic carrier mobilities. [46] In contrast, the rectangular geometry based on the Van der Pauw method is not commonly used for anisotropic samples because the results can be difficult to interpret due to the apparent dependence

of the Hall voltage on the sample's anisotropy. However, Bierwagen et al. [46] have presented numerical calculations and experimental data showing that a sample's anisotropy does not have a significant impact on the measurement of the Hall voltage, so that it should be possible to utilize the Van der Pauw geometry to calculate an anisotropic sample's carrier density and mobility without the need for a correction factor. Here, we used the revised Montgomery method, along with rectangular-geometry Hall measurements, to obtain the anisotropic sheet carrier density and thus the anisotropic mobility of the carriers in doped rub-aligned P3HT films, the results for which are summarized in **Table 4.2**.

In principle, the carrier density should be the same regardless of the measured direction; this is because the same doping-induced charge carriers move either along or against the rubbing direction. However, with the Hall bar geometry, the carrier density measured in the parallel direction is roughly an order of magnitude less than that in the perpendicular directions. We believe that this is an effect of having mixed transport in the rub-aligned system. Only band-like carrier transport is directly affected by the Lorentz force, so the presence of low-mobility carriers that move by hopping in doped organic semiconductors presents challenges for interpreting the results of Hall effect measurements. [6,47,48] Yi *et al.* have proposed a set of analytical expressions to describe Hall measurements in a simple isotropic system with two types of carrier transport: band-like and hopping transport. [6] When a significant fraction of the carriers have hopping-like transport, the measured Hall carrier density can deviate significantly from the actual total carrier density.

We believe that the difference in Hall mobility and Hall carrier density observed in rub-aligned doped P3HT films is due to underestimating and overestimating the total carrier density in

the directions parallel and perpendicular to the rub alignment, respectively. For the Hall bar geometry in the parallel direction, we expect that more carriers would experience band-like transport owing to the chain alignment. This is supported by temperature-dependent conductivity measurements on the rub-aligned films, which are presented in **Figures S19** and **S20** and **Table S10** in the SM [26]. The activation barrier for conduction extracted from these measurements is lower in the direction parallel to the rub-alignment than in the perpendicular direction; the parallel conduction barrier is also lower than that seen in the non-aligned doped films. The lower activation barrier is consistent with reduced energetic disorder, more delocalized carriers and thus a greater degree of band-like versus hopping-like transport. [49]

The small number of carriers that experience hopping-like transport will contribute little to the Hall voltage, so the measured Hall carrier density is slightly less than the total carrier density. In the perpendicular direction, however, carrier transport is primarily via hopping due to the need for interchain carrier motion, particularly due to the face-on polymer texture. Although hopping carriers are not affected directly by the Lorentz force, they are affected by the electric field caused by the separation of the transport of the small number of band-like carriers. [6] This electric field forces the hopping carriers to move against the Lorentz force, resulting in a smaller measured Hall voltage and thus an overestimate of the carrier density.

Interestingly, the Hall carrier density determined using the rectangular geometry is closer to that measured via the Hall bar geometry in the perpendicular direction than the parallel direction. Since the current in the rectangular geometry is sourced ~45^{o} to the parallel direction, the Hall voltage measured in this geometry should be a weighted average of the two transport cases mentioned above, with hopping transport more likely than band-like transport. However, it is

difficult to pinpoint which geometry gives the most correct measurement of the total carrier concentration without knowing the precise extent of the mixed transport effect. Clearly, electrode placement relative to the rubbing direction is crucial since it will govern the contribution of band-like and hopping transport to the anisotropic Hall measurement.

Since they are much more highly doped, the anion-exchanged-doped aligned P3HT films are expected to have a higher carrier mobility due to a lower barrier for hopping. [49] Indeed, higher mobility was observed in both the aligned and non-aligned anion exchange-doped samples than in those that were conventionally doped. However, we observed the same mobility anisotropy trend in the anion-exchange-doped samples doped, with higher mobility in the parallel direction obtained from the Hall bar geometry than that obtained from the rectangular geometry. Similar to the conventional doping case, this was due to a different carrier density being measured in the parallel and perpendicular directions for the Hall bar geometry. This trend is also consistent with having mixed transport.

4.2.5. Comparison of Electrode Geometries Effect on Measuring Anisotropic Effect

As mentioned above, in previous work, Brinkmann and co-workers used a four-line geometry (**Fig. 4. 1c**) to measure the anisotropic conductivity of rub-aligned doped conjugated polymer films. [7–13] To calculate the conductivity for the four-line geometry, Brinkmann and coworkers added a geometrical correction factor, C, to the standard four-point probe equation to account for the use of line instead of point-like electrodes, as summarized in Equation 6: [7,9]

$$\sigma = \frac{\ln(2)}{C\pi}\frac{I}{\Delta V}\frac{1}{t} \tag{6}$$

where ΔV is the measured voltage between the two inner electrodes, I is the current sourced between the two outer electrodes, and t is the film's thickness. The geometrical correction factor is obtained by taking the ratio of resistances obtained from four-point and four-line electrode geometries on non-aligned films. [7,9] For our four-line geometry (1.5-mm spacing between 7.5-mm length electrodes), the correction factor was measured to be ~1.4, as described in the SI. It is also important to point out that the four-line geometry used by Brinkmann and coworkers, shown in **Fig. 4. 1c**, has square contacts at one end. The smaller correction factor we find here compared to that reported by Brinkmann and coworkers ($C = 1.8$) [9] likely results from our use of different electrode sizes relative to the sample area.

Electrode Geometry	**Parallel Conductivity** (S/cm)	**Perpendicular Conductivity** (S/cm)
Rectangular (Montgomery Method; Fig. 4.1b, this work)	2.59 ± 0.09	0.21 ± 0.01
Four-line (Brinkmann and Coworkers; Fig. 4.1c)[9]	3.51 ± 0.22	0.36 ± 0.02
Four-line (without square contacts; Fig. 4.1d)	2.80 ± 0.09	0.28 ± 0.03
Four-line (without square contacts and confined; Fig 1e)	3.27 ± 0.02	0.20 ± 0.02

Table 4. 3. Conductivities of rub-aligned F4TCNQ-doped P3HT films in different directions using the rectangular (**Fig. 4.1b**) and various four-line (**Figs. 4.1c-e**) electrode geometries.

We then used Equation 8, along with the value of 1.4 for the geometrical correction factor C, to calculate the conductivity of rub-aligned doped P3HT films using the four-line electrode

geometry (**Fig. 4.1c**); the results are summarized in **Table 4.3**. The rub-aligned films for this comparison were made in the same way as those whose properties are shown in **Fig. 4.3** and **Table 4.1**, except that the films were sequentially doped using a 1 mg/mL F4TCNQ solution in acetonitrile (instead of n-BA) to directly compare to the previous work by Brinkmann and co-workers. [7] **Table 4.3** shows that the parallel and perpendicular conductivity obtained using the four-line geometry are ~26% and ~40% higher than those obtained using the rectangular geometry, respectively. This overestimation of conductivity using the four-line geometry is likely why Huang and coworkers, [19] who used the Hall bar geometry to measure the electrical conductivity of rub-aligned doped conjugated polymer films, were unable to reproduce the high conductivities reported by Brinkmann and coworkers. [14]

To understand the reasons the 4-line geometry overestimates the conductivity, we performed a set of additional experiments involving further modification of this electrode geometry. First, we created an electrode geometry with four uniform lines that did not have square contact pads (**Fig. 4.1d**). When measured on isotropic doped P3HT samples, the correction factor remained at the same value of 1.4 as that for the geometry with the square contact pads (**Table S7**). However, we find a notable difference when applying this modified 4-line electrode geometries to the aligned doped P3HT samples: the configuration featuring square contacts yields a higher conductivity in both the parallel and perpendicular directions, as summarized in **Table 4.3**. This suggests that the use of a single correction factor that is derived from an isotropic sample cannot be rigorously applied to measuring anisotropic conductivity. We believe that this explains why Brinkmann and co-workers saw an apparent increase in conductivity in the perpendicular

direction of their aligned samples relative to isotropic samples: [7] the isotropic correction factor is too low to properly describe the perpendicular carrier transport.

Next, we examined another factor that might explain why the 4-line geometry electrodes in **Fig. 4.1c** lead to errors in the measured conductivity: the fact that line electrodes do not span the entire size of the doped polymer sample. The issue is that conducting material 'outside' the electrodes may provide for additional current paths that are not reflected in the voltage measured on the center electrodes. [21] To test this, we performed experiments removing the doped aligned polymer material outside the electrodes, which we refer to as the 4-line 'confined' geometry (**Fig. 4.1e**). We find that the 4-line confined geometry leads to an increase in the measured conductivity in the parallel direction and a decrease in conductivity in the perpendicular direction, thus increasing the measured conductivity anisotropy. This is yet another sign that the use of a single correction factor from an isotropic sample cannot account for electrode geometric disparities used on anisotropically conducting samples. It also likely explains why the conductivity anisotropy we measure with the 'confined' Hall bar and Montgomery electrode geometries is higher than that reported by Brinkmann and co-workers with the 'unconfined' 4-line geometry. [7]

4.3. Conclusions

In summary, the anisotropic conductivity of rub-aligned doped conjugated polymer films can be accurately measured using the rectangular electrode geometry via the modified Montgomery method. In addition to comparing the Hall bar and rectangular electrode geometries, we showed that use of a four-line geometry, particularly one with square contact pads, significantly overestimates the anisotropic conductivity of rub-aligned films, a result stemming from the fact that the correction factor measured on isotropic films does not properly transfer to anisotropically-

conducting samples. Overall, the rectangular geometry is significantly more straightforward to fabricate than the Hall bar and allows the conductivity in both directions to be measured simultaneously, making it a better alternative to the Hall bar and four-line geometries for anisotropic conductivity measurements of rub-aligned doped conjugated polymers, although the Hall bar geometry is still preferred for Hall effect measurements.

References

[1] T. M. Swager, 50th Anniversary Perspective: Conducting/Semiconducting Conjugated Polymers. A Personal Perspective on the Past and the Future, Macromolecules **50**, 4867 (2017).

[2] N. Dubey and M. Leclerc, Conducting Polymers: Efficient Thermoelectric Materials, Journal of Polymer Science Part B: Polymer Physics **49**, 467 (2011).

[3] G.-H. Kim, L. Shao, K. Zhang, and K. P. Pipe, Engineered Doping of Organic Semiconductors for Enhanced Thermoelectric Efficiency, Nature Mater **12**, 8 (2013).

[4] R. Noriega, J. Rivnay, K. Vandewal, F. P. V. Koch, N. Stingelin, P. Smith, M. F. Toney, and A. Salleo, A General Relationship between Disorder, Aggregation and Charge Transport in Conjugated Polymers, Nature Materials **12**, 11 (2013).

[5] G. Zuo, Z. Li, O. Andersson, H. Abdalla, E. Wang, and M. Kemerink, Molecular Doping and Trap Filling in Organic Semiconductor Host–Guest Systems, J. Phys. Chem. C **121**, 7767 (2017).

[6] H. T. Yi, Y. N. Gartstein, and V. Podzorov, Charge Carrier Coherence and Hall Effect in Organic Semiconductors, Sci Rep **6**, 1 (2016).

[7] V. Untilova, T. Biskup, L. Biniek, V. Vijayakumar, and M. Brinkmann, Control of Chain Alignment and Crystallization Helps Enhance Charge Conductivities and Thermoelectric Power Factors in Sequentially Doped P3HT:F4TCNQ Films, Macromolecules **53**, 2441 (2020).

[8] L. Biniek et al., High-Temperature Rubbing: A Versatile Method to Align π-Conjugated Polymers without Alignment Substrate, Macromolecules **47**, 3871 (2014).

[9] A. Hamidi-Sakr, L. Biniek, J.-L. Bantignies, D. Maurin, L. Herrmann, N. Leclerc, P. Lévêque, V. Vijayakumar, N. Zimmermann, and M. Brinkmann, A Versatile Method to Fabricate

Highly In-Plane Aligned Conducting Polymer Films with Anisotropic Charge Transport and Thermoelectric Properties: The Key Role of Alkyl Side Chain Layers on the Doping Mechanism, Advanced Functional Materials **27**, 1700173 (2017).

[10] V. Untilova et al., High Thermoelectric Power Factor of Poly(3-Hexylthiophene) through In-Plane Alignment and Doping with a Molybdenum Dithiolene Complex, Macromolecules **53**, 6314 (2020).

[11] Y. Zhong, V. Untilova, D. Muller, S. Guchait, C. Kiefer, L. Herrmann, N. Zimmermann, M. Brosset, T. Heiser, and M. Brinkmann, Preferential Location of Dopants in the Amorphous Phase of Oriented Regioregular Poly(3-Hexylthiophene-2,5-Diyl) Films Helps Reach Charge Conductivities of 3000 S Cm−1, Advanced Functional Materials **32**, 2202075 (2022).

[12] V. Untilova, H. Zeng, P. Durand, L. Herrmann, N. Leclerc, and M. Brinkmann, Intercalation and Ordering of F6TCNNQ and F4TCNQ Dopants in Regioregular Poly(3-Hexylthiophene) Crystals: Impact on Anisotropic Thermoelectric Properties of Oriented Thin Films, Macromolecules **54**, 6073 (2021).

[13] V. Vijayakumar, P. Durand, H. Zeng, V. Untilova, L. Herrmann, P. Algayer, N. Leclerc, and M. Brinkmann, Influence of Dopant Size and Doping Method on the Structure and Thermoelectric Properties of PBTTT Films Doped with F6TCNNQ and F4TCNQ, J. Mater. Chem. C **8**, 16470 (2020).

[14] V. Vijayakumar, Y. Zhong, V. Untilova, M. Bahri, L. Herrmann, L. Biniek, N. Leclerc, and M. Brinkmann, Bringing Conducting Polymers to High Order: Toward Conductivities beyond 105 S Cm−1 and Thermoelectric Power Factors of 2 mW M−1 K−2, Advanced Energy Materials **9**, 1900266 (2019).

[15] J. Li, M. Xue, N. Xue, H. Li, L. Zhang, Z. Ren, S. Yan, and X. Sun, Highly Anisotropic P3HT Film Fabricated via Epitaxy on an Oriented Polyethylene Film and Solvent Vapor Treatment, Langmuir **35**, 7841 (2019).

[16] S. Qu, Q. Yao, L. Wang, Z. Chen, K. Xu, H. Zeng, W. Shi, T. Zhang, C. Uher, and L. Chen, Highly Anisotropic P3HT Films with Enhanced Thermoelectric Performance via Organic Small Molecule Epitaxy, NPG Asia Mater **8**, 7 (2016).

[17] Y. Xu, X. Wang, J. Zhou, B. Song, Z. Jiang, E. M. Y. Lee, S. Huberman, K. K. Gleason, and G. Chen, Molecular Engineered Conjugated Polymer with High Thermal Conductivity, Sci. Adv. **4**, eaar3031 (2018).

[18] A. Salleo, Charge Transport in Polymeric Transistors, Materials Today **10**, 38 (2007).

[19] Y. Huang et al., Design of Experiment Optimization of Aligned Polymer Thermoelectrics Doped by Ion-Exchange, Appl. Phys. Lett. **119**, 111903 (2021).

[20] C. a. M. dos Santos, A. de Campos, M. S. da Luz, B. D. White, J. J. Neumeier, B. S. de Lima, and C. Y. Shigue, Procedure for Measuring Electrical Resistivity of Anisotropic Materials: A Revision of the Montgomery Method, Journal of Applied Physics **110**, 083703 (2011).

[21] I. Miccoli, F. Edler, H. Pfnür, and C. Tegenkamp, The 100th Anniversary of the Four-Point Probe Technique: The Role of Probe Geometries in Isotropic and Anisotropic Systems, J. Phys.: Condens. Matter **27**, 223201 (2015).

[22] H. C. Montgomery, Method for Measuring Electrical Resistivity of Anisotropic Materials, Journal of Applied Physics **42**, 2971 (1971).

[23] J. D. Wasscher, Note on Four-Point Resistivity Measurements on Anisotropic Conductors, Philips Research Reports 301 (1961).

[24] L. J. van der Pauw, Determination of Resistivity Tensor and Hall Tensor of Anisotropic Conductors, Philips Research Reports **16**, 187 (1961).

[25] B. F. Logan, S. O. Rice, and R. F. Wick, Series for Computing Current Flow in a Rectangular Block, Journal of Applied Physics **42**, 2975 (1971).

[26] See Supplemental Material for thin films fabrication methods, polarized UV-Vis spectroscopy data, GIWAXS, conductivity and Hall effect measurements, 4-line geometry correction factor, profilometry, and temperature-dependent conductivity measurements data, which Includes Refs. [27-29].

[27] J. Lindemuth and S.-I. Mizuta, *Hall Measurements on Low-Mobility Materials and High Resistivity Materials*, in *Thin Film Solar Technology III*, Vol. 8110 (SPIE, 2011), pp. 65–71.

[28] F. Werner, Hall Measurements on Low-Mobility Thin Films, Journal of Applied Physics **122**, 13 (2017).

[29] T. J. Aubry et al., Dodecaborane-Based Dopants Designed to Shield Anion Electrostatics Lead to Increased Carrier Mobility in a Doped Conjugated Polymer, Advanced Materials **31**, 11 (2019).

[30] K. J. Winchell, M. G. Voss, B. J. Schwartz, and S. H. Tolbert, Understanding the Effects of Confinement and Crystallinity on HJ-Coupling in Conjugated Polymers via Alignment and Isolation in an Oriented Mesoporous Silica Host, J. Phys. Chem. C **125**, 23240 (2021).

[31] D. T. Scholes, P. Y. Yee, J. R. Lindemuth, H. Kang, J. Onorato, R. Ghosh, C. K. Luscombe, F. C. Spano, S. H. Tolbert, and B. J. Schwartz, The Effects of Crystallinity on Charge Transport and the Structure of Sequentially Processed F_4 TCNQ-Doped Conjugated Polymer Films, Adv. Funct. Mater. **27**, 44 (2017).

[32] F. C. Spano, Modeling Disorder in Polymer Aggregates: The Optical Spectroscopy of Regioregular Poly(3-Hexylthiophene) Thin Films, The Journal of Chemical Physics **122**, 234701 (2005).

[33] D. T. Scholes, S. A. Hawks, P. Y. Yee, H. Wu, J. R. Lindemuth, S. H. Tolbert, and B. J. Schwartz, Overcoming Film Quality Issues for Conjugated Polymers Doped with F4TCNQ by Solution Sequential Processing: Hall Effect, Structural, and Optical Measurements, J. Phys. Chem. Lett. **6**, 4786 (2015).

[34] S. A. Hawks, J. C. Aguirre, L. T. Schelhas, R. J. Thompson, R. C. Huber, A. S. Ferreira, G. Zhang, A. A. Herzing, S. H. Tolbert, and B. J. Schwartz, Comparing Matched Polymer:Fullerene Solar Cells Made by Solution-Sequential Processing and Traditional Blend Casting: Nanoscale Structure and Device Performance, J. Phys. Chem. C **118**, 17413 (2014).

[35] J. C. Aguirre, S. A. Hawks, A. S. Ferreira, P. Yee, S. Subramaniyan, S. A. Jenekhe, S. H. Tolbert, and B. J. Schwartz, Sequential Processing for Organic Photovoltaics: Design Rules for Morphology Control by Tailored Semi-Orthogonal Solvent Blends, Adv. Energy Mater. **5**, 11 (2015).

[36] Y. Yamashita, J. Tsurumi, M. Ohno, R. Fujimoto, S. Kumagai, T. Kurosawa, T. Okamoto, J. Takeya, and S. Watanabe, Efficient Molecular Doping of Polymeric Semiconductors Driven by Anion Exchange, Nature **572**, 634 (2019).

[37] B. J. Boehm, H. T. L. Nguyen, and D. M. Huang, The Interplay of Interfaces, Supramolecular Assembly, and Electronics in Organic Semiconductors, J. Phys.: Condens. Matter **31**, 423001 (2019).

[38] Y. Hosokawa, M. Misaki, S. Yamamoto, M. Torii, K. Ishida, and Y. Ueda, Molecular Orientation and Anisotropic Carrier Mobility in Poorly Soluble Polythiophene Thin Films, Applied Physics Letters **100**, 203305 (2012).

[39] H. S. Lee, J. H. Cho, K. Cho, and Y. D. Park, Alkyl Side Chain Length Modulates the Electronic Structure and Electrical Characteristics of Poly(3-Alkylthiophene) Thin Films, J. Phys. Chem. C **117**, 11764 (2013).

[40] R. Joseph Kline, M. D. McGehee, and M. F. Toney, Highly Oriented Crystals at the Buried Interface in Polythiophene Thin-Film Transistors, Nature Mater **5**, 3 (2006).

[41] J. Zhao, Y. Li, G. Yang, K. Jiang, H. Lin, H. Ade, W. Ma, and H. Yan, Efficient Organic Solar Cells Processed from Hydrocarbon Solvents, Nat Energy **1**, 2 (2016).

[42] H. Lee, D. Lee, D. H. Sin, S. W. Kim, M. S. Jeong, and K. Cho, Effect of Donor–Acceptor Molecular Orientation on Charge Photogeneration in Organic Solar Cells, NPG Asia Mater **10**, 6 (2018).

[43] T. J. Aubry, A. S. Ferreira, P. Y. Yee, J. C. Aguirre, S. A. Hawks, M. T. Fontana, B. J. Schwartz, and S. H. Tolbert, Processing Methods for Obtaining a Face-On Crystalline Domain Orientation in Conjugated Polymer-Based Photovoltaics, J. Phys. Chem. C **122**, 15078 (2018).

[44] C. Piliego, T. W. Holcombe, J. D. Douglas, C. H. Woo, P. M. Beaujuge, and J. M. J. Fréchet, Synthetic Control of Structural Order in N-Alkylthieno[3,4-c]Pyrrole-4,6-Dione-Based Polymers for Efficient Solar Cells, J. Am. Chem. Soc. **132**, 7595 (2010).

[45] P. Y. Yee, D. T. Scholes, B. J. Schwartz, and S. H. Tolbert, Dopant-Induced Ordering of Amorphous Regions in Regiorandom P3HT, J. Phys. Chem. Lett. **10**, 17 (2019).

[46] O. Bierwagen, R. Pomraenke, S. Eilers, and W. T. Masselink, Mobility and Carrier Density in Materials with Anisotropic Conductivity Revealed by van Der Pauw Measurements, Phys. Rev. B **70**, 165307 (2004).

[47] Y. Chen, H. T. Yi, and V. Podzorov, High-Resolution Ac Measurements of the Hall Effect in Organic Field-Effect Transistors, Phys. Rev. Applied **5**, 034008 (2016).

[48] Z. Liang et al., N-Type Charge Transport in Heavily p-Doped Polymers, Nat. Mater. **20**, 518 (2021).

[49] S. A. Gregory, R. Hanus, A. Atassi, J. M. Rinehart, J. P. Wooding, A. K. Menon, M. D. Losego, G. J. Snyder, and S. K. Yee, Quantifying Charge Carrier Localization in Chemically Doped Semiconducting Polymers, Nat. Mater. **20**, 1414 (2021).

CHAPTER 5

Control of the Seebeck Coefficient Conductivity relationship in Doped Semiconducting Polymer Thin Films through counterion coulomb binding and mesoscale correlation length

5.1. Introduction

Doped semiconducting polymers have great potential promise for thermoelectric applications due to their ease of processing, tunability, and inherently low thermal conductivity.[1–4] Interest in these materials has increased in recent years, with the development of new polymers, dopants, and doping methods.[5–10] Most of the work in this field focuses on improving the electrical conductivity of semiconducting polymers to overcome their intrinsically low carrier mobility and density. For thermoelectric devices, however, it is crucial to also consider the Seebeck coefficient (*S*), which is a measure of the voltage difference generated in response to a temperature gradient across a material. This voltage facilitates the flow of charge carriers, enabling the conversion of waste heat into electrical energy.

The efficiency of the thermoelectric conversion process is described by the figure of merit (*ZT*):

$$ZT = \frac{\sigma S^2}{\kappa} T, \quad (1)$$

which depends on the electrical conductivity (σ) and Seebeck coefficient as well as the thermal conductivity (κ). The temperature (*T*) is included to make the quantity dimensionless. Although it is desirable to maximize both the electrical conductivity and the Seebeck coefficient to achieve higher *ZT*, increasing the electrical conductivity through doping often results in a decrease in the Seebeck coefficient.

The inverse relationship between σ and S can be understood using the Boltzmann transport formalism. In the version developed by Kang and coworkers, these factors are described in terms of the transport function σ_E, which is related to the carrier mobility:[11]

$$\sigma = \int \sigma_E(-\frac{\partial f}{\partial E})\, dE \tag{2}$$

$$S = -\frac{k_B}{q}\int \left(\frac{E - E_F}{k_B T}\right)\left(\frac{\sigma_E}{\sigma}\right)\left(-\frac{\partial f}{\partial E}\right) dE, \tag{3}$$

where k_B is the Boltzmann constant, E is the energy of the charge carrier, q is the charge, E_F is the Fermi level, and $f(E)$ is the Fermi-Dirac distribution. Although not explicit in these equations, increasing the conductivity by increasing the carrier density causes the Fermi level to shift, thereby reducing the ($E - E_F$) term in Eq. (3) and lowering the "excess" energy that carriers can contribute to the Seebeck coefficient.[11] This explains why the Seebeck coefficient tends to decrease when electrical conductivity increases at higher doping levels.[12–16]

The electrical conductivity of a doped conjugated polymer depends not only on the number density of carriers but also on their mobility: higher carrier mobility results in higher conductivity at the same carrier density. This suggests that doped semiconducting polymer films with higher carrier mobility will also have higher Seebeck coefficients relative to their electrical conductivity.[17,18]

The charge transport mechanism in doped semiconducting polymer films is typically understood as a hopping process. This process is influenced by several factors, including energetic disorder from the polymer morphology and the Coulomb interactions between polarons and their counterions, both of which can create barriers that trap charge carriers at specific locations.

Temperature also plays a key role in this transport: at higher temperatures, polarons gain enough thermal energy to overcome these energy barriers, so that the electrical conductivity increases.

To improve the carrier mobility in doped semiconducting polymers, it is necessary to understand how the interplay of film morphology and counterion interactions contribute to charge transport.[8,9,12,16,19–22] Recently, Gregory and coworkers[17,18] have expanded on the transport model developed by Kang and coworkers[11] by proposing that the charge transport function takes the following form:

$$\sigma_E(E,T,c) = \sigma_0 \exp\left(-\frac{W_H(c)}{k_B T}\right) \times \left(\frac{E - E_t}{k_B T}\right). \quad (4)$$

This expression for the transport function is termed the semi-localized transport (SLoT) model, which introduces three components: σ_0, the pre-factor or intrinsic conductivity in the absence of localization effects; W_H, the localization energy, which depends on the carrier density (c); and an energy-dependent term, $(\frac{E-E_t}{k_B T})$. By assuming that the material is homogeneous throughout its volume, $W_H(c)$ can further be broken down into a maximum localization energy ($W_{H,max}$) and the rate at which localization decreases with increasing carrier density ($W_{H,slope}$). Equation 4 allows one to determine whether charge transport is primarily influenced by σ_0 or by $W_H(c)$, and how these factors depend on both the doping method and the microscopic and mesoscopic morphology of doped conjugated polymer films.

Different types of dopants and doping methods are known to significantly influence the morphology in doped polymer films.[8,9,12,16,19–25] These morphological changes can occur on microscopic length scales, such as changing the doped polymer crystallite spacing, as well as on mesoscopic length scales, creating new domain lengths.[8,9,12,16,19–25] In this study, we aim to explore

how different dopants and doping methods affect morphology and thus impact charge transport. Specifically, we measure the carrier mobility in conjugated polymer films doped in four different ways, use the SLoT model to analyze charge transport in terms σ_0 and $W_H(c)$, and investigate how the way doping affects these parameters affects the relationship between S and σ.

Our work focuses on the workhorse material poly(3-hexylthiophene-2,5-diyl) (P3HT). P3HT is a semicrystalline conjugated polymer that is widely used for studying chemical doping, allowing us to make meaningful comparisons to the literature. In general, it is easier to dope the crystalline regions of P3HT films where the chains segments are straight and the carriers can delocalize than it is to dope the short-conjugation segments present in the amorphous regions of the films.[20] We then choose dopants and doping methods that are known to dope different regions of P3HT films (e.g., doping the crystallites or both the crystallites and the amorphous regions), provide a different degree of counterion-carrier Coulomb interaction, or both. **Figure 5.1** shows the chemical structures of P3HT and the different dopants used in this study.

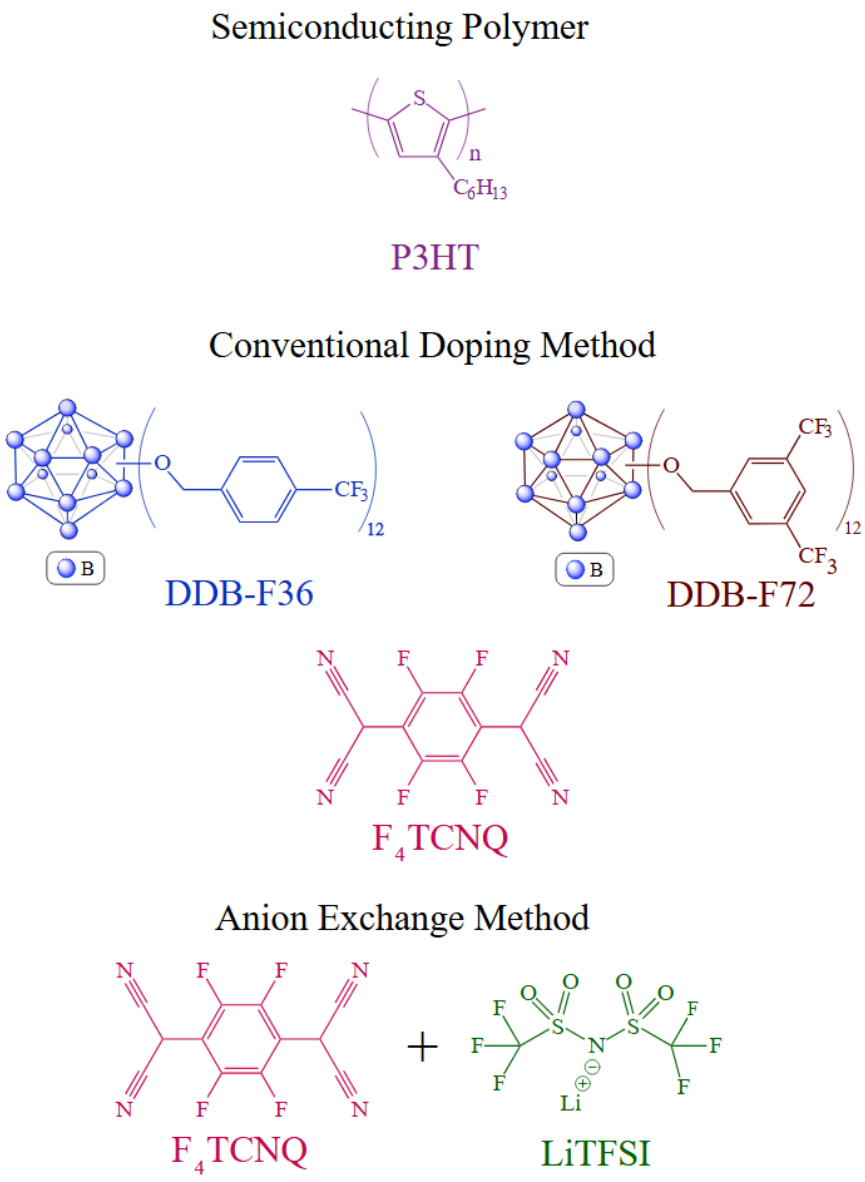

Figure 5. 1. Chemical structure of P3HT and the various dopants used in this study. Two different doping methods are used in this study: conventional (using F_4TCNQ, DDB-F36 and DDB-F72) and anion-exchange. For the anion-exchange method, the dopant is F_4TCNQ dopant is used in the presence of the salt LiTFSI, increasing the doping efficiency and allowing $TFSI^-$ to exchange with F_4TCNQ^- as the counterion.

For our initial dopant, we chose 2,3,5,6-tetrafluoro-7,7,8,8-tetracyanoquinodimethane (F_4TCNQ) because it is widely used in studies of doped semiconducting polymers, particularly with P3HT. F_4TCNQ has sufficient oxidizing power to dope the crystalline regions of P3HT but is not strong enough to fully dope the amorphous regions.[8,21,22,26] After doping, it is known that the F_4TCNQ^- counteranion resides in the lamellar regions of the P3HT crystallites. Spano and co-workers have shown that Coulombic interaction between polarons and counterions can cause localization of the charge carriers on doped semiconducting polymers.[20] For P3HT doped with F_4TCNQ, the F_4TCNQ^- anion is positioned relatively close to the polymer backbone, resulting in strong Coulombic interactions that lead to a significant population of localized and/or trapped charge carriers.

In contrast, one can also take advantage of dodecaborane (DDB)-based dopants, which are so large that they physically cannot reside close to the P3HT backbone, reducing counterion/carrier Coulomb interactions and thus producing more mobile charge carriers.[8,9,27] DDBs can be modified with different substituents to change their oxidation power. [8,9,27] Although both DDB-based dopants help minimize Coulomb trapping, DDB-F72, with its stronger oxidizing power, can dope the amorphous regions of P3HT films more effectively than DDB-F36. DDB-F36 is known to intercalate into P3HT crystallites, expanding them in the lamellar direction by roughly a factor of 2.[8] The very high oxidizing power of DDB-F72, in contrast, can disrupt a P3HT film's crystallinity at high doping concentrations.[9,27] Here, we employ both of these dopants to understand the trade-off between structure and oxidizing power on the charge transport characteristics of doped P3HT.

Recently, Yamashita and colleagues developed a new technique called anion-exchange (AE) doping, which offers several benefits over traditional chemical doping methods.[6] This

approach involves immersing a conjugated polymer film in a solution containing both a chemical dopant and a high concentration of an electrolyte. The dopant oxidizes the polymer, and then the dopant's counterion is replaced by the electrolyte anion from the solution. This method allows precise control over the choice of counterion in the doped polymer films; is also can achieve much higher doping levels than conventional methods,[6] allowing for doping of the amorphous regions of P3HT. For our study, we use F_4TCNQ as the dopant and lithium bis(trifluoromethane)sulfonimide (LiTFSI) as the electrolyte salt to anion-exchange dope P3HT films. The ability to dope the amorphous regions provides a significant structural difference compared to doping with F_4TCNQ alone, providing a way to correlate morphology with the behavior of charge transport, including σ_0, $W_H(c)$, the connection between S and σ.

In this study, we examine how different dopants and doping methods—F_4TCNQ, DDB-F72, DDB-F36, and anion exchange—affect the morphology, charge transport, Seebeck coefficient, and electrical conductivity of P3HT. Our findings show that charge transport, and particularly the connection between the Seebeck coefficient and electrical conductivity, can be improved either by reducing Coulomb trapping or by increasing the domain length through the ordering of originally amorphous regions. Using a combination of temperature-dependent conductivity, Hall effect, and UV-Vis-NIR spectroscopy measurements, we demonstrate that P3HT films doped with DDB-based dopants exhibit a much lower localization energy compared to those doped with F_4TCNQ or via the anion-exchange method. Additionally, our use of the SLoT model shows that films doped via anion exchange have a significantly higher σ_0 than those doped by other methods, which allows them to overcome their high carrier localization energy and achieve a favorable relationship Seebeck coefficient-electrical conductivity relationship. We show

that the higher σ_0 results from an increase in domain length because AE doping is able to order some of the originally amorphous regions of the P3HT films.

5.2 Results and Discussions

5.2.1. UV-Vis-NIR Spectroscopy

To investigate the electronic structure of our doped P3HT films, we performed UV-Vis-NIR spectroscopy on films doped using DDB-F72, DDB-F36, F_4TCNQ, and via anion exchange (AE), all at various doping concentrations (**Figure 5.2**). All of the doped P3HT films in this study were fabricated using the sequential processing (SqP) method.[28–31] First, pristine P3HT films were spin-coated onto glass substrates. After the films were fully dry, they were subject to a second spin-coating step using various dopant solutions, including F_4TCNQ, DDB-F72, DDB-F36, or for the AE method, a combination of F_4TCNQ and 104.5 mM (30 mg/mL) of LiTFSI. Additional details on film fabrication and doping can be found in the Methods section.

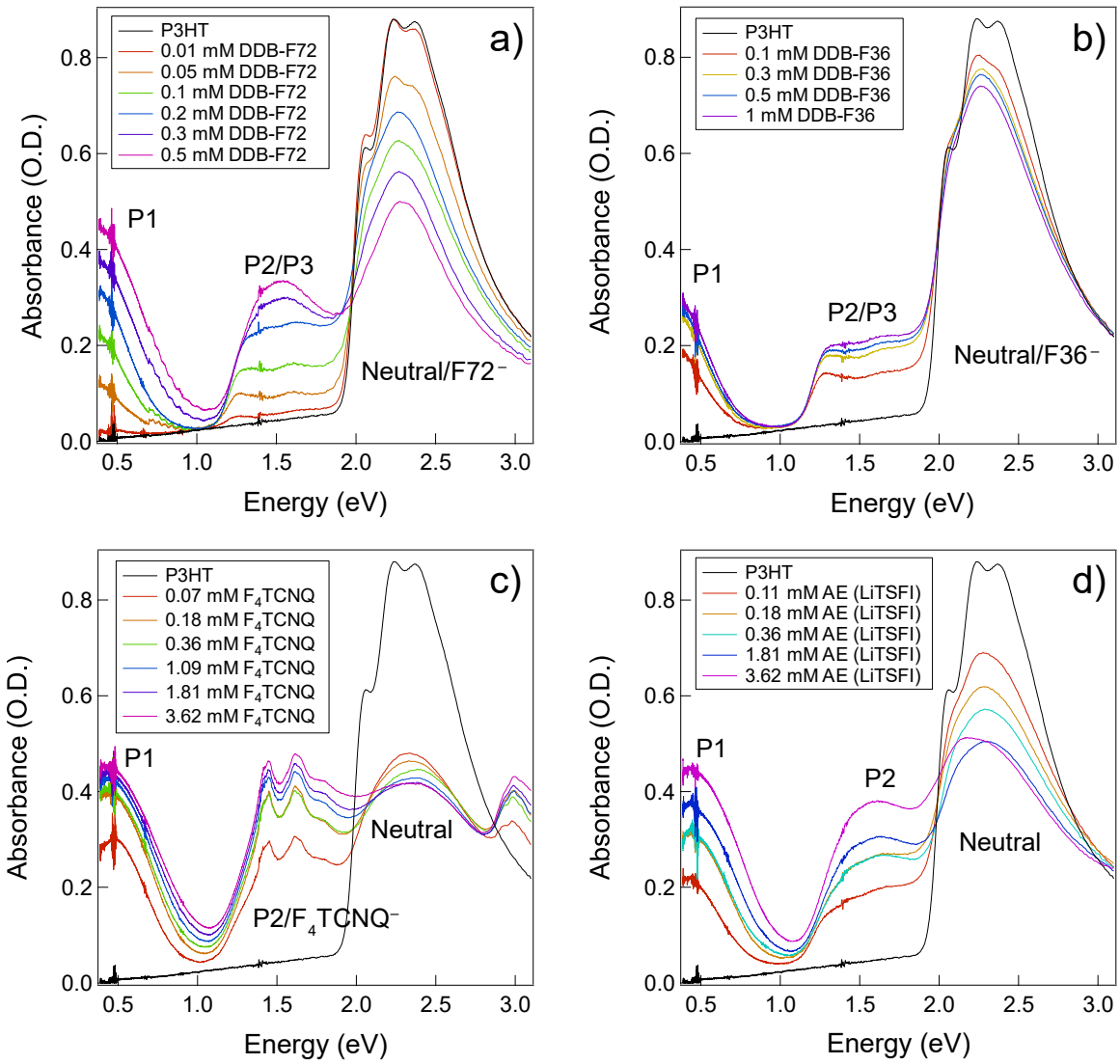

Figure 5. 2. UV-Vis-NIR spectra of doped P3HT films using different dopants: a) DDB-F72, b) DDB-F36, c) F_4TCNQ, and d) anion exchange (AE) at various doping levels. Both DDB-F72 and DDB-F36 doped films show highly redshifted P1 indicating highly delocalized polarons. In contrast, F_4TCNQ and anion-exchange doped films P1 is blueshifted compared to the DDBs doped films, indicating the presence of trapped polarons.

The UV-Vis-NIR spectra for P3HT films doped with all four methods and different doping concentrations are shown in **Figure 5.2**. Pristine P3HT films (black curves in each panel) are

characterized by their neutral bandgap absorption centered near 2.3 eV. For all of the doped P3HT samples (various colored curves with doping concentration increasing in spectral order from red to purple), we observe a decrease of this absorption, verifying that doping removes electrons from the polymer's valence band/HOMO. All of the doped samples also show the presence of two new peaks at ~1.6 eV and <1 eV, which are referred to as P2 and P1, respectively. These features are associated with the presence of charge carriers, which are also referred to as polarons.

In addition to the induced polaron absorption bands, the F_4TCNQ-doped P3HT samples in **Fig. 5.2c** show additional absorption features near ~1.5 eV (overlapping the P2 band) and 3.0 eV due to the F_4TCNQ anion.[32] The P3HT samples doped with DDB-F72 and DDB-F36 in **Figs. 5.2a** and **b** also have a DDB radical anion peak near ~2.5 eV,[8,9] which overlaps the neutral P3HT absorption and thus masks some of the doping-induced depletion of this absorption. Also, at low doping levels, these samples also show a third polaron transition, labelled P3, which results from broken symmetry when only some regions of the polymer crystallites are doped.[19,33,34] Despite the presence of these other absorption peaks, all the samples show that as the dopant concentration is increased, the intensities of both P1 and P2 rise, indicating more polarons and thus a higher doping level.

Based on the P1 absorption intensity, the F_4TCNQ, DDB-F72, and anion-exchange doped P3HT films are able to achieve roughly similar doping levels at the highest dopant concentrations that we used in this study. It is worth noting that DDB-F72, with its higher oxidation potential,[8] is more efficient at doping and reaches this level at 0.5 mM, whereas the other dopants require higher concentrations to reach the same doping level. In contrast, DDB-F36 is less effective at doping P3HT, showing a much lower P1 absorption intensity even at twice the concentration of

DDB-F72. This aligns with DDB-F72's strong oxidizing power, which, as shown by Aubry and coworkers[8], can not only dope the amorphous regions but also further dope the crystalline regions to the point of causing structural disorder. On the other hand, although DDB-F36 is slightly more oxidizing than F_4TCNQ and can likely dope the amorphous regions to some extent, it lacks the ability to further dope and disrupt the structure as DDB-F72.[8]

As previously mentioned, the anion-exchange method is more efficient at doping compared to conventional F_4TCNQ doping. However, the P1 absorption intensity and thus doping level of our samples at the highest doping concentration is nearly identical for both methods. The reason for this is that we used dicholoromethane (DCM) for doping our films with F_4TCNQ, and DCM is a solvent that swells P3HT quite well[21,35] and thus allows efficient access of the dopant into the polymer. For anion-exchange doping, on the other hand, we used *n*-butyl acetate (*n*-BA) as the solvent for doping the films, as LiTFSI is not highly soluble in DCM. Since n-BA is not as effective a swelling agent for P3HT, we end up with about the same doping level using AE as without but with the more swelling solvent.

In addition to providing qualitative insights into the doping level, the position of the P1 band also reveals important information about polaron delocalization. Polarons on conjugated polymers are delocalized over multiple monomers, and their absorption spectrum is roughly that of a particle in a 1-D box; as a result, more delocalized carriers exhibit a more redshifted P1 transition compared to less delocalized carriers.[8,9,21] One of the main sources of polaron localization is the coulomb interaction with the dopant counterion. This is consistent with the observation that the P1 band of P3HT films doped with DDB-F72 and DDB-F36, whose

counterions are too large to interact strongly with the polymer backbone, exhibits a significant redshift compared to those doped with F_4TCNQ or the AE method.[8]

In previous work, we argued that the carrier mobility in doped P3HT films was directly connected to the degree of polaron delocalization and thus the position of the P1 absorption band.[8] Other groups, however, have challenged this notion, arguing that the mobility depends more on doping level that the molecular level degree of delocalization measured by P1.[36] One of the purposes of this study is to use all the different doping methods to examine the connection between macroscopic electrical measurements, such as four-point probe temperature-dependent electrical conductivity and the Hall effect and microscopic measures of polaron delocalization such as the position of the P1 absorption band.

5.2.2. Probing Film Morphology Using Grazing Incidence Wide and Small -Angle X-ray Scatterings

To investigate the morphologies of the P3HT that result from using the various doping methods in this study, we performed Grazing-Incidence Wide and Small-Angle X-ray Scattering (GIWAXS and GISAXS, respectively). **Figure 5.3a-b** displays the out-of-plane and in-plane GIWAXS integrations, respectively, for pristine P3HT (black curves) and the most highly-doped samples whose absorption spectra are shown in **Figure 5.2** in the out-of-plane and in-plane directions used in this study (various colored curves).

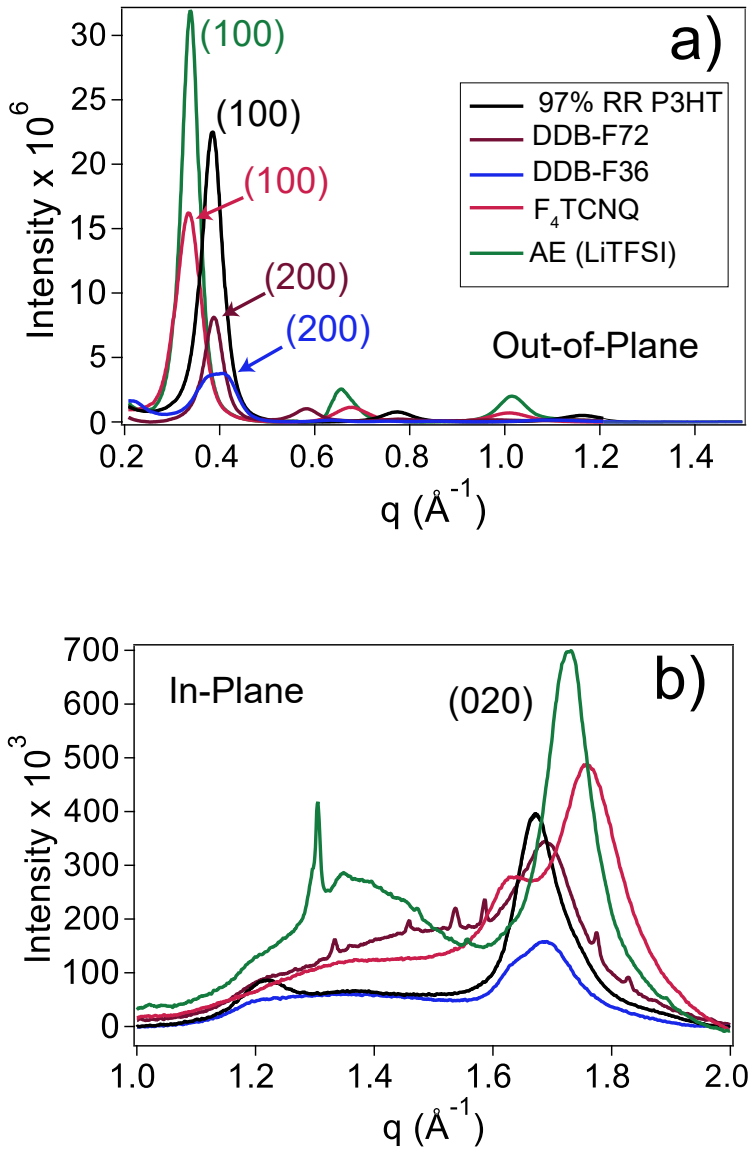

Figure 5. 3. 1-D integrated GIWAXS data for pristine P3HT (black curve) films and for the most highly-doped samples whose absorption spectra are depicted in **Figure 5.2**. The dopant concentration used to obtain the most highly doped samples are 3.62 mM F_4TCNQ, 0.5 mM DDB-F72, 1 mM DDB-F36, and 3.62 mM anion-exchange doping. Both F_4TCNQ and anion-exchange doped samples show similar lamellar expansion to lower q-spacing, indicating that the counterions

are positioned at comparable distances from the polymer backbone. In contrast, DDBs doped samples exhibit a much larger lamellar expansion due to the larger counterion size, suggesting weaker Coulomb interaction. Additionally, both anion-exchange and DDBs doped samples show signs of doping in the amorphous region in the in-plane GIWAXS data. The sharp peak at ~1.3 $Å^{-1}$ is likely from scattering by excess LiTFSI on the film surface.

The out-of-plane scattering in **Figure 5.3a** shows that for the F_4TCNQ-doped samples (red curve), there is a shift of the (100) peak, which corresponds to the lamellar spacing of the P3HT crystallites, from approximately 0.39 $Å^{-1}$ to about 0.35 $Å^{-1}$. This shift, which has been noted in several previous studies, indicates that the lamellar region of P3HT is expanding to accommodate the F_4TCNQ anion within the crystal structure.[20,21,27] The in-plane 1-D-integration in **Figure 5.3b** shows that the F_4TCNQ-doped samples also undergo a shift of the (020) π-stacking peak from approximately 1.65 $Å^{-1}$ to around 1.70 $Å^{-1}$. This shift has been attributed to a reorientation of the unit cell caused by the intercalation of F_4TCNQ anions into the lamellar region.[20,21,27]

Figure 5.3a also shows that the out-of-plane GIWAXS integration for the anion-exchange-doped P3HT films (green curve) also shows a similar shift of the (100) lamellar peak to approximately 0.35 $Å^{-1}$; this indicates that $TFSI^-$ sits at a similar distance from the P3HT backbone as F_4TCNQ, consistent with their similarly-positioned P1 absorption bands. More striking, however, is the fact that the scattering intensity of this peak increases relative to that of pristine P3HT. It is well known that doping can induce order in amorphous conjugated polymer films from the way the dopants fill space,[37–40] so the increased (100) intensity indicates that AE doping is ordering some of the originally-amorphous regions of the P3HT film. The in-plane integration in **Fig. 5.3b** shows a smaller shift for the doped (020) π-stacking peak, indicating that AE doping

causes less reorientation of the unit cell than doping with F_4TCNQ, likely because the TFSI anion is slightly smaller than F_4TCNQ^-. AE doping also creates a new broad peak centered around ~1.4 $Å^{-1}$, which is indicative of more disordered π-stacking,[8,27] another signature of the fact that AE doping has partially ordered the formerly amorphous regions of the P3HT film.

The out-of-plane 1-D integrations for the DDB-doped samples (**Fig. 3a** purple and blue curves) show such a significant shift in the (*h*00) peaks to lower *q* that only the (200) lamellar peak and higher overtones can be observed. This is a direct reflection of the fact that the ~2-nm diameter DDB clusters cannot fit in the P3HT crystal lattice without causing a significant expansion in the lamellar direction.[8] This expansion is consistent with the idea that DDB anions have weaker Coulomb interactions with polarons due to their increased distance from the polymer backbone,[9] as reflected by the red-shifted P1 polaron absorption with these dopants in **Fig. 5.2**.

Unlike the significant expansion in the lamellar region, the in-plane integration in **Fig. 5.3b** reveals that the π-stacking (020) peak of P3HT shows minimal change upon doping with both DDB-F72 and DDB-F36;[8] the large lamellar expansion needed to accommodate these bulky dopants does not require reorientation of the unit cell. One key difference between the two dopants is the broad shoulder that appears near $q \sim 1.4$ $Å^{-1}$, which is much larger for the DDB-F72 doped film (purple curve) than for the DDB-F36 doped film (blue curve). This broad shoulder is a sign of both doping in the originally-amorphous regions and a net loss of the original polymer crystallinity.[8,27] This is because DDB-F72 is more highly oxidizing, so it can dope the amorphous regions, making them more ordered, but it also can more highly-dope the crystalline regions, which requires disrupting the crystal structure to accommodate the larger number of counterions. DDB-F36, on the other hand, cannot dope the crystalline regions to the point where their structure needs

to be disrupted in order to accommodate the counterions, and it can only slightly dope the originally amorphous regions.

All of the GIWAXS results indicate that our four different doping methods produce distinct m, allowing us to test how how these different morphologies affect charge transport. However, GIWAXS can only probes the locally-ordered regions of a doped conjugated polymer sample, yet charge transport must take place over lengths scales much larger than those of a single crystallite. Thus, we also performed a series of GISAXS experiments to investigate the films' structures on a larger length scale.[41–47] The raw GISAXS data and their fits are shown in **Figs. S1** and **S2** of the SI, respectively, and the domain lengths (R_g) extracted from the fits are given in **Table 5.1**.

GISAXS	**Pristine**	**F_4TCNQ**	**AE**	**F72**	**F36**
R_g **(Å)**	89	67	51/120	75	87
σ_0 **(S/cm)**	-	10	125	25	35
$W_{H,slope}$ **(mev)**	-	310	350	1000	1550

Table 5. 1. List of radii of gyration (R_g) obtained from GISAXS data for the highest doping levels of the various doping cases. GISAXS data was fit using the Unified Fitting model (see SI for fitting details) to obtain R_g values. The table also presents the key fitting parameters σ_0 and $W_{H,slope}$ used in the SLoT model to fit the Seebeck coefficient – conductivity data.

The GISAXS data in **Table 5.1** reveal that the initial pristine P3HT film has R_g = 89 Å. Upon doping with F_4TCNQ, R_g decreases to 67 Å, indicating a loss of meso-scale correlation length. This decrease is likely due to dopant-induced disordering, which has been previously

reported in the literatures.[12,12,40,48] Interestingly, both DDB-F72 and DDB-F36 doped films exhibit higher R_g values, 75 Å and 87 Å, respectively, than the F_4TCNQ-doped films. This indicates either that incorporation of the large dopants does not significantly affect the mesoscale domain length, or that these dopants are able to integrate part of the originally amorphous regions with the existing crystalline regions, resulting in less dopant-induced loss of domain length.

In contrast to the F_4TCNQ- and the DDB-doped films, two different domain lengths were observed for anion-exchange doped samples: 51 Å and 120 Å. The higher R_g value of 120 Å, which exceeds that of the pristine film, likely results from the presence of newly-ordered amorphous regions, as observed in the in-plane GIWAXS, that integrate into the original crystalline domains. We believe the lower R_g value results from crystalline regions being doped in areas where the amorphous regions either did not dope or did not integrate with the doped region. This difference prompts interesting questions about how these changes at both the microscopic and mesoscopic levels affect charge transport and the relationship between the Seebeck coefficient and electrical conductivity.

5.2.3. Seebeck Coefficient – Electrical Conductivity Relationship

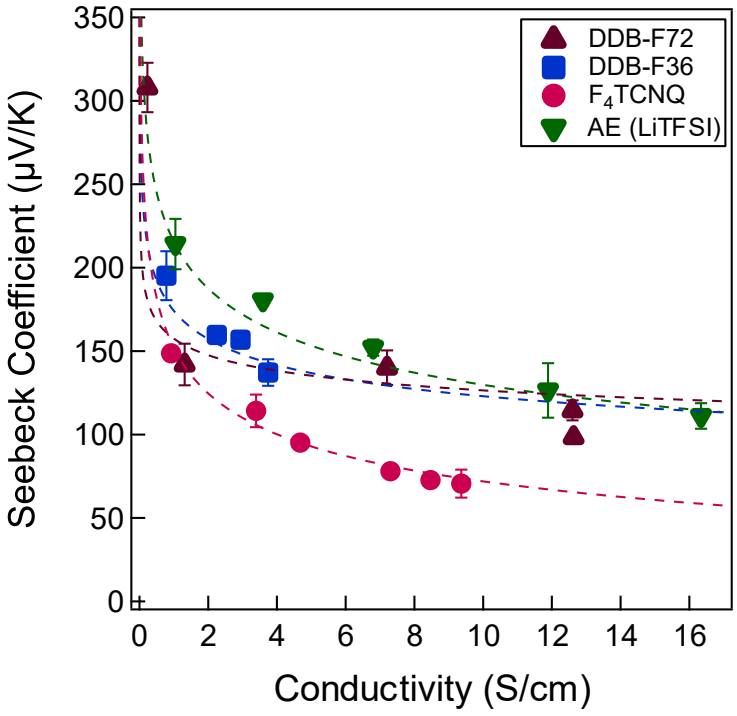

Figure 5. 4. Seebeck coefficient-conductivity (S-σ) relationship for P3HT doped with various dopants/counterions. The dashed lines are fitted using the SLoT model.[18] Both the DDB-based dopants and anion-exchange doping show significantly higher Seebeck coefficient for the same conductivity compared to F_4TCNQ samples.

To investigate how different morphologies resulting from the various doping methods affect charge transport, we measured the Seebeck coefficient and electrical conductivity of the same samples whose absorption spectra were shown in **Fig. 5.2**; we note that some of the lower-doped samples had conductivities too low for accurate measurement and were excluded. To measure the Seebeck coefficient, we deposited two parallel electrode lines on the film to measure

the voltage induced by an applied temperature gradient. Electrical conductivity was assessed using the van der Pauw method, with electrodes placed at the four corners of square film samples. More details of how Seebeck coefficient and electrical conductivity are measured can be found in the Method sections.

Figure 5.4 displays the relationship between the Seebeck coefficient and electrical conductivity of our doped P3HT films. The films doped with F_4TCNQ (red circles) exhibit the lowest Seebeck coefficient for a given conductivity, while the films doped with DDB-F72 (purple triangles), DDB-F36 (blue squares), and via anion-exchange (green triangles) all show a similar Seebeck-conductivity trend. All four samples show that increased doping increases the conductivity and decreases the Seebeck coefficient because the Fermi level is shifted closer to the carrier's average energy, as described in equation (3).

To understand the degree to which the Seebeck coefficient decreases with increased doping, we can analyze the data in **Fig. 5.4** using the SLoT model,[18] which characterizes charge transport as resulting from both the intrinsic conductivity (σ_0) and localization energy ($W_H(c)$), as shown in equation 4. More efficient charge transport—indicated by a higher Seebeck coefficient for a given conductivity level—indicates that a doping method is more effective. Given the data in **Fig. 5.4** for the four different doping cases, it appears that charge transport efficiency for DDB- and anion-exchange-doped films is better than those doped using F_4TCNQ.

5.2.4. Hall Effect Measurements

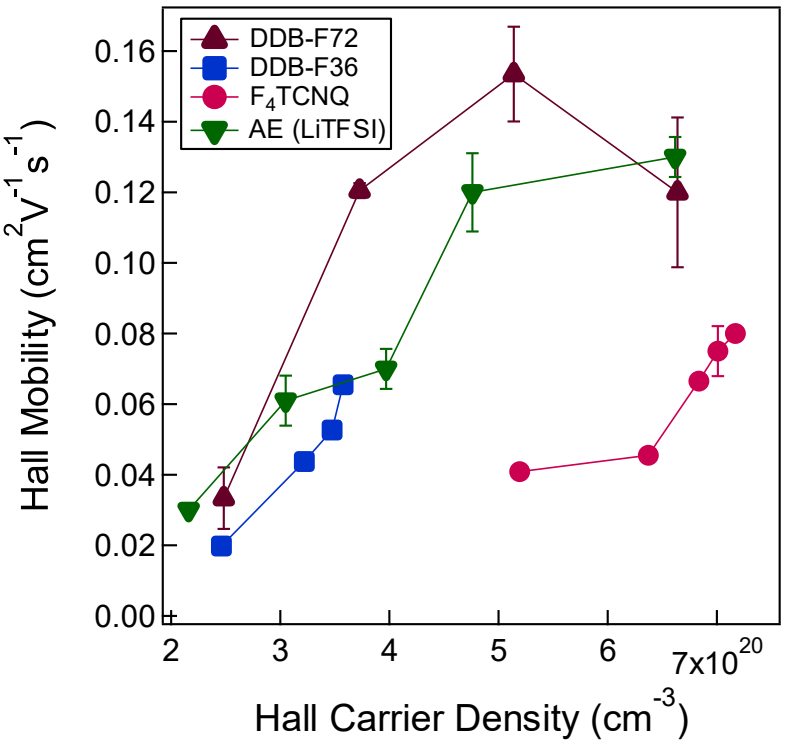

Figure 5. 5. Hall effect measurements obtained for P3HT films doped with various dopants and dopant concentrations. Here, however, the Hall mobility is plotted against the Hall carrier density rather than dopant concentration, allowing us to compare the different doping methods on an identical footing. DDB-based dopants and anion-exchange samples show significantly higher Hall mobility per carrier density than the samples doped using the F_4TCNQ.

To further investigate the charge transport characteristics of our doped P3HT films, we conducted DC Hall effect measurements on the same samples whose charge transport properties were studied in **Fig. 5.4**. **Figure 5.5** shows Hall mobility as a function of Hall carrier density for the four different doping methods. The data show that Hall carrier mobility increases with rising carrier density for all four doping cases. This increase is due to trap filling and screening effects that reduce carrier localization, where Coulomb interactions between the dopant and counterions

decrease as more charge carriers are introduced.[17,18,49–51] However, for DDB-F72 at high doping concentrations, the loss of crystallinity observed in **Fig. 5.3b** and in previous work[8] leads to a decrease in carrier mobility. As with the Seebeck-conductivity relationship in **Fig. 5.4**, the DDB-F72-, DDB-F36-, and anion-exchange-doped samples all show similar carrier mobility at the same carrier density, while the F_4TCNQ-doped samples exhibit significantly lower mobilities at equivalent carrier densities.

5.2.6. Semi-localized Transport Model (SLoT)

The SLoT model uses information from the temperature-dependent conductivity measurements, summarized in **Fig. 5.6**, to fit the measured Seebeck coefficient vs. electrical conductivity data shown in **Figure 5.4**; the fits are shown as the dashed curves in **Fig. 5.4**, and the fitting parameters are summarized in **Table 5.1.** We find that P3HT doped with DDB-F72 and DDB-F36 have very similar σ_0 and localization energy terms ($W_{H,slope}$). As mentioned above, the reduced Coulomb interaction and carrier localization in the DDB-doped samples causes the localization energy to decrease rapidly with increasing carrier density, resulting in larger $W_{H,slope}$ values (1000 and 1550 meV for DDB-F72 and DDB-F36, respectively). In contrast, the F_4TCNQ and anion-exchange doped P3HT samples show much smaller $W_{H,slope}$ values, due to stronger carrier-counterion Coulomb interactions and increased carrier localization. The DDB-F36-doped P3HT samples show a somewhat larger $W_{H,slope}$ than the DDB-F72-doped samples, which we believe could be due to DDB-F72 starting to disrupt the crystal structure at higher carrier concentrations. Overall, however, the SLoT model fits show that reducing the Coulomb interaction and improving carrier delocalization provide a huge advantage when it comes to decreasing the hopping barriers in doped P3HT films.

The other intriguing finding from the SLoT fit is that the intrinsic conductivity (σ_0) of the anion-exchange-doped P3HT samples is significantly higher (125 S/cm) than for any of the other doping methods. This means that despite experiencing a similarly unfavorable carrier localization and hopping barrier as F_4TCNQ-doped samples, the anion-exchange doped samples are able to achieve much more efficient charge transport due to their high σ_0. The σ_0 for the DDB-F72- and DDB-F36-doped samples (25 and 35 S/cm, respectively) is also higher than that of F_4TCNQ-doped samples, which have a σ_0 of just 10 S/cm. This indicates that there are two essentially independent ways to improve charge transport in doped P3HT films: one can either reduce the hopping barrier by increasing carrier delocalization via lowering the coulomb interaction between the carriers and counterions, or one can directly improve the intrinsic conductivity. This is what allows the AE-doped samples to have a similar Seebeck coefficient vs. conductivity behavior as the DDB-doped samples (**Fig. 5.4**), even though the reasons underlying this similarity are quite different.

Why do the AE-doped P3HT samples have such a high σ_0? **Figure 5.6** suggests that the answer lies in a direct connection between σ_0 and the mesoscopic domain structure, as measured by GISAXS and R_g: σ_0 and R_g are nearly perfectly linearly correlated, which is the principal result of this work. As mentioned above, we believe that higher R_g values result from doping of the amorphous regions, which expand the connectivity between ordered domains and provide better charge transport pathways. This finding is particularly interesting, as the electrical data that are used to fit the SLoT model and the GISAXS experiments are entirely independent of one another, yet we observe a strong correlation between them.

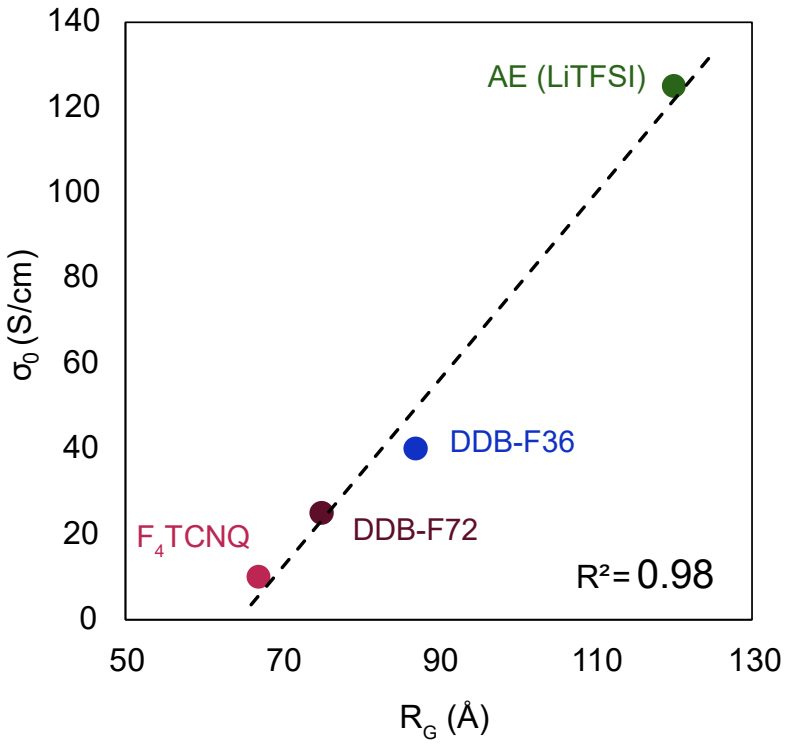

Figure 5. 6. shows the relationship between σ_0 obtained from SLoT fitting and R_g. This indicates that as the domain length increases, the intrinsic conductivity improves proportionally. The linear fitted line is to help guide the eyes.

5.3. Conclusions

In summary, we explored the use of four different doping methods to create doped P3HT thin films with varied charge transport characteristics and morphologies. DDB-based dopants and the anion-exchange method provide better charge transport compared to F_4TCNQ, resulting in higher carrier mobilities and a more favorable relationship between the Seebeck coefficient and electrical conductivity. The lower barriers to charge transport observed with DDB-based dopants results from reduced Coulomb interactions between the carriers and the dopant counterions, while

anion-exchange and F_4TCNQ-doped films experience higher hopping barriers due to carrier localization effects from stronger carrier-counterion coulomb interactions.

Further analysis using the SLoT indicates that the improvement in charge transport for anion-exchange doping is primarily due to a higher σ_0 rather than a reduced localization energy (W_H). GISAXS data suggest that this improvement is linked to the doping and ordering of the amorphous regions, which increases the ordering of these films on more mesoscopic length scales. The fact that σ_0 shows strong correlation with the domain size measured by GISAXS suggests that the doping of the originally amorphous regions of P3HT films leads to better structural continuity on a larger length scales that can contribute to better overall charge transport, even in the presence of strong localization effects. Clearly, a step forward would be to both increase the mesoscale correlation length and decrease carrier localization through the use of large counterions, and we will explore this in future work.

5.4 Experimental Section

Sample Preparation: Device fabrication was performed on pre-cleaned glass substrates for thermoelectric, electrical, and spectroscopy samples, and on pre-cleaned silicon wafer substrates for GIWAXS and GISAXS samples. The cleaning process involved cutting the substrates into 1.2 × 1.2 cm pieces, followed by sequential washes with Alconox detergent, deionized water, and acetone. After drying with nitrogen gas, the substrates were plasma etched for approximately 15 minutes. They were then transferred to a nitrogen glovebox for spin coating and doping.

A 2% (20 mg/mL) P3HT solution from oDCB was stirred until fully dissolved (~6 hours). The 2% P3HT solution was spin-coated onto the substrates at 1000 rpm for 60 seconds, followed by 4000 rpm for 5 seconds. The polymer films were left in the nitrogen glovebox overnight before

doping. For the sequential doping procedure, the pristine P3HT polymer films were exposed to a dopant solution for a set period before spin coating at 4000 rpm for 10 seconds to remove any residual dopant solution. In the case of F_4TCNQ, DDB-F72, and DDB-F36, the dopants were dissolved in DCM at the specified concentrations, and the polymer films were then exposed to the corresponding solution for 10 seconds before spin coating. For anion exchange samples, various concentrations of F_4TCNQ were dissolved in nBA and mixed with an equal volume of 209.0-mM LiTFSI (in nBA) solution to obtain the anion exchange solutions at varying F_4TCNQ levels while keeping LiTFIS concentration constant (104.5 mM). The polymer films were exposed to the dopant solution for 80 seconds before spin coating.

Film Characterization: Electrical conductivity, Hall effect, temperature-dependent conductivity, and NIR-UV-Vis spectroscopy measurements were all performed on the same device. Electrical conductivity was measured by determining the sheet resistance using a Lakeshore MeasureReady M91 FastHall instrument with a Van der Pauw geometry. The device had 1x1 mm square gold electrodes, 45 nm thick, which were thermally evaporated onto the device's corners using a 3D-printed shadow mask in an Angstrom Engineering Nexdep thermal evaporator. Film thickness was measured with a Dektak 150 stylus profilometer. To ensure reproducibility, all conductivity measurements were conducted on three samples.

DC Hall effect measurements were performed using the same Lakeshore instrument, with a source current of 10 μA and a magnetic field of 1.0236 T, and were conducted on three samples for reproducibility. Temperature-dependent conductivity was determined by measuring sheet resistance as a function of temperature in a custom-built Van der Pauw setup using a Keithley 2400 Sourcemeter, controlled by LabVIEW software. The sourced voltage was limited to a total power

of 1 mW. A Peltier plate controlled the temperature, and an RTD sensor measured the film's temperature. NIR-UV-Vis spectra were obtained using a JASCO V-770 spectrophotometer.

The Seebeck coefficient was measured on a separate device due to the different electrode geometry, with electrodes consisting of two parallel gold rectangles (10x1 mm, 45 nm thick) spaced 10 mm apart. This measurement was performed using a custom-built setup with two Peltier plates to generate a temperature gradient, and the film's temperature was monitored with two RTD sensors. Seebeck samples were prepared in parallel with the sheet resistance/Hall/temperature-dependent conductivity samples to ensure all samples were exposed to the same conditions. All Seebeck measurements were conducted on three samples for reproducibility.

GIWAXS measurements were performed at the Stanford Synchrotron Radiation Lightsource (SSRL) on BL 11-3 using a wavelength of 0.9742 Å at incidence angle of 0.12°. Diffraction patterns were collected in a helium chamber to increase signal-to-noise with a sample to detector distance of 250 mm and a spot size of ~150 μm on the image plate. The IgorPro macro, Nika, was used to calibrate the GIWAXS 2-D data. Nika and WAXStools were used to reduce the data. To ensure reproducibility, all samples were made and measured in triplicates.

GISAXS was collected at the Stanford Synchrotron Radiation Lightsource using beamline 1-5. The scattering X-rays with energy set at 12 keV were collected using a 2D detector at a sample-to-detector distance of 3 meters. The incident angle (α_i) was set to 0.12°. The 1D integrations were obtained by horizontally integrating near Yoneda band and were fit using the Unified Fit method from the Irena and Nika package in Igor software. To ensure reproducibility, all samples were made and measured in triplicates.

5.5. References

[1] Swager, T. M. 50th Anniversary Perspective: Conducting/Semiconducting Conjugated Polymers. A Personal Perspective on the Past and the Future. *Macromolecules* **2017**, *50* (13), 4867–4886. https://doi.org/10.1021/acs.macromol.7b00582.

[2] Dubey, N.; Leclerc, M. Conducting Polymers: Efficient Thermoelectric Materials. *J. Polym. Sci. Part B Polym. Phys.* **2011**, *49* (7), 467–475. https://doi.org/10.1002/polb.22206.

[3] Kim, G.-H.; Shao, L.; Zhang, K.; Pipe, K. P. Engineered Doping of Organic Semiconductors for Enhanced Thermoelectric Efficiency. *Nat. Mater.* **2013**, *12* (8), 719–723. https://doi.org/10.1038/nmat3635.

[4] Tang, J.; Pai, Y.-H.; Liang, Z. Strategic Insights into Semiconducting Polymer Thermoelectrics by Leveraging Molecular Structures and Chemical Doping. *ACS Energy Lett.* **2022**, *7* (12), 4299–4324. https://doi.org/10.1021/acsenergylett.2c02119.

[5] Havinga, E. E.; ten Hoeve, W.; Wynberg, H. A New Class of Small Band Gap Organic Polymer Conductors. *Polym. Bull.* **1992**, *29* (1), 119–126. https://doi.org/10.1007/BF00558045.

[6] Yamashita, Y.; Tsurumi, J.; Ohno, M.; Fujimoto, R.; Kumagai, S.; Kurosawa, T.; Okamoto, T.; Takeya, J.; Watanabe, S. Efficient Molecular Doping of Polymeric Semiconductors Driven by Anion Exchange. *Nature* **2019**, *572* (7771), 634–638. https://doi.org/10.1038/s41586-019-1504-9.

[7] McCulloch, I.; Heeney, M.; Bailey, C.; Genevicius, K.; MacDonald, I.; Shkunov, M.; Sparrowe, D.; Tierney, S.; Wagner, R.; Zhang, W.; Chabinyc, M. L.; Kline, R. J.; McGehee, M. D.; Toney, M. F. Liquid-Crystalline Semiconducting Polymers with High Charge-Carrier Mobility. *Nat. Mater.* **2006**, *5* (4), 328–333. https://doi.org/10.1038/nmat1612.

[8] Aubry, T. J.; Winchell, K. J.; Salamat, C. Z.; Basile, V. M.; Lindemuth, J. R.; Stauber, J. M.; Axtell, J. C.; Kubena, R. M.; Phan, M. D.; Bird, M. J.; Spokoyny, A. M.; Tolbert, S. H.; Schwartz, B. J. Tunable Dopants with Intrinsic Counterion Separation Reveal the Effects of Electron Affinity on Dopant Intercalation and Free Carrier Production in Sequentially Doped Conjugated Polymer Films. *Adv. Funct. Mater.* **2020**, *30* (28), 2001800. https://doi.org/10.1002/adfm.202001800.

[9] Aubry, T. J.; Axtell, J. C.; Basile, V. M.; Winchell, K. J.; Lindemuth, J. R.; Porter, T. M.; Liu, J.-Y.; Alexandrova, A. N.; Kubiak, C. P.; Tolbert, S. H.; Spokoyny, A. M.; Schwartz, B. J. Dodecaborane-Based Dopants Designed to Shield Anion Electrostatics Lead to Increased Carrier Mobility in a Doped Conjugated Polymer. *Adv. Mater.* **2019**, *31* (11), 1805647. https://doi.org/10.1002/adma.201805647.

[10] Lüssem, B.; Keum, C.-M.; Kasemann, D.; Naab, B.; Bao, Z.; Leo, K. Doped Organic Transistors. *Chem. Rev.* **2016**, *116* (22), 13714–13751. https://doi.org/10.1021/acs.chemrev.6b00329.

[11] Kang, S. D.; Snyder, G. J. Charge-Transport Model for Conducting Polymers. *Nat. Mater.* **2017**, *16* (2), 252–257. https://doi.org/10.1038/nmat4784.

[12] Untilova, V.; Hynynen, J.; Hofmann, A. I.; Scheunemann, D.; Zhang, Y.; Barlow, S.; Kemerink, M.; Marder, S. R.; Biniek, L.; Müller, C.; Brinkmann, M. High Thermoelectric Power Factor of Poly(3-Hexylthiophene) through In-Plane Alignment and Doping with a Molybdenum Dithiolene Complex. *Macromolecules* **2020**, *53* (15), 6314–6321. https://doi.org/10.1021/acs.macromol.0c01223.

[13] Xuan, Y.; Liu, X.; Desbief, S.; Leclère, P.; Fahlman, M.; Lazzaroni, R.; Berggren, M.; Cornil, J.; Emin, D.; Crispin, X. Thermoelectric Properties of Conducting Polymers: The Case of Poly(3-Hexylthiophene). *Phys. Rev. B* **2010**, *82* (11), 115454. https://doi.org/10.1103/PhysRevB.82.115454.

[14] Statz, M.; Venkateshvaran, D.; Jiao, X.; Schott, S.; McNeill, C. R.; Emin, D.; Sirringhaus, H.; Di Pietro, R. On the Manifestation of Electron-Electron Interactions in the Thermoelectric Response of Semicrystalline Conjugated Polymers with Low Energetic Disorder. *Commun. Phys.* **2018**, *1* (1), 1–10. https://doi.org/10.1038/s42005-018-0016-5.

[15] Bubnova, O.; Khan, Z. U.; Malti, A.; Braun, S.; Fahlman, M.; Berggren, M.; Crispin, X. Optimization of the Thermoelectric Figure of Merit in the Conducting Polymer Poly(3,4-Ethylenedioxythiophene). *Nat. Mater.* **2011**, *10* (6), 429–433. https://doi.org/10.1038/nmat3012.

[16] Zhong, Y.; Untilova, V.; Muller, D.; Guchait, S.; Kiefer, C.; Herrmann, L.; Zimmermann, N.; Brosset, M.; Heiser, T.; Brinkmann, M. Preferential Location of Dopants in the Amorphous Phase of Oriented Regioregular Poly(3-Hexylthiophene-2,5-Diyl) Films Helps Reach Charge Conductivities of 3000 S Cm−1. *Adv. Funct. Mater.* **2022**, *32* (30), 2202075. https://doi.org/10.1002/adfm.202202075.

[17] Gregory, S. A.; Atassi, A.; Ponder, J. F. Jr.; Freychet, G.; Su, G. M.; Reynolds, J. R.; Losego, M. D.; Yee, S. K. Quantifying Charge Carrier Localization in PBTTT Using Thermoelectric and Spectroscopic Techniques. *J. Phys. Chem. C* **2023**, *127* (25), 12206–12217. https://doi.org/10.1021/acs.jpcc.3c01152.

[18] Gregory, S. A.; Hanus, R.; Atassi, A.; Rinehart, J. M.; Wooding, J. P.; Menon, A. K.; Losego, M. D.; Snyder, G. J.; Yee, S. K. Quantifying Charge Carrier Localization in Chemically

Doped Semiconducting Polymers. *Nat. Mater.* **2021**, *20* (10), 1414–1421. https://doi.org/10.1038/s41563-021-01008-0.

[19] Voss, M. G.; Scholes, D. T.; Challa, J. R.; Schwartz, B. J. Ultrafast Transient Absorption Spectroscopy of Doped P3HT Films: Distinguishing Free and Trapped Polarons. *Faraday Discuss.* **2019**, *216*, 339–362. https://doi.org/10.1039/C8FD00210J.

[20] Scholes, D. T.; Yee, P. Y.; Lindemuth, J. R.; Kang, H.; Onorato, J.; Ghosh, R.; Luscombe, C. K.; Spano, F. C.; Tolbert, S. H.; Schwartz, B. J. The Effects of Crystallinity on Charge Transport and the Structure of Sequentially Processed F_4TCNQ-Doped Conjugated Polymer Films. *Adv. Funct. Mater.* **2017**, *27* (44), 1702654. https://doi.org/10.1002/adfm.201702654.

[21] Scholes, D. T.; Yee, P. Y.; McKeown, G. R.; Li, S.; Kang, H.; Lindemuth, J. R.; Xia, X.; King, S. C.; Seferos, D. S.; Tolbert, S. H.; Schwartz, B. J. Designing Conjugated Polymers for Molecular Doping: The Roles of Crystallinity, Swelling, and Conductivity in Sequentially-Doped Selenophene-Based Copolymers. *Chem. Mater.* **2019**, *31* (1), 73–82. https://doi.org/10.1021/acs.chemmater.8b02648.

[22] Untilova, V.; Biskup, T.; Biniek, L.; Vijayakumar, V.; Brinkmann, M. Control of Chain Alignment and Crystallization Helps Enhance Charge Conductivities and Thermoelectric Power Factors in Sequentially Doped P3HT:F4TCNQ Films. *Macromolecules* **2020**, *53* (7), 2441–2453. https://doi.org/10.1021/acs.macromol.9b02389.

[23] Heo, Y.-J.; Jeong, H.-G.; Kim, J.; Lim, B.; Kim, J.; Kim, Y.; Kang, B.; Yun, J.-M.; Cho, K.; Kim, D.-Y. Formation of Large Crystalline Domains in a Semiconducting Polymer with Semi-Fluorinated Alkyl Side Chains and Application to High-Performance Thin-Film Transistors. *ACS Appl. Mater. Interfaces* **2020**, *12* (44), 49886–49894. https://doi.org/10.1021/acsami.0c13176.

[24] Kim, Y.-J.; Kim, N.-K.; Park, W.-T.; Liu, C.; Noh, Y.-Y.; Kim, D.-Y. Kinetically Controlled Crystallization in Conjugated Polymer Films for High-Performance Organic Field-Effect Transistors. *Adv. Funct. Mater.* **2019**, *29* (23), 1807786. https://doi.org/10.1002/adfm.201807786.

[25] Mei, J.; Kim, D. H.; Ayzner, A. L.; Toney, M. F.; Bao, Z. Siloxane-Terminated Solubilizing Side Chains: Bringing Conjugated Polymer Backbones Closer and Boosting Hole Mobilities in Thin-Film Transistors. *J. Am. Chem. Soc.* **2011**, *133* (50), 20130–20133. https://doi.org/10.1021/ja209328m.

[26] Stanfield, D. A.; Wu, Y.; Tolbert, S. H.; Schwartz, B. J. Controlling the Formation of Charge Transfer Complexes in Chemically Doped Semiconducting Polymers. *Chem. Mater.* **2021**, *33* (7), 2343–2356. https://doi.org/10.1021/acs.chemmater.0c04471.

[27] Wu, Y.; Salamat, C. Z.; León Ruiz, A.; Simafranca, A. F.; Akmanşen-Kalayci, N.; Wu, E. C.; Doud, E.; Mehmedović, Z.; Lindemuth, J. R.; Phan, M. D.; Spokoyny, A. M.; Schwartz, B. J.; Tolbert, S. H. Using Bulky Dodecaborane-Based Dopants to Produce Mobile Charge Carriers in Amorphous Semiconducting Polymers. *Chem. Mater.* **2024**, *36* (11), 5552–5562. https://doi.org/10.1021/acs.chemmater.4c00502.

[28] Ayzner, A. L.; Tassone, C. J.; Tolbert, S. H.; Schwartz, B. J. Reappraising the Need for Bulk Heterojunctions in Polymer−Fullerene Photovoltaics: The Role of Carrier Transport in All-Solution-Processed P3HT/PCBM Bilayer Solar Cells. *J. Phys. Chem. C* **2009**, *113* (46), 20050–20060. https://doi.org/10.1021/jp9050897.

[29] Hawks, S. A.; Aguirre, J. C.; Schelhas, L. T.; Thompson, R. J.; Huber, R. C.; Ferreira, A. S.; Zhang, G.; Herzing, A. A.; Tolbert, S. H.; Schwartz, B. J. Comparing Matched

Polymer:Fullerene Solar Cells Made by Solution-Sequential Processing and Traditional Blend Casting: Nanoscale Structure and Device Performance. *J. Phys. Chem. C* **2014**, *118* (31), 17413–17425. https://doi.org/10.1021/jp504560r.

[30] Aguirre, J. C.; Hawks, S. A.; Ferreira, A. S.; Yee, P.; Subramaniyan, S.; Jenekhe, S. A.; Tolbert, S. H.; Schwartz, B. J. Sequential Processing for Organic Photovoltaics: Design Rules for Morphology Control by Tailored Semi-Orthogonal Solvent Blends. *Adv. Energy Mater.* **2015**, *5* (11), 1402020. https://doi.org/10.1002/aenm.201402020.

[31] Scholes, D. T.; Hawks, S. A.; Yee, P. Y.; Wu, H.; Lindemuth, J. R.; Tolbert, S. H.; Schwartz, B. J. Overcoming Film Quality Issues for Conjugated Polymers Doped with F4TCNQ by Solution Sequential Processing: Hall Effect, Structural, and Optical Measurements. *J. Phys. Chem. Lett.* **2015**, *6* (23), 4786–4793. https://doi.org/10.1021/acs.jpclett.5b02332.

[32] *Double doping of conjugated polymers with monomer molecular dopants | Nature Materials*. https://www.nature.com/articles/s41563-018-0263-6 (accessed 2024-08-19).

[33] *Optical Signature of Delocalized Polarons in Conjugated Polymers - Beljonne - 2001 - Advanced Functional Materials - Wiley Online Library*. https://onlinelibrary.wiley.com/doi/10.1002/1616-3028(200106)11:3%3C229::AID-ADFM229%3E3.0.CO;2-L (accessed 2024-08-19).

[34] *Nature of the optical transitions in charged oligothiophenes - Cornil - 1995 - Advanced Materials - Wiley Online Library*. https://onlinelibrary.wiley.com/doi/abs/10.1002/adma.19950070311 (accessed 2024-08-19).

[35] *Crystal Structure Control of the Energetics of Chemical Doping in Rub-Aligned P3HT Films | ACS Materials Letters*. https://pubs.acs.org/doi/10.1021/acsmaterialslett.3c01543 (accessed 2024-08-19).

[36] Ghosh, R.; Pochas, C. M.; Spano, F. C. Polaron Delocalization in Conjugated Polymer Films. *J. Phys. Chem. C* **2016**, *120* (21), 11394–11406. https://doi.org/10.1021/acs.jpcc.6b02917.

[37] *A Versatile Method to Fabricate Highly In-Plane Aligned Conducting Polymer Films with Anisotropic Charge Transport and Thermoelectric Properties: The Key Role of Alkyl Side Chain Layers on the Doping Mechanism - Hamidi-Sakr - 2017 - Advanced Functional Materials - Wiley Online Library*. https://onlinelibrary.wiley.com/doi/10.1002/adfm.201700173 (accessed 2020-11-09).

[38] Vijayakumar, V.; Zhong, Y.; Untilova, V.; Bahri, M.; Herrmann, L.; Biniek, L.; Leclerc, N.; Brinkmann, M. Bringing Conducting Polymers to High Order: Toward Conductivities beyond 105 S Cm−1 and Thermoelectric Power Factors of 2 mW M−1 K−2. *Adv. Energy Mater.* **2019**, *9* (24), 1900266. https://doi.org/10.1002/aenm.201900266.

[39] *The Role of Ordering on the Thermoelectric Properties of Blends of Regioregular and Regiorandom Poly(3-hexylthiophene) - Lim - 2019 - Advanced Electronic Materials - Wiley Online Library*. https://onlinelibrary.wiley.com/doi/full/10.1002/aelm.201800915 (accessed 2024-08-19).

[40] Lu-Díaz, M.; Duhandžić, M.; Harrity, S.; Samanta, S.; Akšamija, Z.; Venkataraman, D. Dopant-Induced Energetic Disorder in Conjugated Polymers: Determinant Roles of Polymer–Dopant Distance and Composite Electronic Structures. *J. Phys. Chem. C* **2024**, *128* (14), 5996–6006. https://doi.org/10.1021/acs.jpcc.3c07197.

[41] Walter, P.; Ilchen, M.; Roeh, J.; Ohm, W.; Zeuthen, C. B.; Klemradt, U. In Situ X-Ray Measurements to Follow the Crystallization of BaTiO3 Thin Films during RF-Magnetron Sputter Deposition. *Appl. Sci.* **2021**, *11* (19), 8970. https://doi.org/10.3390/app11198970.

[42] Sureka, H. V.; Obermeyer, A. C.; Flores, R. J.; Olsen, B. D. Catalytic Biosensors from Complex Coacervate Core Micelle (C3M) Thin Films. *ACS Appl. Mater. Interfaces* **2019**, *11* (35), 32354–32365. https://doi.org/10.1021/acsami.9b08478.

[43] Freychet, G.; Maret, M.; Fernandez-Regulez, M.; Tiron, R.; Gharbi, A.; Nicolet, C.; Gergaud, P. Morphology of Poly(Lactide)-Block-Poly(Dimethylsiloxane)-Block-Polylactide High-χ Triblock Copolymer Film Studied by Grazing Incidence Small-Angle X-Ray Scattering. *J. Polym. Sci.* **2020**, *58* (15), 2041–2050. https://doi.org/10.1002/pol.20200196.

[44] Darko, C.; Botiz, I.; Reiter, G.; Breiby, D. W.; Andreasen, J. W.; Roth, S. V.; Smilgies, D.-M.; Metwalli, E.; Papadakis, C. M. Crystallization in Diblock Copolymer Thin Films at Different Degrees of Supercooling. *Phys. Rev. E* **2009**, *79* (4), 041802. https://doi.org/10.1103/PhysRevE.79.041802.

[45] She, Y.; Lee, J.; Diroll, B. T.; Lee, B.; Aouadi, S.; Shevchenko, E. V.; Berman, D. Rapid Synthesis of Nanoporous Conformal Coatings via Plasma-Enhanced Sequential Infiltration of a Polymer Template. *ACS Omega* **2017**, *2* (11), 7812–7819. https://doi.org/10.1021/acsomega.7b01314.

[46] Smilgies, D.-M. GISAXS: A Versatile Tool to Assess Structure and Self-Assembly Kinetics in Block Copolymer Thin Films. *J. Polym. Sci.* **2022**, *60* (7), 1023–1041. https://doi.org/10.1002/pol.20210244.

[47] Santoro, G.; Yu, S.; Santoro, G.; Yu, S. Grazing Incidence Small Angle X-Ray Scattering as a Tool for In- Situ Time-Resolved Studies. In *X-ray Scattering*; IntechOpen, 2017. https://doi.org/10.5772/64877.

[48] Yan, X.; Xiong, M.; Deng, X.-Y.; Liu, K.-K.; Li, J.-T.; Wang, X.-Q.; Zhang, S.; Prine, N.; Zhang, Z.; Huang, W.; Wang, Y.; Wang, J.-Y.; Gu, X.; So, S. K.; Zhu, J.; Lei, T. Approaching Disorder-Tolerant Semiconducting Polymers. *Nat. Commun.* **2021**, *12* (1), 5723. https://doi.org/10.1038/s41467-021-26043-y.

[49] Warren, R.; Blom, P. W. M.; Koch, N. Molecular *p* -Doping Induced Dielectric Constant Increase of Polythiophene Films Determined by Impedance Spectroscopy. *Appl. Phys. Lett.* **2023**, *122* (15), 152108. https://doi.org/10.1063/5.0146194.

[50] Schießl, S. P.; de Vries, X.; Rother, M.; Massé, A.; Brohmann, M.; Bobbert, P. A.; Zaumseil, J. Modeling Carrier Density Dependent Charge Transport in Semiconducting Carbon Nanotube Networks. *Phys. Rev. Mater.* **2017**, *1* (4), 046003. https://doi.org/10.1103/PhysRevMaterials.1.046003.

[51] Baustert, K. N.; Bombile, J. H.; Rahman, M. T.; Yusuf, A. O.; Li, R.; Huckaba, A. J.; Risko, C.; Graham, K. R. Combination of Counterion Size and Doping Concentration Determines the Electronic and Thermoelectric Properties of Semiconducting Polymers. *Adv. Mater.* **2024**, *36* (29), 2313863. https://doi.org/10.1002/adma.202313863.

APPENDIX A

Supplemental Information for Chapter 2

Materials

Poly(3-hexylthiophene-2,5-diyl) (P3HT; regioregularity 97%) and F_4TCNQ (Purity > 99.0%) were purchased from Ossila. 1,2-dichlorobenzene (ODCB, anhydrous, 99%), n-butyl acetate (nBA, anhydrous, > 99%), bis(trifluoromethane)sulfonimide lithium (LiTFSI), and lithium hexafluorophosphate ($liPF_6$) were purchased from Sigma-Aldrich.

Films Fabrication and Doping

Prior to spin-coating the polymer, the glass substrates underwent several steps. First, they were cut into 1.3 x 1.3 cm pieces and then sequentially cleaned using Alconox detergent, DI water, and acetone. Next, the glass substrates were then plasma etched for approximately 15 minutes. The samples were then transferred to a nitrogen glovebox for spin coating. 2% (20 mg/mL) P3HT in ODCB was then spin-coated onto the substrate at 1000 rpm for 60 seconds, followed by 4000 rpm for 10 seconds. After the spin-coating, the films were then left to dry for approximately 30 minutes before the doping process. For doping, the films were exposed to a doping solution for 80 seconds and subsequently spin-coated at 4000 rpm for 10 seconds to eliminate any residual doping solution.

Conductivity and Hall Measurement

Before conducting the conductivity measurement, a 45nm-thick layer of gold was deposited onto the doped films. This deposition process was carried out using the Angstrom Engineering Nexdep thermal evaporator at pressures below 1x10-6 torr and a deposition rate of 0.5 Å/s.

The conductivity measurement was initially performed within an argon glovebox. A Keithley 2400 Sourcemeter, controlled by LabVIEW software, was utilized for this purpose. The sourced currents were maintained below a total power of 1mW. Following the measurement inside the argon

glovebox, the samples were transferred to the ambient air environment. Subsequently, both conductivity and DC Hall measurements were conducted using Lakeshore's MeasureReady M91 FastHall instrument. In these measurements, a source current of 10 µA was employed. For the DC Hall measurements, a magnetic field strength of 1.0623 Tesla was applied. To obtain the argon purge samples reported in the main text, argon gas was flowed into the MeasureReady M91 FastHall sample compartment for roughly 4 minutes prior to conducting the measurement.

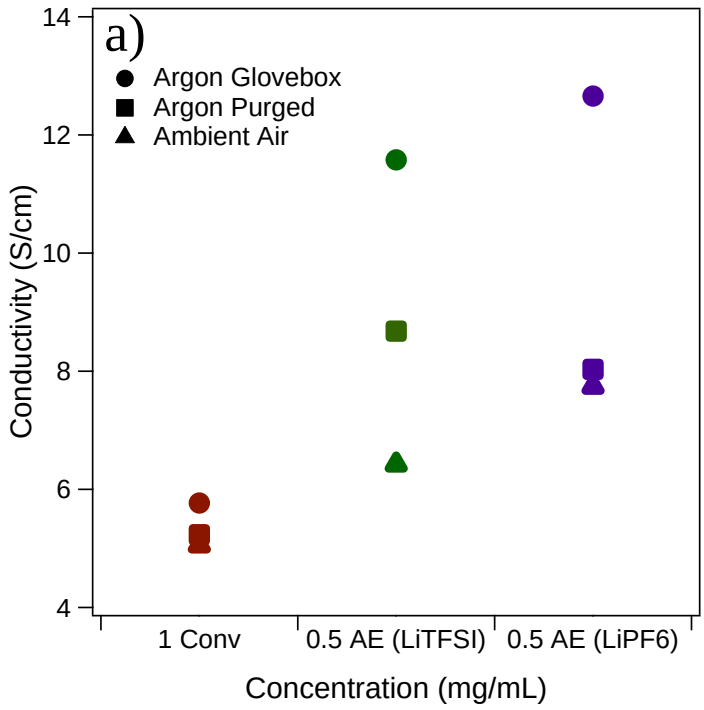

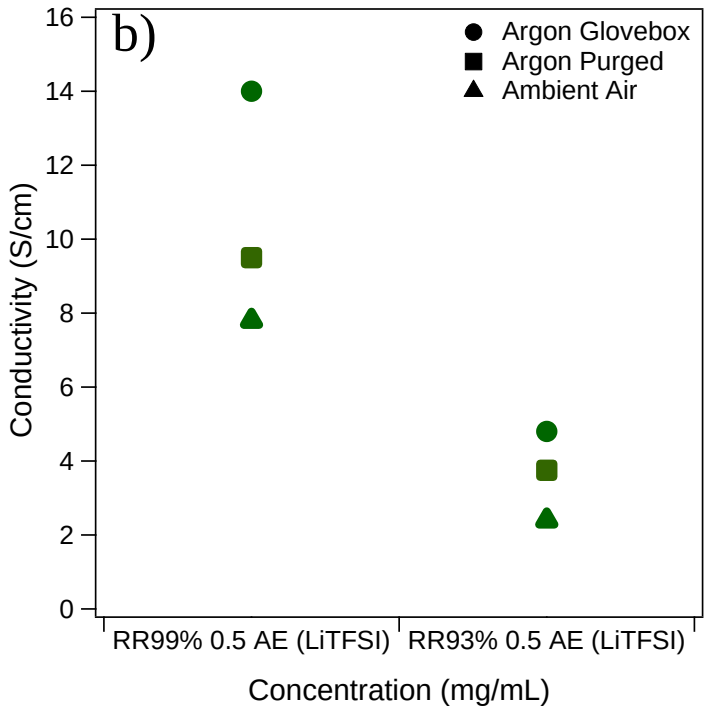

Figure S 1.a. shows conductivity values for higher concentration of dopants for conventional (1 mg/mL F_4TCNQ) and anion-exchange (0.5mg/mL F_4TCNQ + 30mg/mL LiTFSI and 0.5 mg/mL F_4TCNQ + 5 mg/mL $LiPF_6$) doped 97%RR P3HT in three different environment. Similar to the result shown in **Figure 1**, only samples doped with hygroscopic salts (LiTFSI and $LiPF_6$) show a drop in conductivity when exposed to the ambient environment. The sample doped with the conventional method (F_4TCNQ) remains unchanged within measurement error. **Figure S 1.b.** shows the conductivity of various P3HT regioregularities doped with 0.5 mg/mL F_4TCNQ + 30 mg/mL LiTFSI. Like the case for 97% P3HT when doped with anion exchange, the electrical conductivity drops roughly by a factor of 2 for all regioregularities and doping concentrations once the samples are exposed to ambient air, indicating LiTFSI absorbs water independently of the polymer.

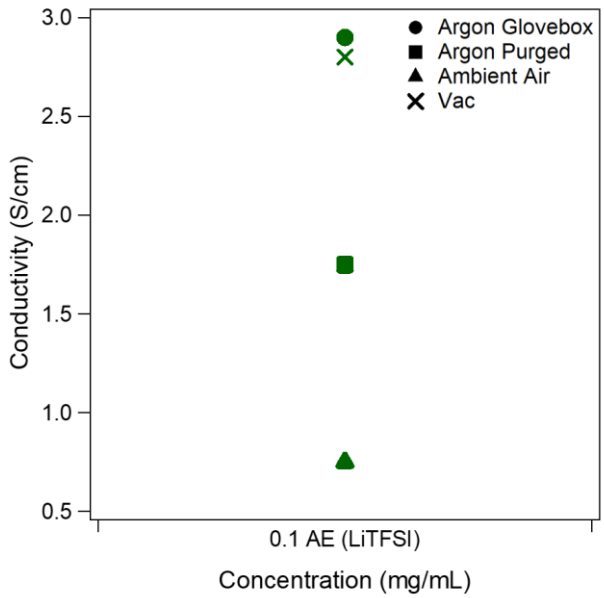

Figure S 2. Conductivity values for the 97% P3HT doped with 0.1mg/mL anion-exchanged LiTFSI (AE) sample were measured inside an argon box; exposed to ambient air for 5 minutes; followed by 5-minute Ar purge; vacuumed/Ar purged cycles for 20 minutes.

The electrical conductivity for 97% P3HT doped with 0.1mg/mL anion exchanged F_4TCNQ is shown if **Figure S2**. The conductivity is first measured in an inert Ar atmosphere followed by air exposure, leading to a drop in the electrical conductivity. Purging the sample with Ar yields some of the conductivity back. Loading the sample into an antechamber and performing four 5-minute cycles of vacuum followed by Ar gas refill and remeasuring the conductivity using the same setup as in the "Ar Box" configuration recovers ≈97% of the conductivity in the same sample (black x "Vac"). It is worth mentioning that the slightly higher conductivity observed in the argon glovebox can be attributed to the elevated temperature within the box compared to the ambient room temperature. Since transport in semiconducting polymer

films is predominantly governed by hopping transport, higher temperatures lead to increased conductivity.

UV-Vis and NIR spectroscopy

The Agilent Cary 600 Series FTIR Spectrometer was employed to measure the near-IR absorption spectra. The spectra were captured within the range of 1666-2500 nm to prevent any overlap with water stretches in the longer wavelength region. In order to investigate the impact of water on the P1 transition, the sample compartment of the FTIR spectrometer was subjected to dry N2 gas flow for various durations, as mentioned in the main text.

Additionally, Shimadzu UV3101PC Scanning Spectrophotometer was utilized for UV-Vis-NIR spectroscopy. The slit width was set at 1 nm, and a sampling interval of 1 nm was employed. To ensure the UV-Vis beam was accurately centered on the sample, a small 3D-printed aperture was utilized.

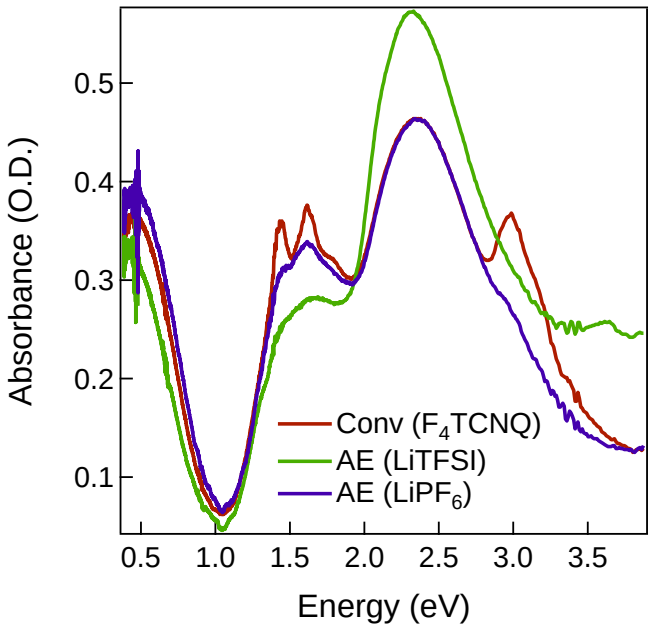

Figure S 3. UV-Vis-NIR of P3HT samples doped with 0.5 mg/mL F4TCNQ (red), 0.1 mg/mL F4TCNQ (green) anion-exchanged with 30 mg/mL LiTFSI, and 0.1 mg/mL F4TCNQ anion-exchanged with 5 mg/mL LiPF6 (blue) taken in ambient air.

Doping P3HT polymer films leads to the emergence of two polaronic transitions referred to as "P1" and "P2," which are centered around approximately 0.5eV and 1.7eV, respectively. In the case of the sample doped solely with F_4TCNQ, the P2 transition overlaps with the F_4TCNQ anion vibronic transition, resulting in the observed peaks in the ~1.7eV region and at ~3.0 eV. It is important to note that at our chosen sequential doping concentration of 0.5 mg/mL F_4TCNQ, we primarily observe only F_4TCNQ anions that absorb at ~3.0 eV and not neutral F_4TCNQ, which absorbs at ~3.2 eV. This indicates that the F_4TCNQ present in our doped films is essentially entirely anionic, engaged in doping the polymer. However, for anion-exchanged-doped P3HT films, the F_4TCNQ anion is substituted with the salt anion used, causing most of the F_4TCNQ absorption features to be absent, as depicted in the green and blue traces.

Humidity Sensing Measurement

A homemade setup was used to measure conductivity as a function of humidity. To prevent additional moisture from entering, the setup was carefully sealed using vacuum grease. Gradual moisture removal was facilitated by using Driedite within the setup. A digital hygrometer was then used to track the humidity, while conductivity was measured using Keithley 2400 Sourcemeter.

APPENDIX B

Supplemental Information for Chapter 3

Materials

Poly(3-hexylthiophene-2,5-diyl) (Mn = 50-70 kg/mol, regioregularity 91-94%) was purchased from Rieke metals inc. F_4TCNQ (Purity > 99.0%) were purchased from Ossila. 1,2 dichlorobenzene (anhydrous, 99%), Acetonitrile (anhydrous, 98%), and Dichloromethane (anhydrous, 99.8% with 40-150ppm of amylene as a stabilizer) were purchased from Sigma-Aldrich.

Experimental Methods

P3HT films were prepared on ~1.5 x 1.5 cm substrates (glass or silicon). The substrates were cleaned sequentially with Alconox detergent, deionized water, isopropanol, and acetone. Immediately after washing, the substrates were plasma cleaned using Harrick Plasma Cleaner PDC-32G for 15 minutes. Substrates were then transferred to a nitrogen glove box and spin-coated with 20 mg/mL P3HT in 1,2 dichlorobenzene. Spin coating was done at 1000 rpm for 60 seconds, followed by 4000 rpm for 5 seconds to remove excess solvent. Next, the pre-cast P3HT films were transferred to an argon glove box for rub-aligning. The rub-aligning was done by heating the pre-cast P3HT films to 140^{o}C and translating it across a rotating microfiber wheel. The downward force applied by the microfiber wheel during the rubbing process was chosen to be ~1 N as it gave the highest dichroic ratio. To accurately controlled the applied rubbing force, we used a load cell to measure and a lab jack to tune the force. After alignment, the films were then transferred back into the nitrogen glove box for doping with F_4TCNQ. The F_4TCNQ solutions were prepared in the nitrogen glove box by dissolving F_4TCNQ powder in acetonitrile (ACN) or dichloromethane (DCM). To dope the films, 100 µL of F_4TCNQ solutions was pipetted onto the film surface and

spread to ensure that the surface was fully covered with solution. The spin coater was then set to allow the solution to sit on the film undisturbed for 5 seconds before spinning off any unreacted solvent at 4000 rpm for 10 seconds.

Spectroscopy

Polarized UV-Vis absorptions were done using a Shimadzu UV3101PC Scanning Spectrophotometer. All samples for polarized UV-Vis absorptions were prepared on glass substrates.

GIWAXS

Samples were prepared on silicon substrates. Measurements were performed on beamline 11-3 at the Stanford Synchrotron Radiation Lightsource. The beam wavelength is 0.9742 Å and incidence angle is 0.12°. Samples were placed in a helium chamber to increase signal-to-noise. The sample to detector distance is 250 mm and the spot size on the image plate is ~150 μm. The 2-D diffractograms were radially integrated with 0-10° and 80-90° to obtain the in-plane and out-of-plane diffraction patterns. The Nika macro was used to calibrate the beam and the WAXStools macro was used to reduce the GIWAXS data and for subsequent analysis in IgorPro.

Grazing-Incidence Wide-Angle X-ray Scattering (GIWAXS)

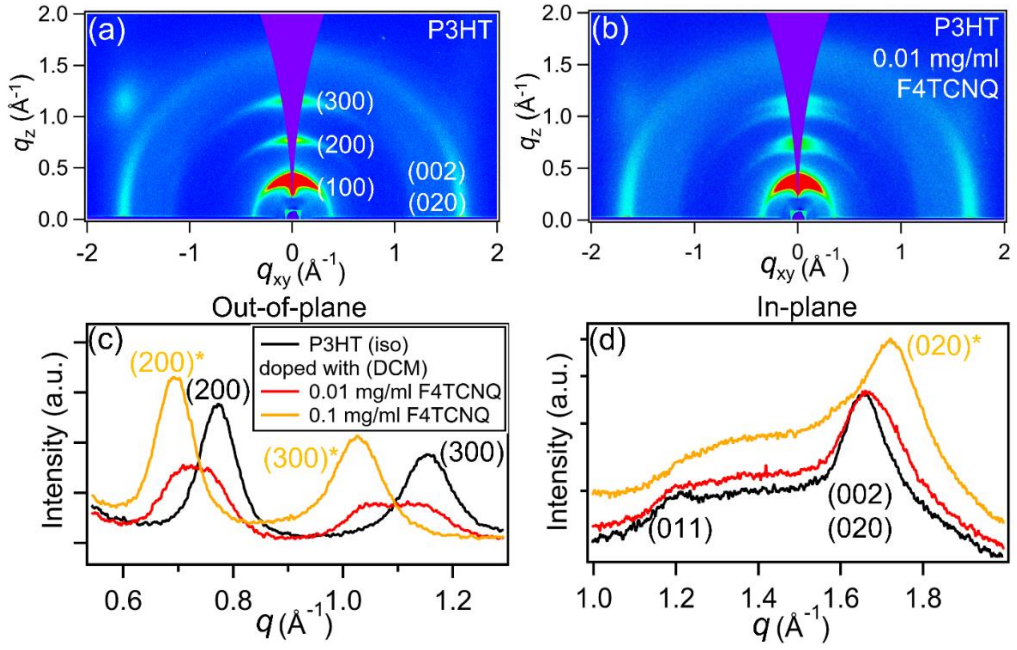

Figure S 4. 2D and integrated GIWAXS Patterns of Unaligned P3HT. (a) GIWAXS data for unaligned P3HT shows only edge-on texture. Lamellar peaks are out-of-plane and labeled as (100), (200) and (300). Monomer and π-π stacking peaks are in-plane and labeled as (002) and (020). (b) GIWAXS data for P3HT doped with 0.01 mg/ml F_4TCNQ from DCM. The lamellar peaks all appear as doublets, indicating the co-existence of undoped and doped P3HT in a first-order phase transition. (c-d) Integrated lamellar (c) and higher-angle (d) peaks for P3HT and P3HT doped with F_4TCNQ at a range of concentrations. The 0.1 mg/ml F_4TCNQ sample is fully transformed to the doped phase, while the 0.01 mg/ml F4TCNQ sample is at the midpoint of the transformation.

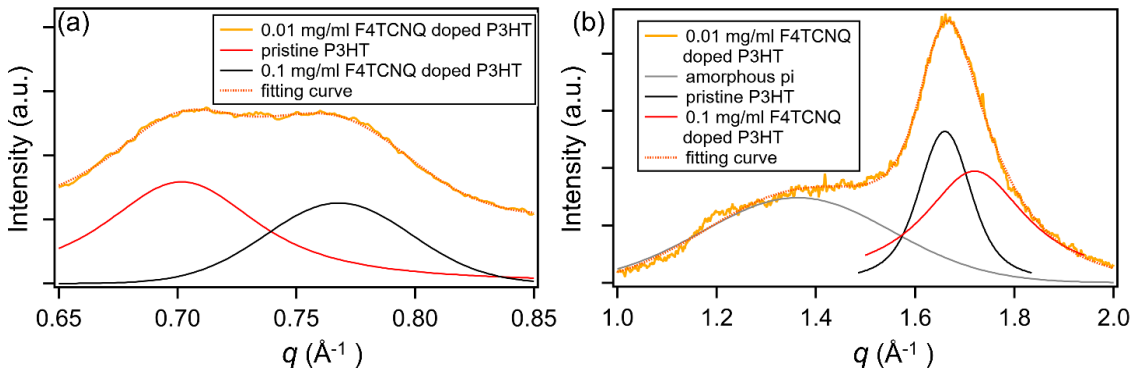

Figure S 5. Peak fits for the 0.01 mg/ml F_4TCNQ doped P3HT GIWAXS data showing the coexistence of undoped and doped P3HT peaks. Data is shown for the (200) peaks (a), and the (020) peaks (b).

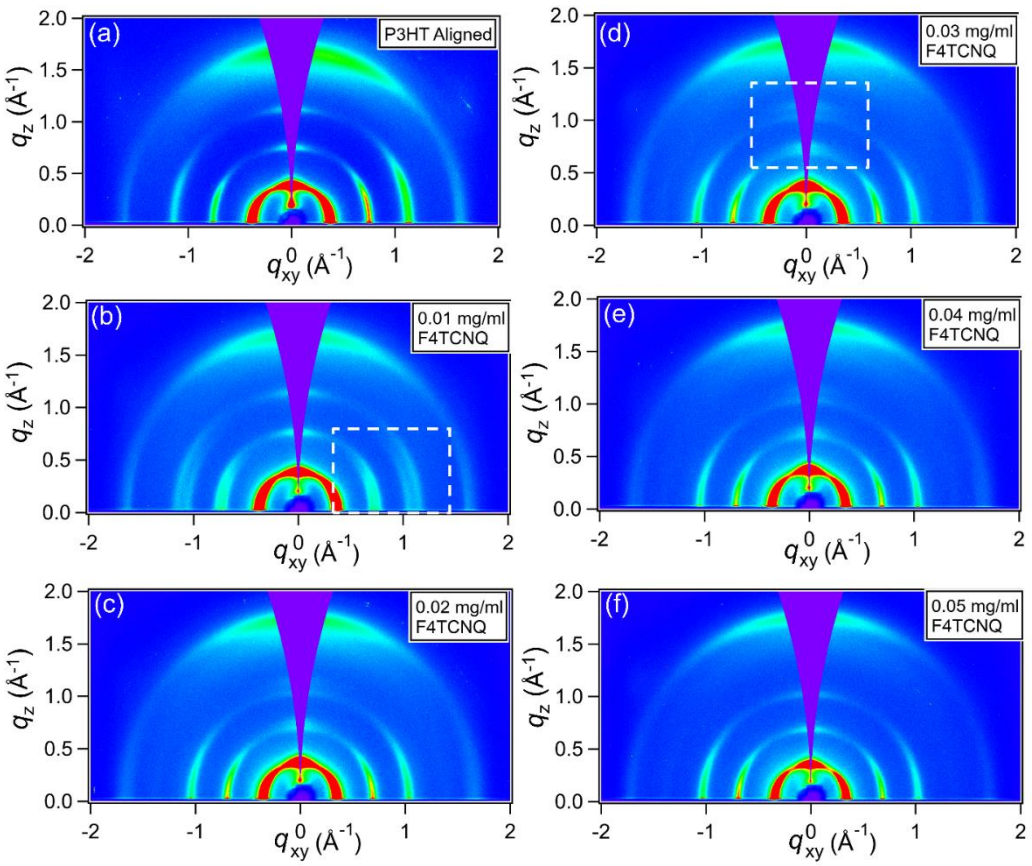

Figure S 6. 2D GIWAXS patterns of aligned P3HT collected in the parallel direction for an undoped polymer film, and a films doped with F4TCNQ at various concentrations in dicloromethane (DCM). (a) Undoped P3HT, P3HT SqP doped from 0.01 mg/ml F4TCNQ in DCM, (b) P3HT SqP doped from 0.02 mg/ml F_4TCNQ in DCM, (c) P3HT SqP doped from 0.03 mg/ml F_4TCNQ in DCM, (d) P3HT SqP doped from 0.04 mg/ml F4TCNQ in DCM, (e) P3HT SqP doped from 0.05 mg/ml F_4TCNQ in DCM. The face-on P3HT polymorph dopes first at 0.01 mg/ml F_4TCNQ, followed by the edge-on polymorph at 0.02 mg/ml F_4TCNQ. Both concentrations are lower than those observed upon doping with acetonitrily (ACN, main text figure 3) because DCM swells the polymer more than ACN and allows for more facile doping.

	Unaligned		Aligned					
			Face-On			Edge-On		
	Undoped	Doped (5 mg/mL)	Undoped	Doped (0.05 mg/mL)	Doped (6 mg/mL)	Undoped	Doped (0.05 mg/mL)	Doped (6 mg/mL)
Lamellar Distance (Å)	16.36 ± 0.03	18.18 ± 0.02	16.64 ± 0.03	18.01 ± 0.01	18.10 ± 0.01	16.03 ± 0.04	17.62 ± 0.06	17.95 ± 0.04
π-stack Distance (Å)	3.8 ± 0.1	3.55 ±0.01	3.77 ± 0.02	3.63 ± 0.02	3.53 ± 0.05	3.76 ± 0.01	3.64 ± 0.01	3.54 ± 0.01

Table S 1. Lamellar and π-stacking distances of undoped and doped unaligned and rub-aligned P3HT. All doped samples were doped using F4TCNQ in acetonitrile at the stated concentrations.

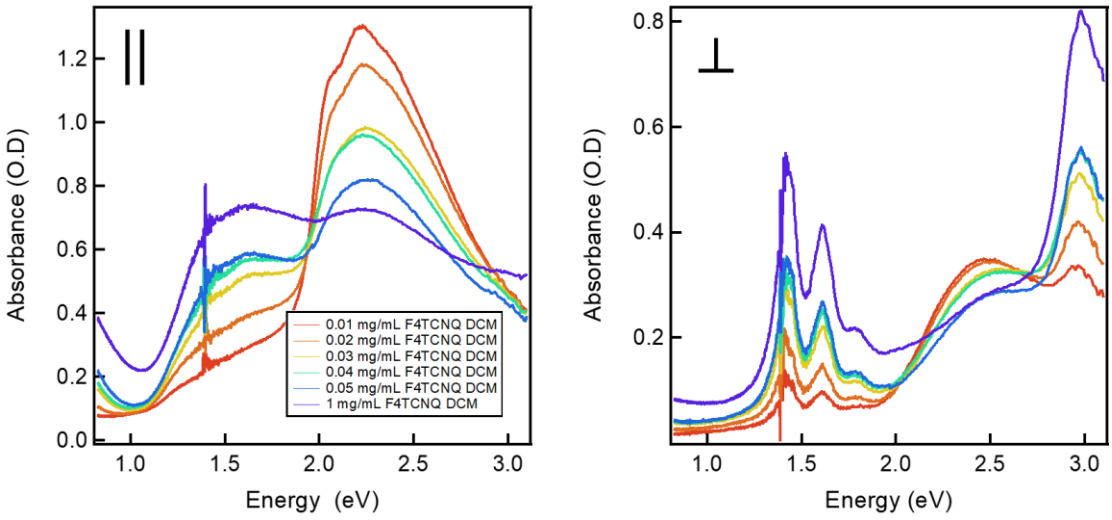

Figure S 7. Polarized UV-Visible absorption spectra of rub-aligned P3HT films doped with F4TCNQ in DCM. Due to the better-swelling power of DCM, the rub-aligned films start doping at a lower F_4TCNQ concentration compared to doping in ACN. At 0.01 mg/mL F4TCNQ, the P2

is already visible in the parallel spectrum and the F_4TCNQ anion peaks are observed in the perpendicular direction, both of which indicates that the polymer is doped.

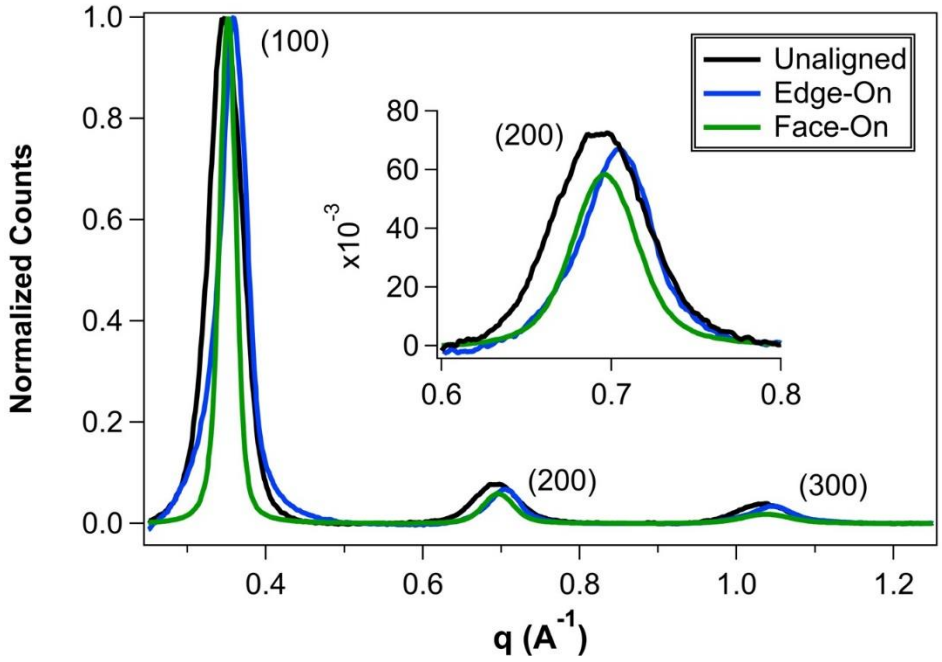

Figure S 8. Selected integrations of GIWAXS data collected on P3HT films doped with high concentrations of F_4TCNQ (6 mg/mL, doped from ACN for edge-on and face-on, from nBA for unaligned). The data show that the final doped structure is almost the same for unaligned P3HT, and both the face-on and edge-on aligned polymorphs. F_4TCNQ dopant peaks near 0.87 $Å^{-1}$ were removed from the unaligned and edge-on curves for ease of analysis.

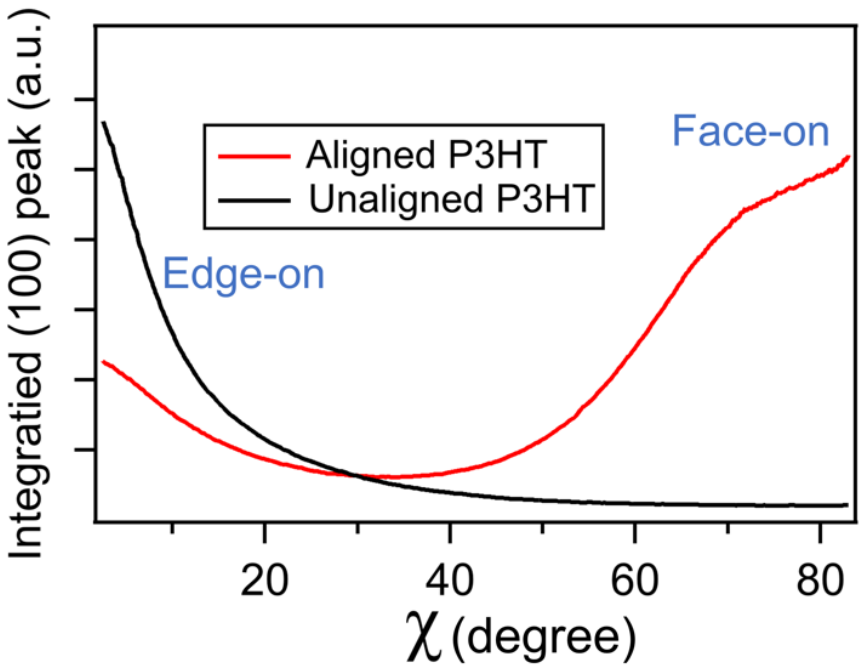

Figure S 9. Radial integrations of the (100) lamellar peak for unaligned and rub-aligned P3HT plotted against altitudinal angle χ, collected with the beam aligned parallel to the rub direction. Unaligned P3HT shows only edge-on texture, while the aligned P3HT has both edge-on and face-on polymorphs.

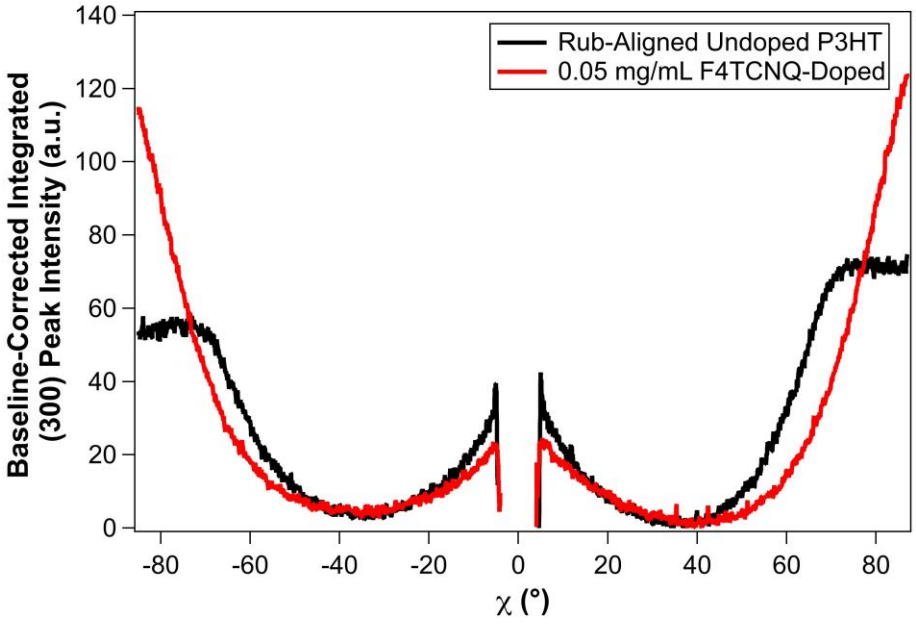

Figure S 10. Radial integration of the (300) lamellar peak of doped and undoped rub-aligned P3HT plotted against altitudinal angle χ for data collected with the beam aligned parallel to the rub direction. GIWAXS patterns that were chosen for analysis were required to have equivalent relative intensity in the left (negative χ) and right (positive χ) halves of the GIWAXS pattern, as this indicated that the beam was well aligned parallel to the rub direction.

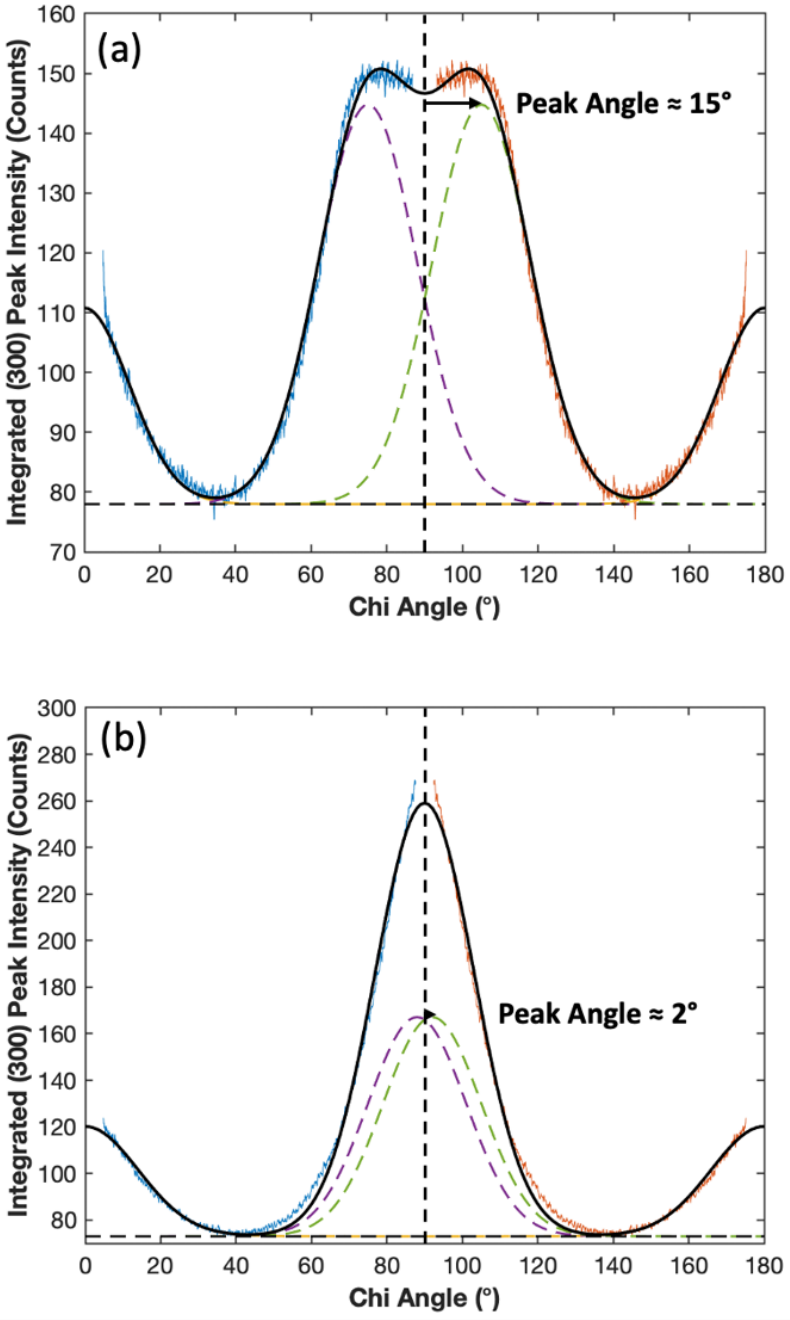

Figure S 11. Gaussian peak-fitting of the radially integrated (300) peak intensity for (a) undoped and (b) 0.05 mg/mL F_4TCNQ-doped face-on P3HT. Experimental data was mirrored over the in-plane axis (90°) to account for the intensity of the diffraction peak below the axis.

2-D Geometric Modeling of the Parallel GIWAXS Pattern

To model the diffraction peaks that will appear in the GIWAXS pattern of the parallel-aligned beam, a 2-D geometric lattice model was designed with variables assigned as shown below:

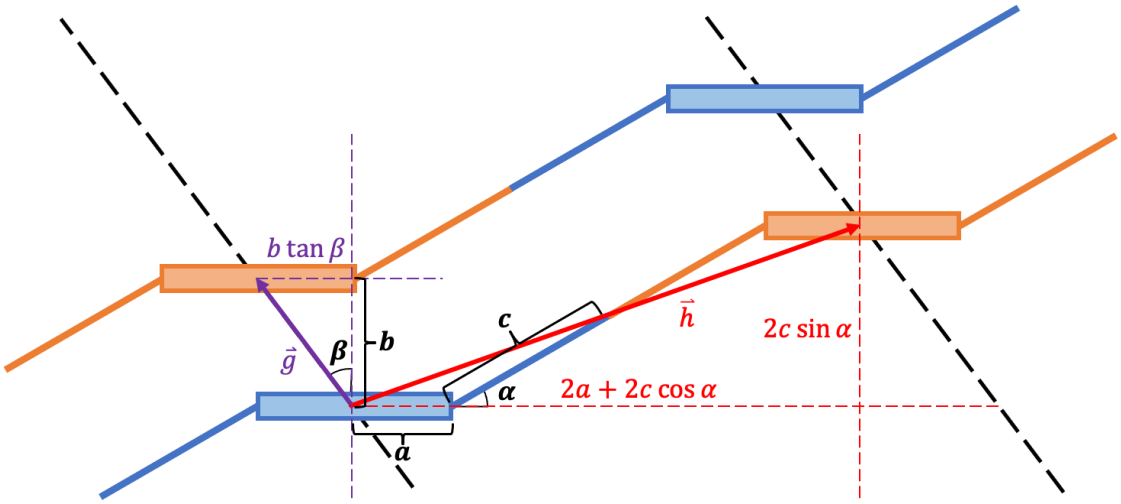

Figure S 12. Geometric variables used in the structural modeling of P3HT crystallites.

The following equations were used to correlate the 2-D lattice model with experimentally

$$d_{\pi,n}(a, b, c, \alpha, \beta) = \vec{g} \cdot \widehat{h_n}^{\perp} = \frac{b\left(2a + 2c(\sin\alpha \tan\beta + \cos\alpha)\right)}{\sqrt{(2a + 2c\cos\alpha - nb\tan\beta)^2 + (2c\sin\alpha + nb)^2}}$$

$$d_{lam}(a, b, c, \alpha, \beta) = \vec{h} \cdot \hat{g}^{\perp} = 2a\,cos\,\beta + 2c(cos\,\alpha\,cos\,\beta + sin\,\alpha\,sin\,\beta)$$

observable π and lamellar peak positions:

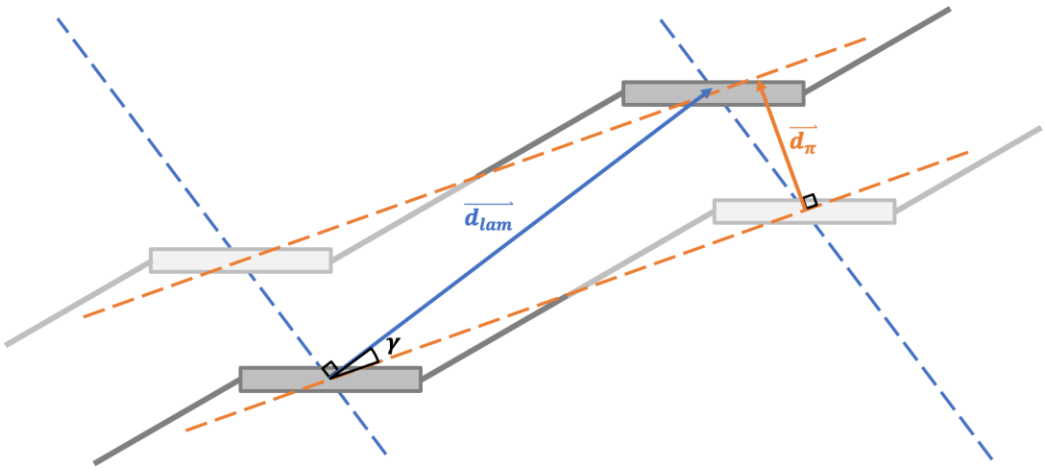

Figure S 13. Experimentally observable lamellar (d_{lam}) and π-stacking distances (d_{π}).

To solve the above equations, the following geometric values were input into a numerical solver:

Variable	Input Value	Source
$\boldsymbol{a}$	2.78 Å	Avogadro modeling estimate
$\boldsymbol{b}$	3.6 Å	Lebert et al., *ACS Omega* 2018, 3, 6, 6388-6394
$\boldsymbol{\alpha}$	55°	Kayunkid et al. *Macromolecules* 2010, 43, 11, 4961-4967

Table S 2. Geometric variable input values and sources.

The parameter n indexes up ($n > 0$) and down ($n < 0$) the π-stacks to produce different π-stack diffraction planes and was set to be $n = 0$. Geometric parameters for doped and undoped edge-on and face-on P3HT were calculated by inputting experimental peak positions d_{lam} and d_{π} along with additional relevant values into a numeric solver and entered into **Table S3**. For undoped edge-on P3HT, the literature angle $\alpha = 55°$ was assumed and used to solve for β and c, from which the lamellar angle γ (i.e., the off-axis angle of the lamellar diffraction peak in face-on-oriented crystallites) could be calculated according to the equation

$$\gamma = \left|\tan^{-1}\left(\frac{2c\sin\alpha + nb}{2a + 2c\cos\alpha - nb\tan\beta}\right) - \beta\right|$$

For undoped face-on P3HT, an experimental lamellar angle of $\gamma = 15°$ (**Figure S8a**) was used to solve for α, β and c. Values for doped face-on P3HT were similarly calculated by inputting an experimental lamellar angle of $\gamma = 2°$ (**Figure S8b**). Because a lamellar angle for edge-on P3HT is not easy to directly measure, values for doped edge-on P3HT were calculated assuming an identical side chain overlap c to doped face-on P3HT, then calculating for α, β and γ.

Variable	Crystallite Population			
	Edge-On	Edge-On Doped	Face-On	Face-On Doped
d_{lam}	16.03 Å†	17.62 Å†	16.64 Å†	18.01 Å†
d_{π}	3.77 Å†	3.64 Å†	3.77 Å†	3.63 Å†
a	2.74 Å‡	2.74 Å‡	2.74 Å‡	2.74 Å‡
b	3.6 Å*	3.6 Å*	3.6 Å*	3.6 Å*
c	**6.45 Å**	6.32 Å	**6.70 Å**	**6.32 Å**
α	55°*	**24°**	**53°**	**14°**
β	**23°**	**8°**	**23°**	**8°**
γ	**16°**	**8°**	15°†	2°†

†Experimental values *Literature values ‡Computational estimates

Table S 3. Summarized results of P3HT lattice 2-D geometric modeling.

APPENDIX C

Supplemental Information for Chapter 4

Materials:

Poly(3-hexylthiophene-2,5-diyl) (P3HT; regioregularity 97%) and F_4TCNQ (Purity > 99.0%) were purchased from Ossila. 1,2-dichlorobenzene (ODCB, anhydrous, 99%), *n*-butyl acetate (*n*-BA, anhydrous, $\geq$ 99%), and dichloromethane (DCM, anhydrous, 99.8%) were purchased from Sigma-Aldrich. No further purification was performed for the materials or solvents.

Film fabrication:

Glass substrates were cut into 1.3 × 1.3 cm shapes for the rectangular, 4-line with square contact pads and 4-line without square contact pads electrode geometries, and into 1.3 × 0.5 cm shapes for the Hall bar electrode geometry. The substrates were washed sequentially with Alconox detergent, DI water, and acetone, sequentially, before plasma etching for 15 minutes. After plasma etching, the substrates were transferred to a nitrogen glove box for spin coating. 2% (20 mg/mL) P3HT in ODCB was spin-coated onto the substrates at 1000 rpm for 60 seconds, followed by 4000 rpm for 10 seconds. The films were left in the nitrogen glovebox to dry overnight.

Rub-aligning Process and Doping:

The dried P3HT films were transferred via a vacuum transfer tank (i.e., under air-free conditions) from the nitrogen glove box to an argon glove box for rub-alignment. The samples were heated to 140 ^{o}C and the rub-aligning was done using a homemade setup comprised of a strain gauge load cell and a stepper motor controlled by an Arduino nano. A lab jack was used to precisely control the starting force applied before rub-aligning the polymer films. The starting downward force applied during the rub-aligning process was ~1.0 N, and the speed of the

microfiber wheel was 500 rpm. After rub-aligning, the films were vacuum transferred back to the nitrogen glove box for sequential doping.

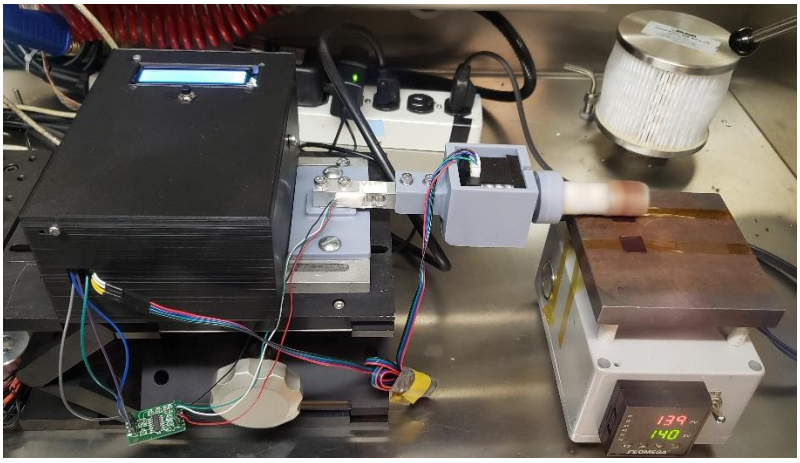

Figure S 14. Home-made rub-alignment setup inside an argon-filled glove box. The polymer films were pre-heated to 140 ^{o}C with a hotplate for ~2 minutes before being rub-aligned at constant force and spin speed of the microfiber wheel.

Different electrode geometry fabrication:

Doped samples were placed onto 3D-printed shadow masks with electrode patterns that were similar to **Figure 4.1** in the main text. For the rectangular geometry, the width and length of the samples were both 10 mm with square corner electrodes with dimensions 1 × 1 mm. The total length of the four-line electrode with square contact pads was 10 mm. The square pads measured 2.5 x 2.5 mm, while the channels measured 7.5 x 1 mm with a spacing of 2 mm. The four-line geometry without square pad electrode dimensions measured 10 x 1 mm with a 1.5-mm spacing. For the Hall bar geometry, the channel width and length (distance between the probe arms) were 3 mm and 4 mm, respectively. The width of the probe electrodes on the Hall bar geometry was 1 mm. After 45-nm-thick gold electrodes were deposited via thermal evaporation, a desktop CNC

was used to scratch patterns onto the films. The electrodes were deposited using an Angstrom Engineering Nexdep thermal evaporator at a pressure < 1×10^{-6} Torr at a rate of 0.5 Å/s.

Polarized UV-Vis Spectroscopy:

Polarized UV-Vis absorption spectra were measured using a Shimadzu UV3101PC Scanning Spectrophotometer. The slit width was set at 1 nm with a sampling interval of 1 nm. A small 3D-printed aperture was used to ensure that the UV-Vis beam was centered on the sample. For polarized measurements, a linear polymer film polarizer was used for wavelengths between 400-700 nm, and a Thorlabs linear nanoparticle polarizer was used for wavelengths between 550-1500 nm.

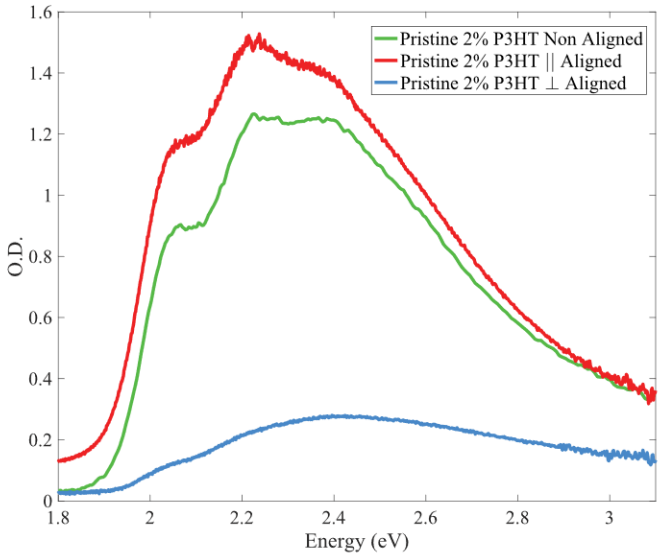

Figure S 15. Polarized UV-Vis of typical aligned (red and blue curves, parallel and perpendicular, respectively and non-aligned (green curve) pristine P3HT films. The dichroic ratio for the absorbance of the aligned film at 610 nm is ~10.

We note that the UV-Vis absorption spectrum does not reveal a significant increase in the 0-0/0-1 absorption ratio upon rub aligning, which might be expected based on the reduced energetic disorder and increased intrachain *J* coupling that rub-alignment provides. We attribute this lack of change in the vibronic structure to our use of a higher regioregularity P3HT polymer (97%) in this current study, which results in the formation of highly crystalline, nonaligned films. Other work that did show enhancement of the vibronic structure used lower regioregularity material (93%). Whether or not the vibronic structure is enhanced, however, does not have a direct impact on the conclusions drawn in this study regarding the use of different electrode geometries for measuring the anisotropic conductivity.

Grazing Incidence Wide-Angle X-ray Scattering (GIWAXS):

For GIWAXS, polymer films of the same concentration were spun onto 1.5 × 1.5 cm Si substrates with a <100> orientation. The substrates were cleaned sequentially in an Alconox/water solution, isopropanol, and acetone. GIWAXS measurements were performed at the Stanford Synchrotron Radiation Lightsource (SSRL) on BL 11-3 using a wavelength of 0.9742 Å at incidence angle of 0.12°. The IgorPro macro, Nika, was used to calibrate the GIWAXS 2-D data. Nika and WAXStools were used to reduce the data. For a 2-D diffractogram, full integrations of the diffraction data provide information on all periodic structures within the film, while integrations of a narrow wedge along the *y*-axis (q_z, blue color in **Fig. S16**) provide information about periodicity perpendicular to the plane of the substrate (out-of-plane, OOP), and integrations of a pie wedge oriented along the *x*-axis (q_{xy}, pink color in **Fig. S16**) provide information about in-plane (IP) periodicity.

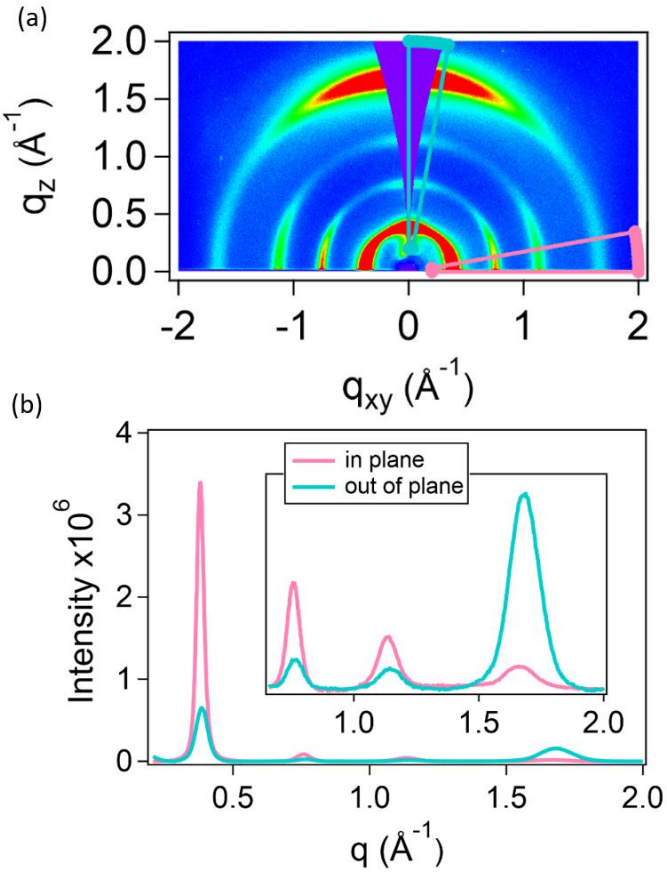

Figure S 16. (a) 2D and (b) integrated GIWAXS of neutral rub-aligned P3HT films. The inset in (b) shows an expanded version of the higher q region. The appearance of the lamellar and π-stacking spacing in both the in-plane and out-of-plane directions, but not at intermediate angles, indicates that the rub-aligned films contain both face-on and edge-on texturing. [1,2]

The GIWAXS 2-D and 1-D diffractograms in **Fig. S16** indicate that rub-aligned P3HT films contain both face-on and edge-on oriented components. **Figure S16a** indicates that the edge-on component has lamellar stacks (100 peak near 0.4 Å^{-1}) in the out-of-plane direction, while the face-on component shows the lamellar peak in the in-plane direction. Similarly, for the edge-on component, the π-stacks (020 peak near 1.7 Å^{-1}) appear in-plane, while for the face-on component,

the π-stacks appear out-of-plane. **Figure S16b** shows 1-D integrated GIWAXS traces, where the appearance of the lamellar and π-stacks in both the in-plane and out-of-plane directions indicates that the rub-aligned film contains both face-on and edge-on texturing, as discussed in the main text.

Conductivity and Hall Effect Measurements:

Conductivity and Hall effect measurement was performed using Lakeshore's MeasureReady M91 FastHall. All reported measurements were measured using 10 μA for source current unless specified. For the Hall effect measurements, we used the DC hall method with a magnetic field of 1.0623 Tesla.

Source Current /μA	**Conventional Rectangular Non-Aligned** (S/cm)	**Conventional Hall Bar Non-Aligned** (S/cm)	**Anion-Exchange Rectangular Non-Aligned** (S/cm)	**Anion-Exchange Hall Bar Non-Aligned** (S/cm)
10	4.66 $\pm$ 0.30	4.25 $\pm$ 1.18	12.36 $\pm$ 0.19	11.07 $\pm$ 0.36

Table S 4. Conductivity of non-aligned doped P3HT films obtained using different electrode geometries.

Before measuring the Conductivity and Hall effect for the samples above, we first thermally evaporated gold contact electrodes onto the doped-polymer films using shadow masks based on the patterns shown in **Figure 4.1** of the main text. Gold was used to avoid unwanted chemical reactions with the sample such as complexing or dedoping; we found that the use of Ag electrodes led to significant dedoping and thus higher sheet resistances.

Since both the Hall bar and modified Montgomery methods require knowledge of the sample dimensions, it was necessary to verify that our electrodes did not spread beyond the pattern on the shadow masks. To do this, we used non-aligned doped P3HT films (3 mg/mL F_4TCNQ in *n*-butyl acetate) and the standard Van der Pauw method to calibrate the Hall bar and modified Montgomery methods. The conductivities obtained for non-aligned doped P3HT films for these three methods agree well are within the error (**Table S4** verifying that our evaporated electrode patterns indeed conform to the designed dimensions).

Conventional in DCM	**Hall Non-Aligned 2% - 97% RR**	**Rectangular Non-Aligned 2% - 97% RR**	**Rectangular Non-Aligned 2% - 93% RR (Ref 7)**
Conductivity (S/cm)	8.62 $\pm$ 0.62	8.00 $\pm$ 0.64	5.7
$Hall\ Carrier\ Density\ (cm^{-3})$	$6.06 \times 10^{20} \pm 4.73 \times 10^{18}$	$6.33 \times 10^{20} \pm 4.2 \times 10^{19}$	7.1×10^{20}
Mobility $(cm^2/V \cdot s)$	0.09 $\pm$ 0.006	0.08 $\pm$ 0.0008	0.05

Table S 5. Comparison between DC hall and AC hall for non-aligned 2% P3HT films doped with 1 mg/mL F_4TCNQ.

Doped semiconducting polymers are low-mobility materials. DC Hall effect measurements for samples with mobilities below 1 $cm^2V^{-1}s^{-1}$ are often challenging to obtain due to the low intrinsic Hall voltage and the fact that there can be large offset or thermoelectric voltages that can be comparable in magnitude or larger than the Hall voltage. [3,4,5] To mitigate this issue, we performed our measurements using both current and field reversal. Our use of current reversal helped remove any contributions from thermoelectric voltages, while employing field reversal

removed any offset voltages due to electrode misalignment. To verify that our DC Hall measurements were accurate, we replicated the samples made in Ref. 7, whose carrier density was determined by AC Hall effect measurements, and obtained similar carrier densities and mobilities as reported Ref. 7. The slightly higher mobilities and conductivities we obtained are likely due to our use of 97% regioregular P3HT, which produced samples with slightly higher crystallinity than those based on P3HT with 93% regioregularity studied in Ref. 7 (**Table S2**). [6,7] This gave us confidence that we can successfully use DC Hall measurement to determine the anisotropic carrier mobility in doped rub-aligned P3HT films that have carrier mobilities of ~0.1 $cm^2V^{-1}s^{-1}$.

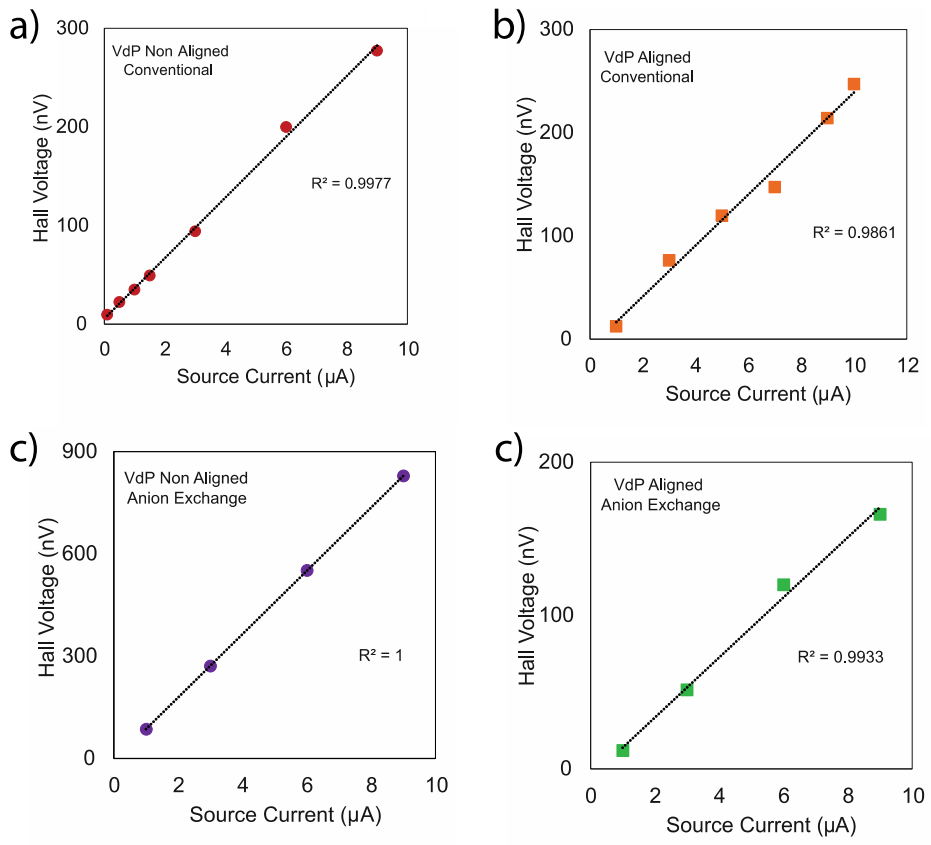

Figure S 17. Hall voltage measured as a function of source current for the DC Hall measurements for the rectangular geometry on both conventionally- and anion-exchange-doped aligned and non-aligned P3HT films.

The Hall voltage should linearly increase with the source current, as described by $V_H = \frac{R_H I B}{d}$, where R_H is the Hall coefficient, I is the source current, B is the applied magnetic field and d is the sample's thickness. Although we cannot vary the strength of the magnetic field with our Hall measurement set-up, we did test the dependence of the Hall voltage on the source current, as shown in **Figure S17**. The fact that we see a linear relationship indicates that our DC Hall

instrument can accurately measure the sheet carrier density and mobility in our doped P3HT samples.

Correction factor for 4-line geometry:

Conventional Non-Aligned	**Sheet Resistance** ($\boldsymbol{k\Omega/\square}$)	**Conductivity** ($\boldsymbol{S/cm}$)	**Correction Factor** $\boldsymbol{C}$
Four-Point	14.5	4.59	1.4
Four-line with square pads (Brinkmann and Coworkers; Fig. 4.1c)	10.0	6.65	

Table S 6. Conductivity comparison between the classic four-point probe method and the four-line with square contact pads geometry on non-aligned P3HT films doped with 1 mg/mL F4TCNQ.

To obtain the geometric correction factor for the four-line geometry using the standard four-point-probe formalism (Eq. 6 of the main text), we prepared two non-aligned reference samples. Both samples were fabricated from a 2% P3HT (97% regioregularity) solution in ODCB doped sequentially with 1 mg/mL F4TCNQ in acetonitrile. The four-line sheet resistance obtained using the four-point probe equation is ~40% lower than that obtained using the correct four-point geometry. The ratio between the two methods gives the correction factor C used in the main text.

Conventional Non-Aligned	**Sheet Resistance** $(k\Omega/\square)$	**Conductivity** (S/cm)	**Correction Factor** C
Four-line (without square contacts; Fig. 4.1d)	10.1	6.60	1.4
Four-line (without square contacts and confined; Fig 4.1e)	13.6	4.90	1.1

Table S 7. Conductivities and correction factors for non-aligned P3HT films doped with 1 mg/mL F4TCNQ for two modified version of the four-line geometry. For the first modified geometry, the alternating square contacts were removed. The same sample were then used to make the second geometry by removing the polymer around the electrodes.

Profilometry:

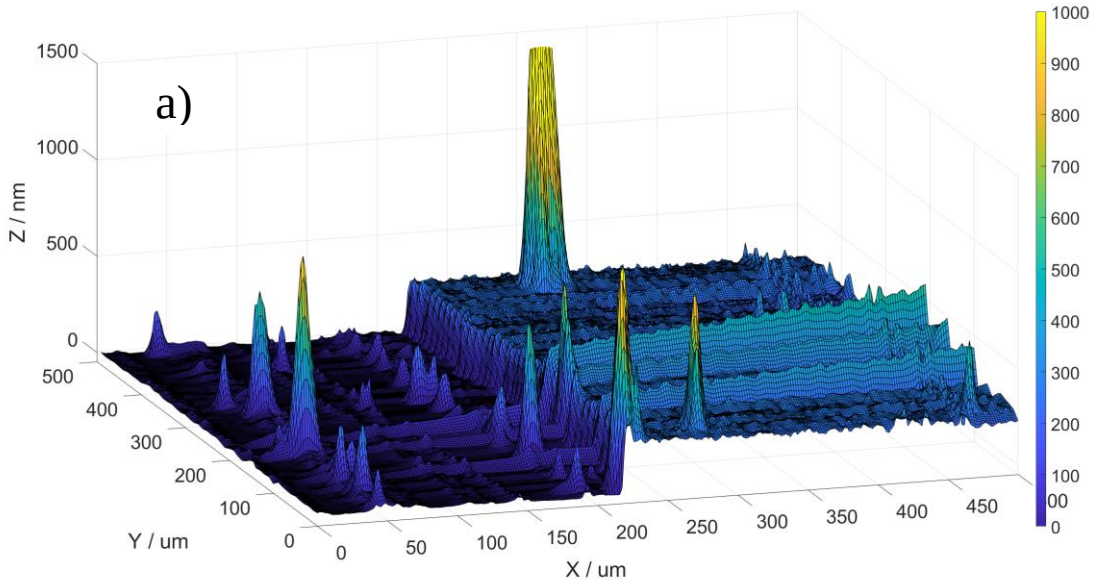

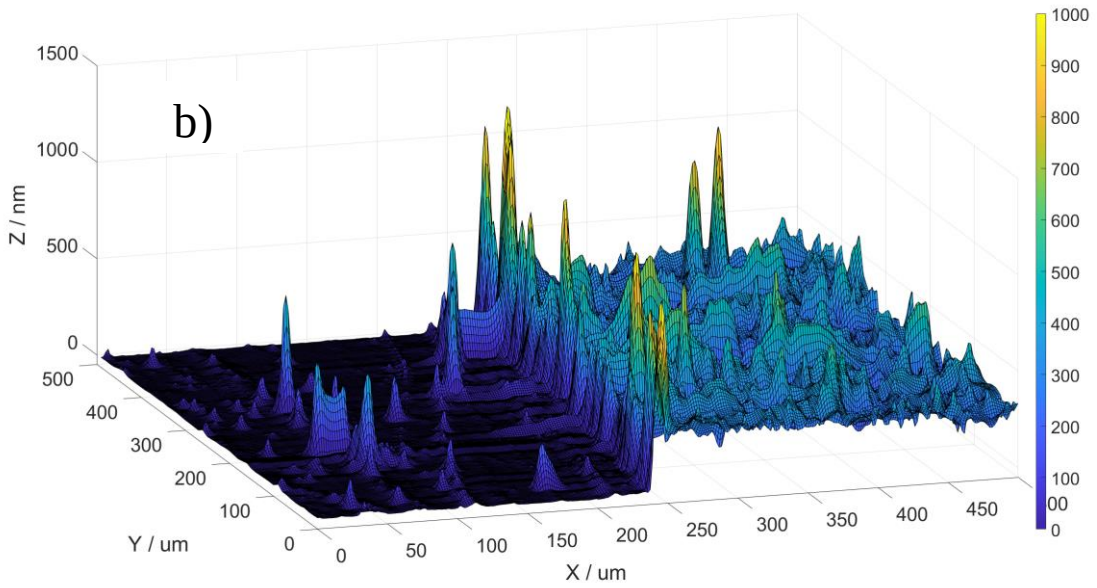
b)
Z / nm
1500
1000
500
0
Y / um
500
400
300
200
100
0
X / um
0
50
100
150
200
250
300
350
400
450
1000
900
800
700
600
500
400
300
200
100
00
0

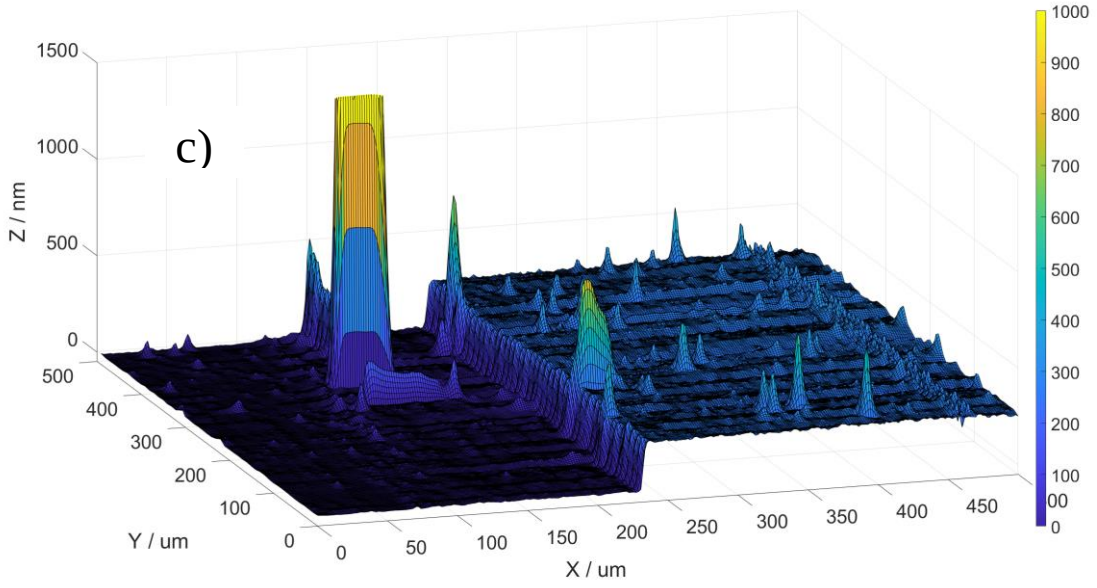
c)
Z / nm
1500
1000
500
0
Y / um
500
400
300
200
100
0
X / um
0
50
100
150
200
250
300
350
400
450
1000
900
800
700
600
500
400
300
200
100
00
0

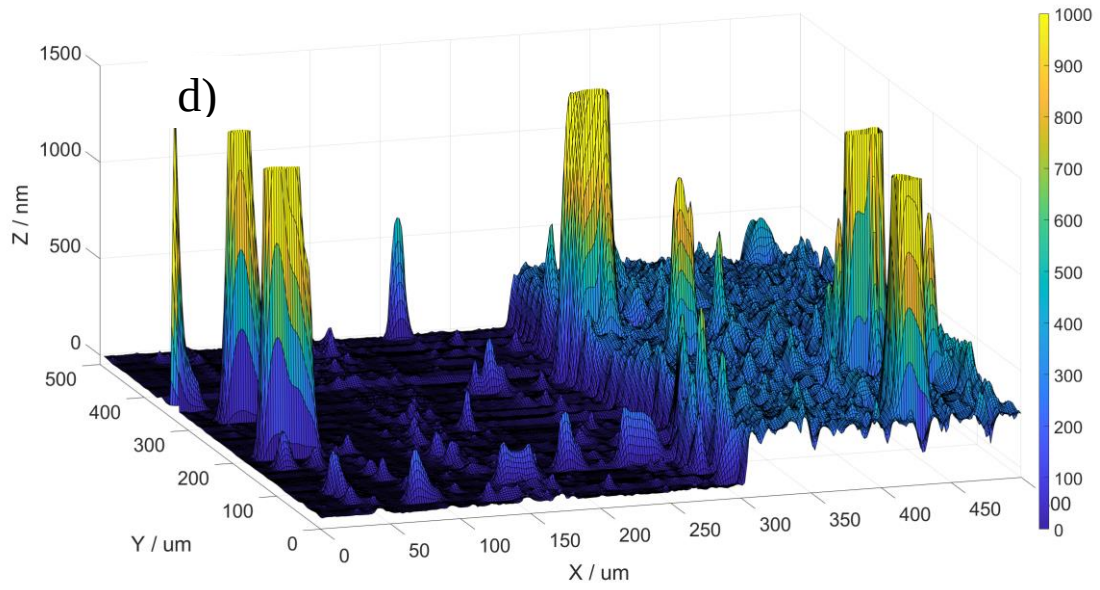

Figure S 18. Profilometry profiles for conventionally-doped non-aligned (panel a) and rub-aligned (panel b) P3HT films. Similar profiles for anion-exchanged-doped non-aligned (panel c) and rub-aligned (panel d) P3HT films are also shown. See Table S6 for details on the profilometric scan parameters.

$$S_a = \frac{1}{RC}\sum_{j=1}^{R}\sum_{i=1}^{C}|Z(x,y)| \qquad \text{(S1)}$$

	Thickness (nm)	Surface Roughness (nm)
Conventional Non-Aligned	262 ± 22	13.2
Conventional Aligned	288 ± 51	55.8
Anion-Exchange Non-Aligned	278 ± 14	11.6
Anion-Exchange Aligned	310 ± 32	52.7

Table S 8. Average film thickness and surface roughness (Eq. S1) extracted from the 3-D profilometry profiles in **Figure S18**.

Profilometer Parameters	
Profilometer Tip Size	12.5 μm
Area Scanned	500 x 500 μm^2
Y Resolution	10 μm
X Resolution	0.167 μm
Tip Force	1 mg
Scan Rate	500 μm / 10 s

Table S 9. Profilometer parameters used to obtain the 3-D maps of the aligned and non-aligned anion-exchanged and conventionally-doped P3HT films shown in Fig. S18.

Figure S18 shows the step 3-D surface profile of aligned and non-aligned P3HT films doped using the conventional and anion-exchange methods. The steps in the profiles were created by physically removing the polymer films to expose the glass substrate to serve as a reference plane. Notably, the aligned P3HT films exhibit significantly rougher surfaces (roughly four times) compared to their non-aligned counterparts. The surface roughness (Eq. S1) as well as the average thickness of the different films are given in **Table S8**.

We noted in the main text that the average thickness of the aligned films, determined by scanning across the entire area, is higher than that of the non-aligned films from which they were created. When a microfiber polishing wheel is moved across the surface of a P3HT film, it can displace polymer material to the sides, creating protrusions that are thicker than the initial film thickness. The corresponding trenches formed should be shallower than the initial film thickness, so that the average thickness is comparable to or slightly thinner than the original film (due to the fact that rub-aligning can remove a small amount of polymer material). The lateral size of the trenches, however, is comparable to the profilometer tip diameter, so that we cannot accurately

measure the depth at the bottom of the valleys, resulting in an overestimation of the film thickness and thus an underestimation of the electrical conductivity.

In addition to the potential underestimation of the conductivity, the formation of trenches along the rubbing direction also can influence the measured anisotropy of the conductivity. In the parallel direction, where the peaks and valleys are parallel to one another, the current will follow the lowest-resistance path through the peaks or thicker regions, avoiding the troughs and thus possibly experiencing a higher effective thickness. Conversely, in the direction perpendicular to the rubbing, the current is forced to go through both peaks and valleys, potentially experience a lower effective thickness and thus higher resistance. This issue, which is inherent to rub-aligned polymer films because of their surface roughness, does not depend on the chosen electrode geometry, and thus does not affect the conclusions of the paper, which is that the rectangular and Hall bar electrode geometries produce consistent anisotropic conductivities, while the 4-line geometry does not.

Temperature-Dependent Conductivity Measurements:

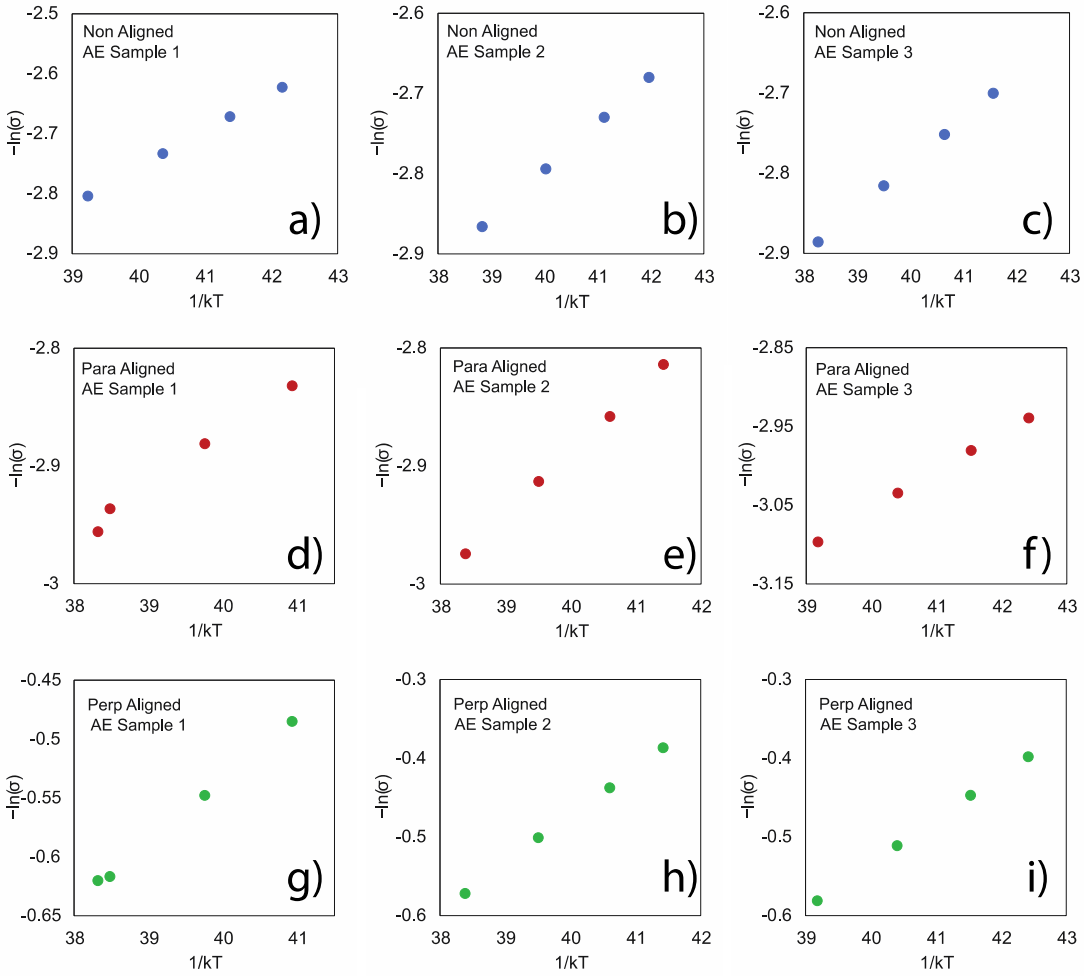

Figure S 19. Temperature-dependent conductivity measurements for non-aligned anion-exchange (AE)-doped P3HT samples (panels a-c) and rub-aligned anion-exchange (AE)-doped P3HT samples in the directions parallel (panels d-f) and perpendicular (panels g-i) to the rub direction. The conductivities for all samples were measured using the rectangular van der Pauw four-point probe geometry. The activation energies, Ea, reported in **Table S10**, were calculated by fitting the temperature-dependent conductivity values to an Arrhenius equation.

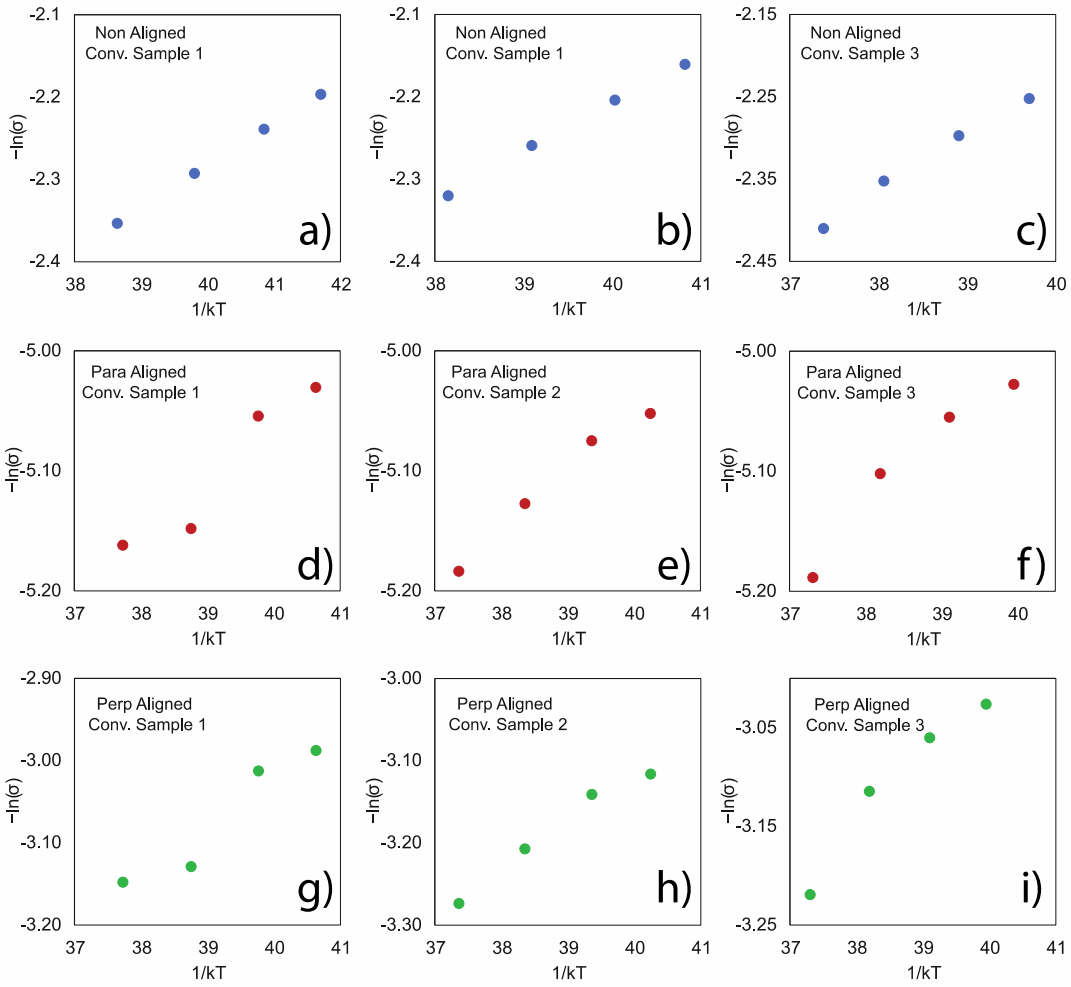

Figure S 20. Temperature-dependent conductivity measurements for non-aligned conventionally (Conv)-doped P3HT samples (panels a-c) and rub-aligned anion-exchange (AE)-doped P3HT samples in the directions parallel (panels d-f) and perpendicular (panels g-i) to the rub direction. The conductivities for all samples were measured using the rectangular van der Pauw four-point probe geometry. The activation energies, Ea, reported in **Table S10**, were calculated by fitting the temperature-dependent conductivity values to an Arrhenius equation.

	Parallel	Perpendicular	Non-Aligned
AE-doped Activation Energy (meV)	48.70 ± 3.98	56.98 ± 3.80	59.19 ± 2.56
Conv-doped Activation Energy (meV)	48.25 ± 8.31	58.14 ± 9.90	57.9 ± 6.93

Table S 10. Conductivity activation barriers, averaged over 3 independent samples, for conventionally (Conv) and anion-exchanged (AE)-doped P3HT films, with the conductivities measured using the rectangular geometry. The values were extracted via fitting to an Arrhenius equation of the form: $\sigma = \sigma 0 \exp[-Ea/kBT]$.

The activation barriers for carrier transport in our doped P3HT samples were explored using temperature-dependent conductivity (here measured using the rectangular electrode geometry), as shown in **Figs. S19** and **S20**. The barrier heights were extracted by fitting to an Arrhenius equation, with the results given in **Table S10**. Due to the intrinsic disorder in doped semiconducting polymer films, the charge transport characteristics are usually a combination of both hopping-like and band-like transport. The activation energy, E_a, provides a measure of the relative amount of hopping-like transport due to energetic disorder. [8] The data in **Table S10** show that the rub-aligned doped P3HT films have a reduced activation barrier for transport in the direction parallel to the rub-alignment compared to non-aligned films or to transport in the rub-aligned films in the perpendicular direction. This implies that rub-alignment leads to reduced energetic disorder and increased carrier delocalization in the parallel direction, resulting in a greater degree of band-like carrier transport. Indeed, the barrier was highest for transport in the

rub-aligned films perpendicular to the rubbing direction, indicating increased disorder due to transport through amorphous regions and thus a larger contribution from hopping-like transport compared to non-aligned films.

APPENDIX D

Supplemental Information for Chapter 5

Grazing-Incidence Small-Angle X-ray Scattering (GISAXS)

Figure S21 shows the horizontal integrations of the 2D GISAXS near Yoneda band for the various concentrations of the dopants presented in our electrical measurements. An additional concentration of DDB-F72 (0.01 mM) is reported in the GISAXS data, however, the doping level was very low to measure any electrical properties in the films. The 1D integrations for the P3HT doped with DDB-F72 shows a significant change in the intensity resulting in a shoulder, near mid-q_y region, compared to pristine P3HT. Similarly, P3HT doped using DDB-F36 observes noticeable changes in the intensity near the mid-q_y region as well, specially at the 0.3 mM concentration.

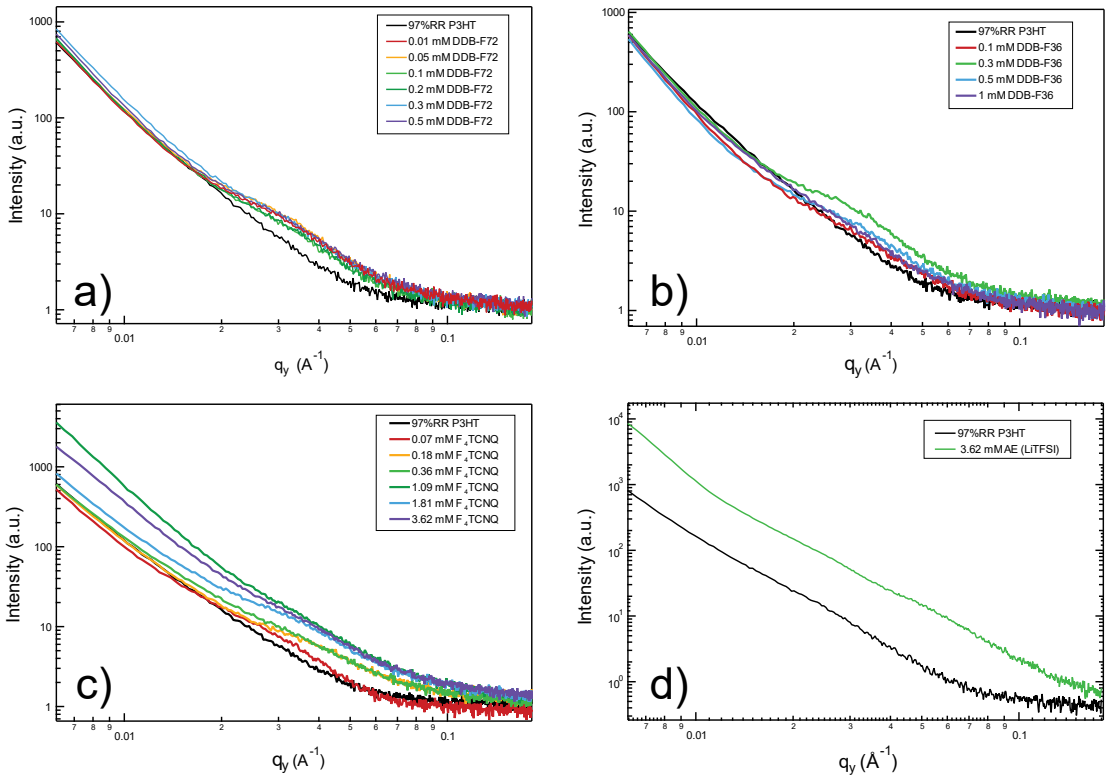

Figure S 21. Horizontal 1D integrations of GISAXS data for all concentrations of doped P3HT a) DDB-F72, b) DDB-F36, c) F_4TCNQ, and d) anion exchange (Only the highest F4TCNQ concentration is shown, as 104.5 mM LiTFSI was added to 3.62 mM F_4TCNQ). Pristine P3HT is also plotted in all figures for reference.

To be able to extract the domain sizes from GISAXS data of our doped P3HT films, we carried out fits for the 1D integrated GISAXS traces using the Unified Fit method[9,10] which has been shown to be an accurate fitting model for weakly correlated films with diffused, non-specular scattering.[9,11] For a system with multilevel structures, the total scattering can be expressed as:

$$I(q) = \sum_{i=1}^{n} [\, G_i \, exp\left(\frac{-q^2 R_{g,i}^2}{3}\right) + B_i (q_i^*)^{-P_i} \, exp\left(\frac{-q^2 R_{g,i-1}^2}{3}\right) \qquad \text{(S4)}$$

where $q_i^* = q[\text{erf}\,(\frac{kqR_{g,i}}{\sqrt{6}})]^{-3}$. For a level *i*, the first term gives the Guinier regime with a prefactor, G_i and a characteristic size given by $R_{g,i}$. The second term represents the power-law regime with prefactor B_i, and structure P_i.[10]

Other than the anion-exchange samples which exhibit two distinct shoulders, we only observed one characteristic shoulder in 1D GISAXS traces for other doped cases. Level 1 Unified Fit is utilized to capture the characteristic Guinier size while G_2 of level 2 is set to an arbitrarily large value so that only P_2 shows up in the observable q range and compensates for the scattering intensity from even larger particles. **Figure S2** has the GISAXS fits of pristine P3HT and P3HT doped with the highest concentration for each dopant, DDB-F72, DDB-F36, F_4TCNQ, and anion exchange.

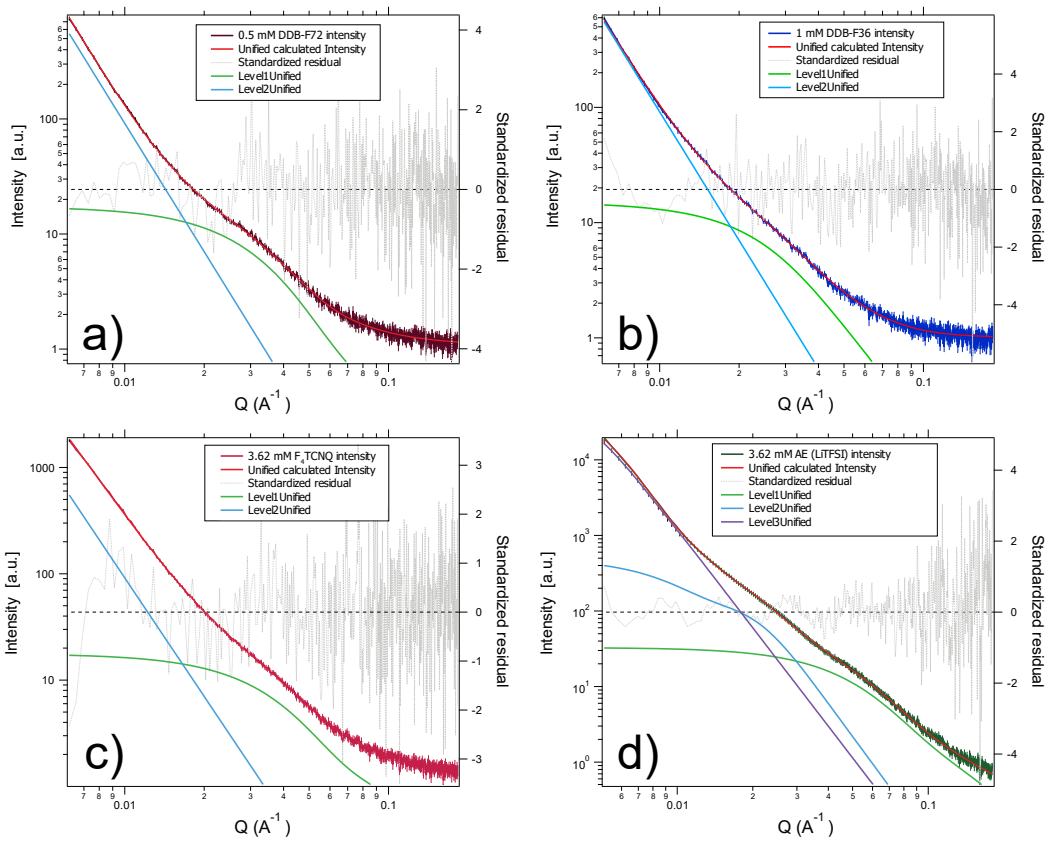

Figure S 22. Unified Fit Modeling of doped P3HT using a) 0.5 mM DDB-F72, b) 1 mM DDB-F36, c) 3.62 mM F_4TCNQ and d) 3.62 mM F_4TCNQ with anion exchanged by 104.5 mM LiTFSI.

Electrical Conductivity Measurements

Multifunctional devices for conductivity, Hall effect and NIR-UV-Vis spec are fabricated on 1.1 × 1.1 cm pre-cleaned substrates via sequential process (SqP). Gold contact electrodes were evaporated on the corners of the samples. The Van der Pauw method was used to measure the conductivity reported in the main text. The conductivity of the doped samples was measured using the Lakeshore MeasureReady M91 FastHall instrument, with a source current of 10 µA. Given the high hygroscopicity of the anion exchange samples, the sample compartment of the MeasureReady

M91 FastHall was Argon purged for 4 minutes before each measurement of the anion exchange samples. In contrast, the doped samples with F_4TCNQ, DDB-F72, and DDB-F36 showed no significant humidity dependence thus purging was not necessary. All reported values were measured and averaged over at least triplicates. All DC Hall effect, conductivity, temperature-dependent conductivity and NIR-UV-Vis spec were measured in the same device.

Figure S23 displays the electrical conductivity as a function of dopant concentration for DDB-F72, DDB-F36, F_4TCNQ, and anion exchange samples. To facilitate comparison of charge transport characteristics across these doped systems, we aimed to maintain similar conductivity ranges (0 – 18 S/cm). In the case of P3HT doped using DDB-F72, the dopant concentrations that gave conductivity values in this range were 0.05, 0.1, 0.2, 0.3 and 0.5 mM in DCM as the solvent. For P3HT doped with DDB-F36, we were able to obtain the conductivity values in this range using 0.1, 0.3, 0.5 and 1 mM in DCM as the dopant concentrations. Furthermore, F_4TCNQ-doped P3HT gave conductivity values within this range at F_4TCNQ concentrations 0.07, 0.18, 0.36, 1.09, 1.81 and 3.62 mM in DCM. Lastly, the conductivities of doped P3HT using the anion exchange doping solutions were obtained at final concentrations of 0.11, 0.18, 0.36, 1.81 and 3.62 mM F_4TCNQ plus 104.5 mM LiTFSI in nBA as the solvent.

As shown in **Figure S21**, all dopants led to an increase in electrical conductivity with higher doping levels, consistent with the expected relationship:

$$\sigma = en\mu \tag{S1}$$

where σ is the conductivity, e is the elementary charge, n is the carrier density and μ is the carrier mobility. Interestingly, all dopants, except DDB-F72, observed a rapid increase in their conductivity in the low doping regime presented in **Figure S21**.

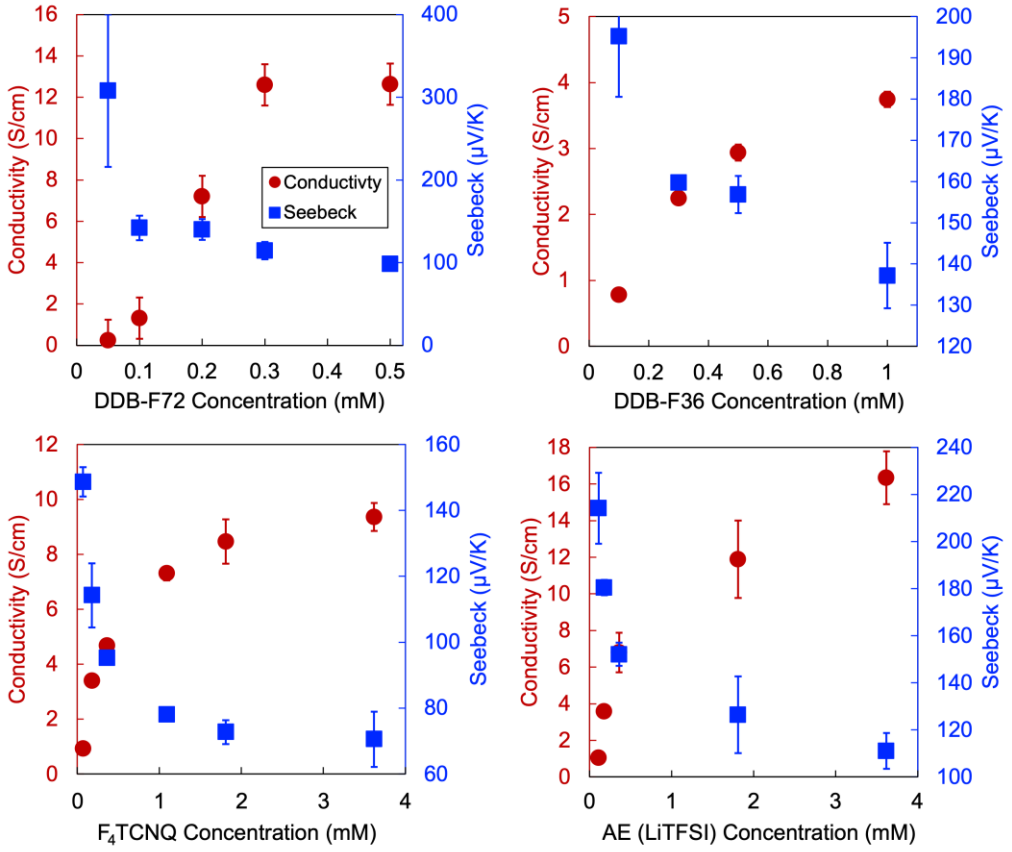

Figure S 23. Electrical conductivity and Seebeck coefficient plotted as a function of dopant concentration for the four dopants used in this study. All doping cases demonstrate an inverse relationship between conductivity and Seebeck coefficient: higher doping levels increase conductivity while decreasing the Seebeck coefficient. For anion exchange (AE) samples, the concentrations are reported based on the amount of F_4TCNQ added, with 104.5 mM LiTFSI not shown in the axis.

Seebeck Coefficient Measurements

The Seebeck coefficient measurements were conducted on separate pre-cleaned substrates with dimensions of 1.2 × 1.2 cm, using the SqP process. Gold contact electrodes, 1 × 10 nm in size, were evaporated onto the doped samples. Due to differences in electrode geometry, it was not possible to measure both electrical conductivity and the Seebeck coefficient on the same device. Therefore, for each doping level, separate devices were prepared for measuring the Seebeck coefficient and electrical conductivity. These devices were fabricated and measured in parallel to ensure that they were fabricated and tested under the same environmental conditions. The Seebeck coefficient measured at the same doping concentrations for each dopant as those described in the conductivity section are shown in **Figure S23**.

The Seebeck coefficient can be obtained from the slope of a linear fitting of the induced voltage due to a temperature gradient (ΔV) and the temperature difference between the hot side and the cold side ($\Delta T = T_{hot} - T_{cold}$). The Seebeck relation is given by equation S2:

$$S = \frac{\Delta V}{\Delta T} \tag{S2}$$

Figure S24 shows the linear fits for the voltages measured versus the temperature difference measured for P3HT doped with DDB-F72, DDB-F36, F_4TCNQ and anion exchange at the various doping concentrations. We use the slopes of these fits to calculate the Seebeck coefficient values presented in this study. We noted the linear fit of ΔV vs ΔT for the 0.32 mM F_4TCNQ is not included in **Figure S24** since it gave a small magnitude compared to the rest linear

fits. However, the relationship gave a straight line with R square value of 0.99 confirming the success of the measurement.

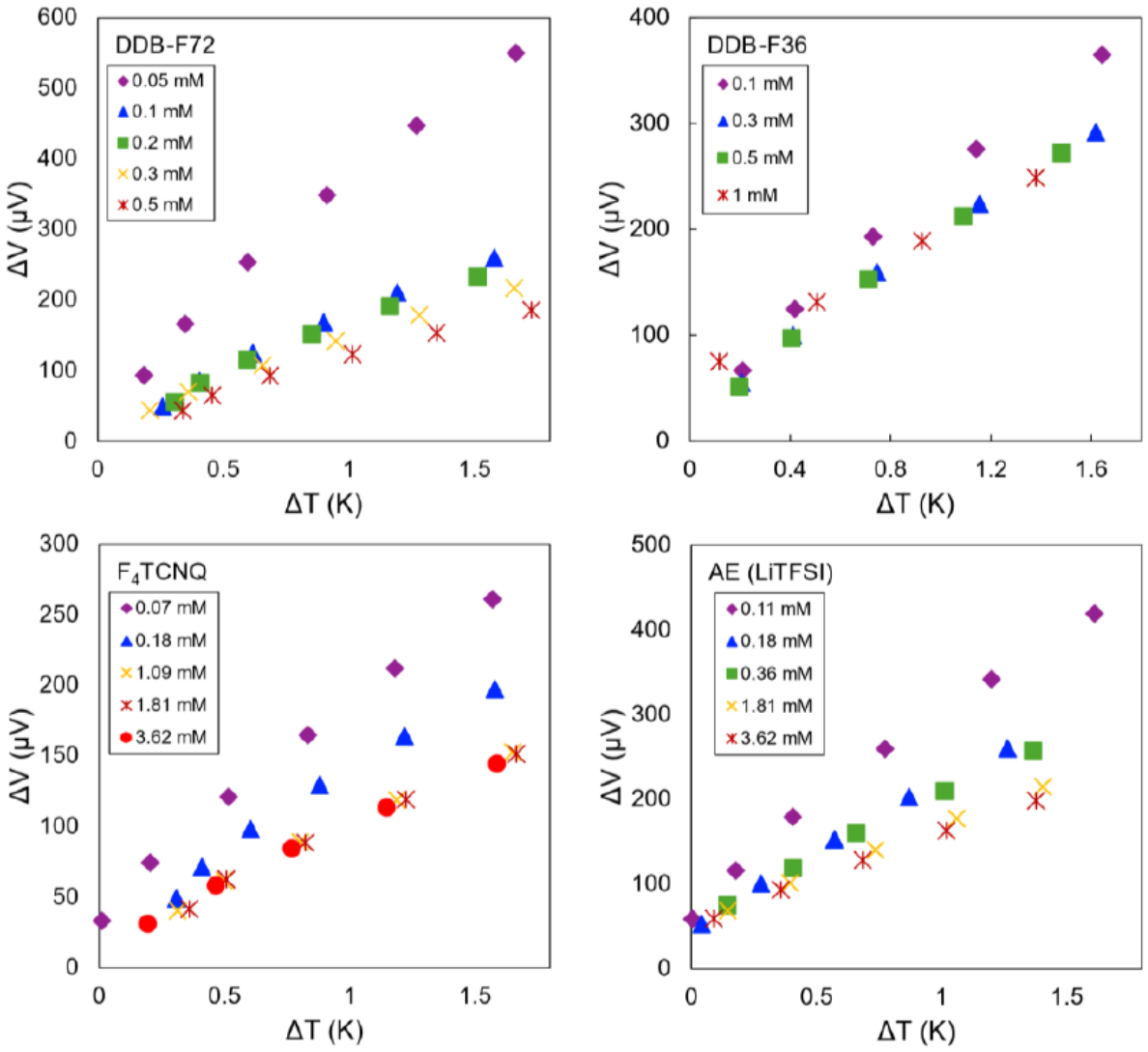

Figure S 24. Linear fits of the measured thermal voltages versus the temperature difference between both ends of the Seebeck setup plotted against one another for all concentrations of DDB-F72, DDB-F36, F_4TCNQ, and anion exchange. The slope of the ΔV vs ΔT plots gives us the Seebeck coefficient.

Hall Effect Measurements

Hall effect measurements are carried out on the multifunctional device mentioned in the electrical conductivity section. Hall values reported were taken and averaged over at least three samples. The Hall effect results are plotted for P3HT doped with DDB-F72, DDB-F36, F_4TCNQ and anion exchange in **Figure S25**. Due to the low doping level observed in the 0.07mM F_4TCNQ doped sample, we were unable to obtain a reliable Hall carrier density and mobility values. Thus, we have omitted this point from the Hall analysis.

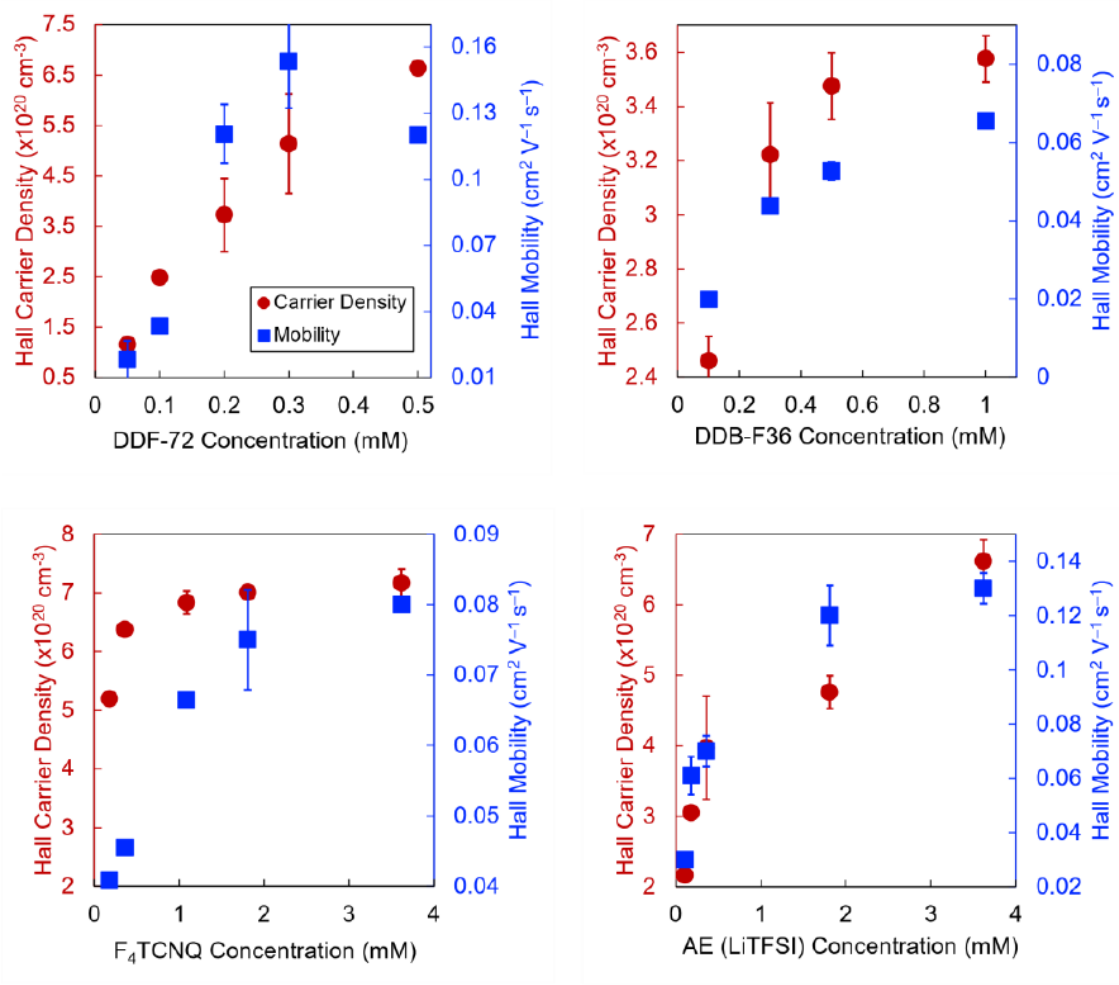

Figure S 25. DC Hall effect Results. Hall carrier density and mobilities for P3HT doped with DDB-F72, DDB-F36, F_4TCNQ, and anion exchange (AE) as a function of dopant concentration.

The Hall Effect measurement is a versatile method of obtaining parameters describing the charge transport, such as carrier mobility, carrier density and Hall coefficient, of doped semiconducting polymer films. However, the effect is primarily useful in high-mobility systems where screening effects are minimized. In specific to our case, Hall effect measurements for samples with low mobilities (≤ 1 cm^2 V^{-1} s^{-1}), such as doped semiconducting polymers, are often

challenging to obtain due to the low intrinsic Hall voltage and the large offset or thermoelectric voltages in the measurement. [12–14] Thus, to minimize these screening effects we use current and field reversal in our DC Hall measurements. Our prior studies have shown in our prior studies that this technique gives similar results as those obtained using AC Hall. [15,16]

Aubry and colleagues previously reported AC Hall mobilities for doped P3HT using DDB-F72, DDB-F36, and F_4TCNQ that are comparable to those observed in this study.[15] It is important to note that the small differences between the AC Hall mobilities reported by Aubry and those in this study are likely due to the higher regioregularity of the P3HT used here.

To further support our DC Hall effect measurements, we compare the frequency-weighted integrated NIR-UV-Vis P1 peak area, from **Figure 2** in the main text, with the Hall carrier density of F_4TCNQ and anion exchange samples. Plotting the integrated P1 peak area for the various concentrations of F_4TCNQ and anion exchange, shown in **Figure S26**, give a linear relationship giving us confidence the DC Hall is providing us with carrier density values that are relatively accurate.

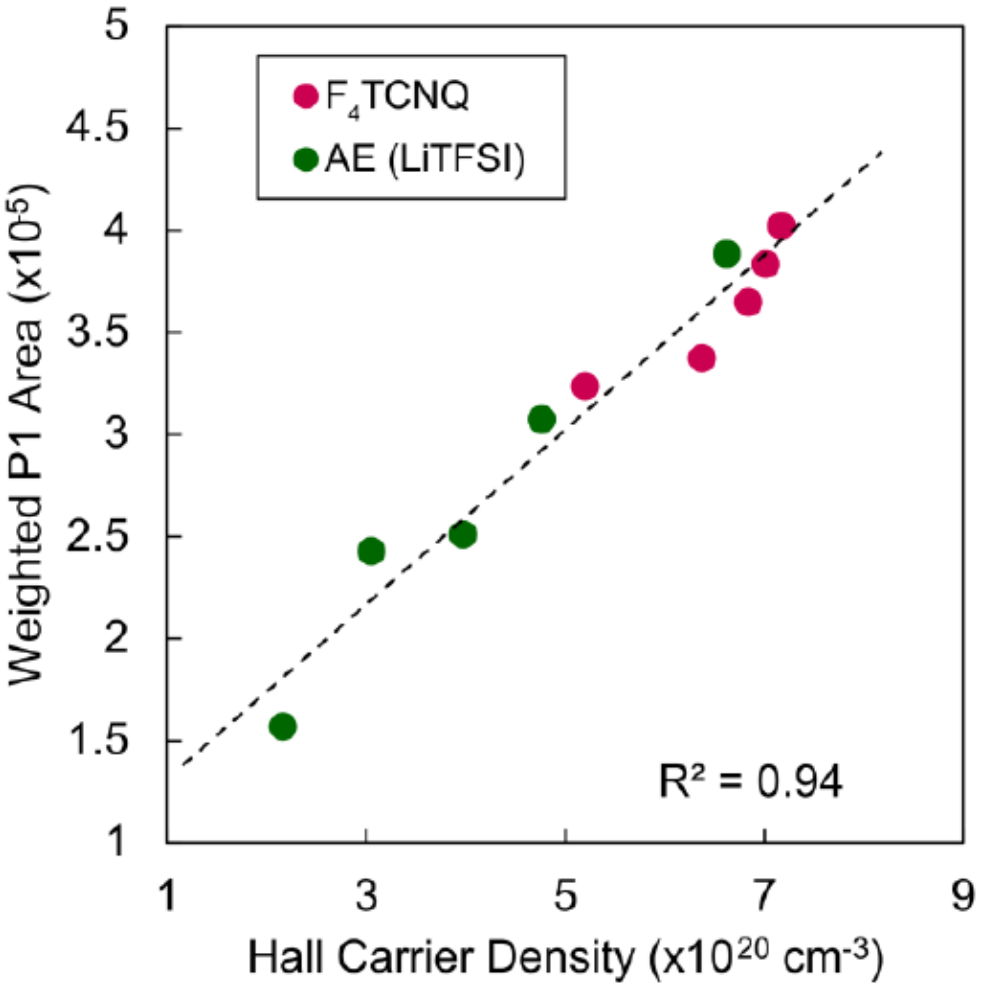

Figure S 26. frequency-weighted P1 area plotted vs Hall carrier density for F_4TCNQ and anion exchange devices show a linear relation.

Furthermore, an additional piece of circumstantial data is Gregory and coworkers reported the carrier densities measured using XPS in their SLoT study[17] were comparable to those measured in Hall effect.[18–20]

Temperature-Dependent Conductivity Measurements

We make use of temperature-dependent conductivity to investigate the activation barriers in the doped P3HT samples. The activation barriers were extracted from a linear fit of the Arrhenius equation $\sigma(T) = \sigma_0 \exp(-E_a / K_B T)$ where σ_0 is the temperature independent pre-exponential factor and E_a is the thermal activation energy of the carriers. Due to the mix transport in doped semiconducting polymer films, hopping and band-like, E_a can provide us with information about the relative amount of hopping-like transport due to energetic disorder in the doped polymer films.[15,17,21–24]

Figure S7 shows the linear fits of $-\ln(\sigma)$ vs $K_B T$ for P3HT doped with DDB-F72, DDB-F36, F_4TCNQ, and anion exchange. All temperature-dependent conductivities were measured on the same multifunctional device described in the conductivity section above. All fits produced a linear relation between $-\ln(\sigma)$ and T^{-1}, with R-square values of 0.98 and up, confirming the success of the measurements.

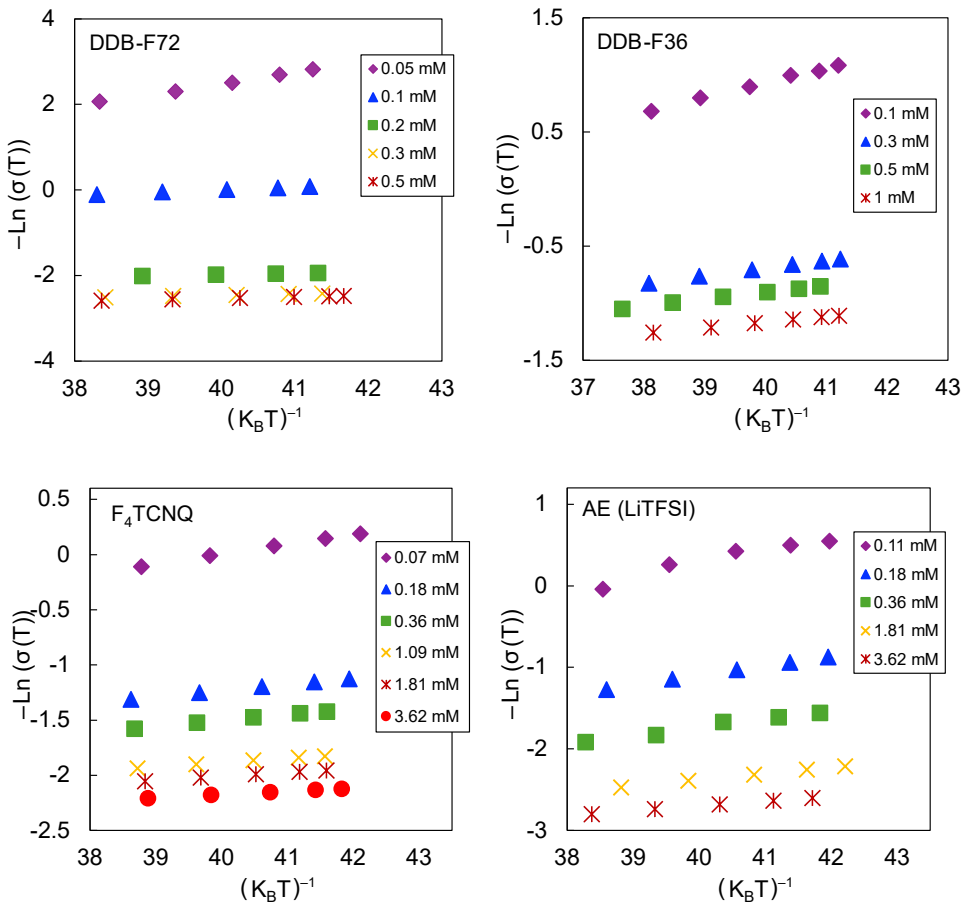

Figure S 27. Conductivity at various temperatures for P3HT doped with DDB-F72, DDB-F36, F_4TCNQ, and anion exchange (AE) at various doping concentrations. $-\ln(\sigma)$ vs $(K_BT)^{-1}$ plots have a linear relationship as expected by the Arrhenius equation $\sigma(T) = \sigma_0 \exp(-E_a / K_BT)$.

Semi-Localized Transport (SLoT) Model

The Semi-Localized Transport (SLoT) model is implemented in our study to quantify the charge transport characteristics of doped P3HT using DDB-F72, DBB-F36, F_4TCNQ and anion exchange. Five key parameters extracted from the SLoT model, which are related to the charge transport of the systems described in this work, are listed in **Table S1**.

As described in the main text, σ_0 is related to the intrinsic conductivity when there are no localization effects present; $W_{H,max}$ represents the localization energy in the low doping regime; and $W_{H,\ slope}$ is how rapidly the localization energy decrease with increasing doping level. Furthermore, Gregory and coworkers define the parameters, c_{max} , A_0 and A_1 as freely adjustable parameters related to the to the carrier concentration ratio:

$$c = f(E) = \frac{c_{max}}{\exp\left[A_0(A_1 - \eta)\right] + 1} \tag{S4}$$

where c is the carrier concertation ratio, $f(E)$ is Fermi-Dirac distribution function and η is the reduced Fermi energy level.

PARAMETERS	F_4TCNQ	AE (LITFSI)	DDB-F72	DDB-F36
σ_0 (S/cm)	10	125	25	35
$W_{H,max}$ (meV)	210	275	500	750
$W_{H,slope}$ (meV)	310	350	1000	1550
c_{max}	0.25	0.4	0.25	0.25
A_0	0.5	0.5	1	0.25
A_1	1.8	2	2	3.8

Table S 11. Parameters obtained from the SLoT fits performed in the P3HT doped with F_4TCNQ, anion exchange (AE), DDB-F72 and DDB-F36.

APPENDIX E

Rub-Aligning Setup Standard Operating Procedure

This Standard Operating Procedure (SOP) outlines the fabrication of rub-aligned films. It also includes detailed information about the components and electrical wiring of the rub-aligning setup, which will be useful for disassembly and repairs. Additionally, the SOP covers the microcontroller code and programming instructions, in case modifications are required.

Procedures for Fabricating Rub-aligned Films

Note: This procedure is optimized specifically to rub-align 97% regioregular (RR) P3HT films with thickness ranging between 100-150 nm. Certain parameters might need to be adjusted when using a different polymer or film thickness.

1. Spin-coat ~120 nm thin films of P3HT
    a. Prepare a solution of 20 mg P3HT in 1mL ODCB solution to make a 2% wt/vol P3HT solution
    b. Stir the solution with a Teflon coated stir bar for at least an hour. Visibly check to make sure that there is no visible solid clinging to the wall of the container.
    c. Cut and clean ~ 1.2x1.2 cm glass or silicon substrates. It is crucial that the substrate is thoroughly clean and plasma etched as this will affect how the quality of the P3HT films.

d. Place the ~1.2x1.2 cm substrate onto the spin coater and deposit ~5-10 µL of the 2% P3HT solution onto the surface of the substrate. It is recommended to try to spread the solution so that the whole substrate is covered.

e. Proceed to spin-coat at a rate of 1000 rpm for 60 seconds. This should give a film with thickness of ~120 nm.

f. Let the film dry for ~ 2-3 hours to before proceeding to rub-aligning

2. Rub-aligning ~120nm P3HT film

a. Heat the P3HT film up to ~140^{o}C on a hot plate. It takes ~2 minutes for the film to fully equilibrate. It is fine to leave the film on for more than 2 minutes as you adjust the setup.

b. To hold the film in place, use two substrates of similar size and thickness to sandwich the P3HT film in between so that it does not move during the rub-aligning process. Use high temperature polyimide tape to secure down the two glass substrate to the hotplate.

c. Turn on the rub-aligning setup. The microfiber wheel will start rotating as soon as the setup is turned on. Make sure that nothing is touching the microfiber wheel at this point.

d. Since no pressure is being applied on the microfiber wheel (which is connected to the load cell), the LCD screen should display a value of 0 (with fluctuation smaller than $\pm$1).

e. In the case that the value shown is above 1, press the button under the LCD screen to tare the load cell reading.
f. To rub-align, start by lowering the rotating microfiber down onto a blank substrate (not the one with the P3HT film) by slowly turning the dial on the lab jack.
g. Keep lowering until the LCD screen reads a value of 140 (this corresponds to ~1 N of force).
h. Once the desired force is reached push the hotplate forward so that the rotating microfiber wheel can go over the P3HT film. The film should now be aligned.
i. Quickly remove the film from the hotplate. This is crucial as if left for too long on the hotplate, the polymer film will lose alignment due to the heat.

General Operation of the Rub-Aligning Setup

The rub-aligning setup (excluding the hotplate) consists of five main parts: the microfiber wheel, stepper motor, load cell, microcontroller box, and lab jack. The microfiber wheel is attached to the stepper motor via a 3D-printed fixture, which is then connected to a load cell fixed to a lab jack stand. Both the stepper motor and load cell are linked to the microcontroller box. The microcontroller controls the stepper motor's RPM, reads the load cell signal, and displays it on the LCD screen.

Schematic of the Electrical Wiring for the Stepper Motor to the Microcontroller

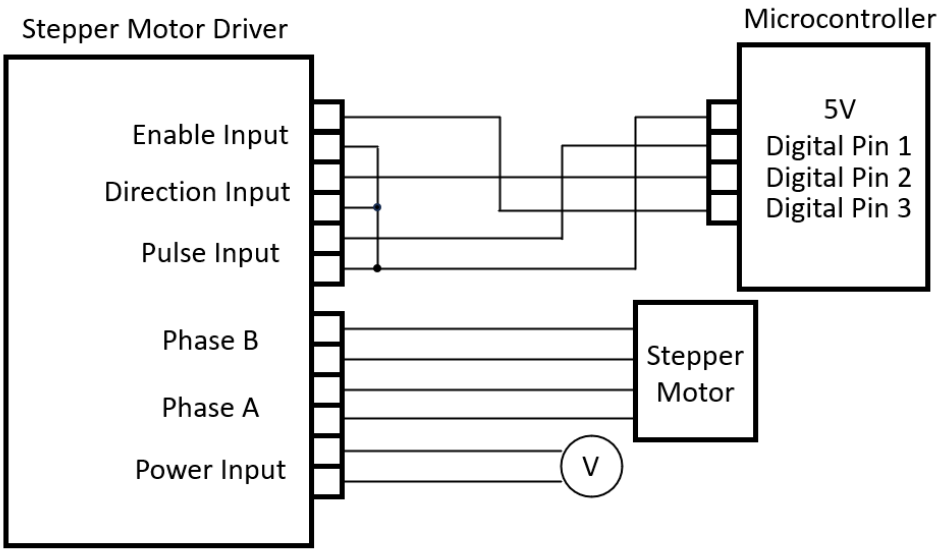

Figure S 28. Schematic of the wiring for stepper motor to microcontroller. The stepper motor driver is used to help convert the pulse signal from the microcontroller to a sequence that alternates between phase A and B to turn the stepper motor at a set rate.

1. How stepper motor works and the wiring involved
    a. First set the positive "enable, direction, and pulse" inputs on the stepper motor driver are connected to the 5V (high voltage reference state) on the microcontroller. This is called "common-anode connection"
    b. Next set the stepper motor driver to enabled state which will allow the driver to respond to the input pulse of the microcontroller, by setting the "enable input"

signal to low (below 3.3V) using one of the digital output pins on the microcontroller.

c. To control the rpm of the stepper motor, connect the negative "pulse input" pin on the stepper motor driver to a digital pin on the microcontroller. The microcontroller is programmed to send out pulses at a set frequency. This frequency is proportional to the rpm.

d. To control the direction of the stepper motor rotation, supply either a high input signal (above 3.3V) or a low input signal (below 3.3V) to the negative "direction input" using one of the digital output pins on the microcontroller.

e. To provide the power to drive the stepper motor, connect an adequate power supply (12-24V and ~1.5 A) to the "power input" of the stepper motor driver.

f. Finally connect the stepper motor to the stepper motor driver "Phase A and B" output.

2. Code for Arduino microcontroller to control stepper motor.

a.
```
// Define which digital pin to use on the arduino microcontroller
const int stepPin = 5;
const int dirPin = 2;
const int enPin = 8;
void setup()
{
  // Sets the pins as Outputs
  pinMode(stepPin,OUTPUT);
```

```
  pinMode(dirPin,OUTPUT);
  pinMode(enPin,OUTPUT);

// Set the "enable pin" as low voltage
  digitalWrite(enPin,LOW);

// Loop between high and low value on the “pulse pin”
void loop()
 {
   digitalWrite(stepPin,HIGH);
   delayMicroseconds(Value); // Replace “Value” with a number
   digitalWrite(stepPin,LOW);
   delayMicroseconds(Value); // Replace “Value” with a number
 }
```

b. For this specific stepper motor (2 Phases), the step angle is 1.8^{o} degree. This means that each pulse of current will move the motor by 1.8^{o} degree and 200 pulses will make a complete revolution. Using the following formula, you can calculate out what pulse frequency to use to obtain certain rpm.

$$Pulse\ frequency = (rpm) \times \left(\frac{1min}{60s}\right) \times \left(200\,\frac{pulse}{revolution}\right)$$

Schematic of the Electrical Wiring for the Load Cell to the Microcontroller

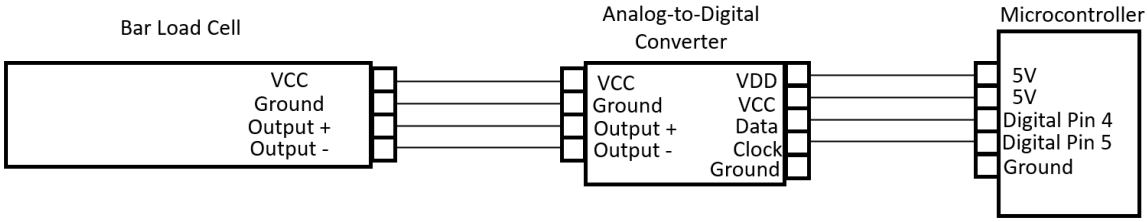

Figure S 29. Schematic of load cell wiring to a microcontroller. The load cell changes in resistance are picked up by the analog-to-digital converter and the signal is then amplified. The amplified signal is then fed and sync up with the microcontroller to read.

1. How load cell works and the wiring involved
    a. The internal operation of the load cell involves strain gauges arranged in a Wheatstone bridge configuration. Voltage is applied between two points in the Wheatstone bridge, and the measurement is taken between another two points, similar to a four-point probe setup. This setup requires four connections: VCC, Ground, Output +, and Output -.
    b. The four connections are connected to an analog-to-digital (ADC) converter. As the resistance changes in the load cell are typically very small, the signal needs to be amplified by an ADC.
    c. The amplified signal is then sent to the microcontroller to read and display on LCD screen. The microcontroller also serve as the power source by supplying the 5V to both the ADC and the bar load cell.

2. Code for Arduino microcontroller to read data off of the ADC.

    a. //Download and install the <Wire.h> and HX711 library. These two library contain the communication protocol to set up I2C devices and interface with the Avia Semiconductor chip used in the ADC.

```
#include <Wire.h>
#include <HX711.h>
//Create an instance of the HX711
HX711 scale;
// Define digital pins for the connections (set to 8bits)
unit8_t dataPin = 6;
unit8_t clockPin = 7;
// Initialize volatile variable of type float
Volatile float f;
void setup()
{
//Initialize serial port communication for the ADC
Serial.begin(115200); //set baud rate to 115200
scale.begin(dataPin, clockPin); //set the digital pins for data and clock
scale.set_scale(127.15); //This is a default calibration number
scale.tare(); //set whatever initial reading is to zero
}
```

```
void loop()
{
f = scale.get_units(5); //average 5 raw readings and subtract from offset and
divide by default calibration value.
Serial.println(f); //Have Arduino send data to computer to read using serial
communication.
delayMicrosceconds(50); //delay for 50 microsceonds
}
```

APPENDIX F

Seebeck Coefficient Experiment Standard Operating Procedure

This Standard Operating Procedure (SOP) goes over details on how to carry out Seebeck experiment. It covers details such as electrode patterning, Seebeck setup, and running the experiment in Labview. The Seebeck experiment itself is relatively straightforward to carry out, however, it is worth to understand how the setup operates in the case that troubleshooting is needed.

Electrode Pattern for Seebeck Coefficient Experiment

The Seebeck Coefficient can be measure with various patterns as long as there is a well define continuous temperature gradient exists between the two points of measurement. The electrode pattern shown here uses a long rectangular electrode pattern that runs along the film. The long pattern is intended as a way to average a larger area rather than using point contacts. The dimension of the substrate in this case needs to be 1.5 x 1.5 cm to fit correctly in the shadow mask.

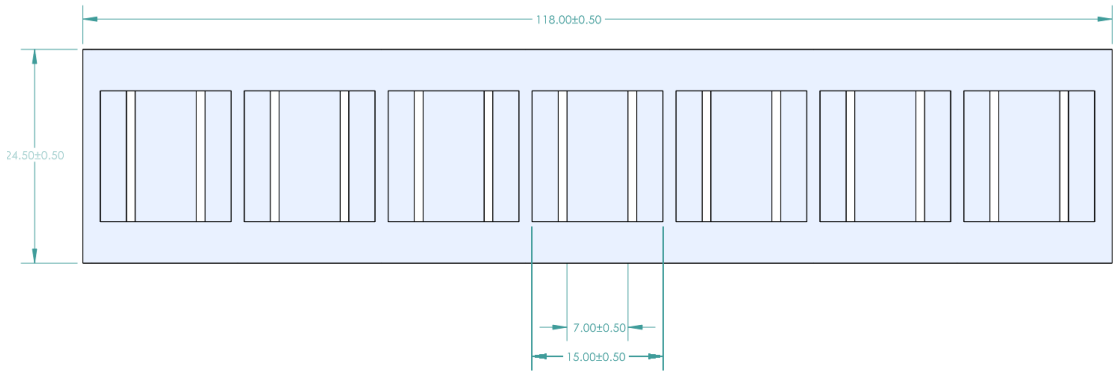

Figure S 30. Drawing of shadow mask use for thermal evaporating metal electrodes on the doped semiconducting polymer films.

Experimental Set Up and Measuring the Seebeck Coefficient

1. Connect the two BNC cables that is labelled RTD A and RTD B to the Keithley 2400 front and back Input/Output. This connection is for measuring the temperature of the hot and cold electrodes.

Figure S 31. Locations of the Input/Output connections on the Keithley 2400 to plug the BNC (w/ banana plug) into for Seebeck coefficient measurement.

2. Connect the BNC cable labelled Voltage to the HP663B power supply. There should be another BNC cable that is already connected to the HP663B. You will just need to connect the Voltage BNC cable to this cable. This connection is to control the Peltier plates that are used to generate the temperature gradient.

Figure S 32. Picture of the HP663B power supply and the location to connect the BNC cable to the power supply.

3. Connect the BNC cable labelled C to the Keithley 2000 Inputs. This connection is for measuring the voltage difference between the hot and cold electrodes.
4. Turn on the Keithleys and the HP663B.
5. Make sure that the Keithleys communication protocol is set to GPIB otherwise the program will not be able to communicate with the instrument.
6. Open the LabView program called Seebeck Measurement.
7. Before you can run the experiment, you must need to place the sample onto the Seebeck setup so that the electrodes are aligned with the two bottom pogo pin contacts.
8. Use the toggle clamp to press down onto the sample to secure it from moving.
9. Place the Peltier plates on each side of the sample.

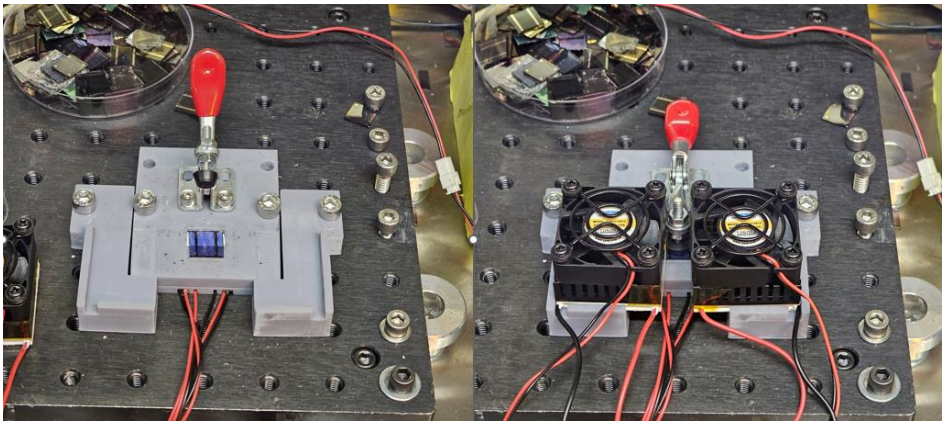

Figure S 33. Picture of the Seebeck setup with and without the Peltier plate on top of the semiconducting polymer film.

10. The Peltier plates have a radiator with fans attached to it. Make sure to plug this into the outlet before measuring as this helps equilibrate the temperature of the Peltier plates faster.
11. On the LabView program type in a value for the voltage apply and run the program. The higher the voltage the bigger the temperature difference. However, do not going above 2V as the radiator fan won't be able to cool the Peltier fast enough.

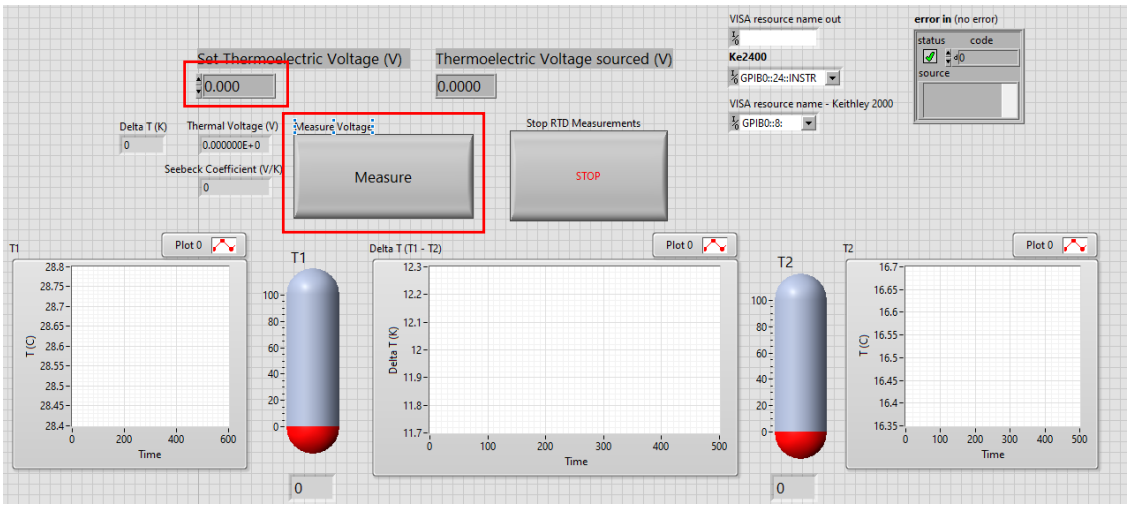

Figure S 34. Front panel of Seebeck measurement LabView program. First enter in the desired voltage to power the Peltier plates then run the program. Once the temperature equilibrate (stabilized) click on the Measure button to measure the voltage difference induced by the temperature gradient.

12. While the program is running it will display the temperature difference on the screen. Wait till the temperature difference stabilize or stop changing too much before clicking on the measure button. The time it takes to equilibrate is ~2 minutes.
13. Pressing the measure button will stop the program and record the voltage difference between the hot and cold electrodes. Copy this along with the temperature difference onto an excel sheet as this is basically your Seebeck Coefficient (Voltage/Temperature).
14. Repeat this for different temperature difference. I recommend at least having 4 data points.
15. After collecting the last temperature difference, set the voltage back to zero before testing a new sample.

APPENDIX G

Temperature-Dependent Conductivity Standard Operating Procedure

This Standard Operating Procedure (SOP) goes over details on how to perform temperature-dependent conductivity experiment. It covers details such as setting up the experiment and running the experiment using Labview.

Experimental Set Up and Measuring the Temperature-Dependent Conductivity

The sample preparation for this experiment is exactly the same as for Hall effect, which uses Van der Pauw electrode geometry (square sample with electrodes deposit at the four corners). The only difference is that the sample will be temperature-controlled.

1. Connect the toggle switch banana plugs connection to the back connections of the Keithley 2400. It doesn't matter which pairs goes into Input/Output or Wire Sensing as long as they are facing in the same direction as shown in the picture.

Figure S 35. Picture of the connection to the Keithley 2400 for electrical conductivity measurement.

2. The toggle switch has four clips that is used to clip onto the 2 wires for sourcing current and 2 wires for measuring voltage. It doesn't matter what color you connect the wires to as long as the same color is being used for either current or voltage.

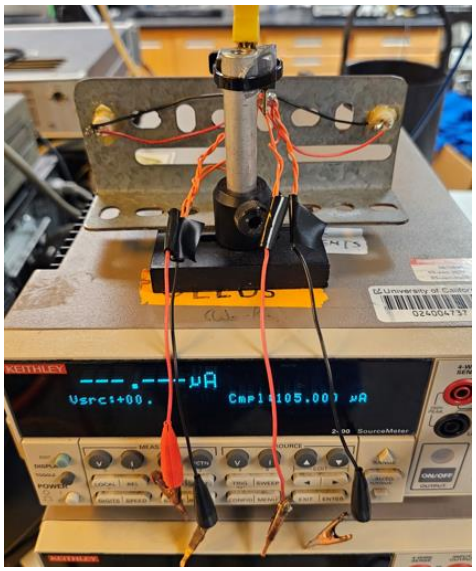

Figure S 36. Picture of the toggle switch with the four clips for sourcing current and measuring voltage difference.

3. Next connect the Peltier plate connection to the HP663B power supply. Similar connection is shown in Appendix E.
4. Next load the film onto the setup inside the argon box. The film should be facing upward, as the contact probes are coming from the top. Use a tweezer to move the RTD probe and the contact probes on top of the film. The contact probes should be touching the electrode pads on the film.

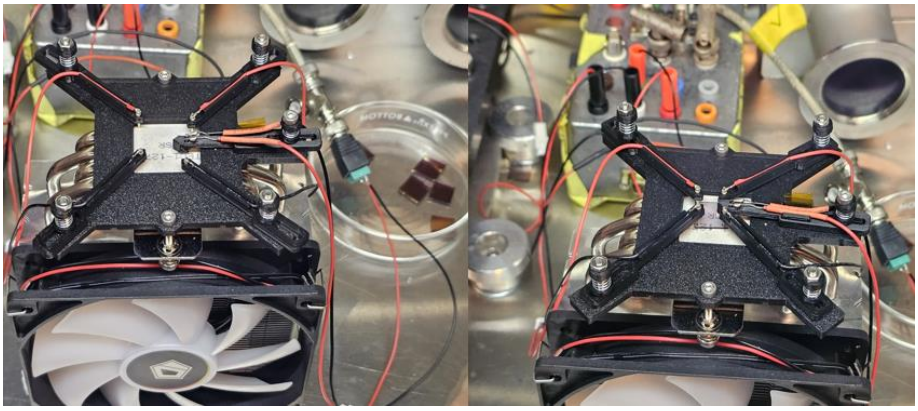

Figure S 37. Picture of the temperature-dependent conductivity setup. The four probes that are at the corner of the square are used to measure conductivity. The probe that is going in through the middle is the RTD which is used to measure temperature.

5. Next open the Temperature_Dependent_Conductivity LabView program.
6. To run the program, first enter in a value for the applied voltage. This voltage will determine the temperature of the Peltier plate and therefore your film. I typically start with 0 V and then move up with increment of 1 or 2 V. Do not exceed 8V as the Peltier plate will be unable to hold the temperature long enough to measure the electrical conductivity as the cooling of the Peltier plate is passive.

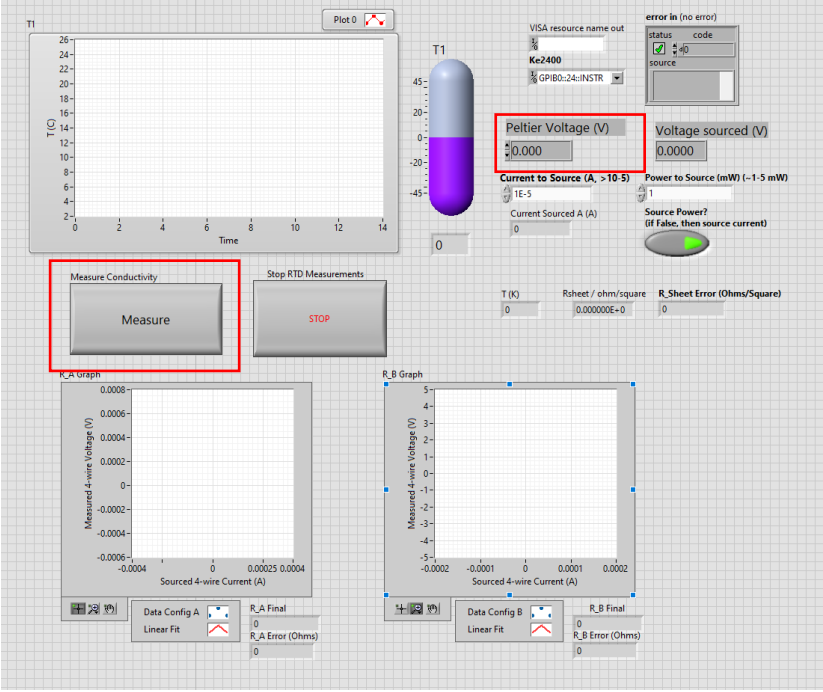

Figure S 38. Labview front panel to measure temperature-dependent conductivity. First type in the desired voltage to power the Peltier plate (the higher the voltage, the colder the plate). Once temperature stop changing click on measure to measure the electrical conductivity of the film at that temperature.

7. Once the temperature that is being plotted stabilized, click on measure. This will initiate the Van der Pauw program to measure the electrical conductivity.
8. Repeat the measurement until you have electrical conductivity for at least four different temperatures.

The activation energy or barrier to hopping can be extract using Arrhenius approach using the equation (1). By plotting the natural log of the conductivity, you measured against 1/T, the activation energy is the slope of the linear fit times the Boltzmann constant (k_B).

$$\ln\big(\sigma(T)\big) = \ln(\sigma_0) - \frac{E_a}{k_B T} \qquad (1)$$

APPENDIX H

Matlab Script for Stitching and Calibrating 3-D profilometer Data to Obtain Average Thickness and Surface Roughness

In most cases, the films produced are relatively smooth, and their thickness can be easily measured by performing a profilometry scan at different spots on the film. However, if the film is extremely rough, it is highly recommended to use a 3-D profilometer to obtain the average thickness of the scanned area. Unlike a standard single scan, where the user can simply level the data in real-time and record the thickness, a 3-D scan may include over a hundred individual scans. It is possible but tedious to level each scan individually and then average them to determine the average thickness. This Matlab script is designed to assist with this process and provide a more systematic method for leveling the data. Although the script can help with automating this process, it is still highly recommended to always double check the result manually with one or two sample scans, hence why this script was not made into a function, so that all variables are kept at the end of the script.

Note: The data must be saved as xyz format without headings in order for the script to work correctly

```
%Open dialog box to select the 3-D profilometer data with .ASC format
clear;
[file,path] = uigetfile('.ASC');
if file == 0
    return;
else
    cd(path);
end

%Read and upload the data into Matlab
opts = detectImportOptions(file,'FileType','text');
DataS = readmatrix(file,opts);
```

```
DataT = DataS;

%Divide the data by 10 so that the unit is in microns
DataS(:,3) = (DataT(:,3)/10);

%Find total number of scans in the X direction
StepS = find(DataS(:,1)== DataS(1,1));
TotalScans = numel(StepS);

%% Align and store 2D Data

 DN = 700; %Number of points to use for moving average
 SN = 600; %number of points use for fitting the glass substrate data

for aa= 1:TotalScans

    TempScanData = DataS(aa:TotalScans:end,[1 3]);

    %Use this to flip data if start scan from polymer to glass
    TempScanData(:,2) = flipud(TempScanData(:,2));

    OrigData{aa,1}(:,:) = TempScanData;

    %Moving window to get lowest point for extrapolation.
    WindowSize = 100;

    %Get correlation step size from cell position to scan step size
    cellMat = [1:DN]';
    corrStep = polyfit(cellMat(SN:DN), TempScanData(SN:DN,1),1);

    for nn = 1:(DN/WindowSize)

        %Convert matrix to cell to use with cellfun
        DataCell = num2cell(OrigData{aa,1}(nn*WindowSize-(WindowSize-
        1):nn*WindowSize,2));

        %value          %position
        [IndexData(nn,1),IndexData(nn,2)] = min(cellfun(@min, DataCell));

        %matrix contaning min y values for each window
       MinMatrix(nn,1) = (IndexData(nn,2)+((WindowSize*nn)-
      WindowSize))*corrStep(1,1)+corrStep(1,2); %Vertical distance or x
        MinMatrix(nn,2) = IndexData(nn,1);  %Height or z

    end

    BaseLine{aa,1}(:,1) = MinMatrix(:,1); %x direction
    BaseLine{aa,1}(:,2) = filloutliers(MinMatrix(:,2),'linear'); %z direction
adjusted for spike in data


    %Flatten Baseline then perform another outlier removal
```

```
    pBaseLine = polyfit(BaseLine{aa,1}(:,1),BaseLine{aa,1}(:,2),1);
    FlatBaseLine = BaseLine{aa,1}(:,2)- BaseLine{aa,1}(:,1)* pBaseLine(1,1);
    SecOutlierRemove{aa,1}(:,1) = filloutliers(FlatBaseLine, 'linear');

    %After removing outliers return the BaseLine back to tilt position to
obtain slope
    SecBaseLine{aa,1}(:,1) = BaseLine{aa,1}(:,1);
    SecBaseLine{aa,1}(:,2) = SecOutlierRemove{aa,1}(:,1)+(BaseLine{aa,1}(:,1)*
pBaseLine(1,1));


    %Get slope and intercept from MinMatrix to remove tilt
    pMinMatrix(aa,:) = polyfit(SecBaseLine{aa,1}(:,1),
SecBaseLine{aa,1}(:,2),1);

    %Subtract tilt from data
    TiltSubData{aa,1}(:,1) = TempScanData(:,1);
    TiltSubData{aa,1}(:,2) = TempScanData(:,2)-
(TempScanData(:,1)*pMinMatrix(aa,1))-pMinMatrix(aa,2);


    %Perform another outlier removal
    %Test = filloutliers(TiltSubData{aa,1}(1:2600,2),'linear');



    LowP(aa,1) = min(filloutliers(TiltSubData{aa,1}(1:DN,2), 'linear'));


    FinalData{aa,1}(:,1) = TempScanData(:,1);
    FinalData{aa,1}(:,2)= TiltSubData{aa,1}(:,2) -LowP(aa,1);


    %Average thickness of each scan
    AveThicknessPerScan(aa) = mean(FinalData{aa,1}(2000:3000,2));
    SumResidualZ(aa) = sum(abs(AveThicknessPerScan(aa)-
FinalData{aa,1}(2000:3000,2)));



end

AveT = AveThicknessPerScan';
Z_xy = SumResidualZ';

%Average thickness of all scans without outlier
figure;
ThicknessOutlier = rmoutliers(AveThicknessPerScan);
FinalAveThickness = mean(ThicknessOutlier)
```

References

[1] L. Biniek et al., High-Temperature Rubbing: A Versatile Method to Align π-Conjugated Polymers without Alignment Substrate, Macromolecules 47, 3871 (2014).

[2] A. Hamidi-Sakr, L. Biniek, J.-L. Bantignies, D. Maurin, L. Herrmann, N. Leclerc, P. Lévêque, V. Vijayakumar, N. Zimmermann, and M. Brinkmann, A Versatile Method to Fabricate Highly In-Plane Aligned Conducting Polymer Films with Anisotropic Charge Transport and Thermoelectric Properties: The Key Role of Alkyl Side Chain Layers on the Doping Mechanism, Adv. Funct. Mater. 27, 1700173 (2017).

[3] J. Lindemuth and S.-I. Mizuta, Hall Measurements on Low-Mobility Materials and High Resistivity Materials, in Thin Film Solar Technology III, Vol. 8110 (SPIE, 2011), pp. 65–71.

[4] F. Werner, Hall Measurements on Low-Mobility Thin Films, J. Appl. Phys. 122, 135306 (2017).

[5] Y. Chen, H. T. Yi, and V. Podzorov, High-Resolution Ac Measurements of the Hall Effect in Organic Field-Effect Transistors, Phys. Rev. Appl. 5, 034008 (2016).

[6] T. J. Aubry et al., Dodecaborane-Based Dopants Designed to Shield Anion Electrostatics Lead to Increased Carrier Mobility in a Doped Conjugated Polymer, Adv. Mater. 31, 11 (2019).

[7] D. T. Scholes, P. Y. Yee, J. R. Lindemuth, H. Kang, J. Onorato, R. Ghosh, C. K. Luscombe, F. C. Spano, S. H. Tolbert, and B. J. Schwartz, The Effects of Crystallinity on Charge Transport and the Structure of Sequentially Processed F 4 TCNQ-Doped Conjugated Polymer Films, Adv. Funct. Mater. 27, 44 (2017).

[8] S. A. Gregory, R. Hanus, A. Atassi, J. M. Rinehart, J. P. Wooding, A. K. Menon, M. D. Losego, G. J. Snyder, and S. K. Yee, Quantifying Charge Carrier Localization in Chemically Doped Semiconducting Polymers, Nat. Mater. 20, 10 (2021).

[9] Lenz, S.; Bonini, M.; Nett, S. K.; Lechmann, M. C.; Emmerling, S. G. J.; Kappes, R. S.; Memesa, M.; Timmann, A.; Roth, S. V.; Gutmann, J. S. Global Scattering Functions: A Tool for Grazing Incidence Small Angle X-Ray Scattering (GISAXS) Data Analysis of Low Correlated Lateral Structures. *Eur. Phys. J. Appl. Phys.* **2010**, *51* (1), 10601. https://doi.org/10.1051/epjap/2010064.

[10] Beaucage, G. Approximations Leading to a Unified Exponential/Power-Law Approach to Small-Angle Scattering. *J. Appl. Crystallogr.* **1995**, *28* (6), 717–728. https://doi.org/10.1107/S0021889895005292.

[11] Buggy, N. C.; Du, Y.; Kuo, M.-C.; Seifert, S.; Gasvoda, R. J.; Agarwal, S.; Coughlin, E. B.; Herring, A. M. Designing Anion-Exchange Ionomers with Oriented Nanoscale Phase Separation at a Silver Interface. *J. Phys. Chem. C* **2021**, *125* (37), 20592–20605. https://doi.org/10.1021/acs.jpcc.1c06036.

[12] Lindemuth, J.; Mizuta, S.-I. Hall Measurements on Low-Mobility Materials and High Resistivity Materials. In *Thin Film Solar Technology III*; SPIE, 2011; Vol. 8110, pp 65–71. https://doi.org/10.1117/12.893100.

[13] Chen, Y.; Yi, H. T.; Podzorov, V. High-Resolution Ac Measurements of the Hall Effect in Organic Field-Effect Transistors. *Phys. Rev. Appl.* **2016**, *5* (3), 034008. https://doi.org/10.1103/PhysRevApplied.5.034008.

[14] Werner, F. Hall Measurements on Low-Mobility Thin Films. *J. Appl. Phys.* **2017**, *122* (13), 135306. https://doi.org/10.1063/1.4990470.

[15] Aubry, T. J.; Winchell, K. J.; Salamat, C. Z.; Basile, V. M.; Lindemuth, J. R.; Stauber, J. M.; Axtell, J. C.; Kubena, R. M.; Phan, M. D.; Bird, M. J.; Spokoyny, A. M.; Tolbert, S. H.;

Schwartz, B. J. Tunable Dopants with Intrinsic Counterion Separation Reveal the Effects of Electron Affinity on Dopant Intercalation and Free Carrier Production in Sequentially Doped Conjugated Polymer Films. *Adv. Funct. Mater.* **2020**, *30* (28), 2001800. https://doi.org/10.1002/adfm.202001800.

[16] Duong, Q. M.; Garcia Vidales, D.; Salamat, C. Z.; Tolbert, S. H.; Schwartz, B. J. Measuring the Anisotropic Conductivity of Rub-Aligned Doped Semiconducting Polymer Films: The Role of Electrode Geometry. *Phys. Rev. Appl.* **2024**, *21* (2), 024006. https://doi.org/10.1103/PhysRevApplied.21.024006.

[17] Gregory, S. A.; Hanus, R.; Atassi, A.; Rinehart, J. M.; Wooding, J. P.; Menon, A. K.; Losego, M. D.; Snyder, G. J.; Yee, S. K. Quantifying Charge Carrier Localization in Chemically Doped Semiconducting Polymers. *Nat. Mater.* **2021**, *20* (10), 1414–1421. https://doi.org/10.1038/s41563-021-01008-0.

10[18] Wang, S.; Ha, M.; Manno, M.; Daniel Frisbie, C.; Leighton, C. Hopping Transport and the Hall Effect near the Insulator–Metal Transition in Electrochemically Gated Poly(3-Hexylthiophene) Transistors. *Nat. Commun.* **2012**, *3* (1), 1210. https://doi.org/10.1038/ncomms2213.

[19] Scholes, D. T.; Yee, P. Y.; McKeown, G. R.; Li, S.; Kang, H.; Lindemuth, J. R.; Xia, X.; King, S. C.; Seferos, D. S.; Tolbert, S. H.; Schwartz, B. J. Designing Conjugated Polymers for Molecular Doping: The Roles of Crystallinity, Swelling, and Conductivity in Sequentially-Doped Selenophene-Based Copolymers. *Chem. Mater.* **2019**, *31* (1), 73–82. https://doi.org/10.1021/acs.chemmater.8b02648.

[20] Fontana, M. T.; Stanfield, D. A.; Scholes, D. T.; Winchell, K. J.; Tolbert, S. H.; Schwartz, B. J. Evaporation vs Solution Sequential Doping of Conjugated Polymers: F_4TCNQ Doping of Micrometer-Thick P3HT Films for Thermoelectrics. *J. Phys. Chem. C* **2019**, *123* (37), 22711–22724. https://doi.org/10.1021/acs.jpcc.9b05069.

[21] Aubry, T. J.; Axtell, J. C.; Basile, V. M.; Winchell, K. J.; Lindemuth, J. R.; Porter, T. M.; Liu, J.-Y.; Alexandrova, A. N.; Kubiak, C. P.; Tolbert, S. H.; Spokoyny, A. M.; Schwartz, B. J. Dodecaborane-Based Dopants Designed to Shield Anion Electrostatics Lead to Increased Carrier Mobility in a Doped Conjugated Polymer. *Adv. Mater.* **2019**, *31* (11), 1805647. https://doi.org/10.1002/adma.201805647.

[22] Hofmann, A. I.; Kroon, R.; Zokaei, S.; Järsvall, E.; Malacrida, C.; Ludwigs, S.; Biskup, T.; Müller, C. Chemical Doping of Conjugated Polymers with the Strong Oxidant Magic Blue. *Adv. Electron. Mater.* **2020**, *6* (8), 2000249. https://doi.org/10.1002/aelm.202000249.

[23] Neusser, D.; Malacrida, C.; Kern, M.; Gross, Y. M.; van Slageren, J.; Ludwigs, S. High Conductivities of Disordered P3HT Films by an Electrochemical Doping Strategy. *Chem. Mater.* **2020**, *32* (14), 6003–6013. https://doi.org/10.1021/acs.chemmater.0c01293.

[24] Untilova, V.; Biskup, T.; Biniek, L.; Vijayakumar, V.; Brinkmann, M. Control of Chain Alignment and Crystallization Helps Enhance Charge Conductivities and Thermoelectric Power Factors in Sequentially Doped P3HT:F4TCNQ Films. *Macromolecules* **2020**, *53* (7), 2441–2453. https://doi.org/10.1021/acs.macromol.9b02389.